Bio-optical Modeling of Aquatic Photosynthesis in the Laurentian Great Lakes

by

Gregory Michael Silsbe

A thesis
presented to the University of Waterloo
in fulfillment of the
thesis requirement for the degree of
Doctor of Philosophy
in
Biology

Waterloo, Ontario, Canada, 2010

AUTHOR'S DECLARATION

I hereby declare that I am the sole author of this thesis. This is a true copy of the thesis, including any required final revisions, as accepted by my examiners.
I understand that my thesis may be made electronically available to the public.

Abstract

Photosynthesis, the conversion of light energy to chemical energy, is amongst the most fundamental and ubiquitous processes on the planet. In virtually every large aquatic ecosystem, photosynthetic organisms are the single largest pool of both total biomass; and organic matter derived through photosynthesis, termed phytoplankton production, energetically supports all other trophic levels. Moreover the most common proxies of water quality theoretically and empirically co-vary with phytoplankton production. Thus accurate measurements of phytoplankton production are important at an ecosystem level, but also at a global level as phytoplankton photosynthesis is a major component of the earth's carbon cycle. The methodology of phytoplankton production measurements in the Laurentian Great Lakes and other freshwater lakes has remained largely unchanged in the past 40 years. In most studies photosynthesis from a single water sample is measured across an *in vitro* light gradient usually using an artificial light source then extrapolating to the *in situ* environment. These traditional methods are laborious, thus limiting the amount of observations in space and time, and may not accurately represent *in situ* photosynthesis. Active chl *a* fluorescence, intrinsically linked to photosynthesis, can be measured *in situ* and instantaneously. Various bio-optical models that scale these fluorescence measurements to phytoplankton production are gaining widespread attention in the marine environment but have not been extensively tested in freshwater ecosystems.

The methodology and efficacy of the various bio-optical models are tested in this thesis using a large dataset of active fluorescence profiles and ancillary water chemistry parameters against synchronously derived *in vitro* phytoplankton production collected across

mixing, trophic and taxonomic gradients in Lake Erie. From this analysis, the most common bio-optical model parameterization yields photosynthetic rates that are largely incongruent with *in vitro* measurements. Bio-optical models are largely a function of two parameters, the absorption spectrum of photosystem II (a_{PSII}) and the photochemical efficiency of PSII (f_{PSII}). In Lake Erie f_{PSII} is relatively constrained suggesting that even nutrient limited phytoplankton achieve balanced growth by adjusting the supply of energy through changes in light harvesting (a_{PSII}) to match the demand for photosynthetic energy. This thesis goes on to demonstrate the success of bio-optical models depends largely on the formulation of a_{PSII}. Alternative methods to derive a_{PSII}, largely ignored in published bio-optical models, are reviewed, formulated, and when incorporated into a bio-optical model and compared to synchronous *in vitro* production measurements, this novel bio-optical model outperforms all other comparative studies performed across a taxonomic gradient.

Having established a method that provides reliable *in situ* estimates of phytoplankton production, this thesis goes on to quantify the magnitude of error associated with common assumptions that are inherent to traditional methodologies but not to the bio-optical model developed here. Photosynthetic rates vary with the spectral quality of irradiance and euphotic zone spectra are highly variable through time and space, especially over depth, and are often poorly reproduced by i*n vitro* light sources. Spectral correction factors (SCFs) can be derived to estimate the disparity of phytoplankton production estimates that arise through differences between *in situ* and *in vitro* light environments. Through the development of an empirical model, this thesis demonstrates that the magnitude of SCFs vary predictably across optical and chl *a* gradients. Moreover the model shows that for commonly employed *in vitro*

light sources, phytoplankton production is routinely underestimated by traditional *in vitro* methods, especially in transparent oligotrophic waters. When applied to historic phytoplankton production estimates in Lake Erie, the model predicts that the reported lakewide decreases of phytoplankton production following nutrient loading abatement has been overestimated by a factor of 2. This thesis also investigates how persistent vertical patterns of *in situ* photosynthesis deviate from nominally scaled *in vitro* measurements across mixing, trophic and taxonomic gradients in Lake Erie and opportunistic measurements in Lake Superior and Georgian Bay. The presence of deep chlorophyll maxima (DCM) in these lakes significantly enhances *in situ* production relative to nominal *in vitro* scaling assumptions. Not only is DCM production enhanced through elevated biomass relative to the epilimnion, but DCM phytoplankton communities appear to be spectrally adapted to these low light environments.

Taken together, the common assumptions employed in traditional *in vitro* phytoplankton production measurements may underestimate *in situ* photosynthesis by a factor of 2. The disparities between *in vitro* and *in situ* estimates are greatest in transparent waters where DCMs are likely to occur when the water column is stratified and where *in situ* spectral irradiance can deviate significantly from *in vitro* light sources. These disparities are large relative to the accuracy of bio-optical estimates of phytoplankton production shown here. Thus the bio-optical model developed here yields better estimates of phytoplankton photosynthesis than the commonly used traditional approach. The main recommendation of this thesis is that the agencies responsible for monitoring and the stewardship of the Laurentian Great Lakes immediately adopt bio-optical measurements. This will not only

obtain more reliable estimates of phytoplankton photosynthesis, but as these measurements can be made autonomously, photosynthesis and its driving constituents can be characterized in these dynamic ecosystems at unparalleled spatial and temporal resolution.

Acknowledgements

This thesis would not have been possible without the unwavering support and patience of my Ph.D. supervisors Ralph Smith and Bob Hecky. Their guidance and thoughtful suggestions throughout fieldwork, data analysis and thesis writing is greatly appreciated. I would also like to thank my committee members Bruce Greenberg and Stephanie Guildford. Bruce's instruction, guidance and deeply appreciated 'first principles approach' in his photobiology graduate course is a defining moment in my education. Stephanie Guildford, as always, showed continuous enthusiasm for all my research endeavors, honed my knowledge of nutrient dynamics, and was instrumental in planning the 2005 fieldwork.

My graduate experience has been significantly through the friendship, advice, and thoughtful discussions amongst my colleagues within the University of Waterloo Aquatic Ecology Group (UWAEG). Foremost within this group I owe a large debt of gratitude to Dave Depew. Over the course of my Ph.D. Dave took responsibility for the UWAEG research vessel and CHN analyzer, was great to bounce ideas off of, and perhaps most importantly introduced me to the wonderful world of R. I'm in awe of the intelligence and depth of knowledge of Sairah Malkin and Mohammed Mohammed, I've learned more about aquatic ecology through them than any textbook, except Aquatic Photosynthesis. Tedy Ozersky, Serghei Bocaniov, Luis Leon, Mark Lampi, Yola Gurska and Anabel Uekermann each helped with either equipment, data analysis or assurance over the course of my Ph.D.

Few people can suffer 41 consecutive hours of filtering, Adam Houben is one of them. The tireless efforts and good humour of various technicians helped create the data in this thesis. I would like to thank Christian Blyth, Tim Kuntz, Amanda Poste, Ryan Hutchins,

Cassie Corrigan and Emily (Hazzard) Colvin for all their help and acknowledge Bob, Stephanie and Ralph for hiring such excellent people. I thank Caren Binding (Environment Canada) for providing valuable water column absorption data, Michael Twiss (Clarkson Univsersity) for providing ^{14}C solution stock and most importantly Todd Howell (Ontario Ministry of the Environment) for providing the FRRF. I would also like to thank the captains and crew of the CGS Limnos and EPA Lake Guardian, and the International Field Year of Lake Erie organization.

Financial support over the course of my Ph.D. was provided through various grants to Ralph Smith, Bob Hecky and Stephanie Guildford and personal NSERC-PGS and OGSST scholarships.

Finally I would like to thank Sairah Malkin for her love and support throughout my entire academic career.

Dedication

For my mother, who passed away on April 19th, 2008.

Table of Contents

List of Figures

List of Tables

Chapter 1: General Introduction

Section 1.1: The Global Significance of Aquatic Photosynthesis

Photosynthesis, the conversion of light energy to chemical energy, is amongst the most fundamental and ubiquitous processes on the planet. Anoxygenic photosynthesis is thought to have first evolved through inheritance of biochemical processes across a complex lineage of chemolithotrophic bacteria living near hydrothermal vents in the anoxic Proterozoic ocean (Xiong and Bauer 2002). The advent of anoxygenic photosynthesis freed autotrophic organisms from their dependence on the chemical energy originating from hydrothermal vents allowing life to spread and evolve throughout the Proterozoic ocean. No less than 2.5 billion years ago, nitrogen-fixing cyanobacteria evolved oxygenic photosynthesis and came to dominate the ocean to the extent that both the ocean and atmosphere were oxidized within ~ 0.5 billion years (Kasting 1993). Through the provision of an oxygenic atmosphere, aquatic photosynthesis fundamentally influenced life on earth allowing for the development of terrestrial photosynthesis and more complex organisms that use aerobic metabolism. Phytoplankton, defined here as any free floating single-celled photoautotroph, have since evolved and diversified with representatives spanning eight major phyla within the Bacteria and Eukarya domains (Reynolds 2006). Photosynthetic eukaryotes evolved 1.5 billion years ago through primary endosymbiosis of a photosynthetic prokaryote by a protistan eukaryote; subsequent secondary and tertiary endosymbiosis produced the remaining present-day phytoplankton groups (Falkowski et al 2004). Though the terrestrial descendents of phytoplankton now dominate global photoautotrophic biomass (~99%), phytoplankton nevertheless contribute approximate 45% of global photosynthesis (IPCC 2007).

The predominant objectives of agencies responsible for stewardship and management of

lakes are maintaining an acceptable level of water quality either for recreational activities, drinking water or both while ensuring a healthy commercial and/or sport fisheries. Both objectives are intimately related to phytoplankton biomass and productivity. In virtually every aquatic ecosystem photosynthetic organisms are the single largest pool of both total biomass and macronutrients and organic matter derived through photosynthesis energetically supports all other trophic levels. In some shallow and oligotrophic lakes, macrophytes and benthic macroalgae can provide a significant portion of the total primary production (Vadeboncoeur et al. 2003), but in most lakes phytoplankton dominate total primary production (Weztel 2001). Given the central role of phytoplankton in aquatic environments, it is no surprise that the most common proxies of water quality (bacterial biomass, water clarity, macronutrient concentrations and total suspended sediments) theoretically and empirically co-vary with phytoplankton biomass and production. The relationships between productivity of phytoplankton to other trophic levels have been formalized in aquatic food web models (Pauly et al. 2000), while empirical models have shown that phytoplankton production is the largest single determinant of fisheries yields across a wide range of lakes (Downing et al. 1990).

Section 1.2: The Photosynthetic Apparatus

Photosynthesis is a reduction-oxidation reaction that can be divided into light-dependent reactions where eight absorbed electrons are removed from the photochemically oxidized of water to produce O_2 and reducing power that supplies energy to the light-independent reactions where is CO_2 fixed into chemical bond energy (CH_2O). The photosynthesis reaction in its simplest form is shown in Equation (Eqn) 1.1. Eqn 1.2 and 1.3 include the role of the dephosphorylated and phosphorylated forms of adenosine biphosphate and triphosphate (ADP, ATP) and nicotinamide adenine dinucleotide phosphate ($NADP^+$, NADPH) in the light and dark

reactions respectively.

[Eqn 1.1.] $2H_2O + CO_2 + 8\ photons \rightarrow CH_2O + H_2O + O_2$

[Eqn 1.2] $2H_2O + 2NADP^+ + 3ADP + 3Pi + 8\ photons \rightarrow O_2 + 2NADPH + 2H^+ + 3ATP$

[Eqn 1.3] $CO_2 + 2NADPH + 2H^+ + 3ATP \rightarrow CH_2O + H_2O + 2NADP^+ + 3ADP + 3Pi$

Light Absorption and the Photosynthetic Light-Dependent Reactions

Absorbance of light energy is carried out by chromophores. Four basic chromophore groups constitute phytoplankton photosynthetic pigments and are shown in Table 1. During the endosymbiotic events that gave rise to the modern phytoplankton, the pigmentation of inherited plastids was largely conserved (Falkowski et al. 2004) so Table 1 also lists the presence or absence of pigments within each phytoplankton group. Absorption of incident photons promotes electrons to distinct excited quantum states, where the energy level difference between excited (E_X) and ground state (E_0) is equivalent to wavelength (λ) of the photon shown in Eqn 1.4, where c is the speed of light and h is Planck's constant. A pigment's chemical structure defines the possible energy gap(s) between excited and ground states that, through equation 1.4, produce distinct absorption spectra. Figure 1 presents the absorption spectra of common photosynthetic pigments.

[Eqn 1.4] $\lambda = h \bullet c \bullet (E_X - E_0)^{-1}$.

After energy is absorbed by the photosynthetic pigments it is then passed through a series of molecular redox reactions that split water and provide the required proton gradient for ATP and NADPH phosphorylation. This photosynthetic electron transport chain (ETC) is commonly

Table 1.1: Photosynthetic pigments classification and their presence in major phytoplankton groups. †Denotes non-photosynthetic pigment. Modified from Wetzel (2001).

Chromophore Groups	Pigment	Cyanobacteria	Chlorophyta	Chrysophyceae	Bacillariophyceae	Cryptophyceae
Chlorins	Chlorophyll a	+	+	+	+	+
	Chlorophyll b	-	+	-	-	-
Porphyrins	Chlorophyll c	-	-	+	+	+
Carotenoids	Lutein	+	+	+	-	-
	Fucoxanthin	-	-	+	+	-
	β-carotene†	+	+	+	+	-
Tetrapyroles	Phycocyanin	+	-	-	-	+
	Phycoerythrin	+	-	-	-	+

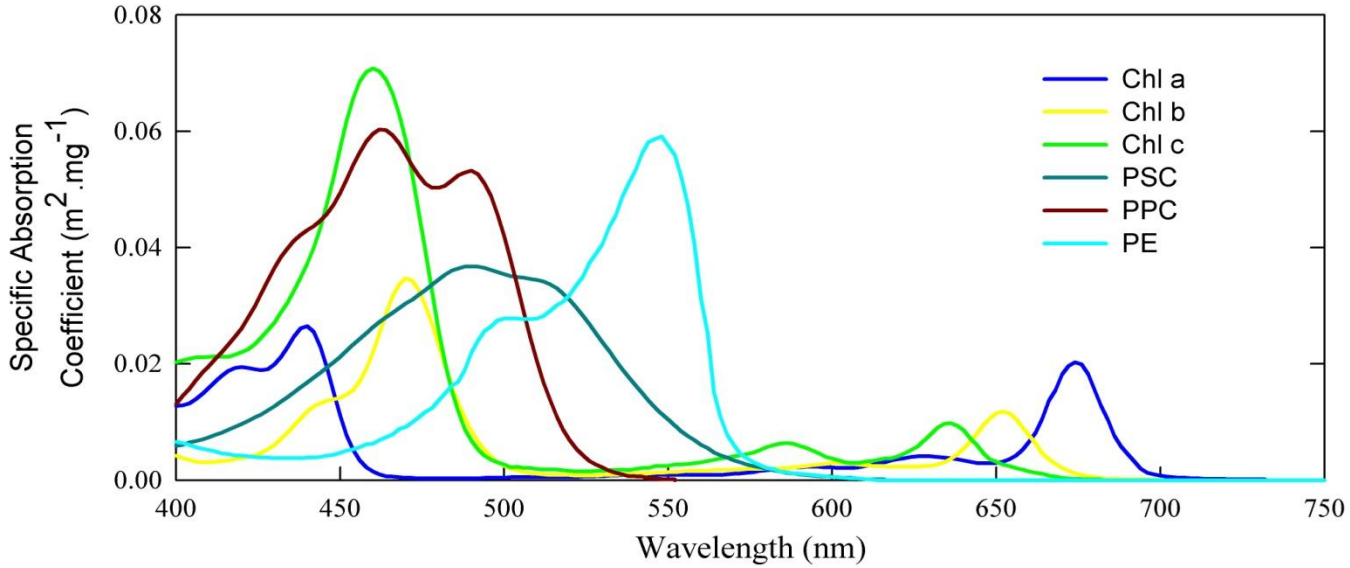

Figure 1.1: Wavelength specific absorption coefficients of chlorophyll a and b (Chl a, b), photosynthetic and non-photosynthetic carotenoids (PSC, PPC) and phycoerythrin (PE). Data from Bidigare et al. (1990).

depicted as a Z-scheme and is shown in Figure 1.2, where the vertical position of each molecule corresponds to its midpoint potential for reduction. Initially, excitons are transferred from pigment molecules to a reaction centre pigment molecule (P680) located in photosystem II (PSII) that then becomes excited to P680*. P680* returns to its ground state in part by the oxidation of water in the thylakoid lumen, but also by passing an electron to a series of consecutive redox reactions and a second photochemical target termed photosystem I (PSI) all of which constitutes the ETC.

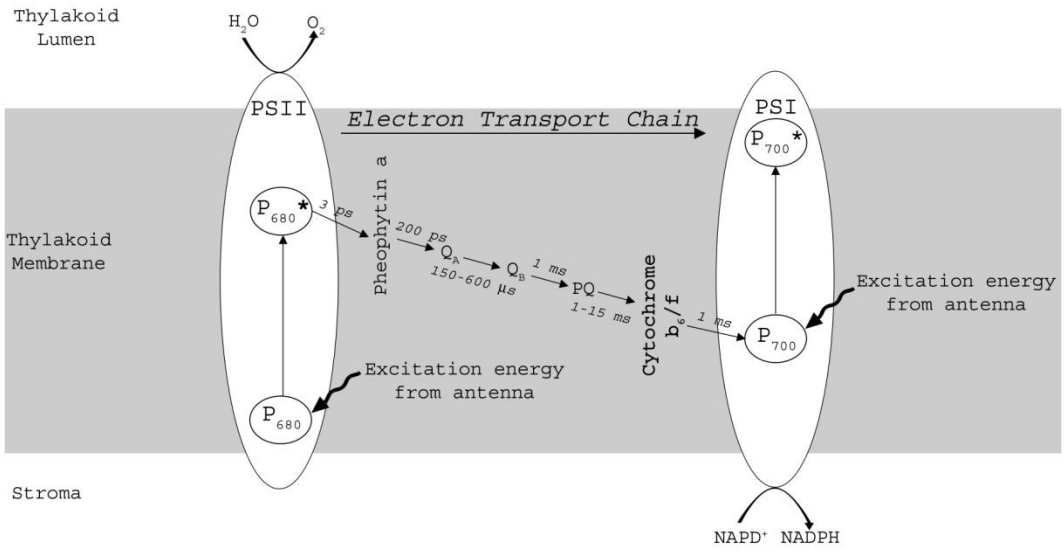

Figure 1.2: Simplified schematic of the Z-scheme showing the pathways of electron transport during the light dependent stage of photosynthesis. Light energy absorbed by the antenna is transferred to P_{680} (the chlorophyll-a molecule of RCII) causing the molecule to be raised to an excited state (P_{680}^{*}). A charge separation then occurs, P_{680}^{*} is oxidised to P_{680}^{+} and a primary acceptor (pheophytin a) is reduced. P_{680}^{+} is reduced by the oxidation of a water molecule. Pheophytin a $^{-}$ is rapidly re-oxidised by the secondary acceptor (Q_A). The electron is then transferred through a series of further redox reactions ($Q_B \rightarrow Q_B^{-} \rightarrow PQ \rightarrow PQH_2$, etc.) until it arrives at P_{700} (the chlorophyll-a molecule of RCI). Here energy is again received from the antenna and causes the molecule to be raised to an excited state (P_{700}^{*}). A second charge separation then occurs with a further electron transport pathway which eventually results in the reduction of $NADP^{+}$ to NADPH.

The light-independent (dark) reactions constitute a series of enzymatic reactions, principal amongst which is ribulose-1,5-bisphosphate carboxylase/oxygenase (Rubisco), that reduce carbon dioxide to carbohydrate (Falkowski and Raven 2007). The dark reactions are energetically fuelled by the light-dependent reduction of NADPH and phosphorylation of ATP, thus coupling the light and dark reactions of photosynthesis.

Eqns 1.1 to 1.3 imply unity, however the molar ratio of oxygen produced per carbon assimilated (photosynthetic quotient, PQ) varies and is on average between 1.1-1.4 (Falkowski and Raven 2007). The production and consumption of ATP and NADPH link the light and dark photosynthetitic reactions (Eqn 1.3) but are also required by a host of other metabolic pathways. The functions of these pathways include synthesis of macromolecules, translocation of solutes and ions and nitrogen assimilation, and collectively divert photosynthetically generated ATP and NADPH away from carbon assimilation and so yield a PQ above unity (Falkowksi and Raven 2007). As further discussed in Chapter 2, careful consideration must be given to the multitude of non-carbon fixation sinks of photosynthetically generated energy when comparing photosynthetic rates measured through different proxies.

Section 1.3: Quantifying Aquatic Photosynthesis

Quantitative estimates of phytoplankton production can be broadly divided into two components, methodology (measuring photosynthetic rates) and scaling (extrapolating photosynthetic rates). Chapter 3 discusses the concepts, models and assumptions related to scaling photosynthetic rates and Chapter 2 reviews comparative studies where multiple methodologies have been employed. What follows are the principles and general approaches of these methodologies.

Section 1.3.1: The P-E Approach

Oxygen evolution (Gaarder and Gran 1927) and carbon assimilation (Steeman-Nielsen 1952) remain the most common end points measured when determining photosynthetic rates. When cells are exposed to an ecologically relevant and measured gradient of light over a known period of time, the rate of photosynthesis (P) varies predictably with light (E) to produce a PE curve. As shown in Figure 1.3, PE curves can be approximated by a rectangular hyperbola that is mathematically defined by two physiologically relevant parameters (Jassby and Platt 1976). The asymptote of the hyperbola represents the maximum photosynthetic rate P_M and is a function of the concentration of functional photosystems present and their mean turnover rate at saturating E. The initial linear slope of the PE curve, symbolically known as α, represents region where photosynthetic rates are light-dependent and is a function of the concentration of functional photosystems present and the efficiency of light-harvesting. The quotient of P_M and α is the light saturation parameter E_k (Talling 1957), and represents the irradiance where light-harvesting and the turnover rate of photosynthesis are optimally balanced (Falkowksi and Raven 2007). Given a PE curve, extrapolation to *in situ* irradiance fields through space and time yields estimates of phytoplankton production (Chapters 3 and 4).

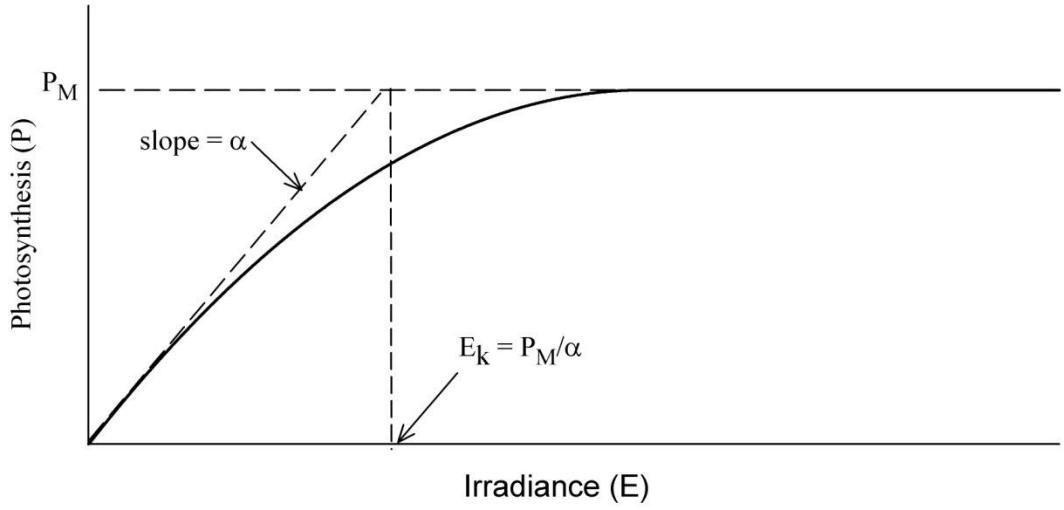

Figure 1.3: PE Curve with Parameters (Jassby and Platt 1976)

Photosynthetic carbon assimilation is routinely measured through cellular incorporation of a ^{14}C tracer. As liquid scintillation counting of ^{14}C is extremely sensitive, the ^{14}C technique is the preferred method in marine and oligotrophic environments. However early (pre-1980) comparative estimates in marine environments revealed ^{14}C-based estimates of phytoplankton production were up to an order of magnitude lower than oxygen based estimates (Eppley 1980) that eventually led to intense scrutiny and modification of the ^{14}C methodology (Peterson 1980). Though methodological pitfalls such as trace metal contamination and loss of labelled picoplankton through filtering are now largely avoided with improved methodology, there is still some debate of where ^{14}C rates lie along the range of gross and net photosynthesis. During incubations, it is possible that assimilated ^{14}C is respired and subsequently either re-assimilated or degassed prior to scintillation, thus leading to an underestimate of gross photosynthesis. The potential of this ^{14}C turnover increases with incubation time, so shorter incubations (~1 hour) are thought to be a better estimate of gross photosynthesis than long incubations (Lewis and Smith 1983).

Unlike the ^{14}C method the oxygen method, also known as the 'light and dark bottle technique', has undergone little change since its inception. Parallel incubations of 'dark' samples provide a measurement of oxygen consumption by respiratory pathways so unlike the ^{14}C method separate estimates of gross and net photosynthesis can be obtained (Wetzel and Likens 1991). The most common technique to measure dissolved oxygen is chemical titration via the Winkler method. This method has poor precision relative to ^{14}C and historically has been largely limited to eutrophic environments where high photosynthetic rates exceed the precision of the method. The continuing advent of improved instrumentation in measuring dissolved oxygen (i.e. oxygen fluorometers) may eventually result in wider spread use of the oxygen method in oligotrophic environments, though currently this instrumentation can still not match the sensitivity of ^{14}C.

Section 1.3.2. Deconvolution of Photosynthetic Parameters

The verb 'scaling' is often used to describe the conversion of fluorometric measurements to photosynthetic rates as several parameters, some measured, others assumed, are integral to this conversion. Alternatively this conversion can be thought of as a deconvolution, as active fluorescence and the required ancillary measurements quantify the relevant and variable underlying physiological processes that influence photosynthetic rates. As a result, i*n situ* active fluorometry is gaining widespread use in ecophysiological (i.e. Behrenfeld et al. 2006) research as well as a tool for generating phytoplankton production estimates (i.e. Moore et al. 2006). Following Behrenfeld et al. (2004), Eqn 1.5 and 1.6 show the deconvolution of photosynthetic parameters while Table 1.2 provides a list of relevant parameters.

[Eqn 1.5] $\alpha = f_{PSII} \bullet \sigma_{PSII} \bullet n_{PSII}$

[Eqn 1.6] $P_M = n_{LF} \bullet 1/\tau_{LF}$

Eqn 1.5 shows that the light-limited slope of photosynthesis (α) is controlled by PSII photochemistry and is equivalent to the product of the number of PSII reaction centres (n_{PSII}) that are photochemically competent (f_{PSII}), and the average functional absorption cross-section of the competent centres (σ_{PSII}). Eqn 1.6 shows that the maximal photosynthetic rate (P_M) is the product of the concentration of the rate-limiting photosynthetic compound (n_{LF}) and its turnover rate ($1/\tau_{LF}$). Evidence that the maximal photosynthetic rate (P_M) is controlled downstream of PSII under most growth conditions is overwhelming (Behrenfeld et al. 2004 and references therein). Consequently n_{LF} and $1/\tau_{LF}$ cannot be derived from active fluorescence techniques alone, however it is worth noting that strong co-variation between α and P_M constrain estimates of the latter based on the former (Behrenfeld et al. 2004, Silsbe et al. 2006). The differing methodologies to arrive at an estimate of P_M from α is discussed in Chapter 2. Of the three terms in Eqn 1.5, only n_{PSII} cannot be derived from active fluorescence techniques. Accordingly, values of n_{PSII} are either assumed or derived (Suggett et al. 2004) when scaling active fluorescence measurements to photosynthetic rates. The product of σ_{PSII} and n_{PSII} is the functional absorption of PSII (a_{PSII}), Chapter 2 reviews and applies various methods that derive a_{PSII} and circumvent the need to assume n_{PSII}. While all active fluorescence techniques can estimate f_{PSII}, only fast repetition rate fluorometry (FRRF) or related single turnover fluorometers provide a measurement of σ_{PSII}. The principles governing estimates of f_{PSII} and σ_{PSII} from active fluorescence measurements are addressed below.

Section 1.3.3: Active Fluorescence: Principle and Terminology

Energy absorbed by photosynthetic pigments is ultimately de-excited through one of three pathways; photochemistry (p), non-photochemistry (d) and fluorescence (f). Each de-excitation pathway is discrete (quanta cannot be shared) and has a rate constant (k_p, k_d, k_f). The

maximum quantum yield (Φ) of a given pathway is the ratio of product formed per quanta absorbed, and can defined by the three rate constants. For example, the maximum quantum yield of photochemistry (ΦP) is shown in Eqn 1.7 and is equivalent to the rate constant of photochemistry (k_p) divided by the sum of all rate constants.

[Eqn 1.7] $\Phi P = k_p/(k_p + k_d + k_f)$

As famously demonstrated by Emerson and Arnold (1932), the quantum efficiency of photochemistry can be manipulated through fast bursts of high energy that reduce (close) PSII reaction centres. Active fluorometers manipulate the redox state of PSII by exposing phytoplankton to a series of rapid pulses of E while synchronously measuring the fluorometric response. The fluorescence of a sample exposed to very short or sub-saturating E is minimal (F_0) when all PSII reaction centres are oxidized (open) with a quantum yield defined in Eqn 1.8. When all PSII centres are closed, kp drops to 0, fluorescence is maximal (F_M) with a quantum yield defined in Eqn 1.9. Eqn 1.8 - 1.9 can be arranged to demonstrate that maximum quantum efficiency of photochemistry (ΦP) is equivalent to $(F_M-F_0)/F_M$ or F_V/F_M where $F_V = (F_M-F_0)$.

[Eqn 1.8] $\Phi F_0 = k_f/(k_p + k_d + k_f)$

[Eqn 1.9] $\Phi F_M = k_f/(kd + k_f)$

In a key paper, Genty et al. (1989) demonstrated that the quantum yield of CO_2 production for a number of plant species over a wide range of physiological conditions was linearly related to the product of the maximum quantum efficiency of photochemistry and the fraction of open reaction centres (q_p as defined in Table 1.2). Thus the convolution of q_P and F_V/F_M, commonly referred to as F_q/F_M provide an estimate of f_{PSII} shown in Eqn 1.5. Both the terminology and methodology related to the derivation of f_{PSII} are inconsistent in the active fluorescence literature. Modifications in the derivation of f_{PSII} and its ensuing influence on

photosynthetic rates are introduced in the following chapter.

FRRF manipulates the redox state of PSII by exposing phytoplankton to a series of 50-100 μs excitation pulses of E while synchronously measuring fluorescence. The cumulative energy over the course of the sequence is sufficient to fully reduce Q_A (see Figure 1.2) while minimizing additional non-photochemical fluorescence quenching in the PSII reaction centres, while the duration of the sequence is sufficiently short to prevent Q_A re-oxidation (150-600 μs) (Kolber et al. 1998). The fluorometric response across the sequence of excitation pulses is referred to as an induction curve. The FRRF has been designed to perform *in situ* induction curves under actinic irradiance as well as in a dark chamber whose flushing rate is sufficient to oxidize photosynthetically reduced reaction centres. The combination of actinic and dark induction curves permits the computation of other parameters of physiological relevance (Chapter 2). Figure 1.4 shows a typical induction curve with fluorescence rises from F_O to F_M as reaction centres become progressively closed.

The slope of an induction curve from F_O to F_M is conceptually and mathematically related to effective absorption cross-section of PSII (σ_{PSII} in Equation 1.5, Ley and Mauzerall 1982). Conceptually, photons striking phytoplankton with a large σ_{PSII} have a higher probability of reducing PSII reaction centres so the slope of the induction curve from F_O to F_M is steeper than phytoplankton with a small σ_{PSII}. Mathematically, Ley and Mauzerall (1982) showed that the probability of a specific reaction centre becoming reduced is a random occurrence over a time-series of intervals such that an induction curve can be modelled as a one-hit Poisson function whose slope is σ_{PSII}. A FRRF induction curve is therefore a one-hit Poisson function with a slope equivalent to σ_{PSII} as shown in Eqn 1.10.

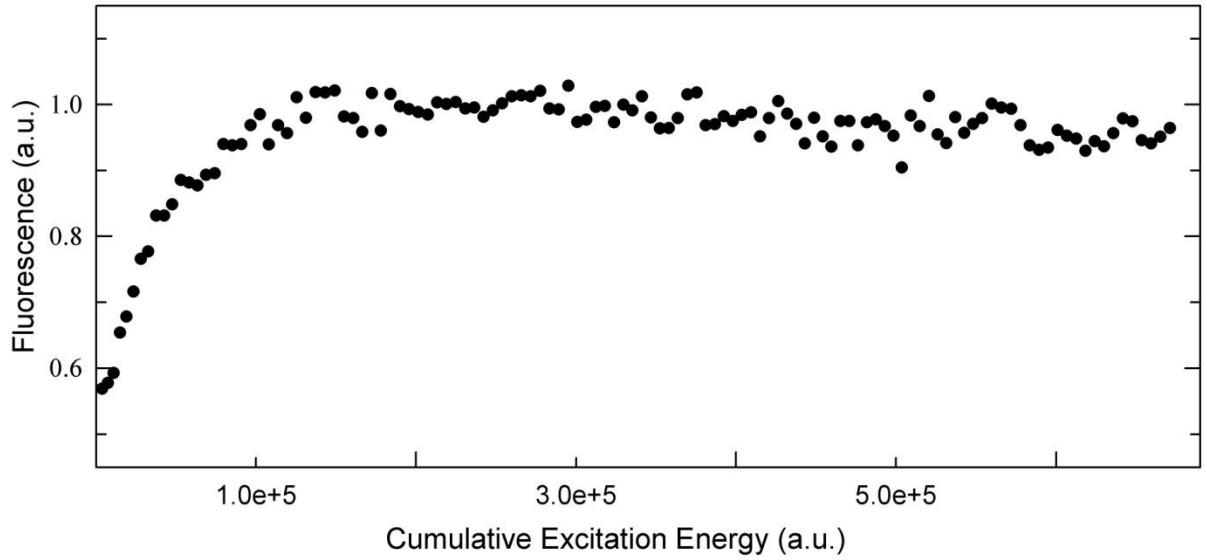

Figure 1.4: FRRF induction showing the rise of fluorescence from F_0 to F_M over the course of 100 excitation pulses. a.u. refers to arbitrary units.

[Eqn 1.10] $$\frac{F(E)-F_0}{F_V}=1-e^{-\sigma_{PSII}E}$$

Finally, coefficients are required to scale measurements of n_{PSII}, f_{PSII} and σ_{PSII} to photosynthetic rates. f_{PSII} is dimensionless and the product of units of n_{PSII} and σ_{PSII} yield units of [m^2 • mol RCII • (mol photons • mol chl a)$^{-1}$]. Implicit to all models that scale active fluorescence measurements to photosynthetic rates are the quantum yields of oxygen evolution (ϕ_e) and electron transfer in RCII (ϕ_{RC}). The latter is assumed as unity with units [mol photons (mol RCII)$^{-1}$] and the former is assumed to be 0.25 with units [mol O_2 (mol photons)$^{-1}$] as four moles of electrons are required to produce 1 mole of O_2.

Section 1.4: Thesis Outline

Chapter 2 reviews published bio-optical models that compare fluorescence-based photosynthetic measurements to contemporaneous ^{14}C photosynthetic rates. The efficacy of the various bio-optical models is tested using a large dataset of FRRF profiles and ancillary water

chemistry parameters against synchronously derived *in vitro* ^{14}C PE parameters collected across mixing, trophic and taxonomic gradients in Lake Erie. In this analysis, recent published estimates of the photosynthetic quotient derived through traditional oxygen and ^{14}C methodologies in Lake Erie provide the statistical benchmark against which contemporaneous bio-optical and ^{14}C measurements is evaluated. Chapter 2 demonstrates that in Lake Erie values of f_{PSII} are relatively constrained, and the success of bio-optical models depends largely on the formulation of a_{PSII} (where $a_{PSII} = \sigma_{PSII} \bullet n_{PSII}$ in Eqn 1.5). Moreover using measured and assumed values σ_{PSII} and n_{PSII} respectively, a common parameterization of published bio-optical models, yields photosynthetic rates that are incongruent with ^{14}C rates. Instead alternative methods to derive a_{PSII}, largely ignored in published bio-optical models, are reviewed and formulated. Chapter 2 demonstrates that the various assumptions required in the alternative formulations of a_{PSII} are likely minor compared to the possible range of n_{PSII} values at an ecosystem level. Based on previously published a_{PSII} methods a novel approach to derive this important parameter is introduced in Chapter 2 that, upon incorporation into a bio-optical model, yields the most statistically significant comparison to concurrent ^{14}C derived photosynthetic rates amongst all bio-optical models. Overall, the bio-optical model presented in Chapter 2 outperforms any published ^{14}C comparison performed across a taxonomic gradient.

The bulk of phytoplankton production estimates in the Laurentian Great Lakes and other freshwater lakes are determined from the PE approach outlined in Section 1.3. *In vitro* light sources employed in these studies vary and rarely do their spectral qualities match the *in situ* environment. Though most of these studies recognize the potential error in assuming equivalency in the *in situ* and *in vitro* spectral environments, no attempt has yet been made to spectrally scale historic PE measurements. Chapter 3 reviews these studies and develops a

rigoruous empirical model that scales these measurements to the *in situ* spectral environment. This analysis demonstrates the phytoplankton production estimates in the Laurentian Great Lakes has been largely underestimated. In conjunction with the large *in vitro* ^{14}C dataset presented in Chapter 2, long term changes in spectrally resolved measurements of phytoplankton production in Lake Erie are analyzed.

Having introduced and validated a bio-optical method capable of measuring gross photosynthetic rates in Chapter 2 and recognizing the importance of spectral quality in Chapter 3, Chapter 4 applies the bio-optical model to *in situ* fluorescence measurements throughout the water column to generate vertically and spectrally resolved estimates of phytoplankton photosynthesis. Persistent vertical patterns of photosynthesis are identified across trophic and mixing gradients using an extensive set of measurements in Lake Erie, and subsequently compared to similar sets of measurements in other freshwater lakes. Chapter 4 is the first study to explicitly examine vertical patterns of photosynthesis in any freshwater lake using a high-resolution bio-optical method. This chapter also investigates how persistent vertical patterns of *in situ* photosynthesis deviate from nominally scaled *in vitro* measurements and identifies when *in vitro* scaling assumptions yield erroneous estimates of areal phytoplankton production.

Chapter 5 summarizes the main conclusions of this thesis and puts forth recommendations for future research and methodological approaches to effectively monitor phytoplankton production in freshwater lakes. Appendix A and B contain tables of all relevant data employed in this thesis.

Chapter 2: Towards autonomous measurements of phytoplankton photosynthesis: A comparison of bio-optical and in vitro photosynthetic rates in a large freshwater lake.

Section 2.1: Introduction

Phytoplankton ecologists have long sought a method that provides rapid, *in situ* estimates of phytoplankton production (PP). One of the most common applications of active fluorometry is the incorporation of measured PSII photochemical indices into bio-optical models that estimate gross phytoplankton production (GPP). The theoretical principles that link active fluorometric measurements to indices of PSII photochemistry are well established and widely accepted (Krause and Weis 1991). Many active fluorometers can operate *in situ* and at an unparalleled resolution to provide measurements free of human error while circumventing assumptions concerning *in* vitro containment of natural phytoplankton assemblages. The various parameters which constitute bio-optical models provide also greater insight into the fundamental processes that affect photosynthesis relative to most other PP methods that examine only the end products of photosynthesis (P) as a function of irradiance (E). Accordingly, active fluorescence has significantly enhanced our understanding on how photosynthetic physiology varies through space and time (Strutton et al. 1997; Behrenfeld et al. 2006) and across environmental (Moore et al. 2006) and taxonomic gradients (Raateoja et al. 2004b; Suggett et al. 2006). Yet when parallel measurements of PP derived from bio-optical and *in vitro* methods are compared, the results are often equivocal (Table 2.1).

The parameterization, assumptions and efficacy of bio-optical models vary in the literature and a critical review of publications that have compared bio-optical and traditional PP estimates does not yet exist. Flameling and Kromkamp (1998) have reviewed the comparative

estimates of photosynthetic electron rates from active fluorometers and other methods, but the publication predates most single-turnover investigations (i.e. fast-repetition rate fluorometry FRRF), and the bulk of research at that time was limited to cultures and terrestrial plants. This chapter first reviews all recent publications that have compared bio-optical PP estimates with concurrent traditional PP estimates, specifically focusing on bio-optical model parameterization including empirical assumptions and common sources of error. The various bio-optical models are then tested using a new bio-optical dataset with contemporaneous *in vitro* ^{14}C photosynthetic measurements. This dataset was acquired over the course of four spatial surveys in Lake Erie, whose morphometry and spatially disparate nutrient loadings provide a large gradient of mixing, trophic state and phytoplankton community composition over which to test the efficacy of the various bio-optical models. The majority of active fluorescence studies are from marine ecosystems, therefore this study is the largest comparative examination of bio-optical and traditional photosynthesis estimates in any freshwater lake.

Section 2.1.1: Bio-optical Model Parameterization

Though the parameterization of published bio-optical models that convert fluorescence measurements to photosynthetic rates vary (Table 2.1), each model can be recast using the simplified equation (Eqn) 2.1. Light-saturated photosynthetic rates are limited downstream of PSII and it must be stressed that Equation 2.1 applies to light-limited photosynthesis only. Bio-optical modelling of light-saturated photosynthesis is addressed further below (Section 2.1.2). Eqn 2.1 defines oxygen-evolving photosynthetic rates (P [mg O_2 m^{-3} h^{-1}]) as a function of four variables. $E_{(\lambda)}$ is irradiance and is wavelength (λ) dependent when photosynthetic rates are light-limited. f_{PSII} is the photochemical efficiency derived from the active fluorescence measurements that are introduced and derived in Chapter 1. $a_{PSII(\lambda)}$ is the mean absorption spectra of

Table 2.1: Model source, description and parameterization. SCF denotes presence (√) or absence (X) of spectral corrections. P_M denotes method used to estimate light saturated photosynthesis. PP Method with incubation time (hrs), w and p denote scintillation of whole water and particulate matter respectively. Env. denotes whether study investigates a marine (O) or freshwater (L) environment or *in vivo* culture (C). PQ gives the average ratio of the two estimates with summary statistics and notes if applicable.

Source: f_{PSII}	a_{PSII}	SCF	P_M	PP Method	Env.	PQ	Summary Statistics and Comments
1: F_V/F_M	$\sigma_{PSII} \bullet n_{PSII}$ [3.3 x 10^{-3}]	√	E_K	^{14}C [1, w]	O	$\alpha^*_{[FRRF]} = 2.27\ \alpha^*_{[14C]}$	*(n.s., n =3)* *(r^2 = 0.94 ,n = 72, p <0.05)*
2: $F_V'/F_M'/0.65$	$\sigma_{PSII}' \bullet n_{PSII}$ [2.00 x 10^{-3}]	√	n.m.	^{14}C [1.5, w]	C	$P^*_{[FRRF]} = 2.17\ P^*_{[14C]}$	$\phi_{[FRRF]} = 1.15\ \phi_{[14C]}$
3: $F_V/F_M/0.65$	$\sigma_{PSII} \bullet n_{PSII}$ [2.00 x 10^{-3}]	√	σ_{PSII}	^{14}C [1-2, p]	O	$\alpha^*_{[FRRF]} >\neq \alpha^*_{[14C]}$	*(n.s., n =21)*
4: $F_V/F_{M[MAX]}/0.65$	$\sigma_{PSII} \bullet n_{PSII}$ [2.00 x 10^{-3}]	X	E_K	^{14}C [3-4, p]	O	$\alpha^*_{FRRF]} = 2.44\ \alpha^*_{[14C]}$	*(n.s., n =)* $\alpha^*_{[FRRF]}$ less variable than $\alpha^*_{[14C]}$
5: F_Q'/F_M'	$\sigma_{PSII} \bullet n_{PSII}$ [2.00 x 10^{-3}]	X	Eqn 2.1	^{14}C [~12, p] *in situ*	O	$P^*_{[FRRF]} = 2.20\ P^*_{[14C]}$	*(r^2 = 0.94 ,n = 72, p <0.05)*
6: $F_V/F_M/0.65$	$\sigma_{PSII} \bullet n_{PSII}$ [2.00 x 10^{-3}]	X	n.m.	^{14}C [3,w] *in situ*	L	$P^*_{[FRRF]} = 1.15\ P^*_{[14C]}$ $\alpha^*_{[FRRF]} >\neq \alpha^*_{[14C]}$	*(r^2 = 0.88, n = 140, p <0.001)* *(n.s., n = 23)*
7: $F_Q'/F_M'/0.65$	$\sigma_{PSII} \bullet n_{PSII}$ [2.00 x 10^{-3}]	X	E_K	^{14}C [1, p]	O	$P^*_{[FRRF]} = 0.36\ P^*_{[14C]}$	*(r^2 = 0.81, n = 470)*
8: q_p	$\sigma_{PSII}' \bullet n_{PSII}$ [2.00 x 10^{-3}]	√	Eqn 2.1	^{14}C [2, p]	O	$P^*_{[FRRF]} = 1.02\ P^*_{[14C]}$	*(r^2 = 0.88, n =16, p < 0.0001)*
9: F_Q'/F_M' $F_Q'/F_M'_{[MAX]}/0.65$	$\sigma_{PSII}' \bullet n_{PSII}$ [2.00 x 10^{-3}]	√	E_K	^{14}C [1,w]	L	$P_{[FRRF]} = 1.08\ P_{[14C]}$ $\alpha^*_{[FRRF]} <\neq \alpha^*_{[14C]}$	*(r^2 = 0.76, n = 12, p <0.05)* *(n.s., n = 12)*
10: F_Q'/F_M'	$\sigma_{PSII}' \bullet n_{PSII}$ [measured]	√	E_K	^{14}C [0.7,w]	C	$P_{[FRRF]} \cong 2.25\ P_{[14C]}$	
11: F_V'/F_M' $[F_V/F_M]^{-1}$	$\sigma_{PSII} \bullet n_{PSII}$ [measured]	√	Eqn 2.1	$[CO_2]$ *in situ*	L	$P_{[CO2]} = 1.02\ P_{[FRRF]}$ $P_{[CO2]} = 1.55\ P_{[FRRF]}$	Diatom bloom Flagellates and N-fixers
12: F_q'/F_M' /0.65	$\sigma_{PSII} \bullet n_{PSII}$ [2.00 x 10^{-3}]	X	E_K	^{14}C [4,p]	O	$P_{[PPF]} = 1.06\ P_{[14C]}$	
13: F_q'/F_M' /0.65	$\sigma_{PSII} \bullet n_{PSII}$ [1.25 x 10^{-3}]	X	E_K	^{14}C [2,?]	O	$\alpha^*_{[14C]} >\neq \alpha^*_{[PPF]}$	
14: F_q'/F_M'	$a_{phy} \bullet 0.5^a$	√	E_K	$O_2{}^{18}$	C	$\Phi_{P[FRRF]} = 0.69 - 1.06\ \Phi_P O_2{}^{18}$	3 Cultures
15: F_q'/F_M'	$\sigma_{PSII} \bullet n_{PSII}$ [2.00 x 10^{-3}]	√	Eqn 2.1	^{14}C [1.5,p] *in situ*	O	$P_{[FRRF]} = 2.23\ P_{[14C]}$ @ 3m $P_{[FRRF]} = 1.17\ P_{[14C]}$ @ 9m	*(r^2 = 0.69, n =16, p < 0.001)* *(r^2 = 0.38, n =16, p < 0.01)*
16: $F_q'/F_M'_{[MT]}$ q_p F_q'/F_M'	$a^*_{ph} \bullet 0.5$ $\sigma_{PSII} \bullet n_{PSII}$ [2.00 x 10^{-3}] $a^*_{ph} \bullet 0.5$	X	Eqn 2.1	^{14}C [2.0,p]	L	$P_{[PAM]} = 2.61\ P_{[14C]}$ $P_{[FRRF]} = 3.08\ P_{[14C]}$ $P_{[FRRF]} = 2.19\ P_{[14C]}$	

Sources: [1]Suggett et al. 2001; [2]Raateoja and Seppala 2001; [3]Moore et al. 2003, [4]Smyth et al. 2004; [5]Corno et al. 2005, [6]Kaiblinger and Dokulil 2006, [7]Melrose et al. 2006, [8]Blanco et al. 2007, [9]Pemberton et al 2007, [10]Ross et al. 2008, [11]Suggett et al. 2006, [12]Kolber and Falkowksi 1993, [13]Boyd et al. 1997. [14]Suggett et al. 2003. [15]Raateoja et al. 2004a. [16]Kromkamp et al. 2008

photosynthetically active pigments serving PSII and is also wavelength dependent. The last term in Eqn 2.1 is the constant (A) that represents the maximum quantum yield of oxygen evolution (ΦO_2 = 1 mole of O_2 requires 4 moles of electrons absorbed by PSII), the quantum yield of electron transfer within a reaction center (Φ_{RC} unity is assumed) and coefficients for unit conversion. Variations of bio-optical models arise through different methods to calculate $a_{PSII(\lambda)}$ and different parameterizations of f_{PSII}, both are discussed in detail below.

[Eqn 2.1] $P = E_{(\lambda)} \bullet f_{PSII} \bullet a_{PSII(\lambda)} \bullet A$

f_{PSII}: Principles, parameterization and sources of error.

In situ estimates of the apparent quantum yield of oxygen evolution (ΦO_2) rarely approach the theoretical maximum ΦO_2 (0.25) dictated by the four photosynthetic S States and the ratio of electrons passed to PSII and PSI (Babin et al. 1996). In the context of bio-optical models, f_{PSII} is a coefficient equivalent to the reduction of the apparent ΦO_2 from its theoretical maximum. Babin (1996) attributes low measurements of ΦO_2 to either the absorbance of energy by non-photosynthetic pigments, cyclic electron flow around the photosystems, and the impairment of PSII reactions centres caused by either excessive irradiance or nutrient deficiency. By definition ΦO_2 refers to quanta that are 'absorbed by PSII', so the presence of non-photosynthetic pigments should not affect ΦO_2. Cyclic electron flow, and other non-photosynthetic electron sinks including the Mehler reaction, is thought to be only significant under light-saturated photosynthesis (Ross et al. 2008), so their impact on ΦO_2 under light-limited conditions is probably minimal. Thus decreases in ΦO_2 during light-limited photosynthesis can be predominantly attributed to the efficiency of PSII that is readily measured through active fluorometry.

The most recognized proxy for f_{PSII}, F_V/F_M, measures the maximum photosynthetic

efficiency of PSII in the dark. F_V/F_M is routinely normalized to 0.65, an empirical upper limit observed in nutrient replete cultures regardless of growth irradiance (Falkowksi and Raven 1997). Supression of F_V/F_M below 0.65, indicative of diminished photosynthetic efficiency, is commonly attributed to nutrient stress and has been observed in nitrogen, iron and phosphorus deficient batch cultures (Berges et al. 1996; Greene et al. 1994; Lippimeir et al. 2001). Further reductions to F_V/F_M *in situ* arise through increased irradiance and photoinhibition (Oliver et al. 2003; Raateoja et al. 2009), while mixed phytoplankton communities contain a 'taxonomic signature' as F_V/F_M of nutrient replete cells is higher for diatoms and chlorophytes relative to cyanophytes and prasinophytes (Cermeno et al. 2005; Suggett et al. 2009). Thus, nutritional reduction of f_{PSII} within mixed communities is superimposed on taxonomic and photo-physiological variability, so measurements of f_{PSII} cannot be interpreted in the context of nutrient deficiency alone (Suggett et al. 2009).

Contemporaneous fluorescence measurements performed in the dark and under actinic irradiance, the latter is denoted with an apostrophe (i.e. F_0'), permit different permutations of f_{PSII}. Table 2.1 lists the various parameterizations of f_{PSII} employed in comparative production studies. F_Q'/F_M', represents the effective photochemical efficiency of PSII under actinic irradiance (Genty et. al. 1989) and is the most common parameterization of f_{PSII}. F_Q'/F_M' is the product of the photochemical efficiency of PSII in the light (F_V'/F_M') and the fraction of functional PSII reaction centres that are oxidized (q_p). q_P varies predictably with irradiance (Kolber and Falkowski 1993), at light limiting irradiances all reaction centres are oxidized and q_p is 1 but as irradiance increases q_p decreases as reaction centres become progressively reduced. Not all studies listed in Table 2.1 normalize F_Q'/F_M' to 0.65. 0.65 has been called 'somewhat arbitrary' (Kromkamp and Forster 2003) as occasional higher values have been found (Berges et

al. 1996). In the context of bio-optical models values of F_Q'/F_M' or F_V/F_M that equal 0.65 represent ΦO_2 that equal 0.25. Thus omission of this coefficient means that presumably nutrient replete phytoplankton (F_V/F_M = 0.65) have a maximum permissible ΦO_2 of only 0.1625 (i.e. 0.25 • 0.65). Since ΦO_2 values higher than 0.1625 have been observed (Suggett et al. 2003), normalization to 0.65 appears logical, while a review of large datasets from marine and culture studies suggests this upper limit is relatively constant (Suggett et al. 2009).

The lure of active fluorometry is the ability to obtain *in situ* and autonomous measurements, in reality however great care and time must be taken to minimize operational sources of error. All fluorescence measurements are affected by instrument noise and 'background' (non-algal) fluorescence, and both signals need to be quantified and deconvolved from the fluorescence induction curves to obtain the algal signal (Laney 2002). The mathematical principles of this correction are given in detail by Laney and Letelier (2008). Briefly instrument noise is a function of the induction protocol and instrument gain (the amplification of fluorescence signals) and is independent of the sampling environment. Background fluorescence is solely a function of the sampling environment and generally increases in importance with decreasing algal biomass (Suggett et al. 2008). Methodologically, background fluorescence signals are measured using filtrate (<0.2 or 0.7 μm) in order to separate it from the algal signal. However the waste products of digested phytoplankton, specifically the chromophore pheophytin-*a*, can be retained on GF/F and GF/C filters and so are not detected using filtrate yet still constitute background fluorescence. The potential magnitude of this error varies with the ratio of chl *a*:pheophytin-*a* (e.g. signal:noise), and is reportedly significant when concentrations of pheophytin-*a* approach 30% of chl *a* concentrations (Fuchs et al. 2002).

$a_{PSII(\lambda)}$: Principles, parameterization and sources of error.

$a_{PSII(\lambda)}$ is the spectrally dependent absorption of photosynthetically active pigments serving PSII. Methodologically, $a_{PSII(\lambda)}$ can be estimated through Eqn 2.2, where $a_{PSII(\lambda)}$ is the product of the absorption spectra of all photosynthetically bound pigments (a_{PS}) and a factor *P* that represents the fraction of pigments associated with PSII. In the literature (Table 2.1), $a_{PSII(\lambda)}$ is more commonly derived as the product of the effective absorption cross-section of PSII ($\sigma_{PSII(\lambda)}$), the ratio of chl *a* molecules serving PSII (n_{PSII}) and the chl *a* concentration as shown in Eqn 2.3. Genotypic variations of $a_{PSII(\lambda)}$ arise through different pigmentation of the various algal groups (Reynold's 2004), while phenotypic alterations (photoacclimation) further alter $a_{PSII(\lambda)}$ as cells seek to balance light harvesting capacity with metabolic demand of ATP and reductant (Falkowski et al. 1981; Dubinsky et al. 1986; Berges et al. 1996).

[Eqn 2.2] $a_{PSII(\lambda)} = a_{PS(\lambda)} \bullet P_{(\lambda)}$

[Eqn 2.3] $a_{PSII(\lambda)} = \sigma_{PSII(\lambda)} \bullet n_{PSII} \bullet$ chl *a*

σ_{PSII}, the effective absorption cross-section of PSII pigments dictates the rate of energy transfer from the light-harvesting complexes to the photosynthetic light reactions. Single turnover fluorometers measure $\sigma_{PSII(\lambda)}$; the rate of energy transfer dictates the slope of fluorescence induction curves. Given the ability for parallel measurements of f_{PSII} and $\sigma_{PSII(\lambda)}$, most bio-optical models shown in Table 2.1 derive $a_{PSII(\lambda)}$ through Eqn 2.3 using measured or assumed values of n_{PSII}. $\sigma_{PSII(\lambda)}$ is highly variable across taxa owing to the diverse absorption spectra of accessory photosynthetic pigments specific to various phytoplankton chromophore groups (Suggett et al. 2009). Within individual cells, $\sigma_{PSII(\lambda)}$ can vary over short time scales by up to 20% as photoacclimative state transitions allow for the transfer of some absorbed energy to either PSI or PSII (Falkowksi and Raven 1997).

Unlike $\sigma_{PSII(\lambda)}$, n_{PSII} can only be independently measured *in vitro* with the oxygen flash yield method that requires such high concentrations of phytoplankton (> 1g.m^{-3} chl *a*) the technique is impractical for natural samples (Falkowski and Raven 1997). Cultures have shown that n_{PSII} varies by a factor of 4 across taxonomic groups and is often highest in prokaryotes (Suggett et al. 2004). Only two comparative studies listed in Table 2.1 employed *in vitro* measurements of n_{PSII} within a bio-optical model; most studies routinely assign a constant value for n_{PSII} that may or may not reflect the dominant taxa under observation. Accurate quantification of n_{PSII} is a significant hurdle in all bio-optical models: The deviation between measured and typically assumed values may introduce up to a 2-fold error in photosynthetic estimates (Suggett et al. 2004, 2006).

Eqn. 2.2 summarizes a second class of methods that estimate $a_{PSII(\lambda)}$ that have been validated on culture experiments spanning four phytoplankton groups (Suggett et al. 2004). Despite this validation and the potential variability of n_{PSII}, only 2 of 16 studies in Table 2.1 estimate $a_{PSII(\lambda)}$ using a variation of Eqn 2.2, perhaps because both studies contain some data from a multiple-turnover fluorometer (PAM) that cannot measure $\sigma_{PSII(\lambda)}$. Indeed a large body of excellent research dedicated to the derivation of $a_{PSII(\lambda)}$ as a compound unit has not found widespread use in bio-optical comparative studies.

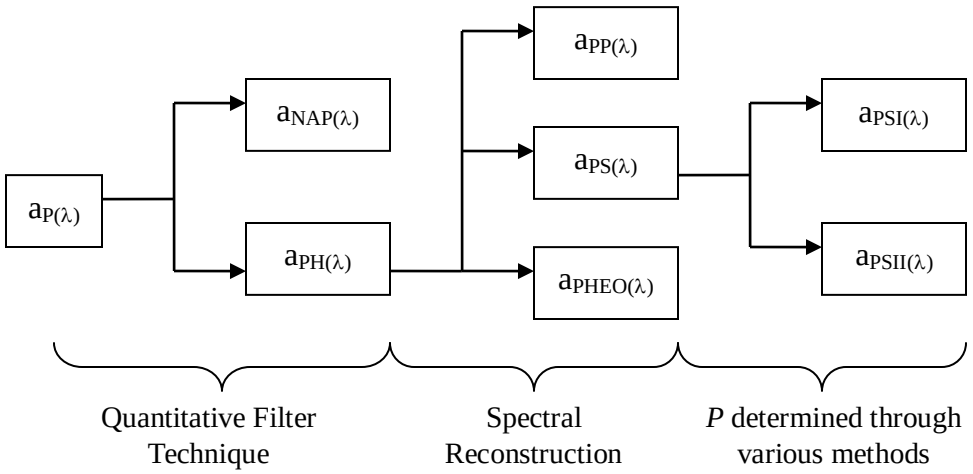

Figure 2.1: Flowchart summarizing techniques and parameters employed in Eqn 2.2. λ is wavelength, a is absorption spectrum with subscripts as follows: P is particulate, NAP is non-algal particles, PH is phytoplankton, PP is photoprotective pigments, PS is photosynthetic pigments, PHEO is pheophytin, PSI and PSII are pigments associated with photosystem I and photosystem II respectively.

Figure 2.1 summarizes the techniques and parameters involved in the derivation of $a_{PSII(\lambda)}$. Amongst the various steps, the quantitative filter technique (QFT) is paramount. The QFT calculates the absorption spectra of phytoplankton pigments ($a_{PH(\lambda)}$) as the difference between the absorption spectrums of particles retained on a filter before ($a_{P(\lambda)}$) and after ($a_{NAP(\lambda)}$) chemical extraction of pigments from the filter (Tassan and Ferrari 1992). $a_{PH(\lambda)}$ is the sum of absorption due to non-photosynthetic (photoprotective) pigments ($a_{PP(\lambda)}$), photosynthetic pigments ($a_{PS(\lambda)}$) and pheophytin ($a_{PHEO(\lambda)}$). Spectral reconstruction methods estimate $a_{PP(\lambda)}$ and $a_{PHEO(\lambda)}$ as the product of the spectra and concentration for a given pigment then scale this measurement to $a_{PH(\lambda)}$ to account for pigment packaging (Babin et al. 1996; Culver and Perry 1999; Section 2.2: Materials and Methods). Removal of pheophytin and photoprotectant absorption from $a_{PH(\lambda)}$ yields the absorption of photosynthetically bound pigments ($a_{PS(\lambda)}$), that in turn constitutes the sum of absorption spectra of PSII ($a_{PSII(\lambda)}$) and PSI ($a_{PSI(\lambda)}$).

The factor *P* in Eqn 2.2 represents an estimate of the fraction of photosynthetically

absorbed energy directed to a_{PSII}. The most basic approach assumes that equal energy is passed to PSII and PSI so $P = 0.5$ (Suggett et al. 2004). This assumption appears valid for some phytoplankton groups, but may be lower in cryptophytes and cyanobacteria that have comparatively low PSII:PSI ratios (Suggett et al. 2004). P is estimated through comparative measurements of spectral PSII fluorescence ($F_{[\lambda]}$) and $a_{PS[\lambda]}$. This analysis can identify regions within the spectrum that preferentially excite one photosystem over the other and generally shows that a higher association of carotenoids and phycobilisomes with PSII is offset with most chl *a* pigments associated with PSI (Suggett et al. 2004). $F_{[\lambda]}$ has arbitrary units and so must be scaled to $a_{PS[\lambda]}$; it is the selection of the scaling technique that ultimately determines the estimate of $P_{[\lambda]}$. Scaling methods either normalize F to a_{PS} at a single wavelength (i.e. 676 nm, Sakshaug et al. 1991; Culver and Perry 1999) or over a series of wavelengths (540 to 650 nm; Johnsen et al. 1997). The 'no overshoot method' assumes all absorption between 540-650 nm is directed towards PSII so $F_{[540\text{-}650\ nm]}$ is scaled to equal to $a_{PS[540\text{-}650\ nm]}$ and P is determined as the ratio of $F_{[400\text{-}700\ nm]}$ to $a_{PS[400\text{-}700\ nm]}$ (see Materials and Methods).

Section 2.1.2: Methodological comparisons of bio-optical and *in vitro* photosynthetic rates

While Eqn 2.1 yields estimates of light-limited oxygenic photosynthesis, most *in vitro* methods measure both light-limited and light-saturated carbon assimilation rates. Such methodological differences require three additional steps to allow for a robust evaluation of bio-optical efficacy and are discussed below. Outlined below, these steps are the application of spectral correction factors to light-limited photosynthetic rates, the bio-optical derivation of light-saturated photosynthetic rates (P_M), and empirical assumptions that reflect the inherent differences between *in situ* oxygenic evolution and *in vitro* carbon assimilation.

Spectral Correction Factors. Bio-optical measurements of $\sigma_{PSII(\lambda)}$, $a_{PSII[\lambda]}$ and $\alpha_{[14C]}$ are

rarely measured under similar spectral environments. By design, the excitation energy emitted by FRRFs overlap a region of high PSII absorption common to most non-phycobilisome containing algae (Figure 2.2). The Soret absorption bands of chl *a* dominate absorption in this region, yet many *in vitro* light sources are 'red-shifted' with comparatively little irradiance in the Soret bands. Spectral correction factors (SCF) must therefore be derived when comparing photosynthetic rates from different spectral environments (Section 2.2: Materials and Methods). SCFs generally indicate that the spectral quality of blue excitation energy is 2-fold more effective than *in vitro* light sources (Ross et al. 2008; Suggett et al. 2006). Despite this large but quantifiable source of error, not all comparative studies have spectrally corrected their data (Table 2.1). In many of the bio-optical studies, measurements of $a_{PH(\lambda)}$ are used to derive SCFs (Eqn 2.8) for $\sigma_{PSII(\lambda)}$. Spectral fluorescence measurements of PSII yield the shape of $a_{PSII(\lambda)}$ and such measurements underscore the potential spectral differences between $a_{PSII(\lambda)}$ and $a_{PH(\lambda)}$ (and therefore $a_{PSI(\lambda)}$; Suggett et al. 2004). For example, in many cyanobacteria the phycobilisomes are predominantly associated with PSII and chl *a* with PSI, so the spectral shapes of $a_{PSII(\lambda)}$ and $a_{PS(\lambda)}$ are quite different (Figure 2.10). Ideally $\sigma_{PSII((\lambda)}$ should be scaled to $a_{PSII(\lambda)}$, due to contribution of non-photosynthetic pigments, pheaophytin and PSI pigments to $a_{PH(\lambda)}$.

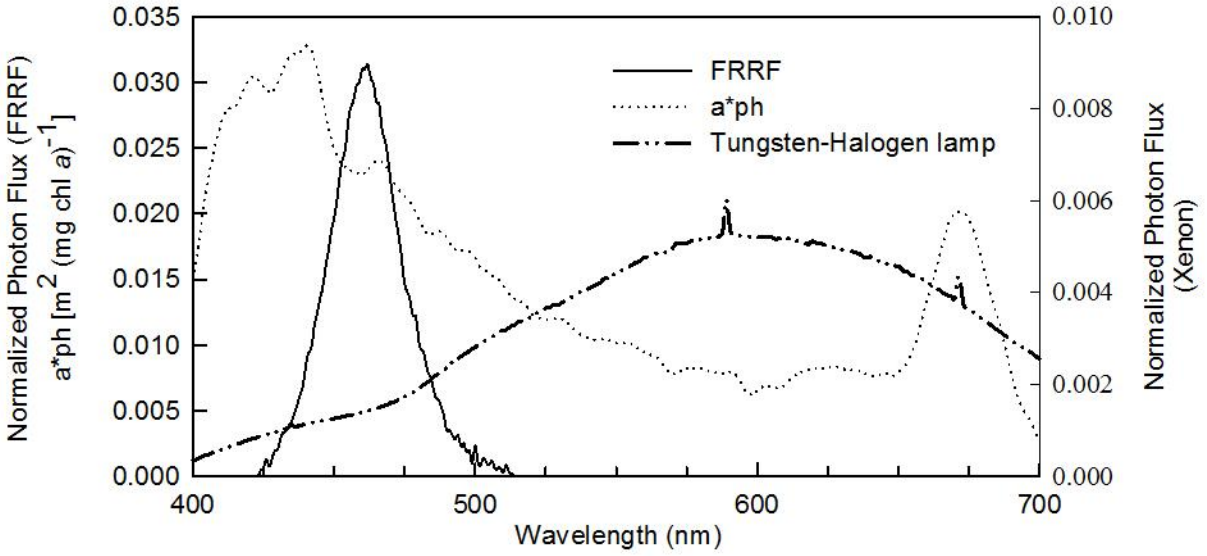

Figure 2.2: The excitation spectrum of the FRRF and a Tungsten-Halogen lamp normalized to photon flux and compared to the mean a^*_{PH} spectra in Lake Erie. Note the different scales for the FRRF and Xenon-arc lamp.

Bio-optical Derivation of P_M. The direct conversion of bio-optical photosynthetic rates to light-saturated rates are confounded by three inherent problems: 1. In high light environments PQ can be oxidized through a variety of pathways that do not result in net oxygen evolution or carbon fixation. 2. Actinic fluorescence measurements can be contaminated by natural red light found in near-surface high light environments that artificially reduces F_V/F_M (Raateoja and Seppala 2004). 3. Photosynthesis is limited downstream of PSII and not dependent on the redox state of the primary acceptor, (Q_A). Comparative studies that do not take these considerations into account invariably show the greatest divergence between bio-optical and *in vitro* photosynthetic rates occurs in the upper water column (Table 2.1). Early recognition of these active-fluorescence limitations (Kolber and Falkowksi 1993) have led many researchers to estimate maximum photosynthetic rates (P_M) as the product of the light-limited photosynthetic rate (α) and the light-saturation index E_K ($=P_M/\alpha$ Talling 1957). The principals of bio-optical and *in vitro* derivations of E_K are analogous: Light dependent models (f_{PSII} vs E or P vs E) yield

curve-fitting parameters that are then used to derive E_K (Ross et al. 2008; Section 2.2: Materials & Methods). A significant drawback to this technique is that, unlike *in vitro* experiments, it necessarily constrains bio-optical profiling to periods when the water column is sufficiently illuminated so as to include both light-limited and light-saturated responses. This method must also assume homogeneity of the photosynthetic population throughout the measured water column. Fortunately as α and P_M generally co-vary in lakes and oceans, E_K is comparatively constrained and decreases with increasing optical depth (Behrenfeld et al. 2002). *A priori* knowledge of 'typical' E_K values for the optical environment under study can serve as an approximation or empirical boundary in the bio-optical derivation of P_M through E_K. Moreover, the potential error introduced by erroneous values of E_K diminishes as the contribution of light-limited to daily integrated photosynthesis increases.

14 of the 16 studies listed in Table 2.1 measured *in vitro* photosynthetic rates using the ^{14}C assimilation technique. Because bio-optical models estimate *oxygenic* photosynthesis, these models overestimate carbon assimilation by a factor equivalent to the photosynthetic quotient (PQ). *A priori* knowledge of the mean PQ (and variance) based on paired ^{14}C and O_2 studies within the ecosystem under investigation provides a 'benchmark' in which to validate bio-optical photosynthetic rates. Conceptually, the PQ represents the ratio of photosynthetically-generated reductant (ATP, NAPDH) to that spent exclusively on carbon assimilation. Nitrate assimilation, nitrogen fixation, photorespiration, chlororespiration, and respiratory phosphorylation each use photosynthetic reductant (Behrenfeld et al. 2002) so the PQ in lakes (Depew et al. 2006) and oceans (Grande et al. 1989) is variable and typically exceeds 1.2. In comparative studies, the apparent PQ has additional uncertainty owing to differing ^{14}C methodologies and differences between *in situ* and *in vitro* environments. In Table 2.1, 12 studies assayed only particulate ^{14}C

so any cellular excretion of ^{14}C-labelled exudates such as glycolate, likely in long incubations or nutrient stressed phytoplankton (Fahnenstiel and Carrick 1988; Beardall et al. 2009), will underestimate carbon assimilation and overestimate the PQ. Furthermore i*n vitro* experimentation can introduce artefacts associated with handling and isolating phytoplankton assemblages in bottles (Eppley 1980), and constraining phytoplankton within a constant *in vitro* light environment may evoke different photoacclimative responses relative to a mixing *in situ* environment (MacIntyre 1993). Thus critical evaluation of bio-optical photosynthetic rates must recognize that inherent sources of error in the 'benchmark' (*in vitro*) photosynthetic measurements may also exist and lack of reconciliation between both methods may not be caused by bio-optical models alone.

The data gleaned from the 14 comparative studies that have employed ^{14}C assimilation in Table 2.1 has been reformulated to show the mean PQ derived in each study. Originally, each study presents either the ratio or slope of the linear regression between bio-optical and ^{14}C photosynthetic rates. Some but not all studies in Table 2.1 assume a fixed PQ (ranging from 1.1-1.5) in their bio-optical formulation, so for consistency all data has been normalized by setting the PQ to 1.0 (and $\Phi O_{2[max]} = 0.25$ respectively). For example the original data at 9 m depth in Study 15 reported $P = 0.56\ P_{[14C]}$ using a PQ and $\Phi O_{2[max]}$ of 1.5 and 0.18 respectively, so Table 2.1 reports $P = 1.07\ P_{[14C]}$ ($1.07 = 0.56 \bullet [0.25/0.18] \bullet [1.5/1.0]^{-1}$). If the relationship between bio-optical and traditional photosynthetic rates is not statistically significant, Table 2.1 omits the reformulated PQ. Summarized in Table 2.1, the PQs derived from each comparative study vary widely with a range of 0.42 to 3.08 with a grand mean value of 1.78. While some variability in the PQs are expected given differing ^{14}C methodologies and environments, the following section highlights how bio-optical model parameterization also affects the apparent PQ.

Section 2.2: Materials and Methods

Table 2.2: Symbols, definitions, units and derivations of the various parameters employed in this chapter. All fluorescence units are dimensionless with arbitrary units [au].

Symbol	Definition and units	Derivation
f_{PSII}	Fluorescence parameters that represent PSII photochemistry	
$F_{M[IRF]}$	Maximum fluorescence yield corrected for Instrument Response Frequency	
$F_{M[Filtrate]}$	Maximum fluorescence yield of filtrate (0.2 μm)	
F_M, F_M'	Maximum fluorescence yield - dark, actinic E	
F_0, F'	Minimum fluorescence yield – dark, actinic E	
F_O'	$F_0' = [Fo \bullet (F_V / F_M' + F_0/ F_M')^{-1}]$	
F_V/F_M	Maximum photochemical efficiency – dark	$[(F_M-F_0)/ F_M]$
F_V'/F_M'	Maximum photochemical efficiency - actinic E	$[(F_M'-F_0')/ F_M']$
q_p	Fraction of oxidized reaction centers	$[(F_M'-F')/(F_M'-F_0')]$
$F_q'F_M'$	PSII photochemical efficiency - actinic irradiance	$[(F_M'-F')/F_M']$
$a_{PSII(\lambda)}$	PSII absorption spectra [m^{-1}] λ denotes wavelength	Figure 2.1
σ_{PSII}	Effective absorption cross-section of PSII - dark, actinic E [$Å^2$]	σ_{PSII}
n_{PSII}	Photosynthetic unit size of PSII [mol RCII (mol chl *a*)$^{-1}$]	
a_{PH}	Phytoplankton pigment absorption spectra [m^{-1}]	Eqn 2.4
a_{PHEO}, a_{PP}	Pheophytin, photo-protectant pigment absorption spectra [m^{-1}]	Eqn 2.5
a_{PS}	Photosynthetic pigment absorption spectra [m^{-1}]	Eqn 2.6
P	The fraction of absorbed photosynthetic energy passed to PSII	Section 2.4
$F_{[\lambda]}$	PSII fluorescence measured at 665 nm following excitation at λ	
SCF_{APS}	Spectral correction factor [au] normalized to $a_{PS[\lambda]}$	Eqn 2.8
SCF_F	Spectral correction factor [au] normalized to $F_{[\lambda]}$	Eqn 2.9
Φ_{O2}	Maximum quantum yield of oxygen evolution [mol O_2 (mol photons)$^{-1}$]	$\Phi_{O2} = 0.25$
Φ_{RC}	Quantum yield of electron transfer with a reaction center [quanta $^{-1}$]	$\Phi_{RC} = 1.0$
$E_{[\lambda]}$	Photosynthetically active radiation (PAR) [μmol.m^{-2}.s^{-1}]	$E_{[\lambda]}$
k_{PAR}	The mean attenuation of PAR [m^{-1}]	k_{PAR}
Chl *a*	Extracted chl *a* [mg m^{-3}]	Chl *a*
P	Photosynthetic rate [mg C m^{-3} hr^{-1}]	
α	Light-limited P [mg C m^{-3} hr^{-1} (μmol.m-^{2}.s^{-1})$^{-1}$]	Section 2.4
P_M	Light-saturated P [mg C m^{-3} hr^{-1}]	Section 2.4
E_K	Light saturation index [μmol.m^{-2}.s^{-1}]	$P_M \alpha^{-1}$
PQ	Photosynthetic quotient [mol C (mol O_2)$^{-1}$]	
*	Denotes normalization to chl *a*	

Study Site and Summary. Four spatial surveys were conducted in Lake Erie in 2005 (May 2-5th, June 7-11th, July 18-21st, September 6-9th). Stations west of 80°W were sampled only in the June and September cruises. Bio-optical and CTD profiles were performed at each station, and spectral radiometric profiles were performed opportunistically during each cruise. At each station discrete water samples were taken at 2 m depth during the May and July cruises and halfway to the thermocline (range 1.5 to 7 m) during the June and September cruises for ^{14}C incubations and water chemistry parameters using 1 meter Niskin bottles (exact depths given in Appendix A). Where deep chl *a* maxima were present, additional water samples were opportunistically retrieved from these features for ^{14}C incubations and water chemistry. Figure 2.3 shows the morphometry and spatial distribution of sampling stations used in this study.

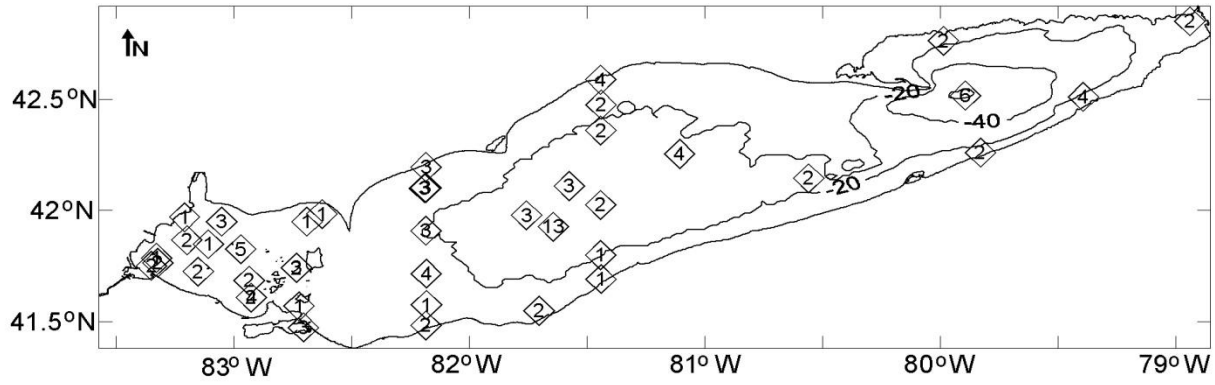

Figure 2.3: Lake Erie sampling stations (◊) with 20, 40 and 60 m isobars. The number inside each ◊ denotes the number of discrete 14C samples taken over all seasons and through depth.

Radiometric and physical profiles - CTD profiles (Seabird 911, Bellevue, Washington) at each station measured water temperature through depth. The FRRF was equipped with 4π quantum sensors (LI-COR, Omaha, Nebraska) to measure photosynthetically active radiation (PAR) through depth. The vertical attenuation of PAR (k_{PAR}) was calculated using the logarithmic slope of PAR through depth.

Bio-optical profiles - A FAST^{tracka} (Chelsea Technologies Group) FRRF with dual 'light' and 'dark' chambers was used to measure vertical profiles of active fluorescence. The FRRF was deployed where possible over the sunward side of the deck, to avoid ship shadow, and the system profiled slowly at less than 0.1m s^{-1}. Eight acquisition sequences of 100 μs saturation flashes, 20 μs relaxation flashes every 60 μs with 10 ms sleep time between acquisitions were averaged into one fluorescence induction curve. For each profile, instrument response frequencies (IRFs that quantify instrument noise) discussed in Laney and Letelier (2008) were deconvolved from FRRF measurements using the V6 Matlab software. IRFs were determined by measuring the above noted acquisition sequence on a gradient of neutral fluorophores (Chl *a* standard, Sigma-Alrich) at the various gain settings. At each station, background fluorescence was determined by measuring filtrate (filtered successively through 0.7 μm GFF and 0.22 μm polycarbonate filters) in the FRRF dark chamber. As above, filtrate measurements were passed through the V6 software to deconvolve IRF. Following Suggett et al. (2006), an empirical linear relationship describing the signal to noise ratio was constructed using profile and filtrate measurements. This relationship yields the percent noise for a given measurement of F_M (Figure 2.6B), so using this relationship the estimated percent noise of each FRRF measurement was determined then subtracted from all F_0 and F_M data. Additional quality control of FRRF data was performed by removing noisy induction curves defined here as having a χ^2 estimator of good fit (quantified in the V6 software) greater than 0.05. Finally, profile data was binned into 0.25 m intervals and F_O' and q_P were calculated following Oxborough and Baker (1997) and Falkowski and Kolber (1993) respectively.

A spectral fluorometer (Fluoroprobe, BBE moldaenke, Germany) was deployed alongside each FRRF profile. The Fluoroprobe measures the chl *a* fluorescence (detection at 685 nm)

following saturating light pulses centered at 450, 525, 570, 590 and 610 nm (approximate bandwidth of 20 nm). Fluorescence at each wavelength was corrected for instrument noise using a cuvette filled with double-distilled water. Wavelength-specific background fluorescence signals were quantified for each basin in Lake Erie using the same filtrate technique described above for the FRRF, and these signals were subtracted from raw fluorescence data. Generally background fluorescence was <10% of total fluorescence at 450 nm and <5% at all other wavelengths.

Chl a and pheophytin a. At each sampling depth, triplicate measurements of chl *a* were performed by passing 200 ml of water through 47 mm Whatman GF/F filters and immediately frozen. In the lab, filters were immersed in 20 ml of 90% acetone and passively extracted at 4°C for 24 hours. Extracts were quantified fluorometrically before and after acidification on a 10-AU fluorometer (Turner Design, Sunnyvale, California) calibrated with pure chl *a* standard (Sigma) to determine concentrations of chl a *a*nd pheophytin *a* respectively (Holm-Hansen et al. 1965).

Quantitative Filter Technique. At each sampling depth 1500 ml of lake water was passed through a 47 mm Whatman GF/F filter and immediately frozen. In the lab, 5 ml of deionized water was passed through each filter to thaw it. The absorption spectra (350-750 nm) of the particulate matter retained on each filter ($a_P(\lambda)$) was measured immediately after thawing using a Cary 100 dual beam scanning spectrophotometer. Each filter was subsequently de-pigmented by bleaching the filter with NaClO for approximately 5 minutes and then re-scanned to determine absorption by non-algal particles ($a_{NAP}(\lambda)$; Tassan and Ferrari 1995). Shown in Eqn 2.4, the absorption spectra of phytoplankton pigments, $a_{PH(\lambda)}$, is calculated as the difference between $a_P(\lambda)$ and $a_{NAP}(\lambda)$, where 2.303 is the natural logarithm of 10, β is the path length amplification factor ($\beta = 2$, Roesler 1998; Binding et al. 2008) and V_f/A_f is the ratio of volume filtered to the

clearance area of the filter. To account for filter scattering, the mean absorption between 746-750 nm was subtracted from both $a_P(\lambda)$ and $a_{NAP}(\lambda)$. Following Culver and Perry (1999), $a_{PHEO(\lambda)}$ was first determined at 676 nm given the concentrations of chl *a* and pheophytin *a* with an absorption ratio of 1:0.58 at this wavelength (Eqn 2.5). $a_{PHEO(676\ nm)}$ was then scaled to the pheophytin *a* absorption spectra (Eijckelhoff and Dekker 1997) to yield $a_{PHEO(\lambda)}$. Unfortunately, a similar approach was not performed for photoprotective pigments, so we assume that $a_{PP(\lambda)}$ is 0 and $a_{PS(\lambda)}$ is $a_{PH(\lambda)} - a_{PHEO(\lambda)}$ (Eqn 2.6). The impact of this assumption is discussed further below. The slope of $a_{PS(\lambda)}$ between 488 and 532 nm was used to estimate the ratio of photoprotectant to photosynthetic carotenoids (PPC:PSC) following the empirical relationship presented in Eqn 2.7 (Eisner et al. 2003). Finally, the contribution of absorption through chl *a* ($a_{CHL(\lambda)}$) and all other pigments ($a_{ACC(\lambda)}$) were separated from $a_{PS(\lambda)}$ by assuming $a_{PS(676)}$ was solely related to chl *a*, and then scaling this value to the absorption spectra of chl *a*. Figure 2.4 provides examples of these techniques.

[Eqn2.4] $a_{PH(\lambda)} = 2.303 \bullet [a_P(\lambda) - a_{NAP}(\lambda)] \bullet \beta^{-1} [V_f/A_f]^{-1}$

[Eqn 2.5] $a_{PHEO}(676) = a_{PH}(676) \bullet [0.58 \bullet \text{pheophytin } a] \bullet [0.58 \bullet \text{pheophytin } a + \text{Chl } a]$

[Eqn 2.6] $a_{PS(\lambda)} = a_{PH(\lambda)} - a_{PHEO(\lambda)}$

[Eqn 2.7] $\text{PPC:PSC} = \{[a_{ph}(488) - a_{ph}(532)] \bullet [a_{ph}(676) \bullet (488\text{-}532)]^{-1} - 0.0056\} \bullet [-0.0126]^{-1}$

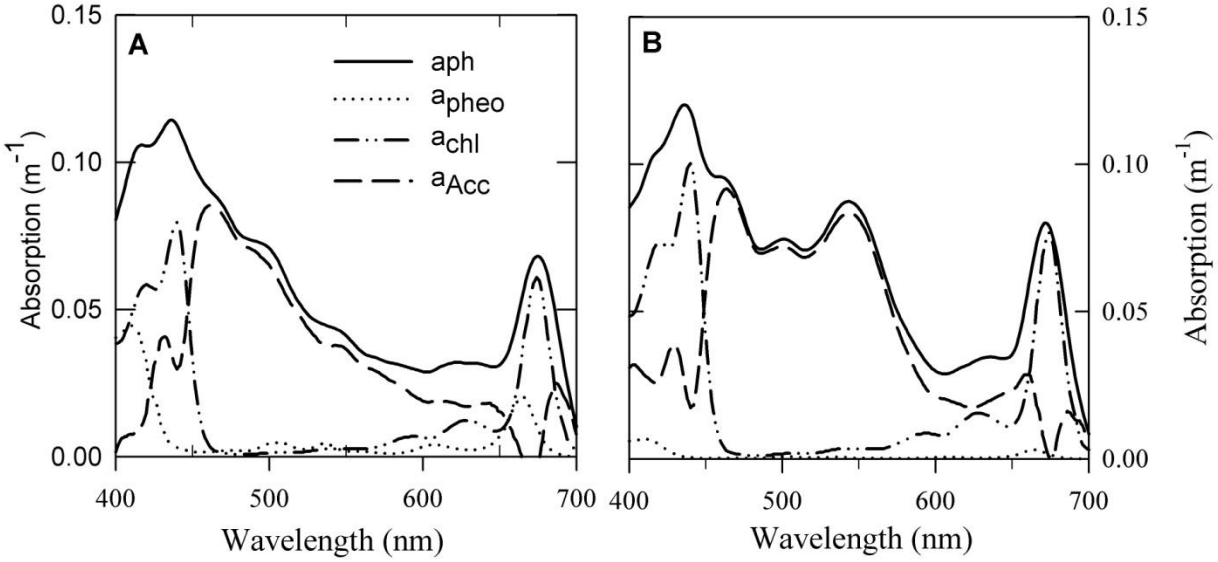

Figure 2.4: Derived absorption spectra of phytoplankton pigments (a_{ph}), pheophytin *a* (a_{pheo}), chl a (a_{Chl}) and accessory pigments (a_{Acc}). Absorption spectra are from the same station (ER73 on day 160) sampled from the A) the epilimnion (5 m) and B) the deep chlorophyll maxima (14 m).

Spectral correction factors. To remove the spectral bias of different light sources (Figure 2.1), measurements of $\alpha_{[14C]}$ and σ_{PSII} were spectrally scaled to a 'white' (flat) spectra. Normalization to white spectra is preferential as it is the least ambiguous method to facilitate future comparisons of spectrally dependent measurements. Shown in Eqn 2.8, normalization requires the derivation of a spectral correction factor (SCF), where $a_{PS[\lambda]}$ is described above, $E_{[\lambda]}$ is the measured spectra of the light source (FRRF, incubator, *in situ*) and $W_{[\lambda]}$ represents a constant irradiance (i.e. 1) over the wavelength of interest (PAR, 400-700 nm).

[Eqn 2.8] $SCF_{APS} = \Sigma[a_{PS[\lambda]} \bullet E_{[\lambda]}] \bullet \Sigma[E_{[\lambda]}]^{-1} \bullet [\Sigma[a_{PS[\lambda]} \bullet W(\lambda)] \bullet \Sigma[W(\lambda)]^{-1}]^{-1}$

[Eqn 2.9] $SCF_F = \Sigma[F_{[\lambda]} \bullet E_{[\lambda]}] \bullet \Sigma[E_{[\lambda]}]^{-1} \bullet [\Sigma[F_{[\lambda]} \bullet W_{[\lambda]}] \bullet \Sigma[W_{[\lambda]}]^{-1}]^{-1}$

Eqn 2.8 assumes the spectral shapes of a_{PSII} is equivalent to the spectral shape of a_{PS}. This assumption was tested by substituting $a_{PS(\lambda)}$ in with fluorescence data ($F_{[\lambda]}$) acquired within 1 meter of sampling depth from the submersible spectral fluorometer as shown in Eqn 2.9. $F_{[\lambda]}$ is

measured at only 5 wavelengths (450, 525, 570, 590, 610 nm), this decreased resolution was tested by comparing the SCF_{APS} using all wavelengths to SCF_{APS} using $a_{PS[\lambda]}$ only the 5 wavelengths above: The 5 wavelengths seem well chosen as the two SCFs were significantly correlated ($r^2 = 0.90$, $n = 110$, $p < 0.001$), though the 5-wavelength SCF was on average 7% lower. This exercise demonstrates the statistical validity estimating a SCF_F, and all SCF_F derived from the fluorescence spectra are multiplied by 1.07.

^{14}C PE parameters. Whole water samples collected from discrete depths were filtered through Nitex mesh (60 μm pore size) to remove large zooplankton. Screened samples (80 ml) were inoculated with ^{14}C sodium bicarbonate (ICN Biomedicals, Irvine, CA; 2 mCi mL^{-1}) and dispensed into 20 ml borosilicate glass scintillation vials in 5 ml aliquots. For each experiment, a time zero sample (A_{T0}) was acidified with 100 μL of 6M HCl, allowed to de-gas for 24 hrs, and subsequently fixed with 15 ml of Ecolume scintillation cocktail (ICN Pharmaceuticals, Costa Mesa, CA). Duplicate total activity samples (TA, 100 μL) were taken to verify the specific activity, and fixed with ethanolamine. Twelve vials were placed into a light gradient incubator modelled after Lewis and Smith (1983), equipped with a 300 W Quartzline lamp (General Electric Co. Cleveland, OH) that provided different light intensities from 3 – 1400 μmol photons m^{-2} s^{-1}. Water baths maintained a constant temperature in the incubator within 2°C of the *in situ* temperature. Irradiance (E) at each position in the incubator was measured using a flat plate LI-COR quantum sensor. Flat plate measurements of E were slightly lower than when measured with a 4-π LI-COR quantum sensor, so amplification factors specific to each incubator position were subsequently applied to measurements of E. At the end of each incubation (1 hr), 100 μL of 6M HCl was added to each scintillation vial to drive off any unincorporated ^{14}C, and samples were allowed to de-gas and chemically fixed as above. The activity of all samples was

determined by liquid scintillation counting (LKB Wallac 1209 Rackbeta) using external standards for quench correction. Photosynthetic carbon assimilation rates were calculated using dissolved inorganic carbon concentrations that were determined by Gran titration (Wetzel and Likens 1991) on filtered (GF/F, 0.7 μm) lake water at each station. PE data was fitted to the hyperbolic tangent model (Jasbby and Platt 1976) to derive α and P_M using the nonlinear least squares regression function in the *stats* package of R (version 2.70). Following the notation of Table 2.1, the subscript $_{[14C]}$ differentiates *in-vitro* measurements of α and P_M from bio-optical estimates of the same parameters.

Bio-optical derivation of PE parameters (α and P_M). By definition α is the photosynthetic rate per unit E when E is limiting. Eqn 2.1 can therefore be rearranged to show $P/E_{(\lambda)} = A \bullet f_{PSII} \bullet a_{PSII(\lambda)} = \alpha$. Therefore bio-optical measurements of α are a function of f_{PSII} and $a_{PSII(\lambda)}$ and are independent of E. The most significant implication of this formulation is that it allows bio-optical estimates of α from profiles taken either during the day of night. As ^{14}C PE parameters and a_{phy} were derived from discrete samples of water, *in situ* measurements of f_{PSII} and $a_{PSII(\lambda)}$ were calculated as the average value within 1 m of the depth of the corresponding sample (i.e. the length of Niskin bottles). However, as f_{PSII} varies somewhat predictably with increasing E (Section 2.3.5), if mean *in situ* E at the corresponding depth exceeded 50 $\mu mol.m^{-2}.s^{-1}$ deeper measurements within the epilimnion of f_{PSII} were used below this stated E threshold. On six occasions E exceeded 50 $\mu mol.m^{-2}.s^{-1}$ throughout the epilimnion so f_{PSII} was instead derived from dark-adapted (~1 hr) samples taken from the same discrete depth.

Bio-optical estimates of P_M were derived as the product of bio-optically derived α and either an optical or bio-optical estimate of E_K. Optical estimates of E_K here are approximated

using E_{24}, the daily mean irradiance in the epilimnion (Eqn 2.10). Measurements of k_{PAR} for nocturnal profiles were approximated from the beam attenuation coefficient that was statistically correlated with k_{PAR} during diurnal measurements ($r^2 = 0.92$, $n=58$, $p<0.001$). Using binned fluorescence data, E-dependent decreases of q_p and F_q'/F_M' were fit to a modified exponential curve model (Eqn 2.11; Smyth et al. 2004). If the two parameters describing the exponential curve were statistically significant ($p < 0.05$), E_K was derived following Eqn 2.12 in an approach analogous to traditional PE curves.

[Eqn 2.10] $E_{24} = k_{PAR} \bullet z_{epi}$

[Eqn 2.11] $f_{PSII} = (b - (1 - \exp^{-a*PAR})$

[Eqn 2.12] $E_K = (1 - 0.5 \bullet b) \bullet (-1 \bullet a)^{-1}$

Section 2.3: Results

Results are divided into five sections. Section 2.3.1 introduces the range of physical and optical data under investigation. Sections 2.3.2 and 2.3.3 explore the various bio-optical derivations of f_{PSII} and a_{PSII} respectively. Section 2.3.4 uses three different combinations of bio-optical parameters to estimate $\alpha_{[FRRF]}$ and compares these estimates to *in vitro* derived α_{14C}. Finally Section 2.3.5 compares bio-optical and *in vitro* estimates of E_K and P_M.

Section 2.3.1:Physical and Optical gradients.

Table 2.3 and Figure 2.5 underscore the large physical and optical gradients over which the efficacy of bio-optical PP models is tested. Figure 2.5A documents the seasonal evolution of Lake Erie's thermal structure as measured in the central basin. Bio-optical measurements in early May coincided with isothermal water columns in many central basin stations and the onset of seasonal stratification in the warmer western basin. Successive surveys documented a progressive warming and deepening of the epilimnion, typical of most temperate lakes (Wetzel 2001).

Over the course of this study, discrete measurements of epilimnetic chl *a* spanned nearly two orders of magnitude. In addition to this spatial and seasonal variability, chl *a* fluorescence profiles and discrete sampling within the metalimnion revealed a deep chlorophyll maxima (DCM) at many stations. Chapter 3 further investigates the vertical distribution of chl *a* and other bio-optical measurements, here we focus on comparative production estimates only. Shown in Figure 2.5B, epilimnetic measurements of chl *a* generally co-vary with k_{PAR} though the relationship is not strong ($k_{PAR} = 0.18$ chl $a^{0.78}$; $r^2 = 0.51$, $n = 88$, $p < 0.05$) and attenuation per unit chl *a* is higher than oceanic 'Case 1' waters (Morel 1988). In addition to large range of

Table 2.3: Mean, standard deviation and range of depth and temperature of the epilimnion, k_{PAR}, E_{24} and Chl *a*.

Parameter	Mean (Standard Deviation)	Range
Physical		
Depth of Epilimnion [m]	10.6 (4.7)	3.7 - 24.5
Temperature of Epilimnion [°C]	19.3 (6.1)	5.2 - 27.2
Optical		
k_{PAR} [m]	0.46 (0.35)	0.20 - 3.60
E_{24} [$\mu mol.m^{-2}.s^{-1}$]	147 (73)	48 – 303
Biological		
Chl *a* [$mg.m^{-3}$]	3.23 (3.46)	0.34 - 30.20

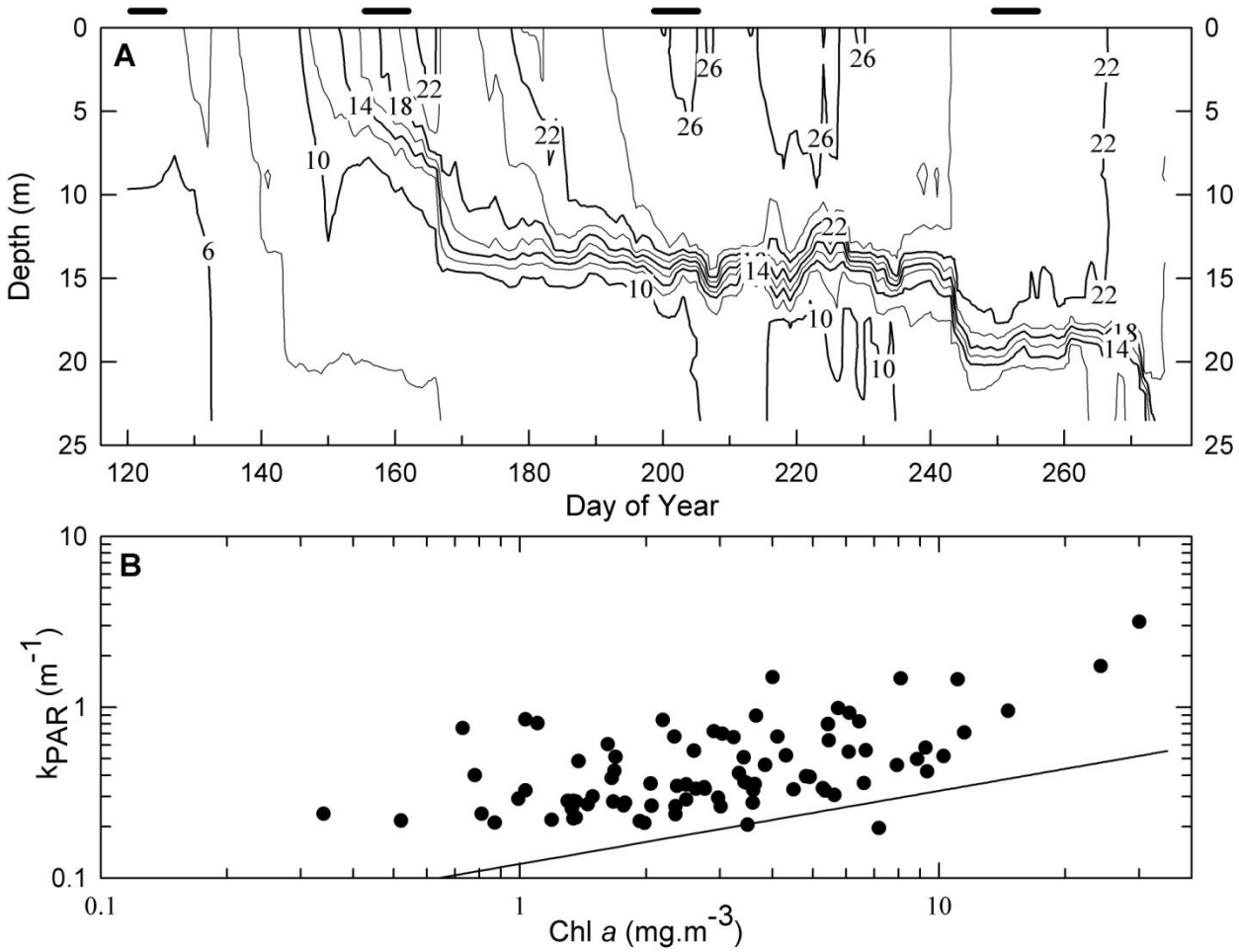

Figure 2.5: A) Seasonal evolution of the thermal structure in Lake Erie's central basin. Isobars are temperature (2°C increments), solid lines above the graph correspond to dates of spatial surveys. B) The relationship between k_{PAR} and Chl *a* in the epilimnion. The solid line is the derived value for 'Case 1' oceanic waters presented by Morel (1988).

chl *a*, sediment resuspension at some shallow stations and variable concentrations of dissolved organic matter further increase the variability of Lake Erie's optical properties (Binding 2008).

Section 2.3.2: Bio-optical model parameterization – f_{PSII}.

Figure 2.6A and Table 2.4 reports the mean, standard deviation and 95% outliers of the various f_{PSII} parameters employed in bio-optical models and measured in this study. Surrogates of photochemical quenching (F_V'/F_M' $[F_V/F_M]^{-1}$ and q_P) on average approached their theoretical maximum (1.0) and had low coefficients of variance (c.v. < 10%) indicating that the data filter applied here to remove high E values was generally successful. The ensuing variability in the remaining f_{PSII} measurements therefore represents underlying taxonomic and nutritional signatures (Suggett et al. 2008). Upon normalization to 0.65, average values of the f_{PSII} parameters were moderately high and numerically constrained (c.v. < 15%). Light driven reductions to f_{PSII} parameters are presented in Section 2.3.5.

Corrections for instrument noise and background fluorescence are critical when deriving f_{PSII}. Relative to marine waters, the high chl *a* concentrations in Lake Erie permit fluorescence measurements to be made with little amplification of the fluorescence signal (low instrument gain) so correction for instrument response frequencies (IRF) on average increased F_V/F_M by 3%. Shown in Figure 2.6B a statistically significant linear correlation was found between background fluorescence ($F_{M\,[Filtrate]}$) and profile measurements corrected for instrument noise only ($F_{M\,[IRF]}$) at the corresponding sampling depth *($r^2 = 0.69$, $n=59$, $p < 0.001$)*. The mechanisms driving this relationship are unknown but suggest that some form of dissolved organic matter that absorbs and fluoresces blue and red light respectively, possibly dissolved pheophytin, approximately covaries with chl *a* in Lake Erie. Similar to the findings of Suggett et al. (2006), the quantitative

Table 2.4: Mean, standard deviation and range of derived f_{PSII} parameters (*n = 110*).

	$F_V/F_M/0.65$	$F_q'/F_M'/0.65$	$F_V'/F_M'/0.65$	F_V'/F_M' $[F_V/F_M]^{-1}$	q_P
Mean (St. Dev.)	0.76 (0.10)	0.72 (0.10)	0.78 (0.10)	0.98 (0.07)	0.93 (0.08)
Range	0.52-1.04	0.37-0.98	0.38-1.06	0.55-1.13	0.60-1.00

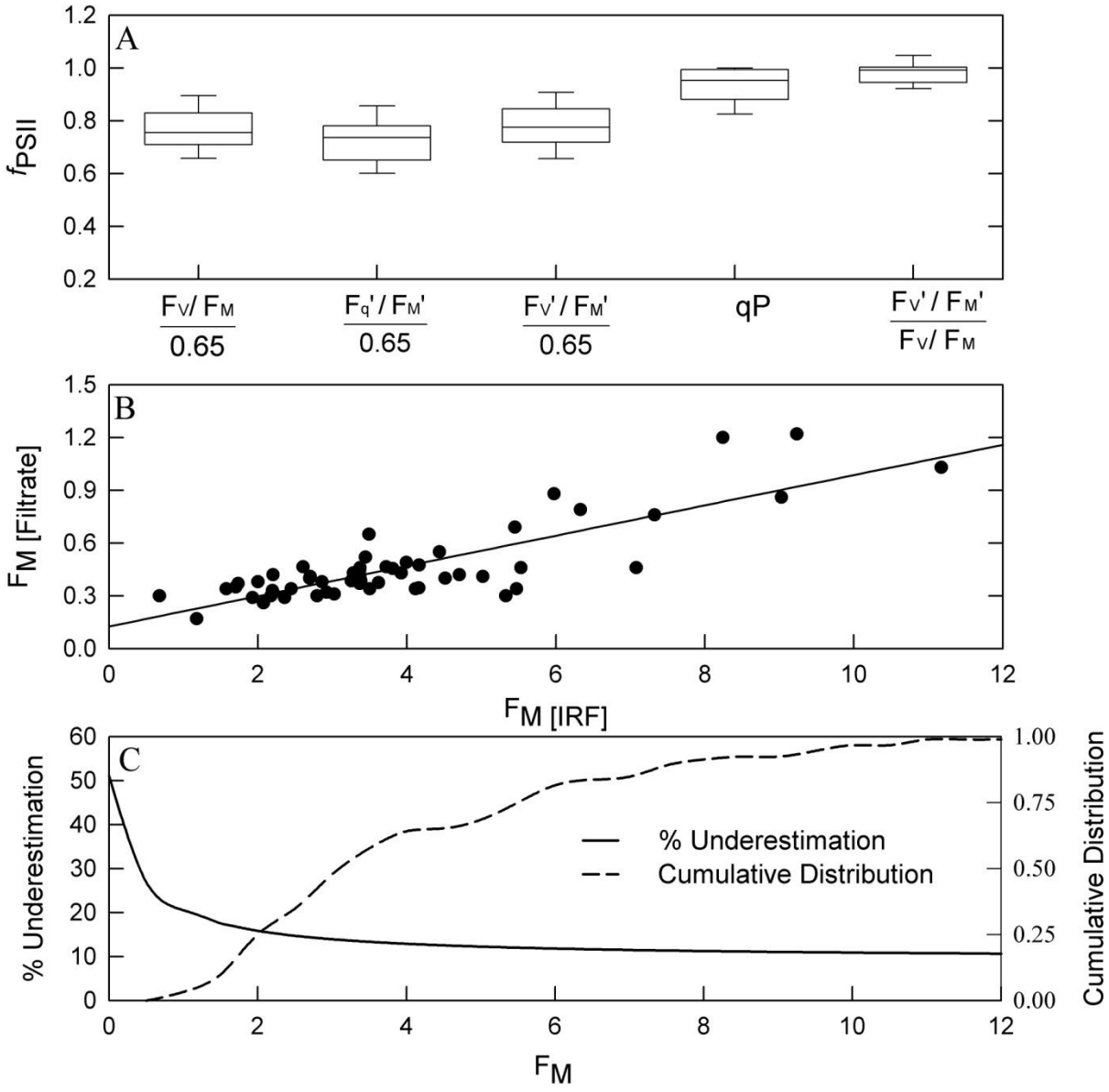

Figure 2.6: A) Box plots showing the median and standard deviation of commonly used f_{PSII} parameters, whiskers are the 5th and 95th percentile for each value. Comparison of signal ($F_{M\ [IRF]}$) against B) noise (F_M [filtrate]) and C) Cumulative distribution of corrected F_M values with % underestimation of F_V/F_M at a given corrected F_M value.

importance of background fluorescence increased with decreasing signal. Figure 2.6C further demonstrates the impact of background fluorescence on estimations of f_{PSII}: Using the linear regression in Figure 2.6B, the % underestimation of F_V/F_M was computed across a range of corrected F_M values. The same plot also shows the cumulative distribution frequency of all corresponding F_M values from Figure 2.6A. From this comparison failure to account for background fluorescence would have resulted in a minimum 10% and maximum 20% underestimation for all F_V/F_M values.

Section 2.3.3: Bio-optical model parameterization – a_{PSII}.

This section first presents measurements of $\sigma_{PSII[\lambda]}$, $a_{PS[\lambda]}$ and *P*. Following Eqns 2.2 and 2.3 these parameters are then used derive $a_{PSII[\lambda]}$. SCFs derived through absorption and fluorescence measurements are then presented.

σ_{PSII} in the dark, light (σ_{PSII}') and epilimnetic maxima of dark values ($\sigma_{PSII[Max]}$) have each been employed to estimate a_{PSII} in bio-optical models (Table 2.1). Figure 2.7A and Table 2.5 show the mean, standard deviation and 5th and 95th percentiles of each measured value and Figure 2.7B shows the relationship between values. Empirically, inclusion of any of three parameters will not produce significant differences in bio-optical estimates of a_{PSII}: Dark measurements of σ_{PSII} were on average lower and highly correlated to both σ_{PSII}' ($r^2 = 0.95$, $n=100$, $p<0.001$) and $\sigma_{PSII}'_{[Max]}$ ($r^2 = 0.95$, $n=100$, $p<0.001$). Similar to f_{PSII}, high irradiance values (> 50 μmol m^{-2} s^{-1}) have been removed from Figure 2.7 so significant co-variation between σ_{PSII} and σ_{PSII}' is expected.

Table 2.5 and Figure 2.7 also summarize pigment absorption measurements derived through the QFT. On average, absorption of pheo *a* (a_{PHEO}) constituted 13% of total pigment

absorption (a_{PH}). In 16 of the 110 samples, 8 of which were sampled from the DCM, failure to account for a_{PHEO} would have resulted in at least a 20% overestimation of a_{PS}. Figure 2.8C shows the a_{PS} spectra of all samples normalized to their respective maxima. The absorption peaks of all samples were within a few nanometers of 440 nm, the peak of the chl *a* Soret band. A linear regression of chl *a* concentrations against $a_{PS[\lambda]}$ for all wavelengths in the PAR waveband demonstrates that chl *a* alone predicts between 59 and 84% of the variance in $a_{PS[\lambda]}$ (Figure 2.7D). The slope of the linear regression at 676 nm (Figure 2.7D inset) was 0.018 m^2.mg chl *a*, consistent with other literature values (Bricaud et al. 1995; Binding et al. 2008). Wavelengths where chl *a* explained the least variance in a_{PH} (440 to 590 nm) correspond to regions of peak absorption of phycobilisomes as well as photosynthetic and photoprotectant carotenoids (Figure 1.2). However the statistically significant regressions (p<0.01) between chl *a* and accessory pigment wavelengths (440 to 590 nm) indicate that concentrations of accessory pigments and chl *a* co-vary. The slopes of these linear regressions across the PAR spectrum are highest between 500 and 650 nm (data not shown). This suggests that as chl *a* increases, light absorption by photosynthetic accessory pigments becomes increasingly important.

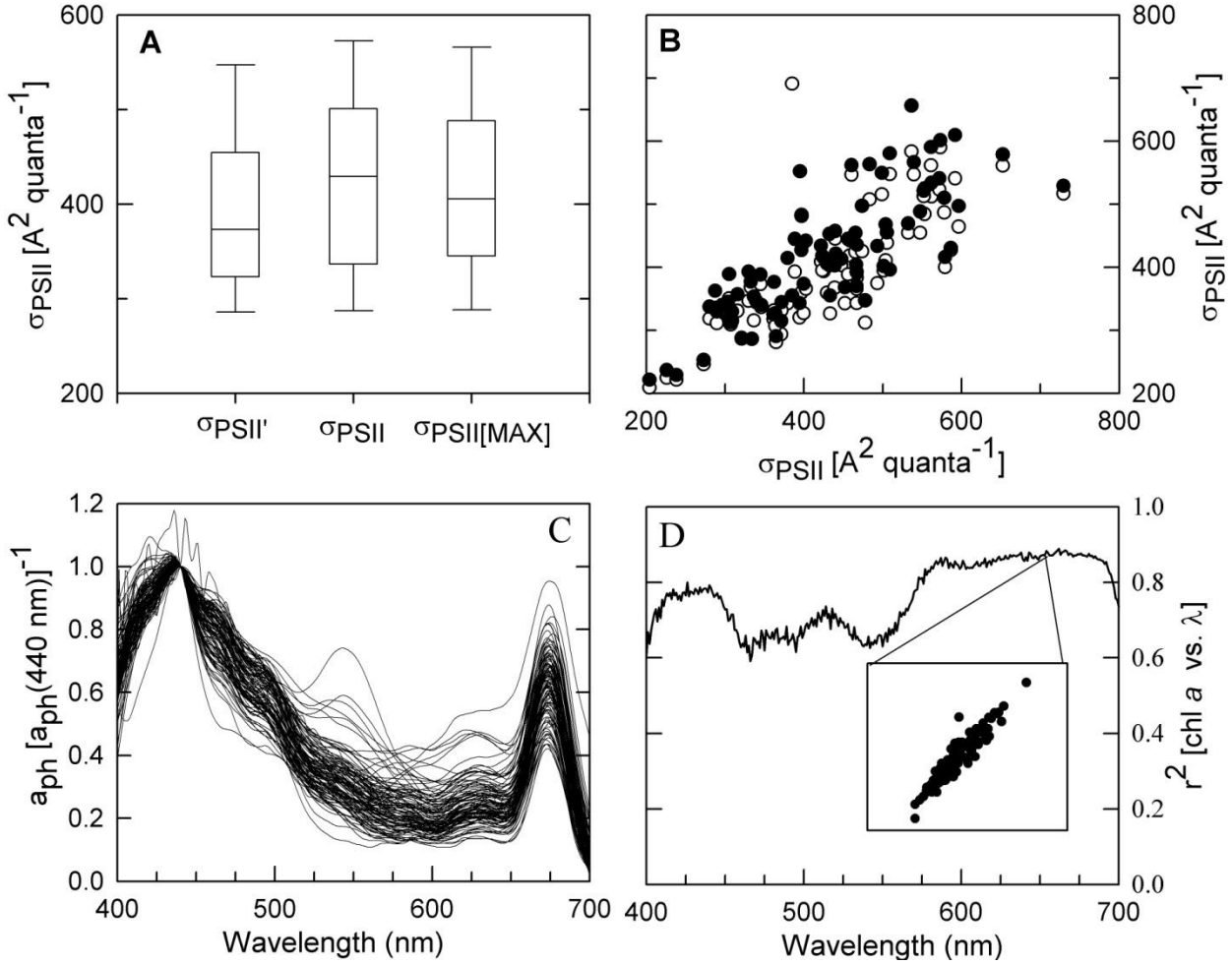

Figure 2.7: A) Box and whisker plots showing variability in σ_{PSII}', σ_{PSII} and $\sigma_{PSII[Max]}$. B) Co-variation of σ_{PSII} with σ_{PSII}' (open symbols) and $\sigma_{PSII[Max]}$ (closed symbols). C) Absorption spectra of all phytoplankton pigments (a_{ph}) normalized to their respective maxima. D) Wavelength-specific linear regressions of a_{ph} and chl *a*, inset is linear regression of a_{ph} (675 nm) and chl *a*.

Table 2.5: Mean, standard deviation and range of derived σ_{PSII} [$Å^2$ $quanta^{-1}$] values by three methods and relevant phytoplankton absorption measurements (*n = 110*).

Parameter	$\sigma_{PSII'}$	σ_{PSII}	$\sigma_{PSII}'_{[max]}$	a_{PH}	a_{PHEO}	a_{PS}
Mean (St. Dev.)	393 (119)	423 (122)	416 (122)	0.053 (0.029)	0.007 (0.006)	0.046 (0.027)
Range	73-393	97-823	73-994	0.008-0.204	0-0.027	0.008 - 0.202

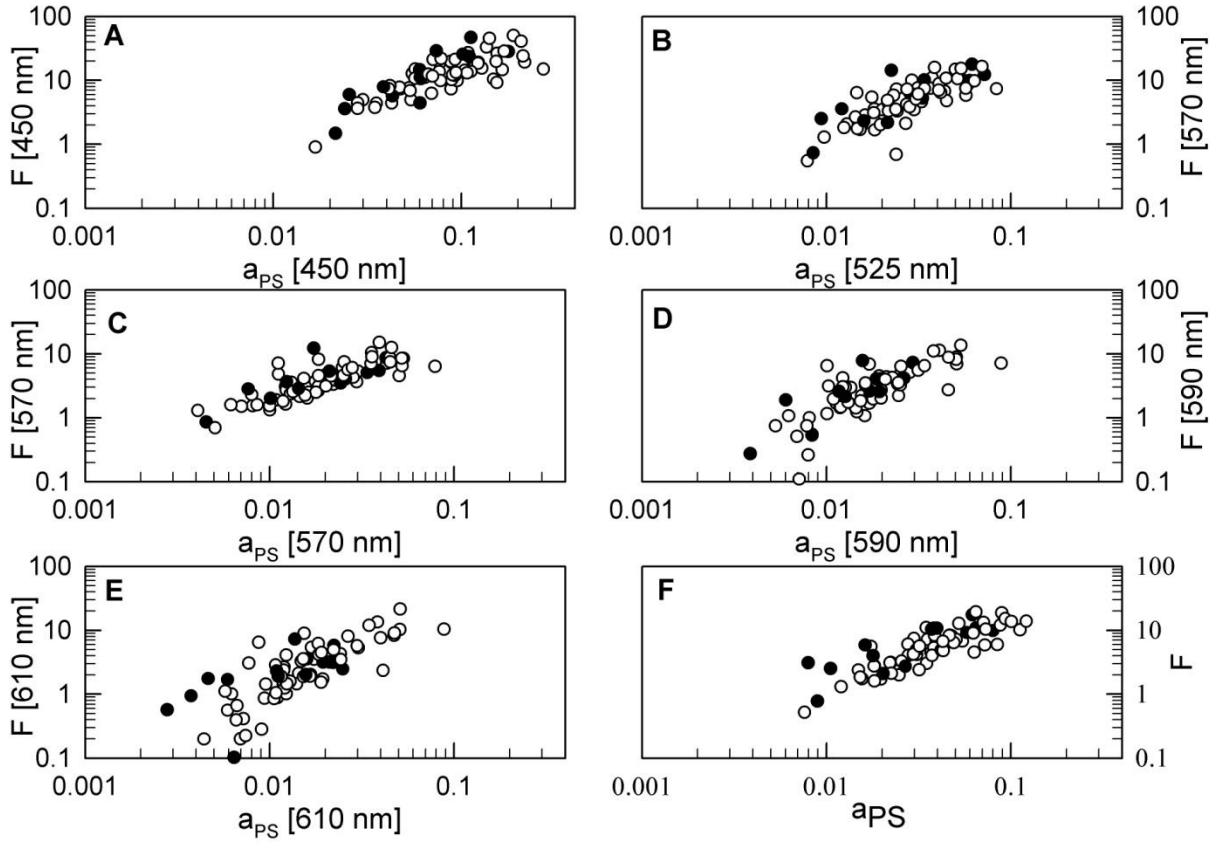

Figure 2.8: Comparisons of spectral fluorescence (F) and pigment absorption (a_{PS}) at A) 450 nm B) 525 nm, C) 570 nm, D) 590 nm, E) 610 nm, and F) mean spectral fluorescence (F) and a_{PS}. Filled circles are from samples taken beneath the surface mixed layer.

Table 2.6: Linear regression analysis of data shown in Figure 2.8.

Panel	$F_{[\lambda]}$ per $a_{PS[\lambda]}$ Mean (St. Dev.)	Statistical Fit
A: 450 nm	174 (105)	*(r^2 = 0.69, n = 71, p < 0.001)*
B: 525 nm	186 (135)	*(r^2 = 0.68, n = 71, p < 0.001)*
C: 570 nm	165 (71)	*(r^2 = 0.71, n = 71, p < 0.001)*
D: 590 nm	177 (184)	*(r^2 = 0.67, n = 71, p < 0.001)*
E: 610 nm	191 (123)	*(r^2 = 0.68, n = 71, p < 0.001)*
F: a_{PS} vs. F	164 (80)	*(r^2 = 0.74, n = 71, p < 0.001)*

Figure 2.8 and Table 2.6 summarize comparative measurements of *in situ* PSII fluorescence ($F_{[\lambda]}$) and $a_{PS[\lambda]}$. Figure 2.8A to 2.8E compare fluorescence ($F_{[\lambda]}$) and absorption ($a_{PS[\lambda]}$) measurements at the 5 fluorescence excitation wavelengths of the fluoroprobe. All $F_{[\lambda]}$ were significantly correlated to wavelength specific measurements of $a_{PS[\lambda]}$ with coefficients of determination ranging from 0.67 to 0.71 for log-transformed data (Table 2.6). Figure 2.8F compares the mean fluorescence (F, average of the 5 wavelengths) to corresponding measurements of a_{PS}. Both measurements were significantly correlated, so through the empirical relationship listed in Table 2.6 reasonable estimates of a_{PS} can be obtained from *in situ* fluorescence measurements alone. *In situ* spectral fluorometers like the Fluoroprobe used here are marketed as a tool to discriminate pigment groups, but their apparent ability to estimate a_{PS} is not surprising as the excitation wavelengths are strategically chosen to overlap with chl *a* and the major photosynthetic accessory pigments. Furthermore some variability in the correlation between F and a_{PS} as shown in Figure 2.8F is anticipated, as the fluorescence yield per unit a_{PS} should vary with *P* that describes the amount of absorbed energy directed towards PSII where F originates.

Measurements of F are scaled to a_{PS} to derive a_{PSII} using two different techniques and *P* is simply the ratio of derived a_{PSII} to a_{PS} for each technique. First, an approximation of the "no overshoot" method was used by assigning the mean F at 570, 590 and 610 nm to equal the mean a_{PS} at these three wavelengths then taking the resultant mean F is equivalent to a_{PSII}. Shown in Figure 2.9B and consistent with other studies (Johnsen et al. 1997; Johnsen and Sakshaug 2007), the no-overshoot method yields high values of *P*. A second novel scaling method to estimate a_{PSII} and *P* is proposed here and will be termed $P_{0.5}$. This method, summarized in Figure 2.9A, simply scales F to a_{PSII} using the mean F per unit a_{PS} from the entire population (Table 2.6) where

it assumed that over a large taxonomic gradient *P* is on average 0.5. The logic of this method simply recognizes that phytoplankton assemblages that direct more absorbed energy to PSII have higher F per unit a_{PS} than assemblages that direct more energy to PSI. Figure 2.9A gives two examples for samples with the same a_{PS} and different F. The y-axis is the mean F derived from the 5 Fluoroprobe wavelengths and the x-axis is the 0.5 times a_{PS} of the attendant value. The slope and offset of the linear regression between F and a_{PS} * 0.5 was derived and a_{PSII} was calculated as (F-offset)*slope^{-1}. Upon determing a_{PSII}, *P* is simply a_{PSII}/a_{PS}. The scaling method for the sample with higher F per unit a_{PS} yields higher value of a_{PSII} (*P* = 0.65) than the sample with lower F per unit a_{PS} (*P = 0.33).* The advantage of this scaling technique over the no-overshoot method is that, given a large dataset that establishes an empirical relationship between F and a_{PS}, estimates of a_{PSII} can be obtained in the absence of a_{PS}. In this study, Fluoroprobe profiles were performed alongside FRRF profiles so estimates of a_{PSII} have the same vertical resolution as f_{PSII}.

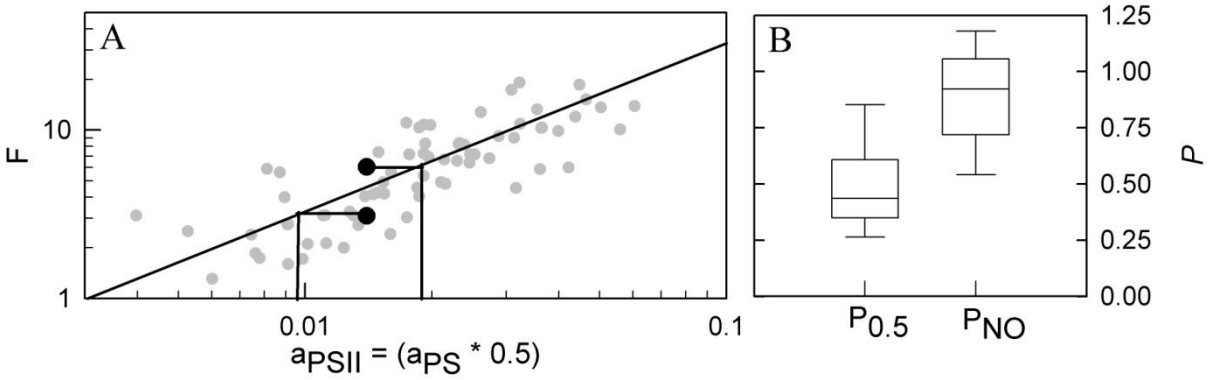

Figure 2.9: A) Figure 2.8F recast showing derivation of a_{PSII} and $P_{0.5}$ from F measurements. All a_{PS} measurements from Figure 2.8F are multiplied by 0.5 and the solid line is the mean F per unit a_{PS} • 0.5. B) Estimates of $P_{0.5}$ and P_{NO} from this study. Box and whiskers are explained in Figure 2.6.

Figure 2.10 summarizes methodological-specific variability of a^*_{PSII} estimates used here. Relative to Figure 2.6 that shows the variability of f_{PSII} parameterization, Figure 2.10 clearly

shows that methodological selection of a^*_{PSII} has a greater influence on bio-optical estimates of phytoplankton photosynthesis. In this study, the product of measured σ_{PSII} with a constant n_{PSII} (0.002 mol PSII (mol chl *a*)$^{-1}$) yielded the lowest mean estimates of a^*_{PSII} (2.8×10^{-3} m^2 mg chl *a*$^{-1}$) while fluorescence measurements scaled to a_{PS} using P_{NO}, an approximation of the "no overshoot method", yielded the highest estimates of a^*_{PSII} (1.3×10^{-2} m^2 mg chl *a*$^{-1}$).

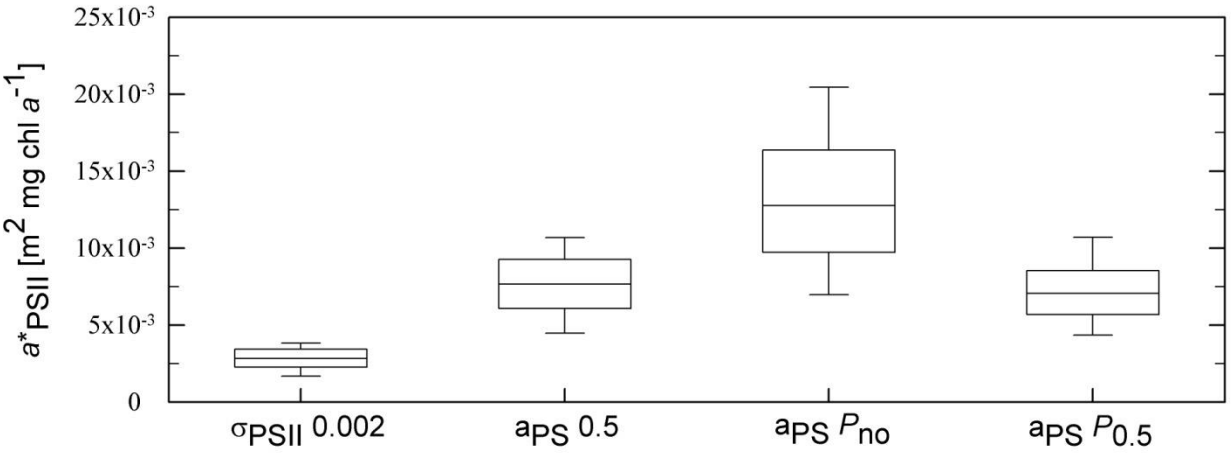

Figure 2.10: Variation of a^*_{PSII} estimates arising through different methodologies. σ_{PSII} is normalized to a constant spectrum to facilitate direct comparisons with other methods. Box and whiskers are explained in Figure 2.6.

The shape of $a_{PSII[\lambda]}$ is critical for determining spectral correction values when comparing photosynthetic rates measured under different light regimes. Bio-optical models that have necessarily derived SCFs (Table 2.1) often use $a_{PS[\lambda]}$ and thus assume spectral equivalency to $a_{PSII[\lambda]}$. Figure 2.11 compares the spectral shapes and resultant SCFs derived through measurements of a_{PS} (SCF_{APS}) and F (SCF_F). Figure 2.11A demonstrates that on average, the mean spectra of $F_{[\lambda]}$ at the 5 wavelengths of measurement closely matched the mean spectral shape of a_{PS} where both measurements were available (*n = 75*). However, predictable exceptions occurred in samples dominated by cyanobacteria (Rattan 2009): Shown in Figure 2.11B and consistent with other studies (Suggett et al. 2004), fluorescence per unit absorption is highest in

phycocyanin region and low in the chl *a* Soret band in cyanobacterial dominated samples. Figure 2.11C compares SCF_{APS} and SCF_F normalized to the *in vitro* photosynthetron spectrum. Overall SCF_{APS} and SCF_F were not correlated ($p > 0.5$) and on average SCF_F was significantly higher than SCF_{APS} (Welch's t-test, $p < 0.001$) by a factor of 1.07. The peak spectral energy emitted by the *in vitro* photosynthetron (Figure 2.1) overlapped with the absorption spectra of phycocyanin. Consequently, stations with the largest difference between SCF_{APS} and SCF_F were those dominated by cyanobacteria.

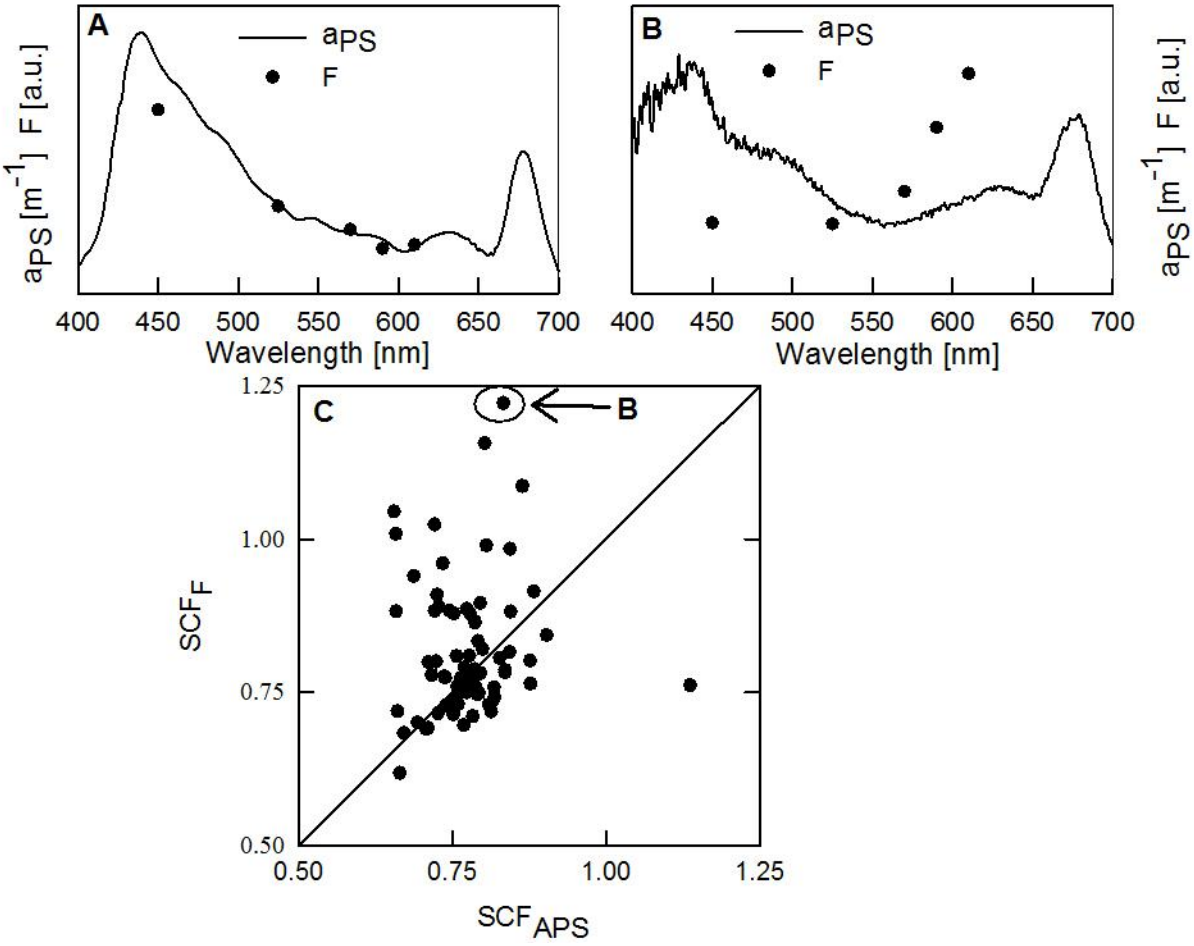

Figure 2.11: A) The mean spectral shapes of all a_{PS} and $F_{[\lambda]}$ measurements in this study. B) a_{PS} and $F_{[\lambda]}$ measurements from a sample dominated by cyanobacteria. C) Comparison of spectral correction factors derived from scaling all a_{PS} (SCF_{APS}) and $F_{[\lambda]}$ (SCF_F) measurements to the *in vitro* photosynthetron spectra. The circled value in Panel C corresponds with cyanobacteria dominated spectra shown in Panel B.

Section 2.3.4: Bio-optical model comparisons to α_{14C}

Table 2.7 and Figure 2.12 compare various bio-optical derivations of α against *in vitro* α_{14C} measurements. Bio-optical derivations of α are formulated using different combinations of f_{PSII} parameters, a_{PSII} methodologies, and SCFs derived from either a_{PS} or F. Each set of bio-optically derived α estimates are compared against contemporaneous ^{14}C values to photosynthetic quotients ($PQ = \alpha/\alpha_{14C}$). Specifically Table 2.7 documents the mean ± standard deviation of the resultant photosynthetic quotients and the correlation coefficients of the linear regression of α versus α_{14C}. Table 2.7 clearly shows methodologies that derive a_{PSII} impart more variability on bio-optical model efficacy than the parameterization of f_{PSII}. Accordingly, Figure 2.12 summarizes comparative estimates of *in vitro* α_{14C} measurements with bio-optical models that hold f_{PSII} constant ($f_{PSII} = F_q'/F_M' [0.65]^{-1}$) but vary a_{PSII} methodology. Figure 2.12 also shows the standard deviations (±0.48) from the mean photosynthetic quotient (PQ = 1.29) measured over the course of one year in Lake Erie's Eastern Basin (Depew et al. 2006). Specifically, Depew et al. (2006) derived PQ as the maximum photosynthetic rate of oxygen evolution measured through the light and dark bottle technique using a 6 hour incubation divided by P_M as measured using the exact same ^{14}C methodology in this study. These recent PQ measurements provide an approximate benchmark to validate the various bio-optical production estimates presented here.

In this study, spectral normalization using SCF_F improves bio-optical model efficacy relative to SCF_{APS}: Shown in Table 2.7, comparative estimates of α_{14C} and bio-optical estimates of α yield consistently higher correlation coefficients and lower coefficients of variance (standard deviation divided by mean) when SCF_F is used in lieu of SCF_{APS}. Bio-optical derivation of α through the most common a_{PSII} method ($\sigma_{PSII} \bullet 0.002$) yield unrealistic PQs that

are significantly lower than the benchmark PQ (1.29, one-sample t-test: $p = 0.05$) and are on average less than 1 regardless of f_{PSII} parameterization. Bio-optical derivation of α using the no-overshoot method ($a_{PS} \bullet P_{NO}$) yields the highest PQs and lowest correlation coefficients that ranged from 0.40-0.58. When a_{PSII} is derived assuming $P = 0.5$ (either through $a_{PS} \bullet 0.5$ or $a_{PS} \bullet P_{0.5}$), the resultant PQs are the most comparable to those of Depew et al. (2006), though in all cases PQs are significantly larger than the 1.29 (one-sample t-test: $p = 0.05$). Despite the similar mean PQ values when a_{PSII} is derived using either $a_{PS} \bullet 0.5$ or $a_{PS} \bullet P_{0.5}$, bio-optical derivation of α through $a_{PS} \bullet P_{0.5}$ yields consistently higher correlation coefficients and smaller coefficients of variation than bio-optical derivation of α through $a_{PS} \bullet 0.5$. Of all the various bio-optical models presented in Table 2.7, derivation of α through $F_q'/F_M' [0.65]^{-1} \bullet a_{PS} \bullet P_{0.5} \bullet SCF_F$ yielded the highest correlation coefficient, the lowest coefficient of variance and a PQ closest to the benchmark value.

Table 2.7: Summary of bio-optical α model estimates compared to α_{14C}. Parameterization of f_{PSII} and SCF varies across table rows and a_{PSII} methodologies varies down table columns. For each model parameterization, the mean ± standard deviation PQ is reported with the correlation coefficient (r^2) given in parentheses.

		a_{PSII}			
f_{PSII}	SCF	$\sigma_{PSII} \bullet 0.002$	$a_{PS} \bullet 0.5$	$a_{PS} \bullet P_{NO}$	$a_{PS} \bullet P_{0.5}$
$F_V/F_M [0.65]^{-1}$	a_{PS}	0.64 ± 0.34 (*0.64*)	1.80 ± 0.97 (*0.64*)	2.48 ± 1.45 (*0.41*)	1.45 ± 0.64 (*0.90*)
$F_V/F_M [0.65]^{-1}$	F	0.53 ± 0.31 (*0.88*)	1.72 ± 0.88 (*0.67*)	2.36 ± 1.27 (*0.48*)	1.47 ± 0.60 (*0.92*)
$F_q'/F_M' [0.65]^{-1}$	a_{PS}	0.63 ± 0.34 (*0.66*)	1.69 ± 0.86 (*0.66*)	2.35 ± 1.35 (*0.45*)	1.39 ± 0.59 (*0.93*)
$F_q'/F_M' [0.65]^{-1}$	F	0.51 ± 0.30 (*0.87*)	1.64 ± 0.83 (*0.69*)	2.24 ± 1.19 (*0.52*)	1.38 ± 0.56 (*0.94*)
$F_V'/F_M' [0.65]^{-1}$	a_{PS}	0.68 ± 0.37 (*0.64*)	1.84 ± 0.97 (*0.63*)	2.54 ± 1.47 (*0.40*)	1.49 ± 0.65 (*0.91*)
$F_V'/F_M' [0.65]^{-1}$	F	0.55 ± 0.32 (*0.88*)	1.76 ± 0.88 (*0.66*)	2.42 ± 1.30 (*0.47*)	1.50 ± 0.60 (*0.93*)
q_P	a_{PS}	0.82 ± 0.46 (*0.71*)	2.24 ± 1.23 (*0.71*)	3.09 ± 1.85 (*0.52*)	1.82 ± 0.82 (*0.94*)
q_P	F	0.66 ± 0.41 (*0.90*)	2.19 ± 1.22 (*0.72*)	2.95 ± 1.65 (*0.58*)	1.83 ± 0.83 (*0.94*)

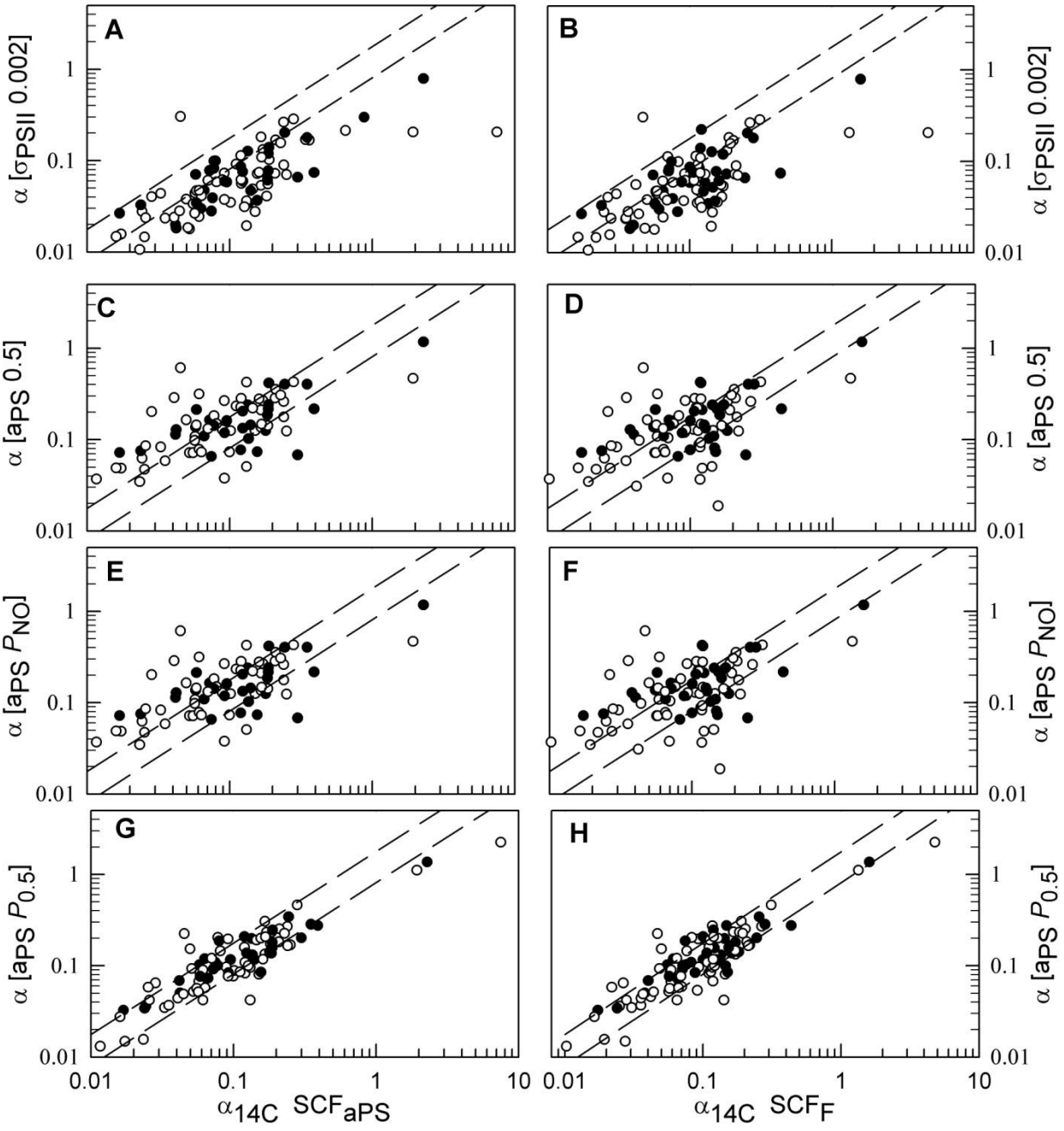

Figure 2.12: Comparison of the light-limited photosynthetic rates derived from *in vitro* ^{14}C incubations (α_{14C}) against 4 bio-optical models where f_{PSII} is constant (F_q'/F_M' $[0.65]^{-1}$) and a_{PSII} methodology varies (α [a_{PSII} method]). α_{14C} is spectrally normalized using SCF_{APS} in Panels A, C, E and G and SCF_F in Panels B, D, F and H. For each graph, dashed lines are standard deviations from the experimentally determined mean PQ in Lake Erie (Depew et al. 2006). Open and closed symbols represent samples from the epilimnion and DCM respectively.

Figure 2.13 demonstrates the diel dependence of resultant PQ estimates shown in Figure 2.12H. PQs were binned into 3-hour time bins and generally reflect the circadian demand of photosynthetically generated ATP and reductant for carbon fixation. Specifically, the median and mean PQs were lowest at the beginning of the photoperiod when most photosynthetic reductant is consumed in the Calvin cycle and so independent measurements of photosynthetic oxygen evolution and carbon fixation should be proximal. PQ measurements were highest in the late afternoon and evening when photosynthetic reductant is increasing diverted away from carbon fixation and instead used for cell maintenance (Mori et al. 1996; Behrenfeld et al. 2004). The differences in PQs were significantly different between 0-3 and 6-9 hrs (two-sample t-test, $p < 0.05$), 0-3 and 12-15 hrs (two-sample t-test, $p < 0.10$) and between 6-9 and 18-21 hrs (two-sample t-test, $p < 0.10$).

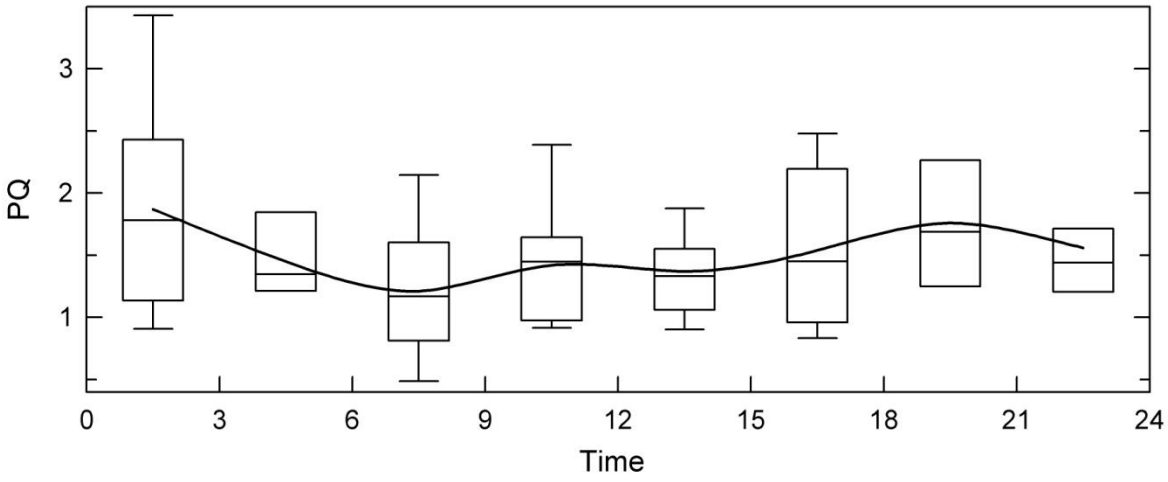

Figure 2.13: Photosynthetic Quotient (PQ) derived from Figure 2.12H (best fit to independently measured PQ) grouped into 3-hour time bins, n gives the sample size for each 3-hour bin. Boxes and whiskers are explained in Figure 2.6 and the solid line is the mean PQ for each 3-hour bin.

Section 2.3.5: Bio-optical model derivation of E_K and P_M

This section first presents *in vitro* measurements of $E_{K\,14C}$ and compares them to optical (E_{24}) and bio-optical estimates of E_K. Estimates of E_K are then multiplied to Eqn 2.1 (F_q'/F_M', SCF_F and $a_{PS}\,P_{0.5}$ in Eqn 2.1 and hereafter referred to as α_F) to generate bio-optical estimates of P_M that are then compared to P_{M14C}.

Figure 2.14 compares E_{K14C} values derived *in vitro* with optical (E_{24}) and bio-optical (E_{KFRRF}) parameters. E_{24} and E_{KFRRF} were spectrally normalized to the photosynthetron spectra, and this analysis precludes metalimnetic and hypolimnetic samples where light-limited photosynthesis dominates daily integrated phytoplankton production. Deep metalimnetic and hypolimnetic E_{K14C} values were statistically smaller than epilimnetic E_{K14C} values (two sample t-test, $p < 0.001$), the average ± standard deviation of E_{K14C} values beneath and within the epilimnion are 59 ± 20 $\mu mol.m^{-2}.s^{-1}$ and 102 ± 35 $\mu mol.m^{-2}.s^{-1}$ respectively. Temporally, epilimnetic E_{K14C} was lowest in the spring and late summer and highest in the early summer. Shown in Figure 2.14A, this pattern generally reflects E_{24}, as average cruise values of both parameters are highly correlated ($r^2 = 0.93$, $n = 4$, $p < 0.01$). The average ± standard deviation of E_{24} is 82 ± 37 $\mu mol.m^{-2}.s^{-1}$ so is statistically smaller than E_{K14C} (two sample t-test, $p < 0.001$). This difference is prevalent in the early spring and late summer when deep mixing diminishes E_{24}. When all comparative values are considered, E_{24} and E_{K14C} are significantly correlated though the predictive power of the linear regression is limited (Figure 2.14D; $r^2 = 0.12$, $n = 73$, $p = 0.001$).

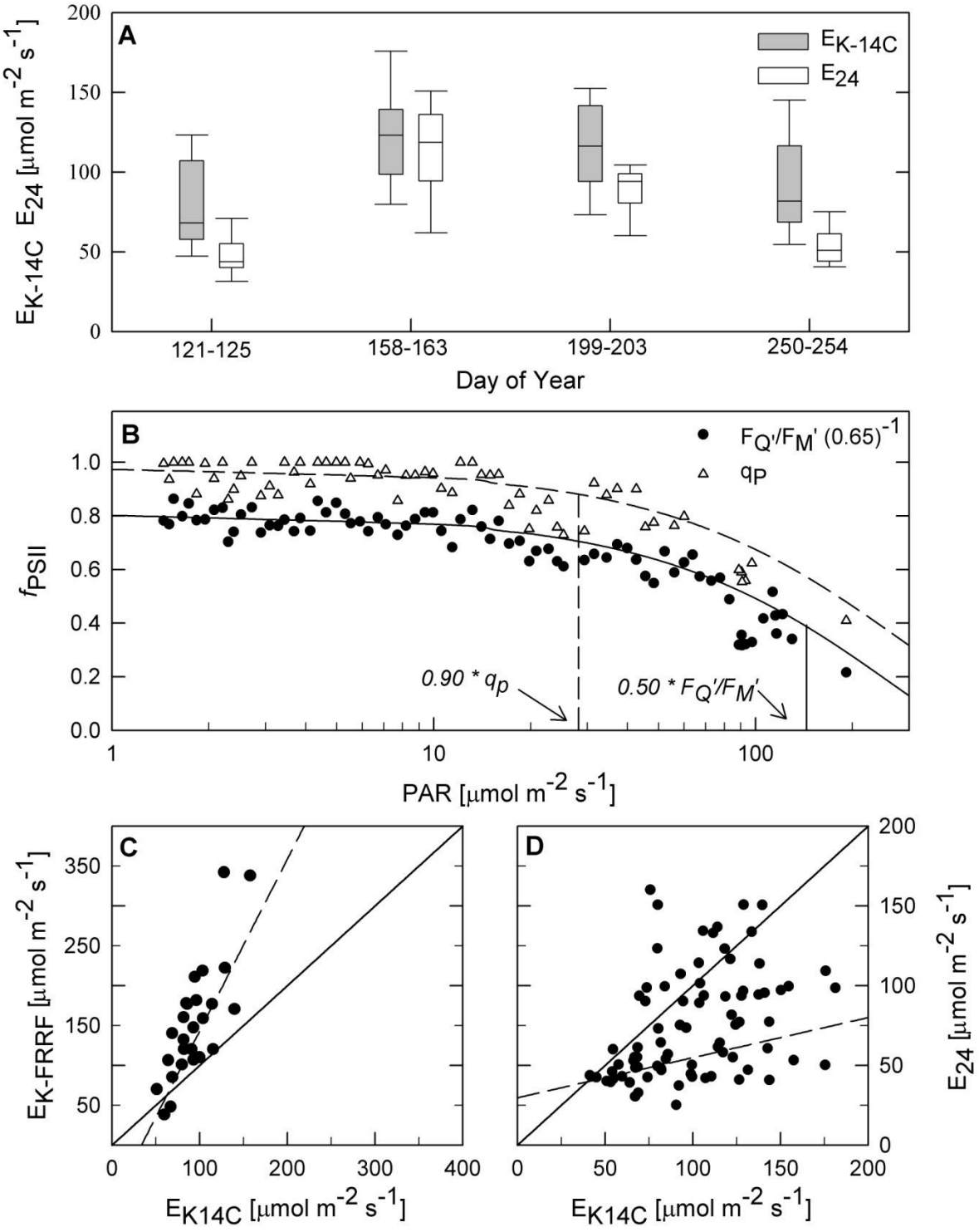

Figure 2.14: Examples of light-dependent decreases in F_Q'/F_M' and q_p. The solid and dashed lines represent hyperbolic and exponential approximations respectively.

Figure 2.14B provides an example of the light-dependent decreases in both F_Q'/F_M' and q_P fit to a modified exponential model (Eqn 2.10). The utility of bio-optically derived E_K is constrained to the photoperiod when sufficient irradiance decreases f_{PSII}. Of the 29 profiles where visible E-dependent decreases in f_{PSII} occurred, the exponential model failed to produce statistically significant model coefficients ($p > 0.05$) in 5 of the 29 profiles. Following Smyth et al. (2004), E_{KFQFM} is derived as the half-saturation constant of F_q'/F_M' as a function of E. Alternatively, Kolber and Falkowksi (1993) argue that E_K corresponds to the initial inflection of q_P, which is the onset of photochemical quenching. Kolber and Falkowksi (1993) do not present a mathematical formulation for this derivation, so it assumed here that E_{KQP} occurs when q_P is 90% of its maximal value (Figure 2.14B). Consistent with Raateoja et al. (2009), E_{KQP} yielded ~58% lower values than E_{K14C} though the parameters were positively correlated ($r^2 = 0.36$, $n=25$, $p < 0.001$). Conversely, E_{KFQFM} was on average 51% higher than E_{K14C} and the parameters were also positively correlated (Figure 2.14C, $r^2 = 0.78$, $n=19$, $p < 0.001$).

Figure 2.15A and B compares in vitro measurements of P_{M14C} to bio-optical estimates of PM derived as the product of $\alpha_F \bullet E_{KFQFM}$ and $\alpha_F \bullet E_{24}$ respectively. Bio-optical derivation of P_M through $\alpha_F \bullet E_{KFQFM}$ was highly correlated to P_{M14C} ($r^2 = 0.97$, $n=25$, $p < 0.001$) and, as E_{KFQFM} generally exceeded E_{K14C}, yielded a PQ with a mean and standard deviation (1.83 ± 0.79) higher than α_F (Table 2.7). Bio-optical derivation of P_M through $\alpha_F \bullet E_{24}$ was also correlated to P_{M14C} ($r^2 = 078$, $n=65$, $p < 0.001$) and, as E_{24} was on average close to E_{K14C}, the resultant mean and standard deviation of the PQ (1.25 ± 0.70) is closer to both the PQ of α_F (Table 2.7) and the benchmark value (1.29 ± 0.48).

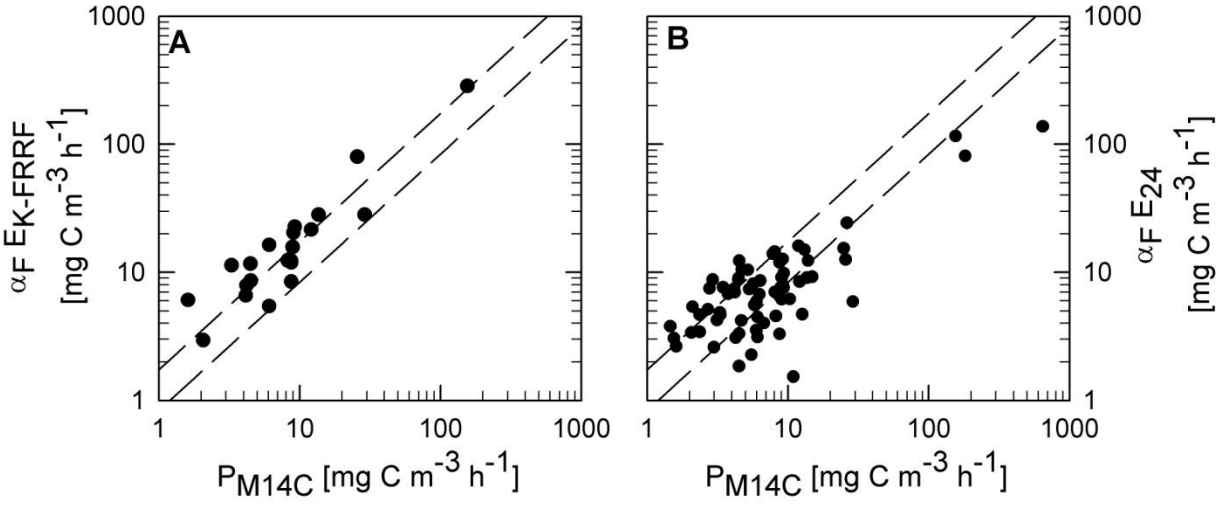

Figure 2.15: Comparison of the maximum photosynthetic rates derived from *in vitro* ^{14}C incubations (P_{M14C}) with bio-optical derived PM taken as the product of A) α_F and $E_{K\text{-}FRRF}$ and B) α_F and E_{24}. Dashed lines are standard deviations from the experimentally determined mean PQ in Lake Erie (Depew et al. 2006)

Section 2.4: Discussion

Bio-optical models derive light-limited photosynthetic rates as a function of f_{PSII} and a^*_{PSII} (Eqn 2.1). Table 2.7 demonstrates that the efficacy of bio-optical models is more dependent on the methodology to derive a^*_{PSII} than the parameterization of f_{PSII}. Of the various methodologies, derivation of a^*_{PSII} through spectral fluorescence measurements yielded the most statistically significant correlation to independently measured α_{14C} with a resultant photosynthetic quotient close to previous measurements in Lake Erie This finding is a significant departure from the majority of the literature that derive a^*_{PSII} from measured and assumed values of σ_{PSII} and n_{PSII} respectively (Table 2.1). In the following discussion, the limited variability of f_{PSII} in this dataset and its lack of correlation with α_{14C} are first addressed. In light of a recent review of limited f_{PSII} variability in cultures and marine environments, we propose that the empirical importance a^*_{PSII} in driving photosynthetic rates in this study is not unique and, as recently hypothesized (Marra et al. 2007), may be the largest driver affecting observed photosynthetic rates. The following section then discusses the advantages and limitations of the various methodologies employed in this study to derive a^*_{PSII}.

Section 2.4.1: Bio-optical model parameterization – f_{PSII}.

Figure 2.6 and Table 2.4 present f_{PSII} values measured under low light that are then employed in Eqn 2.1 to estimate light-limited photosynthetic rates. In the absence of light driven reductions, f_{PSII} values were high and demonstrated limited variability despite significant taxonomic and nutrient gradients measured over the course of this study (Rattan 2009). A detailed examination of taxonomic and nutritional drivers of f_{PSII} values is outside the scope of this thesis; however some general inferences are warranted.

Suggett et al.'s (2009) review of F_V/F_M variability across taxonomic and nutrient gradients as

measured in cultures and diverse marine environments provides the most robust benchmark against which to interpret f_{PSII} measurements in Lake Erie. Drawing upon numerous continuous and batch culture experiments across nutritional gradients, their review supports the earlier findings of Parkhill et al. (2001) by demonstrating that F_V/F_M serves as a reliable proxy for the degree of nutrient limitation only during unbalanced growth (batch cultures). In contrast, phytoplankton grown in continuous cultures (balanced growth) and exposed to similar nutritional gradients adapt to nutrient deficient environments such that relatively high values of F_V/F_M are achieved after one cell cycle (Parkhill et al. 2001).

Suggett et al. (2009) then compares F_V/F_M measured in cultures and diverse marine environments. Only the iron-limited high-nutrient low chlorophyll (HNLC) southern ocean has consistently low F_V/F_M, presumably due to the high requirement of iron within the photosynthetic electron transport chain (Behrenfeld et al. 2006). F_V/F_M measurements in all other marine environments are relatively high with limited variability and are insensitive to macronutrient additions (Suggett et al. 2009). The data presented in this study is similar to these non-HNCL marine environments, and 'may thus potentially be in balanced growth' (Suggett et al. 2009). Given that F_V/F_M is insensitive to nutrient limitation under balanced growth, Parkhill et al. (2001) statement that 'a robust measure of nutrient stressed oceanic waters is still required'.

Rapid recovery of F_V/F_M in nutrient deficient continuous cultures coincides with decreasing cellular pigment concentrations (Parkhill et al. 2001), so it is likely that balanced growth is primarily achieved through changes in light-harvesting. If indeed balanced nutrient-limited growth is achieved through alterations in the light-harvesting complexes, a_{PSII} may serve as a better indicator of nutrient status under balanced growth. In support of this argument, Figure 2.16 shows the relationship between $\alpha^*_{[14C]}$ with f_{PSII} and a^*_{PSII} ($a^*_{PS} \bullet P_{0.5}$) where both values

are normalized to a white spectrum using SCF_F (see discussion below). Despite a 5-fold $\alpha^*_{[14C]}$ gradient, $\alpha^*_{[14C]}$ was not significantly correlated to f_{PSII} ($p<0.5$) but did show significant co-variation to $a^*_{PS} \bullet P_{0.5}$ ($r^2 = 0.38$, n=89, $p<0.05$). This figure suggests that in Lake Erie biomass specific photosynthetic rates are insensitive to photosynthetic efficiency and are largely driven by changes in cellular pigmentation that in turn may reflect taxonomic composition.

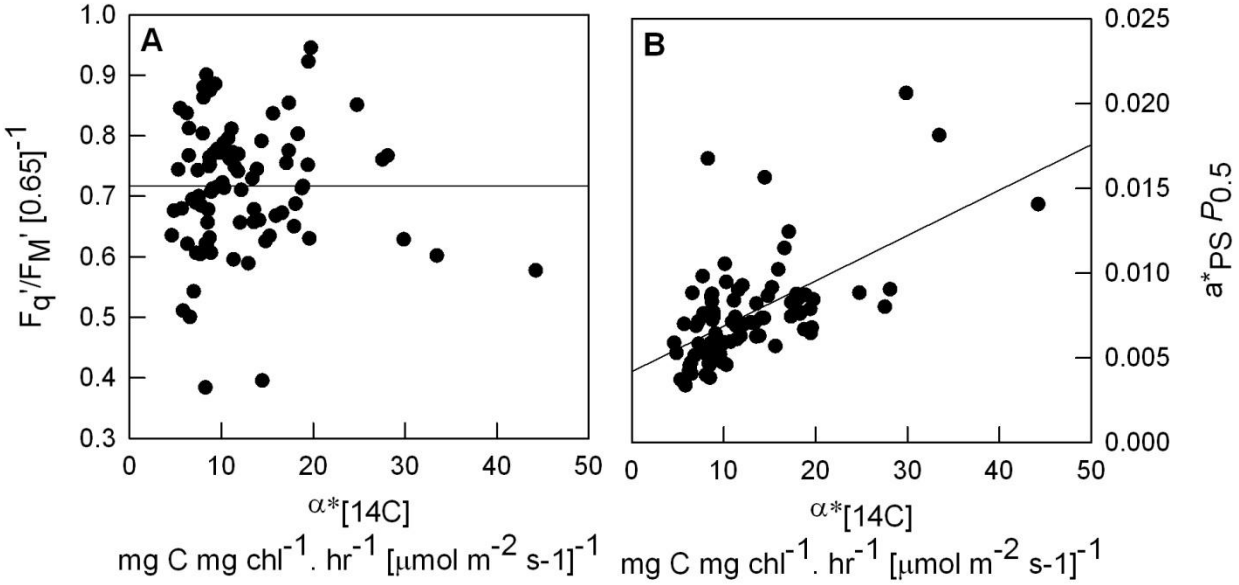

Figure 2.16**:** Comparisons of $\alpha^*_{[14C]}$ against a) F_Q'/F_M' [0.65]-1 and B) $a^*_{PS} P_{0.5}$ (a^*_{PSII}). Solid line in each panel is the linear regression.

Section 2.4.2: Bio-optical model parameterization – a_{PSII}.

This section evaluates theoretical and empirical considerations of the various methodologies that derive a^*_{PSII}. This discussion first argues that given both theoretical and empirical considerations the commonly employed method (Table 2.1) of assuming n_{PSII} is constant should be abandoned in lieu of spectral absorption and fluorescence methods. The advantages and necessary assumptions pertaining to spectral absorption and fluorescence methods are then discussed. Finally, this section argues the critical importance of incorporating spectral fluorescence measurements in bio-optical models.

The *in situ* variability of n_{PSII} is largely unknown given the paucity of measurements of natural phytoplankton assemblages relative to cultures. Culture measurements of diverse taxa (Suggett et al. 2004; Figure 2.17) demonstrate a 4-fold range with values twice as high and twice as low as the normally assumed value ($n_{PSII} = 2.0 \times 10^{-3}$ [mol PSII (mol chl *a*)$^{-1}$]). Other culture n_{PSII} measurements across 3 phyla indicate an even greater range with all measured values exceeding 2.0×10^{-3} (Dubinsky et al. 1986; n_{PSII}: 3.8×10^{-3} to 1.96×10^{-2}). These important measurements underscore the potential magnitude of error introduced when assuming a fixed value of n_{PSII} in bio-optical modelling within mixed or variable phytoplankton assemblages. Indeed, variability of n_{PSII} is commonly evoked as the greatest source of uncertainty in many of the bio-optical models that do not reconcile with *in-vitro* photosynthetic measurements. When considering measurements of n_{PSII}, it is important to also recognize potential errors in the oxygen flash technique: As concentrations required by the technique are very high (~1 mg chl *a* m^{-3}), filtration and handling is necessary and may introduce errors not readily quantifiable. Secondly, measurements of n_{PSII} are based on net O_2 evolution, so cellular O_2 consumption through the Mehler reaction or photorespiration will yield apparently low n_{PSII} measurements (Suggett et al. 2004).

Conceptually, n_{PSII} and σ_{PSII} should negatively co-vary: Phytoplankton with a large chl *a* antenna (low n_{PSII}) should saturate PSII reaction centres faster (high σ_{PSII}) relative to phytoplankton with small antennae, at least up to the point where self-shading limits further advantages (Falkowksi and Raven 1997). As evidence, a statistically significant negative correlation ($r^2 = 0.29$, $p < 0.01$, $n = 22$) between σ_{PSII} and n_{PSII} occurs in Suggett et al. (2004) dataset. If σ_{PSII} and n_{PSII} negatively co-vary in nature, estimates of a^*_{PSII} using a fixed n_{PSII} value will inherently be more variable than actual values. Figure 2.17 shows n_{PSII} estimated from this

study ($n_{PSII} = a^*_{PS} \bullet P_{0.5} (\sigma_{PSII} \bullet 0.00675)^{-1}$) as a function of σ_{PSII}. Similar to the culture data of Suggett et al. (2004), n_{PSII} was negatively correlated to σ_{PSII} ($r^2 = 0.23$, n = 100, $p < 0.001$) and always exceeded the standard assumed value (2.0×10^{-3}). Owing to this negative co-variation, low σ_{PSII} measurements in this study are offset with high n_{PSII} values and so yield a^*_{PSII} values similar to previously published measurements. The mean and standard deviation of n_{PSII} values shown in Figure 2.17 (0.0069 ± 0.0004 mol PSII (mol chl *a*)$^{-1}$) are much larger than the nominal assumption and thus may seem unrealistic, however only three values lie above the range of n_{PSII} of culture measurements (Dubinsky et al. 1986).

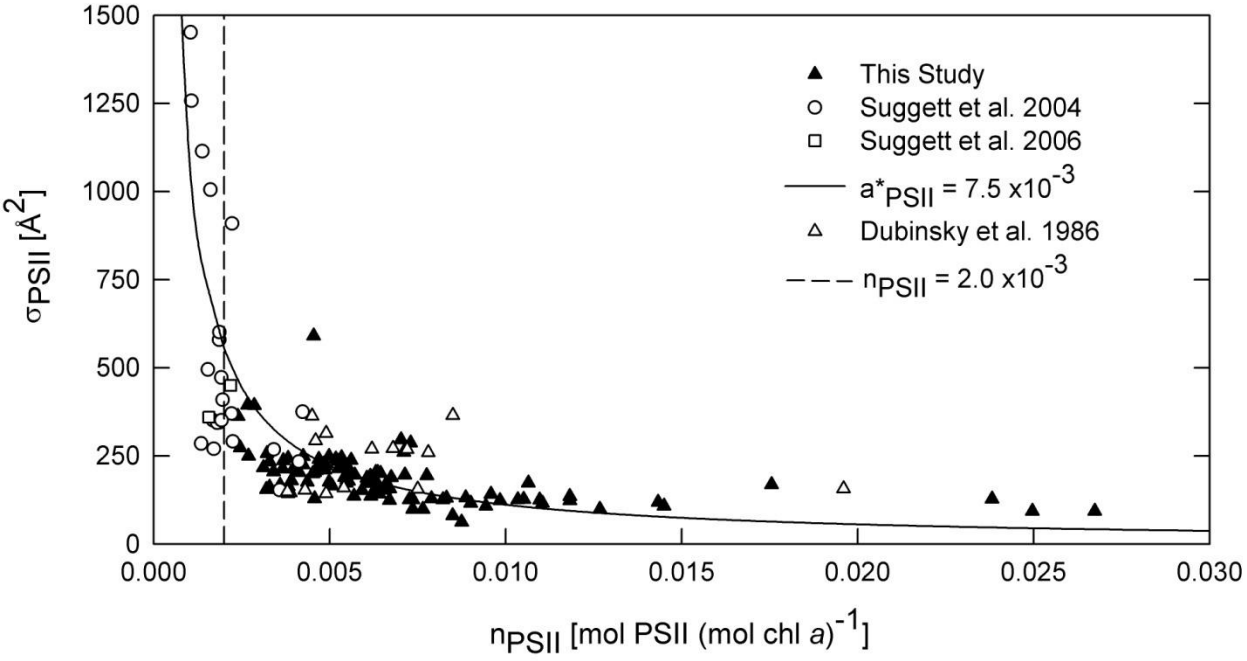

Figure 2.17: Covariation of σ_{PSII} and n_{PSII} from this and other studies.

Potential errors are inherent to each of three methodological steps (Figure 2.1) used to derive a^*_{PSII}. Fortunately (and unlike n_{PSII}) there is also a large body of literature that investigates the validity of these methodologies. Potential errors associated with the QFT, including isolation of pigment absorbance, are thoroughly reviewed elsewhere (Tassan and Ferrari 1995; Roessler

1998). These reviews show that, given proper care, errors associated with the QFT are small, especially relative to potential error magnitude of assuming a constant n_{PSII}. The largest uncertainty in the QFT is selection of the pathlength amplification factor β. For example, selection of β through the empirical formula of Tassan and Ferrrari (1995) yielded a^*_{PH} values ~11% greater than the β value presented in Roessler (1998).

The second set of methods shown in Figure 2.1 involves partitioning pigment absorption (a_{PH}) into non-photosynthetic (a_{NPS}) and photosynthetic (a_{PS}) components through spectral reconstruction. Spectral reconstruction techniques that derive a_{PS} here (i.e. Eqn 2.5) have three major assumptions. First, HPLC measurements on non-photosynthetic measurements were unavailable in this study so derived values of a_{PS} invariably include absorption of these pigments. Fortunately the contribution of a_{NPS} to a_{PH} has been widely studied in marine environments, and these studies provide an estimate of the sources of error here, particularly with respect to absorption by non-photosynthetic carotenoids. Numerous studies have documented that non-photosynthetic carotenoids concentrations are highest in well-lit and nutrient deficient environments (Bricaud et al. 1995; Lindley et al. 1995; Babin et al. 1996; Culver and Perry 1999; Marra et al. 2000). Babin et al. (1996) present an empirical model relating the contribution of a_{NPS} to a_{PH} as a function of mean daily irradiance (E_{24}): Only in extreme oligotrophic waters where E_{24} is high (~410 μmol m^{-2} s^{-1}) do non-photosynthetic pigments contribute up to 31% of a_{PH}. Over the typical range of E_{24} in this study (Table 2.3), Babin et al.'s (1996) empirical formula suggests that non-photosynthetic pigments contribute only ~ 5-10% of a_{PH}. Not only is this error most likely smaller than assuming a constant n_{PSII}, the magnitude of the error is unidirectional – failure to account for a_{NPS} will only overestimate a_{PS}. The magnitude of this overestimation is consistent with the slightly higher mean PQ (1.38) derived through the a_{PS} $P_{0.5}$

relative to previous PQ measurements in Lake Erie (1.29).

The third methodological step shown in Figure 2.1 involves partitioning photosynthetic pigment absorption (a_{PS}) into absorption associated with PSII and PSI where the ratio of a_{PSII}:a_{PS} is denoted by the factor *P*. The approximation of the 'no overshoot method' here yielded a high mean P_{NO} (0.88) with 37% above the upper theoretical limit ($P > 1$). The *in-situ* P_{NO} estimates presented here do suffer from coarser spectral resolution that may explain the anomalously high values. However this high mean is consistent with spectrally resolved (1 nm) culture measurements that yielded similarly high values ($P_{NO} > 0.70$) in 9 of 13 pigments groups (Johnsen and Sakshaug 2007).

The novel method introduced here assumes that over a large sample set *P* is on average 0.5 ($P_{0.5}$). It is difficult to independently test the validity of *P* estimates, though the significantly improved correlation between α_{14C} and α_F shown in Figure 2.12H relative to any other bio-optical model strongly suggests the utility of this method. Moreover, a realistic range of PSII:PSI ratios from 2:1 (diatoms) to 1:2 (cyanobacteria) suggests most values of *P* should lie between 0.33-0.67; only 18% of P_{NO} values fell within this range compared to 64% of derived $P_{0.5}$ values. Spectrally resolved measurements of *P* can be otherwise estimated through measuring the shape of a_{PSI} and a_{PSII} through spectral fluorescence of filtered phytoplankton at cryogenic temperatures (Subramaniam et al. 1999). Indeed 77K fluorescence spectroscopy of cyanobacteria shows significant PSI absorption in the 540 – 650 nm (Subramaniam et al 1999), further suggesting that the 'no overshoot method' may overestimate *P*. Little is known concerning the *in-situ* variability of *P*. The culture observations that have been made may be biased towards the scaling technique used to derive *P*. In this study, *P* significantly decreased with increasing a^*_{PS}, as shown in Figure 2.x and 15 of the 17 DCM samples had *P* values greater

than predicted by the linear regression.

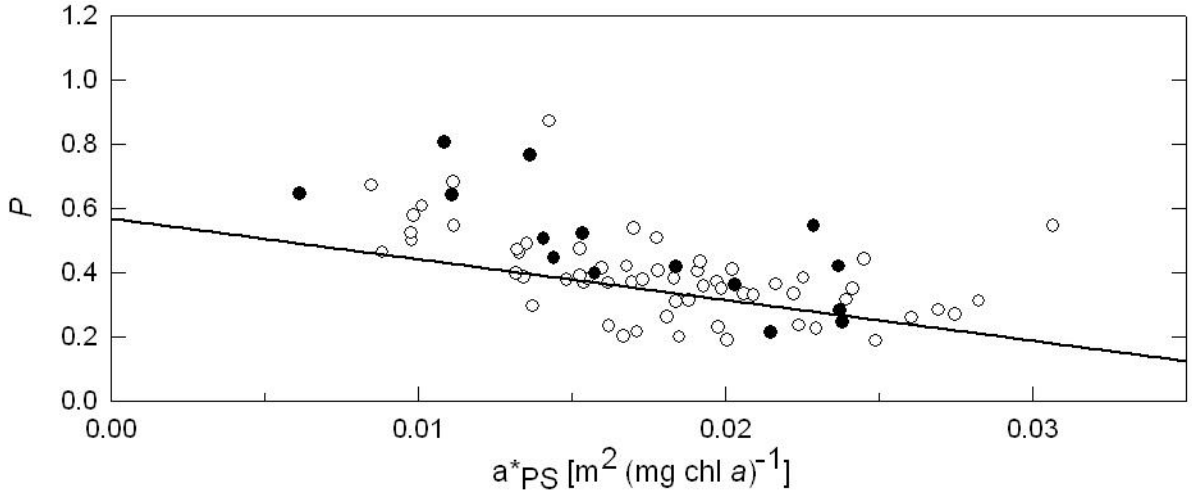

Figure 2.18: Negative co-variation of $P_{0.5}$ with a^*_{PS}.

The immediate advantage of this novel technique is that by scaling *in-situ* fluorescence to a set of a^*_{PS} measurements, the ensuing resolution of a^*_{PSII} matches that of f_{PSII} so high-resolution measurements of photosynthesis can be performed. This is in contrast to the 'no overshoot method', where the resolution of a^*_{PSII} is dictated by coarser pigment absorption measurements. Highly resolved estimates of a^*_{PSII} are particularly advantageous through depth as deep chlorophyll maxima (DCM) can be vertically heterogeneous in respect to both biomass and pigment composition (Figure 2.19, Chapter 3).

Section 2.4.3: Bio-optical model parameterization – E_K and P_M.

Bio-optical derived values of E_{KFRRF}, through modelling E-dependent changes in f_{PSII}, were significantly correlated to E_{K14C} (Figure 2.14). However, E_{KFRRF} routinely underestimated and overestimated E_{K14C} when E_{KFRRF} was derived as $0.90 \bullet q_P$ and $0.5 \bullet F_q'/F_M'$ respectively. This lack of co-variation around unity is consistent with a detailed analysis of E-dependent changes in f_{PSII} (Raateoja et al. 2009) and other published bio-optical models (Table 2.1). Several factors may contribute to observed differences between E_{K14C} and E_{KFRRF}, and these

differences further underscore inherent difficulties in deriving light saturated photosynthetic rates from active fluorescence measurements alone: The maximum rate of carbon assimilation is dictated by processes downstream of PSII (Falkowski and Raven 2007), so the energy required to saturate photosynthetic electron transport (E_{KFRRF}) and carbon assimilation (E_{K14C}) are not necessarily equivalent. Furthermore, a recent study has shown that a plastid terminal oxidase (PTOX) located between PSII and PSI can direct excess reductant produced by PSII when carbon assimilation is saturated and thus minimize donor side photoinhibition (Mackey et al. 2008). Both PTOX activity and downstream PSII limitation dictate that E_{KFRRF} should exceed E_{K14C}, and so are consistent with Figure 2.14C, especially in high light.

Photoacclimation is keyed to the median mixed layer light level and statistically significant relationships between E_{K14C} and optical water column properties have been derived in diverse marine environments (Behrenfeld et al. 2003). In this study, monthly mean E_{K14C} values generally tracked the mean daily water column irradiance (E_{24}), though when all data was considered the relationship was not strong (Figure 2.14). E_{K14C} varies on a diel cycle and increases with incident irradiance (MacCaull and Platt 1977), and in this study daylight measurements of E_{K14C} (6-18 hrs LST) were significantly higher than nocturnal (18-6 hrs LST) measurements (*t*-test, $p < 0.05$). Diel variability explains some of the scatter in Figure 2.14D, nocturnal E_{24} underestimated E_{K14C} (87%) less than diurnal measurements (66%). It should be noted that E_{K14C} is measured on phytoplankton constrained in a static *in vitro* light environment, whereas *in situ* cells often circulate through a spectrally variable light gradient (MacIntyre 1993). *In vitro* containment may invoke photoacclimative processes that alter E_K and thus misrepresent $E_{K\textit{in situ}}$ (MacIntyre et al. 2000). Bio-optically derived P_M [$\alpha_F \bullet E_{24}$] significantly co-varied with P_{M14C} and though the relationship was more variable than the comparison of light-limited slopes

(Figure 2.12H), the bio-optical model yielded a mean PQ value (1.25) close to the benchmark (1.29). The influence of E_K variability on daily integrated photosynthesis is further discussed in Chapter 3.

Section 2.4.4: Utility of bio-optical measurements

Bio-optical models cannot supplant ^{14}C measurements, not because the latter is entrenched as the benchmark photosynthetic methodology, but because each method approximates different processes. Behrenfeld et al. (2008) recently defined photosynthesis 'as the light-driven production of ATP and reductant (photosynthate) by the photosynthetic electron transport chain', the process that bio-optical models seek to measure. ^{14}C-uptake 'does not measure photosynthesis' (Behrenfeld et al. 2008), rather it measures the fraction of photosynthate consumed by the Calvin-cycle. The ratio of photosynthate supply to carbon demand is approximated here by the photosynthetic quotient (PQ), and this ratio varies predictably within a cell cycle (Behrenfeld et al. 2004): Early in the photoperiod most photosynthate is consumed by the Calvin cycle so carbon fixation and photosynthesis are proximal (PQ ~ 1), but at all other times photosynthate is increasingly consumed by a myriad of other processes so carbon fixation underestimates photosynthesis (PQ > 1). The diel PQ periodicity derived in this study (Figure 2.13) broadly follows this cell cycle as mean PQ values are lowest early in the photoperiod. Thus Figure 2.13 further validates the bio-optical methodology used here as the discrepancy between photosynthesis and ^{14}C uptake generally follows expected diel patterns. Finally the fundamental differences between carbon assimilation and photosynthesis cannot be understated: The validation of bio-optical models against ^{14}C uptake should never follow a 1:1 relationship and variability in resultant PQs is certainly expected.

Though bio-optical models cannot supplant ^{14}C measurements, incorporating spectral

and active fluorometers into monitoring and research programs significantly augment the quantity and quality of limnological and oceanographic measurements. The proposed bio-optical model (α_F) presented here is virtually autonomous as only occasional samples for background (filtrate) fluorescence and particulate absorption are necessary. Given this autonomy and the rapid sampling frequency of the instruments (< 1 s), the spatial and temporal resolution of photosynthetic measurements through bio-optical constituents dwarfs that of the ^{14}C methodology. It is through high resolution bio-optical models that an increased understanding how physical processes drive spatial and temporal patterns of photosynthesis (Moore et al. 2005; Behrenfeld et al. 2006).

Figure 2.19 presents an example of the utility of bio-optically resolved photosynthetic measurements. Green and blue lines correspond to bio-optical measurements of a_{PSII} and F_q'/F_M' respectively from which α_F (black line) is derived. The shaded grey area corresponds to the maximum vertical resolution of ^{14}C measurements, as dictated by a 1 metre Niskin bottle employed in this study from which a measurement of α_{14C} was made (solid vertical black line). Given that about 2-5% of bio-optical variability shown in this figure is most likely due to instrument noise (as quantified from the variability of continuous a_{PSII} and F_q'/F_M' measurements from a discrete sample), all bio-optical measurements are highly variable through the metalimnion. Within the 1 m sampled by the Niskin bottle, α_F alone varied from 0.127 to 0.179 [mg C m^{-3} hr^{-1} (μmol m^{-2} s^{-1})$^{-1}$]. Moreover, the discrete 1 metre sample missed the deep chlorophyll maxima (DCM), so ^{14}C measurements alone would have underrepresented photosynthesis. Finally the disparate vertical resolution of bio-optical models and 'discrete' ^{14}C samples add to the variability of derived PQs shown in Figure 2.12: Relative to α_{14C}, the vertical variability in α_F within 1 m of the water sample results in PQs that vary from 1.06 to 1.49.

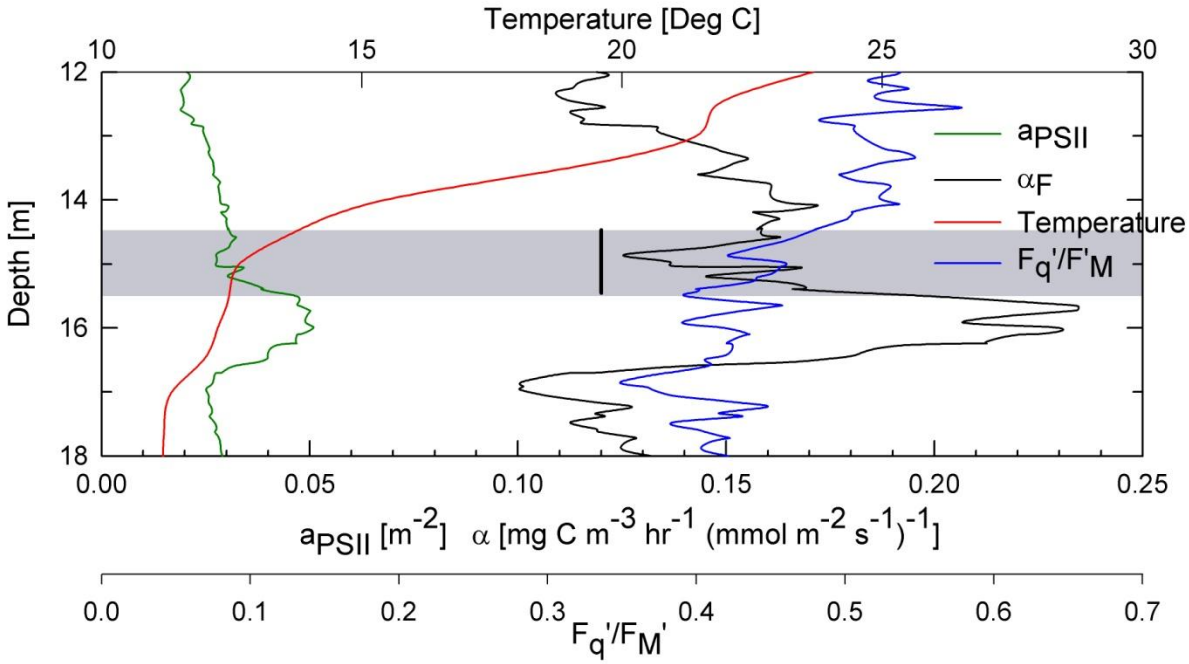

Figure 2:19: Bio-optical measurements of a_{PSII}, F_q'/F_M' and α_F through depth. The solid grey box corresponds to the depth sampled with a 1 metre Niskin Bottle. The solid vertical grey line is the corresponding value of α_{14C}.

Section 2.5: Conclusions and Recommendations

This is the first study to extensively evaluate the various a_{PSII} methodologies in natural phytoplankton communities. The importance of accurate a_{PSII} parameterization within bio-optical photosynthetic models is paramount given the recent recognition that f_{PSII} is empirically constrained in most marine environments. In this study, f_{PSII} values were generally constrained and relatively high despite large optical, taxonomic and nutritional gradients (Rattan 2009), suggesting that phytoplankton communities under investigation may be close to balanced growth (Suggett et al. 2009). Unlike a^*_{PSII}, f_{PSII} was not statistically correlated to light-limited ^{14}C assimilation rates. Like previous research (Cullen and Davis 2003; Laney 2003), this study reinforces the necessity of deconvolving instrument and background noise from active fluorescence measurements, failure to account for these artefacts would have significantly underestimated f_{PSII}, especially in low biomass environments.

Of the various a_{PSII} methodologies, the most commonly applied method of measured and assumed values of σ_{PSII} and n_{PSII} yielded the least realistic estimates of light-limited photosynthetic rates as they were lower than *in vitro* ^{14}C photosynthetic rates. This study highlights the potential errors in assuming a fixed value of n_{PSII} and specifically demonstrates that n_{PSII} most likely negatively co-varies with σ_{PSII}. Alternative estimates of a_{PSII} can be generated through the quantitative filter technique (QFT), and such measurements are useful in deriving spectral correction factors that are required when comparing light-limited photosynthetic rates measured in different spectral environments. Deriving a_{PSII} through the QFT requires some methodological assumptions, most important of which is separating PSII from PSI absorption. PSII spectral fluorescence excitation data yields the dimensionless spectral shape of PSII, but scaling techniques are further required to estimate a_{PSII}. Incorporation of the most

common scaling technique into a bio-optical model, the 'no-overshoot' method, yielded unrealistically high PQ values that were significantly larger than an assumed benchmark value (1.29; Depew et al. 2004). Instead, a novel and simple scaling method is introduced that assumes over a large sample size 50% of energy is directed towards PSII and deviations from this mean (as dictated by the significant co-variation between a_{PS} and F) dictate the magnitude of a_{PSII}. This novel and autonomous method to derive a_{PSII} yielded PQs closest to the benchmark value and ensuing bio-optical estimates of α_F had the most statistically significant linear relationship with α_{14C}. Deviations between α_F and α_{14C} followed an expected diel pattern that reflects the amount of photosynthetic energy directed towards carbon assimilation.

Maximum carbon assimilation rates (P_M) cannot be directly estimated from active fluorescence alone, but instead derived at the product of α_F and an optical estimate of E_K (i.e. Behrenfeld et al. 2003). In this study, temporal patterns of E_K and E_{24} were similar though when all data was considered the linear relationship was weak. P_M and α covary in lakes and oceans so E_K is relatively constrained (Behrenfeld et al. 2004), so the efficacy of bio-optical P_M estimates is more dependent on accurately quantifying α_F than E_K. Despite the weak relationship between E_K and E_{24}, $\alpha_F \bullet E_{24}$ estimates of P_M were significantly correlated to P_{M14C} with a resultant mean PQ (1.25) very close to the benchmark value (1.29).

This study demonstrates that, given proper parameterization, bio-optical models yield accurate estimates of photosynthetic electron transport rates. Metabolic demand of photosynthetic energy other than carbon assimilation dictates the divergence between bio-optical and *in vitro* ^{14}C measurements. As carbon assimilation rates are more ecologically relevant than photosynthetic electron transport rates, an approximation of the PQ will always be required. This is not an endorsement of the ^{14}C technique. Carbon assimilation undergoes diel variability

so most ^{14}C measurements cannot truly approximate daily carbon assimilation. Often daily areal estimates of phytoplankton production are made from a single ^{14}C incubation at various times of day, so the magnitude of diel ^{14}C error may even exceed the error in approximating a daily mean PQ. When further considering that the bio-optical model presented here is virtually autonomous, much less prone to human-error and can easily be deployed to measure photosynthesis at unparalleled and yet ecologically relevant spatial and temporal resolutions, it is not surprising that such techniques are becoming increasingly common in marine research and should be adopted by government and research agencies responsible for the stewardship of inland waters.

Chapter 3: The Spectral Dependence of Phytoplankton Photosynthesis: Disparities Between *in vitro* and *in situ* Environments

Section 3.1: Introduction

Chapter 2 and many other studies have demonstrated the critical importance of recognizing the spectral dependency of photosynthesis. Comparative estimates of photosynthetic rates in studies where the spectral quality of techniques or measuring environments differ require spectral correction factors (SCFs). Euphotic zone spectra are highly variable through time and space, especially over depth, and are often poorly reproduced by i*n vitro* light sources (Markager and Vincent 2001), thus *in vitro* based estimates of phytoplankton production (ΣPP) require SCFs to estimate ΣPP accurately *in situ* (Lewis et al. 1985). ΣPP models scaled to *in situ* light environment (spectrally-resolved) are now common in marine studies (Behrenfeld and Falkowski 1997), and unnecessary for widely used oceanographic protocols that measure 24-hour ^{14}C uptake *in situ* (e.g. JGOFS, Knap et al. 1996). Amongst freshwater scientists *in vitro* measurements are now generally favoured over *in situ* incubations, in part because *in vitro* methodologies allow greater spatial coverage as measurements can be performed while a ship is underway. Some of the first the studies using *in vitro* incubators scaled ensuing ΣPP estimates to parallel (and less frequent) *in situ* measurements (Table 3.1; Fee 1978), where the ratio of *in vitro* to *in situ* ΣPP generally respresents a SCF. Now, parallel *in situ* and *in vitro* measurements in lakes are rare and amongst the multitude of *in vitro* ΣPP estimates, seemingly none are spectrally-resolved.

This purpose of this chapter is to quantify the disparities between *in vitro* and spectrally-resolved estimates of ΣPP through the derivation of SCFs. SCFs are a function of the spectral shapes of *in vitro* and *in situ* irradiance (E_Z), as well as the absorption spectra of photosystem II

(a_{PSII}). While the *in vitro* spectrum is dictated by methodology, E_Z and a_{PSII} spectra vary according to the optical properties and attendant phytoplankton communities under investigation. This study, for the first time, explicitly examines how predictable and concurrent changes in E_Z and a_{PSII} occur across optical and trophic gradients, and models their interaction to derive SCFs applicable for a wide range of ecosystems for commonly used *in vitro* light sources. Data gleaned from an empirical SCF model are explicitly applied to historic ΣPP measurements in Lake Erie, and discussed in general relative to other ΣPP measurements in the Laurentian Great Lakes.

The quantitative importance of SCFs when scaling *in vitro* measurements to the *in situ* environment to ΣPP estimates has been demonstrated in Antarctic waters (Figueiras et al. 1999) and the sub-tropical Pacific Ocean (Laws et al. 1990), where spectrally-resolved ΣPP was 24% and >35% higher than respective *in vitro* estimates. SCFs from these two marine studies were derived from single *in vitro* light sources and are applicable only to environments with similar optical classifications and PSII absorption spectra. Markager and Vincent (2001) derived SCFs using 11 commonly cited *in vitro* light sources with spectrally resolved *in situ* irradiance measurements through depth in a set of 6 Arctic lakes, and is the only study to explicitly examine the spectral dependence of photosynthesis in freshwater lakes. However the study sites of Markager and Vincent (2001) span a limited trophic and optical gradient and the study only derives SCFs but does not address their contribution to disparate estimates of *in vitro* and *in situ* estimates of ΣPP.

Table 3.1 lists in chronological order synoptic (multiple measurements at more than one station repeated through a year) phytoplankton production surveys conducted in the Laurentian Great Lakes, specifically focusing on the methodology of each survey.

Table 3.1: Methodology of synoptic phytoplankton production surveys in the Laurentian Great Lakes. M – Lake Michigan, S – Lake Superior, H- Lake Huron, E – Lake Erie, O – Lake Ontario, number of measurements given in square brackets. ^{14}C Method with incubation time (hrs), w and p denote scintillation of whole water and particulate matter respectively. X denotes if measurements were performed *in situ* or *in vitro*, where *in vitro* measurements were performed details on the light spectra are given where PE denotes a light gradient incubator.

Reference: Lake [Sample Size]	Date	^{14}C Method	Depths Sampled	*In situ*	*In vitro*	Light Spectra
1: M[?]	May 1970-Feb 71	Unknown	Unknown		X	PE – Light Source unknown
2: M[4], S[22], H[9], E[13]	Jul 1970	[4-6,p]	0-5 m		X	53% and 68% of Incident Irradiance
3: H[207]	Apr–Dec 1971	[5,p]	0-10 m	X	X	~500 μmol.m^{-2}.s^{-1} Fluorescent
4: E[209], O[209]	Apr–Dec 1971	[5,p]	1-5 m	X	X	~133 μmol.m^{-2}.s^{-1} Fluorescent and Incadescent
5: O[25]	Apr 72- Apr 1973	[2-4,p]	0-25 m	X		
6: S[259]	Mar–Sep 1973	[2-4,p]	*In situ* 0-50 m *In vitro* 0-20 m	X	X	~320 μmol.m^{-2}.s^{-1} Fluorescent
7: O[~30]	Apr-Nov 1982	[2-3,p]	5 m		X	PE – Fluorescent
8: M[20]	Jul-Aug, 1982-1984	[24,p]	*In situ* 0-40 m	X		
M[20]	Jul-Aug, 1982-1984	[1-2,p]	*In vitro* depths not given		X	PE – Light source not given
9: S [~20]	Jun- Oct 1990-1991	[3,p]	0-4 m		X	PE – High Pressure Sodium
10: O [268]	May–Oct 1987-1992	[3-5,w]	0 – Z_M		X	PE – High Pressure Sodium
11: E[117], O[404]	May-Oct 1990-1991	[3-4,w]	0 – Z_M		X	PE – High Pressure Sodium
12: E[46]	May–Sep 1997	[1,w]	2 or 5 m [4 DCM]		X	PE – Tungsten Halogen
13: E[127]	Feb 2001- Mar 2002	[1,w]	0 – Z_M [9 DCM]		X	PE – Tungsten Halogen
14: O[37]	May – Oct 2003,2004	[1,w]	0-10 m Integrated		X	PE – Tungsten Halogen
15: E[116]	May-Sep 2005	[1,w]	2 or 0.5 Z_M [9 DCM]		X	PE – Tungsten Halogen

[1]Fee 1971; [2]Schelske and Roth 1973; [3]Glooshenko et al. 1973, [4]Glooshenko et al. 1974, [5]Stadlemann et al. 1974, [6]Watson et al. 1975, [7]Lean et al. 1987, [8]Fahnenstiel and Scavia 1987, [9]Fee et al. 1992, [10]Millard et al. 1996, [11]Millard et al. 1999, [12]Smith et al. 2005, [13]Depew et al. 2006, [14]Bocaniov et al. 2009, [15]This Study .

Direct measurements of phytoplankton photosynthesis in the Laurentian Great Lakes predate the earliest surveys listed in Table 3.1, but those surveys (reviewed in Vollenweider et al 1974) are omitted as they were temporally constrained and limited to a single station in a given lake. By the early 1970's, concerns over deteriorating water quality through anthropogenic eutrophication spurred comprehensive seasonal and basin scale surveys of phytoplankton production in all the Laurentian Great Lakes. The timing of these first lakewide surveys coincided near the onset of 1972 Great Lakes Water Quality Agreement (GLWQA) that established lower target levels for annual phosphorus loadings, the limiting nutrient in the Laurentian Great Lakes (Guildford et al. 2005). While the GLWQA has had a measurable impact on reduced phosphorus loadings (Dolan and McGunagle 2005), decreased hypolimnetic deoxygenation and increased water clarity in Lake Erie (El-Shaarawi 1987), the quantitative impact of reduced phosphorus loading on ΣPP in the Laurentian Great Lakes has not been accurately defined.

As shown in Table 3.1, since the GLWQA there has not only been but an alarming paucity of synoptic surveys, but comparative estimates between most surveys are hindered by shifts in ^{14}C methodology and ΣPP scaling (sensu Chapter 1). Table 3.1 demonstrates that 2-4 hour *in vitro* incubations were commonplace before 1990 while more recent studies have 1-hour incubations. Around 1990 there has also been a shift from assaying only particulate ^{14}C sequestration towards assaying whole water ^{14}C sequestration that includes respired labelled glycolates to provide a better approximation of gross primary production (Marra 2009). The quantitative impact of these methodological changes can only be estimated and as discussed in Chapter 2, particulate ^{14}C uptake increasingly underestimates whole water ^{14}C uptake with incubation duration. All *in vitro* studies listed in Table 3.1 have necessarily assumed homogeneity in the vertical patterns of photosynthetic efficiency and biomass with the exception

of opportunistic measurements of deep chlorophyll maxima (DCM) as noted. The impact of this scaling assumption is addressed in Chapter 4.

The spectral environments of synoptic ΣPP measurements have also changed over time. In the earliest synoptic surveys, *in vitro* measurements were performed at a single light intensity and compared to less frequent *in situ* measurements. In the first synoptic survey of Lakes Erie and Ontario (Glooshenko et al. 1974), *in vitro* photosynthetic rates were measured at a single light intensity under a combination of 'fluorescent lamps and 40W incandescent lamps' and compared to *in situ* measurements performed at integrated over 'various depths to 15 m' at select stations. The ratio of areal *in situ* to volumetric measurements (dependent variable) was linearly correlated to Secchi depth (r^2 =0.64, Glooshenko et al. 1974) and the slope of this relationship was used to convert the more numerous *in vitro* measurements to *in situ* measurements given a concomitant Secchi disc measurement. Derived ratios that scale *in vitro* to *in situ* measurements in part reflect the conversion of volumentric to areal photosynthetic rates but also represent disparaties between the spectral environments (eg a SCF). The slope of the linear relationship (1.85) dictates that as water transparency increases *in vitro* rates increasingly underestimate *in situ* rates. Subsequent synoptic ΣPP measurements in the Laurentian Great Lakes were performed only *in vitro*, first using high-pressure sodium vapour lamps then tungsten-halogen lamps in light gradient incubators whose spectra are markedely different. These data combined with direct broadband measurement of light extinction and variable surface irradiance over the day were then used the generate estimates of ΣPP (Fee 1971). This chapter focuses on SCFs derived from these two light sources, and estimates the disparities between *in situ* and *in vitro* ΣPP estimates in Lake Erie as caused by the inaccurate representation of the *in situ* spectral environment. This example raises caution about comparing historical measurements with recent

measurements using different methodologies and illustrates the need for the adoption of a common methodology across the lakes in order to monitor the changing productivity of lakes with highly transparent water columns and in particular great lakes.

Section 3.2: Materials and Methods

Optical Properties - Wavelength-specific attenuation ($k_{PAR[\lambda]}$) was measured every 20 nm for wavelengths ranging from 410 to 710 nm at 22 stations in Lake Erie with an *in situ* spectrophotometer (Wetlabs AC-9, Philomath, Oregon; data courtesy of Caren Binding). Data from each profile was averaged through depth to obtain station-specific spectral attenuation values that are shown in Figure 3.1B. The 22 stations span a large optical gradient (k_{PAR} ranged from 0.22 to 1.0 m^{-1}) and encompassed 89% of all k_{PAR} measurements in this study and relevant historic measurements in Lake Erie.

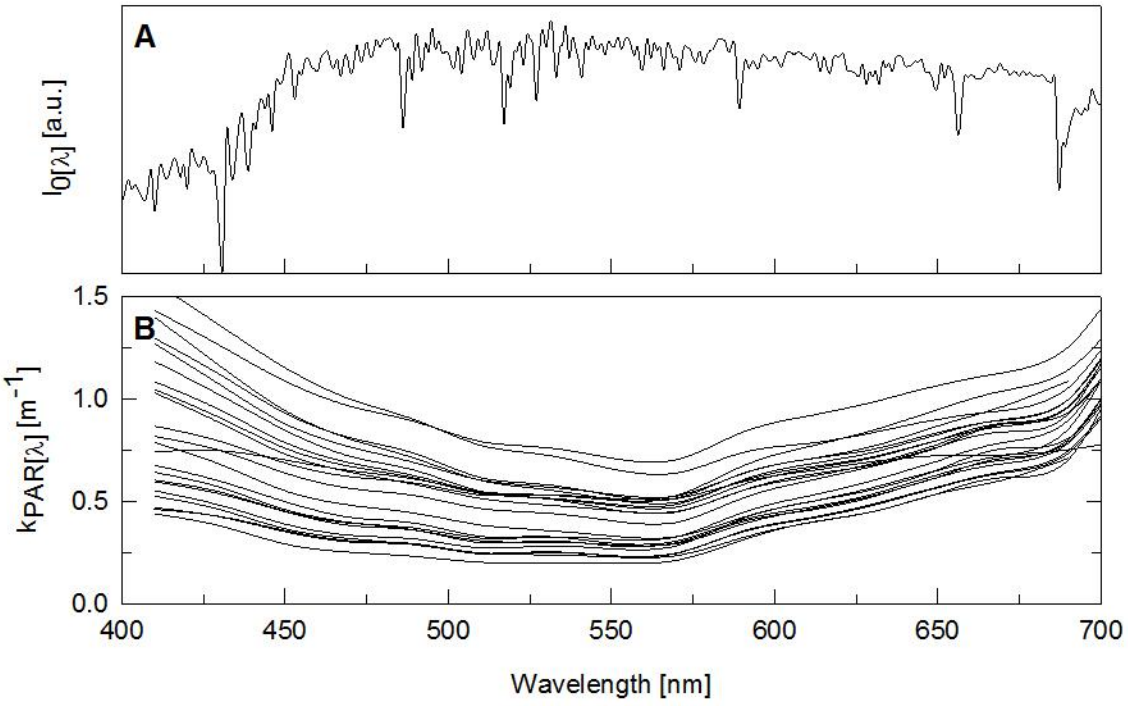

Figure 3.1: A) $E_{O[\lambda]}$ in this chapter set to the solar reference spectrum ASTM-G173. B) Wavelength-specific attenuation of PAR ($k_{PAR[\lambda]}$) measured at 22 stations in Lake Erie.

Linear regressions between inherent $k_{PAR[\lambda]}$and apparent k_{PAR} for the 22 stations across all 15 wavelengths were statistically significant (r^2 between 67-88%, n =22, $p<0.01$), consistent with historical measurements in Lake Erie (Jerome et al. 1983). Wavelength-specific slopes ($m_{[\lambda]}$)

and offsets ($b_{[\lambda]}$) of these linear regressions are shown in Figure 3.2B. Following Eqn 3.1, $m_{[\lambda]}$ and $b_{[\lambda]}$ allow the prediction of wavelength-specific attenuation ($k_{PAR[\lambda]}$) from a single k_{PAR} measurement. Substitution of Eqn 3.1 into the Beer-Lambert equation (Eqn 3.2) shows that the *in situ* spectral energy at depth z ($E_{Z[\lambda]}$) is equal to incident irradiance ($E_{O[\lambda]}$) multiplied by the exponent of the negative product of $k_{PAR[\lambda]}$ and depth (z). The spectral shape of $E_{O[\lambda]}$ is set to the reference terrestrial solar spectrum of the American Society for Testing and Materials (ASTM G173) shown in Figure 3.1A. These equations can therefore be combined to predict $E_{Z[\lambda]}$ across an optical gradient by varying k_{PAR} to predict $k_{PAR[\lambda]}$ (Eqn 3.1) then substituting $k_{PAR[\lambda]}$ into Eqn 3.2. This approach is easily transferable to other marine (Smith and Baker 1978) and freshwater (Jerome et al. 1983) ecosystems whose optical properties are tabulated in the literature.

[Eqn 3.1] $k_{PAR[\lambda]} = k_{PAR} \bullet m_{[\lambda]} + b_{[\lambda]}$

[Eqn 3.2] $E_{Z[\lambda]} = E_{O[\lambda]} \bullet \exp^{[-kPAR[\lambda] \bullet z]}$

In this chapter spectra are described using the terms spectral centroid and half-bandwidth. The spectral centroid refers to the geometric mean wavelength of the *in situ* spectrum and is derived using Eqn 3.3. The half-bandwidth refers to the wavelength range that encompasses 50% of PAR about the spectral centroid and is determined using an iterative algorithm by expanding the spectral range by nanometre increments until half the spectral energy between 400 and 700 nm is met.

[Eqn 3.3] Spectral Centroid $= \Sigma[E_{Z[\lambda]} \bullet \lambda] \ [\Sigma[E_{Z[\lambda]}]]^{-1}$

Photosynthetic absorption spectra – The methodology employed to derive photosynthetic absorption spectra ($a_{PS[\lambda]}$) is described in Section 2.2. Statistically significant wavelength-specific linear relationships between $a_{PS[\lambda]}$ and chl *a* in Lake Erie have been previously documented (Figure 2.7D). Similar to the approach to derive *in situ* spectral irradiance, the

slopes and linear regressions between $a_{PS[\lambda]}$ and chl *a* are used to derive $a_{PS[\lambda]}$ spectra across a chl *a* gradient. This method can be similarly applied to marine $a_{PS[\lambda]}$ spectra whose wavelength-specific variability across a chl *a* gradient is tabulated in the literature (Bricaud et al. 1995).

SCFs – Two types of spectral correction factors are presented in this Chapter. In general SCFs are calculated by first summing (Σ) the products of a given light spectra $E_{[\lambda]}$ and $a_{PS[\lambda]}$ for all PAR wavelengths (400 to 700 nm) and normalizing this value to the sum of $E_{[\lambda]}$. This calculation is shown on the right side of Eqn 3.4 and 3.5 and the result describes the 'effectiveness' of the light spectra (see Figure 3.4). To derive a SCF this effectiveness is then divided by an identical equation where either $a_{PS[\lambda]}$ or $E_{[\lambda]}$ is changed. Eqn 3.4 yields SCFs that are used in this chapter to describe how changes in $a_{PS[\lambda]}$ spectra alone yield different SCFs against a constant *in vitro* light source ($E_{In\ vitro[\lambda]}$) by normalizing a variable $a_{PS[\lambda]}$ to its maximum effectiveness. Eqn 3.5 describes SCFs that normalize *in vitro* light spectra to the *in situ* light spectra ($E_{Z[\lambda]}$).

[Eqn 3.4] $SCF = \Sigma[E_{In\ vitro[\lambda]} \bullet a_{PS[\lambda]}]\ [\Sigma[E_{In\ vitro[\lambda]}]]^{-1} \bullet \max(\Sigma[E_{In\ vitro[\lambda]} \bullet a_{PS[\lambda]}]\ [\Sigma[E_{In\ vitro[\lambda]}]]^{-1})^{-1}$

[Eqn 3.5] $SCF = \Sigma[E_{In\ vitro[\lambda]} \bullet a_{PS[\lambda]}]\ [\Sigma[E_{In\ vitro[\lambda]}]]^{-1} \bullet (\Sigma[E_{Z[\lambda]} \bullet a_{PS[\lambda]}]\ [\Sigma[E_{Z[\lambda]}]]^{-1})^{-1}$

Areal Phytoplankton Production (ΣPP) - ΣPP is calculated using the Fee (1990) algorithm's in the mathematical program R. A comparison of 10 ΣPP estimates with the original model written in Turbo Pascal with the R version were not statistically different (t-test, $p < 0.01$). ΣPP computed with R was on average 0.3% higher, this small difference is likely a consequence of different integration algorithms used by the original model and R. For consistency with previous studies (Millard et al. 1999; Smith et al. 2005), ΣPP was calculated from epilimnetic measurements of the photosynthetic irradiance (PE) parameters and chl *a*, whose methodology is

described in Section 2.2, and ΣPP estimates are calculated using theoretical cloud-free incident irradiance. Following Millard et al. (1999) and Smith et al. (2005), seasonally averaged estimates of phytoplankton production (SAPP) are computed for each study to assess historic ΣPP changes in Lake Erie. SAPP from all studies are first derived for each of Lake Erie's basins whose geographic boundaries are shown in Figure 4.1 by taking the mean ΣPP estimates of each basin and multiplying by 183 days (May 1st – Oct 31st). Lakewide estimates of SAPP are then estimated using geographically weighted means of each basin derived from GIS data where the west, central-west, central and east basins occupy 25%, 21, 42% and 12% of total lake area respectively. No correction for lake morphometry is performed, and the stations in Millard et al. (1999) where the euphotic depth extends beyond station depth have been omitted from this analysis for consistency with Smith et al. (2005) and data from this study.

SCFs for historic *in vitro* data were derived using the basin specific mean k_{PAR} and chl *a* values to derive *in situ* irradiance spectra and $a_{PS[\lambda]}$ respectively. Not all the historic data (i.e. station specific sets of PE parameters, k_{PAR} and chl data) were available so only one SCF was derived per basin per study. The error of this assumption was tested by applying SCFs to individual sets of measurements from the 2005 dataset and averaging the data to derive basin specific SAPP estimates as above, then comparing these estimates to SAPP estimates using only a single SCF for the basin. Though station specific SCFs deviated from the mean basin value, final SAPP estimates using both methods were within 1.5% for all four basins.

Section 3.3: Results

Results are divided into four sections. Section 3.3.1 introduces *in situ* spectral irradiance ($k_{PAR[\lambda]}$) measurements in Lake Erie and demonstrates how predictable spectral changes occur along an optical (k_{PAR}) gradient. Sections 3.3.2 documents the spectral shapes of $a_{PSII[\lambda]}$ in Lake Erie and demonstrates how predictable changes occur along a chl *a* gradient. Section 3.3.3 then combines the two empirical $k_{PAR[\lambda]}$ and $a_{PSII[\lambda]}$ models to derive spectral correction factors (SCFs) across optical and chl *a* gradients for the two commonly used *in vitro* light sources shown in Table 3.1. Finally Section 3.3.4 examines historic measurements of *in vitro* and *in situ* phytoplankton production (ΣPP) in Lake Erie, and examines how SCFs applied to the *in vitro* data effect estimated ΣPP.

Section 3.3.1 *In situ* spectral irradiance

Figure 3.2 summarizes the underwater spectral environment in Lake Erie through depth and across an optical (k_{PAR}) gradient derived through the empirical *in situ* irradiance model. Figure 3.2A depicts the wavelength-specific slopes ($m_{[\lambda]}$) and offsets ($b_{[\lambda]}$) of the model. Derived $b_{[\lambda]}$ has units of m^{-1} and represents $k_{PAR[\lambda]}$ minima across the PAR spectrum in Lake Erie. The close match between $b_{[\lambda]}$ and the attenuation of pure water (k_W, Pope and Fry 1997) in both magnitude and spectral shape is an excellent validation of the empirical model. As k_{PAR} increases, $m_{[\lambda]}$ dictates that attenuation of PAR is highest at wavelengths less than 550 nm. Back-scattering and absorption by dissolved and particulate matter in water columns exponentially increase at wavelengths smaller than 550 nm (Kirk 1994), consistent with the spectral shape of $m_{[\lambda]}$ in Figure 3.2A.

The spectral attenuation of irradiance across an optical gradient and through depth, as

predicted by the *in situ* irradiance model, influences the quality of the underwater light spectrum in two important ways. Shown in Figure 3.2B, increasing k_{PAR} disproportionately attenuates blue light. Figure 3.2C shows the underwater spectra at an optical depth (ξ) of 4.7 for three water columns with respective k_{PAR} values of 0.17, 0.63 and 1.49 m^{-1}: The three spectra have the same spectral quantity (PAR), but the centroid (geometric mean) of the underwater light spectra of k_{PAR} = 0.63 and 1.49 m^{-1} are 'red-shifted' (occurring at longer wavelengths) by 30 and 54 nm respectively relative to k_{PAR} = 0.17 m^{-1}. Figure 3.2D summarizes this spectral red-shift across an optical gradient at ξ = 4.7. A second, more subtle shift in the shape of the underwater light spectrum also predictably occurs through depth and across an optical gradient: In oligotrophic (low k_{PAR}) waters optical depths occur at deeper physical depths than eutrophic waters. The increased path length of irradiance in oligotrophic water to a given optical depth allows for greater attenuation by water alone, that as shown in Figure 3.2A is highest in the red spectral region. While light attenuation by water also influences the above noted red-shift, it also constrains *in situ* irradiance to a narrower spectrum in oligotrophic waters. In other words, shallower optical depths in turbid water allow more red light to penetrate and so have broader spectra. This phenomenon is depicted in Figure 3.2D and E where the half-bandwidth of underwater spectra are shown across an optical gradient and through depth respectively.

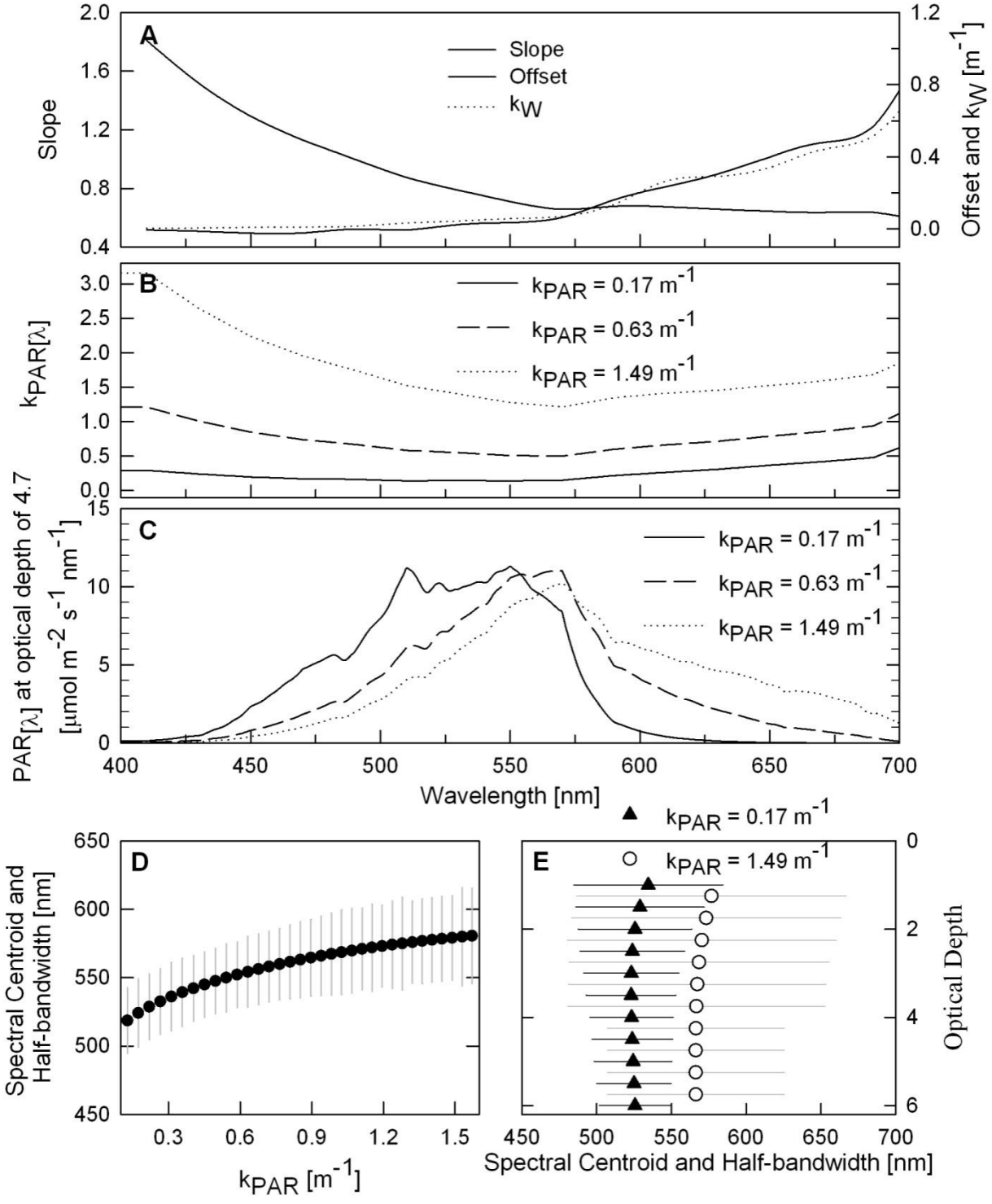

Figure 3.2: A) The slopes and offsets of the k_{PAR} vs $k_{PAR[\lambda]}$ linear regressions with the attenuation of pure water (k_W) for reference. B). $k_{PAR[\lambda]}$ and C) the *in situ* spectrum at an optical depth of 4.7 for 3 k_{PAR} values. The spectral centroid and half bandwidth at D) an optical depth of 4.7 as a function of k_{PAR} and E) through depth for two k_{PAR} values.

Section 3.3.2: a_{PSII} across a chl gradient

While Section 2.3.3 focused on quantitative estimates of a_{PSII}, this section exclusively examines the spectral quality of a_{PSII} across the PAR spectrum. Similar to the *in situ* spectral irradiance model described above, the slopes and offsets from the linear regressions of $a_{PS[\lambda]}$ versus chl are used in an empirical model that predicts the shape of $a_{PS[\lambda]}$ across a chl gradient. Figure 3.3A summarizes the normalized slopes and offsets of these linear regressions. Along an increasing chl gradient, absorption is depleted in the wavelengths where the offsets exceed the slopes (440-550 m) relative to increased absorption in the wavelengths where the slopes exceed the offsets (550-700 nm).

The absence of accessory pigment concentrations in this study precludes a definitive interpretation of $a_{PS[\lambda]}$ changes along a chl gradient, though some basic changes in pigment content can be inferred from the spectral data alone. The spectral shape of the offset depicts $a_{PS[\lambda]}$ in low biomass waters. Shoulders in the offset spectrum at 465 and 490 nm suggest the presence of photoprotectant pigments (Figure 1.1). Photoprotectant pigments should not contribute to $a_{PS[\lambda]}$ and thus introduce a bias in this model, however the steep drop in the slope at these wavelengths suggest the spectral contribution of these pigments are rapidly diminished with increasing chl *a*, as documented in marine ecosystems (Bricaud et al. 2004). Pigment packaging may also influence $a_{PS[\lambda]}$ across a chl *a* gradient. Increased cellular chl *a* reduces absorption of chl in the blue relative to the red spectrum, and the slope of the linear regression of $a_{PS[440]}$:$a_{PS[665]}$ versus chl in Lake Erie was significantly smaller than zero ($p < 0.01$), though absorption of other pigments at these wavelengths again precludes a definitive quantification of pigment packaging.

Chapter 2 demonstrated that the spectral shapes of $a_{PS[\lambda]}$ and $a_{PSII[\lambda]}$ are not always identical, particularly in cyanobacterial dominated waters. To investigate if changes in $a_{PS[\lambda]}$ along a chl *a* gradient are consistent with changes in $a_{PSII[\lambda]}$, *in situ* spectral fluorescence data was taken from the same depths as $a_{PSII[\lambda]}$ samples similarly statistically regressed against chl *a*. The linear regressions of $F_{[\lambda]}$ versus chl *a* were highly significant at the 5 measuring wavelengths ($p < 0.01$) with r^2 ranging from 0.65 for 450 nm to 0.73 for 525 nm. Figure 3.3B compares $F_{[\lambda]}$ and $a_{PS[\lambda]}$ data computed from their respective empirical models at three chl *a* concentrations, where both $F_{[\lambda]}$ and $a_{PS[\lambda]}$ measurements are normalized to their respective means for clarity. The slopes and offsets of the linear regressions of $F_{[\lambda]}$ versus chl *a* (data not shown) are remarkably consistent with $a_{PS[\lambda]}$, so Figure 3.3B shows $F_{[\lambda]}$ also undergoes a red spectral shift along an increasing chl gradient. Furthermore both normalized values of $a_{PS[\lambda]}$ and $F_{[\lambda]}$ show remarkable agreement at 570 nm as both are invariant at the chl *a* concentrations shown. At 10 μg chl *a* L^{-1} some disparities between $a_{PS[\lambda]}$ and $F_{[\lambda]}$ are apparent, as $a_{PS[\lambda]}$ appears to slightly overestimate $F_{[\lambda]}$ at 450 nm and underestimate $F_{[\lambda]}$ above 525 nm. Fortunately, such high concentrations are infrequently encountered in the Laurentian Great Lakes and represent less than 5% of ambient chl concentrations in the historic datasets to which SCFs are applied to in the following section.

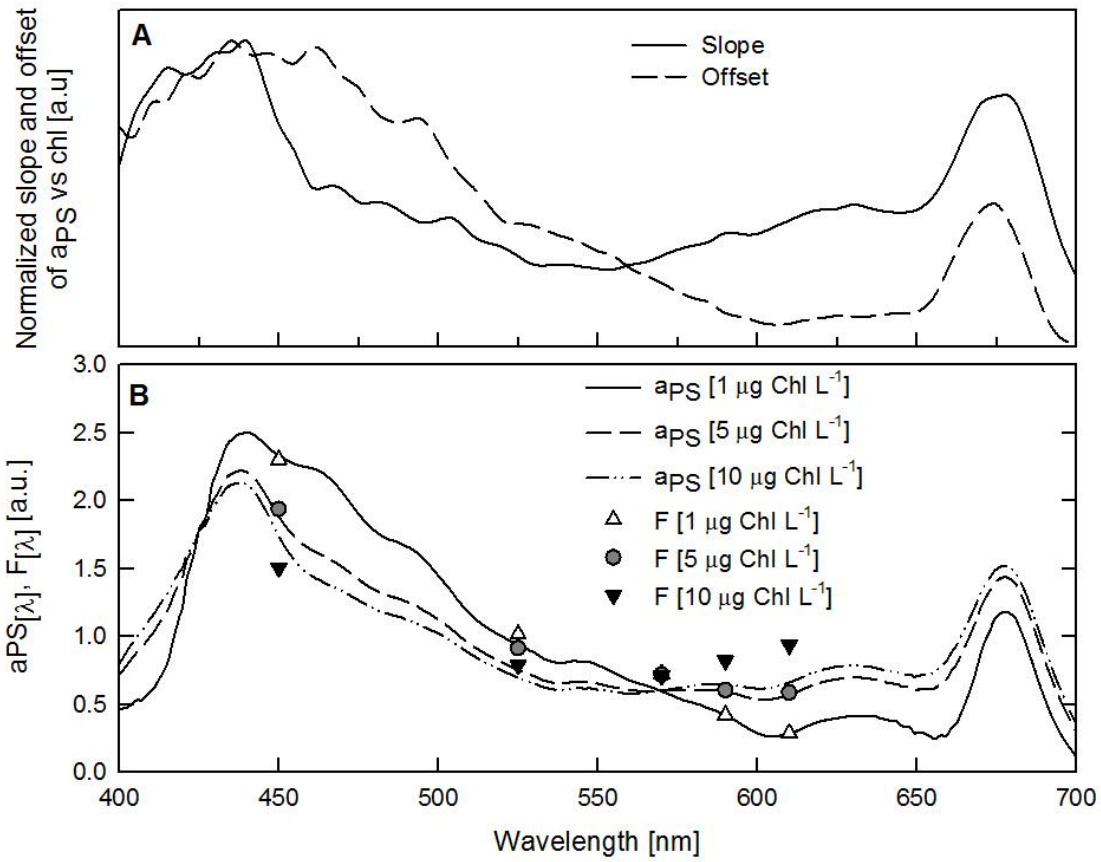

Figure 3.3: A) Wavelength specific slopes and offsets from linear regressions $a_{PS[\lambda]}$ versus chl *a*, values are normalized to each other for clarity. B) Empirically derived $a_{PS[\lambda]}$ and $F_{[\lambda]}$ at three chl *a* concentrations.

Section 3.3.4: Spectral Correction Factors

Figure 3.4 documents the interaction of *in vitro* light sources with spectral changes of $a_{PS[\lambda]}$ along a chl gradient. In Figure 3.4A, the top panels show the *in vitro* spectra of the tungsten halogen (E_{TH}) and high pressure sodium vapour (E_{SV}) light sources. E_{TH} and E_{SV} are then multiplied by $a_{PS[\lambda]}$ derived for 1 and 10 $\mu g.L^{-1}$ of chl *a* and shown in the centre of Panel A, and the products ($E_{in\ vitro} * a_{PS}$) are shown at the bottom of Panel A. Figure 3.4B shows SCFs for both light sources following Eqn 3.4.

Figure 3.4 underscores the large sensitivity of $a_{PS[\lambda]}$ spectra to *in vitro* light sources. For two phytoplankton communities with $a_{PS[\lambda]}$ spectra shown in Figure 3.4A, apparent light-limited photosynthetic rates are 12% and 77% enhanced in the 10 $\mu g.L^{-1}$ chl a $a_{PS[\lambda]}$ for the E_{TH} and E_{SV} light sources respectively. 84% of irradiance emitted from E_{SV} occurs at wavelengths greater than 570 nm, so this light source becomes increasingly ineffective as $a_{PS[\lambda]}$ spectra become blue shifted. In comparison, only 59% of E_{TH} occurs at wavelengths greater than 570 nm, so its increasing effectiveness with red-shifted $a_{PS[\lambda]}$ spectra is not as severe as E_{TH}. SCFs as a function of chl in Figure 3.4B can be described by a two parameter power curve ($SCF = a\ chl^{b}$) where the coefficients a and b = 0.58 and 0.21 respectively for E_{SV} (r^2=0.97) and a and b = 0.90 and 0.04 respectively for E_{TH} (r^2=0.98).

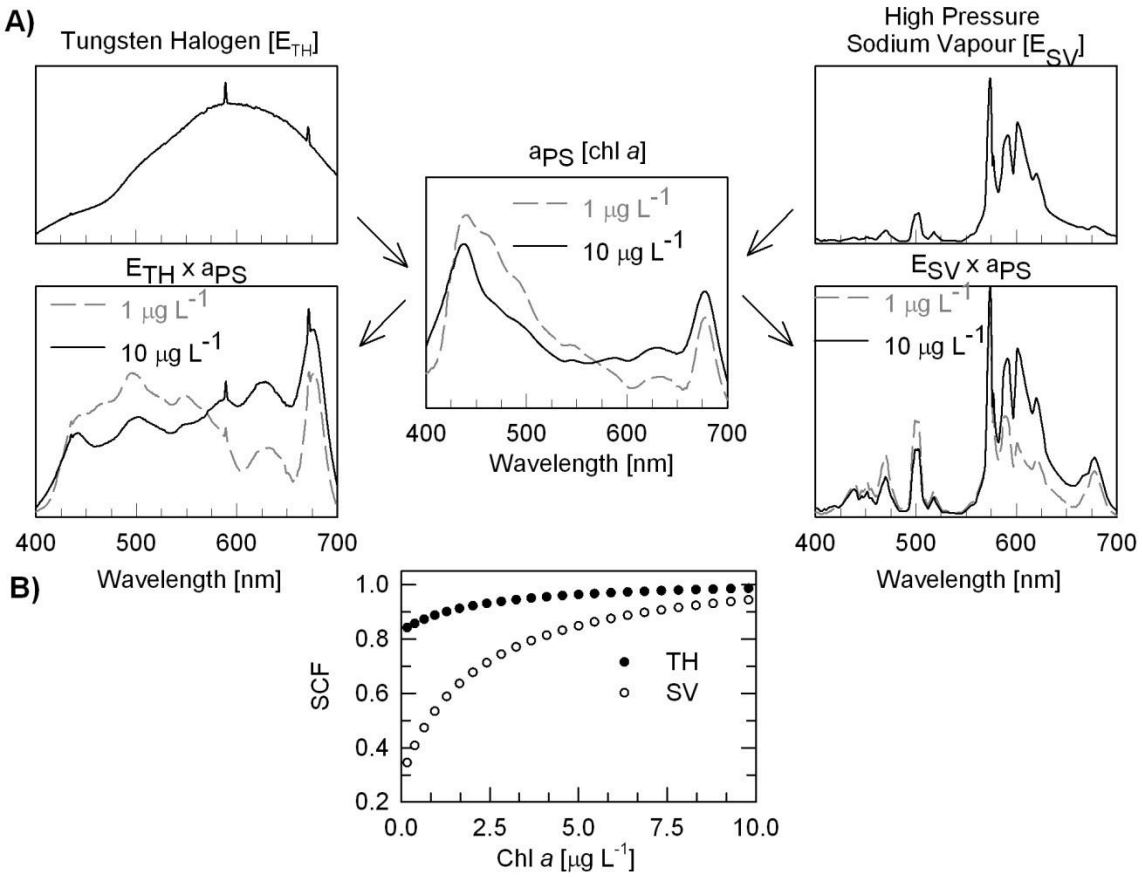

Figure 3.4: A) Spectra of tungsten halogen [TH] and high pressure sodium vapour [SV] lamps are each multiplied by two a_{PS} spectra representative of 1 and 10 $\mu g.L^{-1}$, the resultant spectra are shown beneath each lamp spectra. B) SCFs derived using Eqn 3.4 for TH and SV lamps.

Figure 3.5A documents SCFs through depth and across an optical gradient according to Eqn 3.5 where $E_{in\ vitro[\lambda]}$ is E_{TH}, $E_{z[\lambda]}$ is derived from the empirical k_{PAR} model and $a_{PS[\lambda]}$ is derived from the empirical chl *a* model and realted to k_{PAR} using the relationship between chl *a* and k_{PAR} (Figure 2.5). Similar to marine ecosystems (Bricaud et al. 1995), *in situ* spectra through depth are enriched in the wavelengths of algal absorption in clear waters (SCFs increase), but as k_{PAR} increases *in situ* spectra are depleted through depth (SCFs decrease) in the wavelengths of algal absorption. Figure 3.5B is an extension of Figure 3.5A where SCFs are shown as a contour plot through depth and across an optical gradient, Figure 3.5C is the same as 3.5B but $E_{in\ vitro[\lambda]}$ is E_{SV}.

Figure 3.5B and C shows that *in vitro* light sources increasingly underestimate the *in situ* spectra as k_{PAR} decreases. This underestimation in clear water is particularly pronounced for E_{SV} as *in situ* blue-shifted spectra have significantly higher overlap with attendant $a_{PS[\lambda]}$ spectra than the red-shifted E_{SV} spectrum. As k_{PAR} increases and the *in situ* spectra becomes increasingly centred around 550-600 nm (Figure 3.2D), E_{TH} and E_{SV} spectra better approximate the *in situ* environment and will actually overestimate light-limited photosynthetic rates at depth.

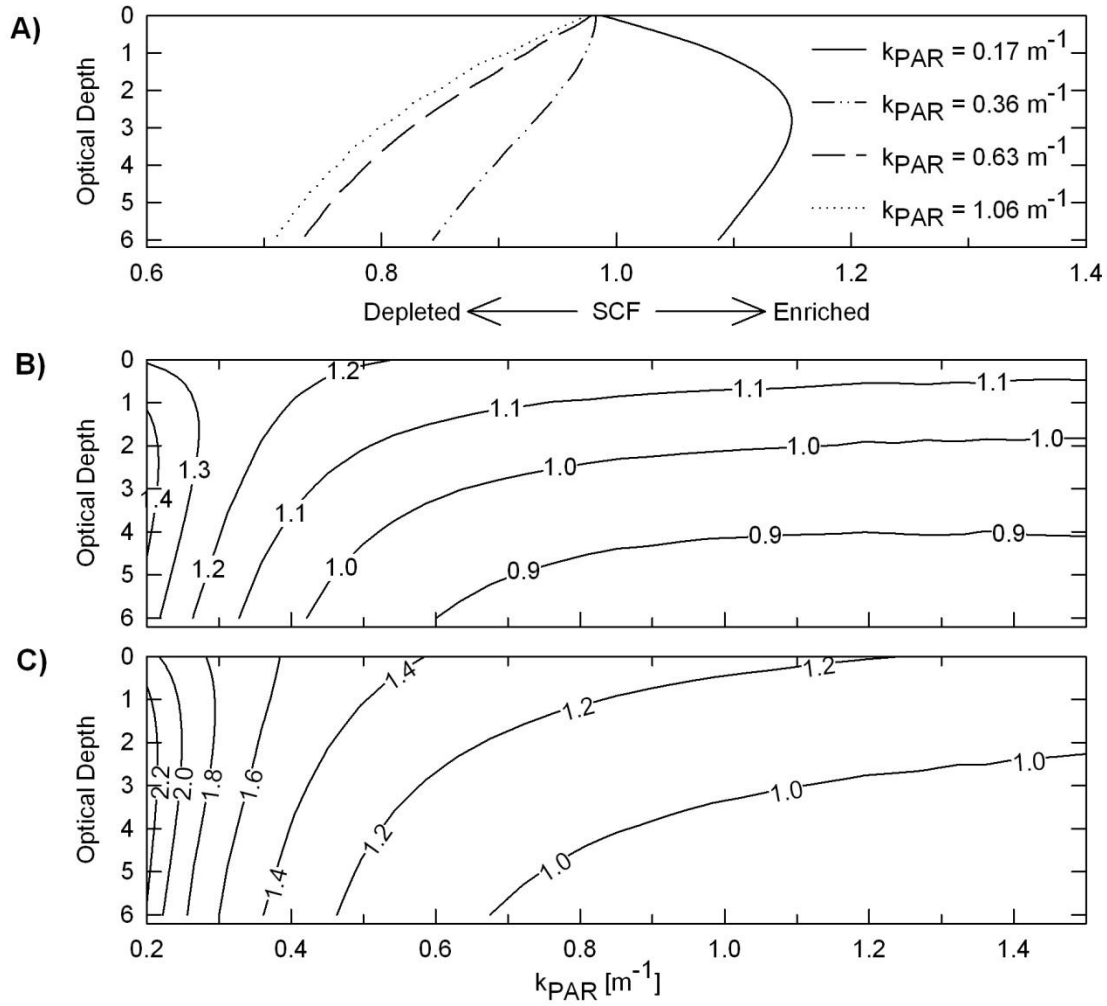

Figure 3.5: A) SCFs through depth calculated using 4 k_{PAR} values and $a_{PS[\lambda]}$ spectra derived using the chl *a* to k_{PAR} relationship in Figure 2.5. Multiplicative SCFs required to extrapolate *in vitro* photosynthetic rates through depth and across an optical gradient for B) a tungsten-halogen light source and C) a high pressure sodium vapour light source.

SCFs presented in Figure 3.5B and C are applicable only when correcting light-limited photosynthetic rates. Within the topmost optical depths, photosynthesis is light-saturated for long periods of the day and is insensitive to the spectral quality of light. Figure 3.6 demonstrates the qualitative impact of SCFs on photosynthetic rates for a theoretical water column described in the Section 3.2 where the light saturation parameter (E_K) is set to 100 $\mu mol.m^{-2}.s^{-1}$. The contour plots in Figure 3.6A and B describe the ratio of *in situ* and *in vitro* daily volumetric phytoplankton production through depth and across an optical gradient, while Figure 3.6C describes the ratio of *in situ* to *in vitro* daily areal phytoplankton production (ΣPP). Relative to Figure 3.5, the magnitude of spectral sensitivity is reduced in the shallowest optical depths where light-saturated photosynthesis dominates. The ratio of *in vitro* to *in situ* ΣPP across an optical gradient dictated by SCFs is sensitive to changes in E_K, shown in Figure 3.6C as E_K decreases *in vitro* ΣPP increasingly underestimates *in situ* ΣPP.

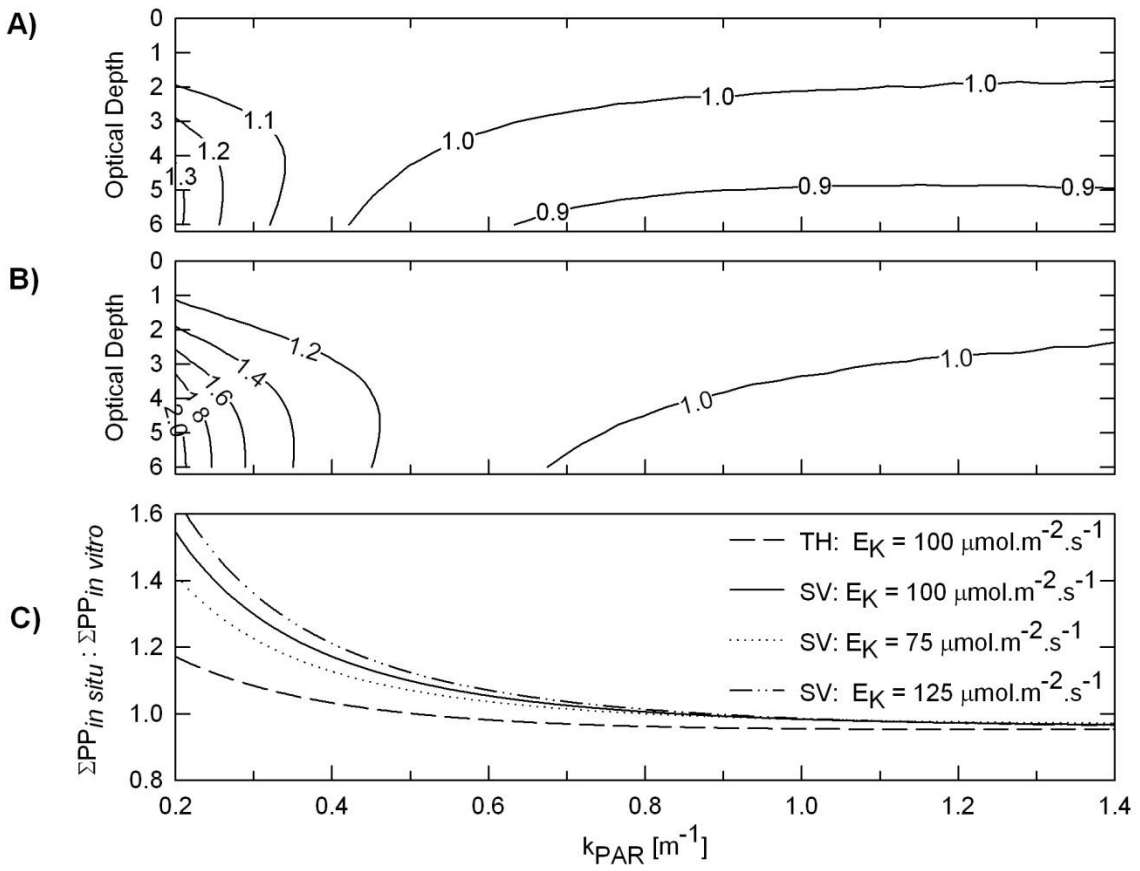

Figure 3.6: The ratio of *in situ* and *in vitro* daily volumetric photosynthetic rates through depth and across an optical gradient for A) a tungsten-halogen light source and B) a high-pressure sodium vapour light source. C) The ratio of *in situ* to *in vitro* ΣPP across an optical gradient with different values of E_K.

Section 3.3.4: Resolving Historic ΣPP Measurements in Lake Erie

Table 3.2 summarizes the relevant basin-specific data compiled from major synoptic ΣPP estimates performed in Lake Erie. The survey of Glooshenko et al. (1974) has been omitted from Table 3.2 as only basin-specific seasonal areal phytoplankton production (SAPP) can be culled from this reference. Unlike the studies shown in Table 3.2, SAPP in Glooshenko et al. (1974) was calculated using the period April 1st to December 31st with values of 310, 210 and 160 g C.m^{-2} for the west, central and east basin respectively. Subsequent lakewide surveys derive SAPP for the period May 1st to October 31st, so Millard et al. (1999) reduced the 1974 SAPP estimates by 10% (based on 'Millard et al. 1996 estimated winter photosynthesis at 20% of annual rates') to correct for Glooshenko's et al. (1974) longer study period. Glooshenko et al. (1974) graphically displays monthly variability of ΣPP in Lake Erie, and from this graph it appears that approximately 90% of SAPP does fall within the May 1st to October 31st period.

The purpose of this section is not to provide a robust statistical analysis of all ΣPP estimates and attendant measurements. The frequency of observation, timing of field campaigns and station selection vary between all studies listed in Table 3.2, and a detailed error analysis of how this variability propagates through estimated SAPP is beyond the scope of this thesis. Instead, the focus is to simply apply SCFs to each dataset to estimate the degree of disparity between *in vitro* and *in situ* ΣPP estimates (and therefore SAPP) to minimize sources of error pertaining to differences in *in vitro* light sources only. Shown in Table 3.2, consistent with the above analysis derived SCFs were highest for the study of Millard et al. (1999) that employed a high pressure sodium vapour light source and reported the lowest values of α^*. SCFs applied to this study

ranged from 1.12 in the mesotrophic West basin to 1.49 in the oligotrophic East basin. When applied to lakewide estimates of SAPP, these SCFs predict that *in situ* estimates are 22% higher than reported *in vitro* estimates. Relative to Glooshenko et al. (1974) *in situ* based SAPP estimates, Millard et al. (1999) reported a reduction of SAPP by 47, 22 and 55% in the west, central and east basin, equivalent to a mean lakewide SAPP reduction of 32%. However if Millard et al.'s data is appropriately scaled to the *in situ* environment, SAPP is reduced by 41% in the west basin but only by 4% and 1% in the central and east basins respectively for a mean lakewide reduction of 16% relative to Glooshenko et al. (1974). Thus, by these calculations spectral differences account for half of the reported decrease of SAPP in Lake Erie between these two studies. Other methodological discrepancies between these two studies need also be considered. Shown in Table 3.1, Glooshenko et al. (1974) measured only particulate ^{14}C assimilation after a 5-hour incubation. As discussed in Chapter 2, particulate estimates do not account for assimilated ^{14}C that is respired during the incubation, whereas the methodology of the studies shown in Table 3.2 assay whole water samples to capture assimilated and respired ^{14}C.

SCFs performed by Smith et al. (2005) and this study are comparatively small as tungsten-halogen light sources offer better approximations of the *in situ* environment (Figure 3.6). Only in the oligotrophic East basin of Smith et al.'s (2005) dataset yield SCFs greater than 1.10, while in the same study the SCF derived for the turbid west basin indicate *in vitro* SAPP slightly overestimated *in situ* SAPP. When SCFs are applied to these studies, mean lakewide SAPP estimates remarkably fall within 5% of the spectrally corrected estimates of Millard et al. (1999).

Table 3.2: Historic Chl *a*, k_{PAR} and PE parameters derived from 3 lakewide *in vitro* ΣPP surveys of Lake Erie. Values in parentheses are standard deviations, n is sample size. Source refers to reference given in Table 3.1. Basin is W – West, C – Central (CW – Central-West and CE Central East) and E –East. SAPP is seasonal areal phytoplankton production (1st May – 31st Oct). The derivation of SCF is described in Section 3.2. SCF • SAPP approximates *in situ* SAPP. Lakewide SAPP is the geographically weighted mean of basin SAPP estimates.

Source	Basin (n)	Chl *a* [$\mu g.L^{-1}$]	k_{PAR} [m^{-1}]	P^*_M [g C g Chl a^{-1} h^{-1}]	α^* [g C m^2 g Chl a^{-1} $mmol^{-1}$]	SAPP [g $C.m^{-2}$]	SCF	SCF • SAPP [g $C.m^{-2}$]
11	W (>20)	4.55	0.85	5.83	4.91	147	1.12	165
11	C (>20)	3.35	0.33	3.99	4.97	147	1.23	181
11	E (>20)	1.68	0.24	3.72	3.99	96	1.49	143
					Lakewide SAPP =	**141**		**172**
12	W (14)	4.94 (4.11)	1.12 (0.68)	5.26 (1.94)	7.53 (2.69)	155	0.96	152
12	CW (8)	4.44 (5.06)	0.50 (0.19)	4.51 (1.74)	8.64 (3.31)	169	1.00	169
12	C (15)	2.24 (1.64)	0.35 (0.15)	4.04 (1.65)	7.50 (2.28)	167	1.08	180
12	E (9)	2.11 (1.15)	0.33 (0.08)	3.90 (1.41)	7.93(2.60)	152	1.12	170
					Lakewide SAPP =	**163**		**170**
15	W (30)	4.49 (3.40)	0.68 (0.28)	3.79 (2.04)	10.37 (5.53)	187	1.00	187
15	CW (37)	2.89 (1.82)	0.36 (0.12)	2.57 (1.18)	9.24 (4.85)	145	1.03	149
15	C (25)	3.01 (1.80)	0.37 (0.15)	2.60 (1.41)	9.64 (4.15)	159	1.02	162
15	E (15)	1.80 (1.12)	0.26 (0.04)	3.02 (1.19)	10.27 (4.52)	150	1.08	162
					Lakewide SAPP =	**162**		**165**

Section 3.4: Discussion

This chapter has demonstrated that, consistent with marine literature, the spectral shapes of *in situ* irradiance ($E_{Z[\lambda]}$) and photosynthetic absorption ($a_{PS[\lambda]}$) co-vary with k_{PAR} and chl *a* respectively. Through these relationships, an empirical model has been developed that extrapolates *in vitro* estimates of ΣPP to the *in situ* spectra. The model input parameters (chl *a*, k_{PAR} and E_K) are common to frequently cited *in vitro* ΣPP numerical models (Fee 1977) so, as demonstrated, the model can be readily applied to correct a multitude of historic *in vitro* photosynthetic measurements. The interaction between $a_{PS[\lambda]}$ and the *in situ* spectral environment drive this model, and so are discussed below first. Next, the consequences of variable $a_{PS[\lambda]}$ and $E_{Z[\lambda]}$ spectra on *in vitro* photosynthetic measurements are considered in general. The implications of the model to the interpretation of historic ΣPP estimates in Lake Erie completes the discussion.

3.4.1 How the underwater irradiance spectra influences $a_{PS[\lambda]}$

Concomitant shifts in the *in situ* and $a_{PS[\lambda]}$ spectra suggests that, to a certain degree, Lake Erie`s phytoplankton community chromatically adapts to the *in situ* environment. A red-shift in $a_{PS[\lambda]}$ spectra with increasing chl matches the red-shift of the *in situ* spectra with increasing k_{PAR} (and therefore chl, Figure 2.5). Indeed, regressing $a_{PS[\lambda]}$ against k_{PAR} from this study yielded highly significant relationships ($p<0.01$) across the PAR spectrum with normalized slopes and offsets that also predict that $a_{PS[\lambda]}$ becomes red-shifted with increasing k_{PAR}. Chl *a* is chosen here as a predictor of the spectral shape of $a_{PS[\lambda]}$ to be consistent with marine studies that have investigated relative changes in pigment concentration and $a_{PS[\lambda]}$ spectra across a chl gradient (Bricaud et al. 1995; Barlow et al. 2002).

Concepts pertaining to the *in situ* spectra as an ecological driver of phytoplankton community composition have recently been proposed (Stomp et al. 2004, 2007, 2007B). The relevance of these studies to this chapter are now discussed. The attenuation (scatter plus absorbance) of PAR through a water column is a function of three components, the attenuation due to water ($k_{W[\lambda]}$), phytoplankton ($k_{PH[\lambda]}$) and other particulate and dissolved material ($k_{BG[\lambda]}$) (Kirk 1994). While $k_{W[\lambda]}$ can be assumed constant, $k_{BG[\lambda]}$ varies in magnitude but its spectral shape is relatively conserved and decreases exponentially along an increasing k_{PAR} gradient (Kirk 1994). Stomp et al. (2007) cleverly investigated changes in the *in situ* spectral environment by simulating a range of particulate and dissolved material concentrations (the magnitude of $k_{BG[\lambda]}$) in the absence of phytoplankton absorption. Figure 3.6 shows a reproduction of this analysis, the input data of $k_{W[\lambda]}$ and $k_{BG[\lambda]}$ are shown in Panel A and the resultant euphotic depth spectra in Panel B (calculated using Eqn 1 and 2 from Stomp et al. 2007). This analysis clearly shows that as k_{BG} (and hence k_{PAR}) increase, spectral energy at depth is progressively red-shifted and small shoulders in the absorption spectrum of k_W (shown as dashed lines) create large gaps in the *in situ* spectral environment. Between these gaps are a series of distinct spectral niches that match the absorption of photosynthetic pigments (Figure 1.1). Figure 3.6C extends the approach of Stomp et al. (2007) and averages the *in situ* spectra over their respective euphotic depths to simulate the mean light climate of a circulating cell. This theoretical analysis shows that though the spectra are more broad, spectral niches are still evident.

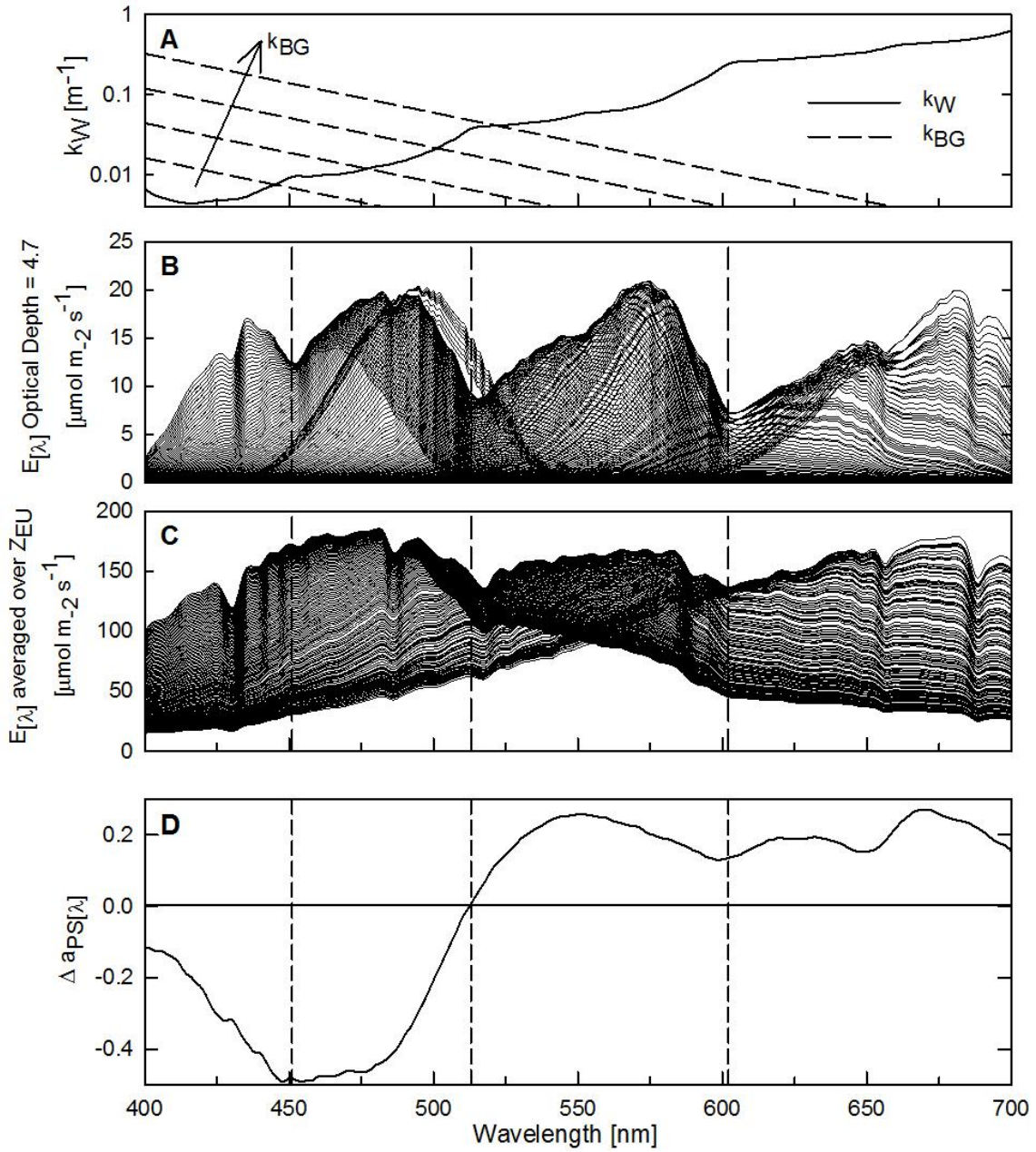

Figure 3.7: A) Absorption spectrum of pure water (k_W) and an increasing gradient of background (k_{BG}) attenuation, vertical dashed lines correspond to shoulders in k_W spectrum. B) 120 euphotic depth spectra where k_{BG} at a reference wavelength of 440 nm varies from 0.007 to 10 m^{-1} (A and B Modified from Stomp et al. 2007). C) 120 spectra as described for B but the spectra are averaged over the euphotic depth. D) Wavelength specific differences is $a_{PS[\lambda]}$ between 1 and 10 µg chl *a*.L^{-1} predicted from Bricuad et al. (1995), $a_{PS[\lambda]}$ spectra were normalized to their mean to emphasize changes in spectral quality and not quantity.

To what degree are these spectral niches filled and how closely do $a_{PS[\lambda]}$ spectra match attendant *in situ* spectra? *In situ* spectral shifts are consistent with relative abundances of accessory pigments along increasing optical gradients. Photoprotectant carotenoids (PPC) have peak absorption below 490 nm, and the ratio of PPC:chl *a* across diverse marine environments significantly increases towards optically clear water (Babin et al. 1996, Barlow et al. 2002, Bricaud et al. 2004). The absorption spectra of photosynthetic carotenoids (PSC) are centred around 500 nm, and though the ratio of PSC:chl *a* is variable in marine environments the highest values are often found in mesotrophic environments where the underwater spectra is relatively enriched at 500 nm (Bricaud et al. 2004). The absorption spectrum of phycoerythrin occurs at smaller wavelengths than phycocyanin, the ratio of phycoerythrin:phycocyanin generally declines along increasing chl *a* and optical gradients in oceans (Stomp et al. 2007B) and lakes (Voros et al. 1998) consistent with a red-shifted spectrum along similar gradients. The model of Stomp et al. (2007) has not been thoroughly tested against $a_{PS[\lambda]}$ spectra. As shown in Figure 3.7D, the relative spectral changes between $a_{PS[\lambda]}$ at 1 and 10 ug chl *a*.L^{-1} as predicted using the equations of Bricaud et al (1995) are broadly consistent with the model of Stomp et al. (2007). As chl (and hence k_{PAR}) increases, absorption in the blue spectrum is decreased relative to absorption at longer wavelengths. Chapter 4 further explores how $a_{PS[\lambda]}$ spectra match attendant *in situ* spectra in Lake Erie.

3.4.2: Interpretation of *in vitro* photosynthetic rates requires caution

Any study that examines *in vitro* photosynthetic rates across chl *a* or k_{PAR} gradients (i.e. Table 3.1) without measuring attendant $a_{PS[\lambda]}$ spectra likely introduces significant but predictable errors in estimates of light-limited photosynthetic rates (α) and as areal phytoplankton production (ΣPP). Most *in vitro* light sources are red-shifted as the majority of PAR emitted

from these lamps occurs above 550 nm (Markager and Vincent 2001). Consequently, *in vitro* measurements of α are artificially reduced in oligotrophic environments as phytoplankton communities from these environments generally have relatively low absorption in the red spectrum relative to mesotrophic and eutrophic phytoplankton communities (Figure 3.4). The magnitude of the error introduced in measurements of α increases with the greater proportion of *in vitro* PAR emitted above 550 nm. Consequently the spectra of high-pressure sodium vapour lamps and other metal halide lamps (Markager and Vincent 2001) introduce greater errors in α across a chl *a* gradient than flatter spectra such as tungsten halogen lamps (Figure 3.4).

Carignan et al. (2000) measured *in vitro* photosynthetic rates using a metal halide lamp from a set of 12 oligotrophic and mesotrophic lakes. Their study explicitly linked the summer metabolic balance (the ratio of gross photosynthesis to community respiration) to measured PE parameters and demonstrated that contrary to previous studies (Del Giorgio and Peters 1994), photosynthesis exceeds community respiration in most Canadian shield lakes. Surprisingly, this significant finding is despite the fact that photosynthetic rates were performed *in vitro* using a metal halide lamp and so are likely underestimated, especially in many of the optically clearer lakes of their study (Carignan et al. 2000). The *in vitro* light source used by Del Giorgio and Peters (1994) is not stated, but the findings of this chapter call into question the assertion that community respiration exceeds photosynthesis in oligotrophic environments (Duarte and Agusti 1998).

3.4.3: Interpreting Historic ΣPP Measurements in Lake Erie

The transformation of *in vitro* ΣPP measurements into spectrally resolved *in situ* measurements for Lake Erie's historical datasets reveal some interesting trends. Overall seasonal areal phytoplankton production (SAPP) has decreased between the 1970s and early 1990s,

consistent with reduced phosphorus loadings through the GLWQA, though this reduction is only half of originally reported (Millard et al. 1999). Since the invasion and proliferation of *Dreissena* mussels throughout most of Lake Erie there have been notable decreases in water clarity and chl *a* in Lake Erie (Barbiero and Tuchman 2004), raising concerns that presumed attendant decreases in SAPP may no longer be able to support historic levels of secondary production (Johannson et al. 2000). Despite the 2005 dataset reporting the lowest mean lakewide k_{PAR} and chl *a* values, SAPP has not significantly changed between 1990 and 2005 (Table 3.1) suggesting that *Dreissena* mussels have not impacted SAPP in Lake Erie's offshore waters.

Figure 3.8 documents average basin production efficiency (SAPP* = SAPP normalized to chl *a*) as a function of chl *a* for the major ΣPP surveys in Lake Erie. Production efficiency is an insightful parameter, as calculated here it represents the basinwide mean efficiency in which chl *a* is used to assimilate carbon over the growing season. A highly significant relationship negative relationship between SAPP* and chl *a* using all historic data (stats) demonstrates that as chl *a* has declined in Lake Erie, whether through reductions in P loading or dreissenid mediated re-engineering of nutrient pathways (Hecky et al. 2004), SAPP* increases. This trend can be seen spatially across basins, with the eutrophic and meso-oligotrophic western and eastern basins respectively having the lowest and highest production efficiency across all studies. Figure 3.8 clearly demonstrates that historic chl *a* decreases in Lake Erie have not caused comparable decreases in SAPP.

The calculated SAPP 16% decrease of between 1970 and 1990 should be taken with caution, owing to the aforementioned changes in ^{14}C that likely underestimates ΣPP relative to all other surveys. Similarly, the longer incubation times performed by Millard et al. (1999) relative to the two more recent surveys may also yield artificially lower photosynthetic

rates due to the assimilation of respired and labelled ^{14}C (Harris and Piccinin 1977). Variable station selection between surveys also affects estimated values of SAPP: If two eutrophic western basin stations at the mouths of the Maumee and Sandusky rivers sampled in 2005 were omitted from the above analysis (as they were not sampled in other historic surveys), mean lakewide SAPP in 2005 is reduced by 7%. Furthermore, it must be stressed that the above analysis is valid for epilimnetic production only and as shown in the next chapter sub epilimnetic production is quantifiably important in Lake Erie. These and other potential errors are just some of the issues that arise when traditional methodologies are used to assess longterm changes in phytoplankton production. Data from this and the following chapter further build an argument that bio-optical methodologies be immediately implemented in the various water quality monitoring programs in the Laurentain Great Lakes.

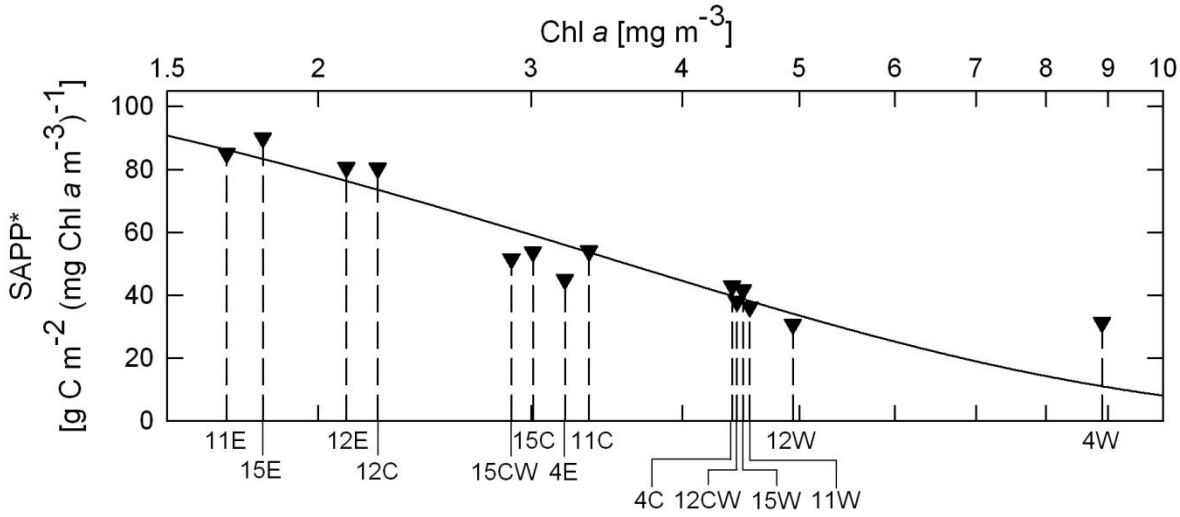

Figure 3.8: The relationship between basin averaged production efficiency (SAPP*) and chl *a* for major ΣPP surveys in Lake Erie. Labels along the x-axis refer to the study number and basin given in Table 3.2. Chl *a* values for Glooshenko et al. (1974, study 4) are from Vollenweider et al. (1974).

3.5 Conclusions

This chapter has identified how predictable differences between *in situ* and *in vitro* spectral irradiance can produce disparate estimates of spectrally-resolved (*in situ*) and unresolved (*in vitro*) ΣPP. Along a decreasing k_{PAR} gradient the underwater spectra becomes progressively blue-shifted and constrained within narrower wavebands. The spectral shift in the underwater spectra along a k_{PAR} gradient creates a series of *in situ* spectral niches that overlap with the absorption spectra of the various phytoplankton pigments. Data from Lake Erie and marine environments suggests that the phytoplankton community composition is in part shaped by the prevailing *in situ* spectra, as pigment composition and attendant photosynthetic absorption spectra predictably co-vary with *in situ* spectra. An empirical model developed in this chapter exploits the predictable changes in the *in situ* and photosynthetic absorption spectra and demonstrates that, for two commonly employed *in vitro* lamps, *in vitro* based ΣPP measurements increasingly underestimate *in situ* ΣPP as water clarity increases. The spectral energies of the *in vitro* lamps investigated in this study are comparatively reduced in the blue spectrum, and thus poorly characterize oligotrophic environments where the *in situ* and photosynthetic absorption spectra are maximal.

Lake Erie is the most eutrophic of the Laurentian Great Lakes so the disparities between *in situ* and *in vitro* estimates of ΣPP are presumably small relative to the other Laurentian Great Lakes. Yet applying spectral correction factors to historic surveys in Lake Erie have shown that *in vitro* measurements can still substantially underestimate *in situ* ΣPP. By comparison the underestimation of *in situ* ΣPP from *in vitro* measurements in oligotrophic Lake Superior may be quite large, and in part explain substantial deficits in the lake's organic carbon budget where it

has been reported that ΣPP is approximately 10-fold lower than community respiration (Urban et al. 2005).

Chapter 4: Vertical Patterns of Phytoplankton Biomass and Photosynthesis in Freshwater Lakes

Section 4.1: Introduction

Chapter 2 devoloped a bio-optical model that derives gross oxygen evolution photosynthetic rates from *in situ* fluorescence measurements and validated the model against concurrent *in vitro* carbon assimilation measurements. This chapter applies the bio-optical model to *in situ* measurements throughout the water column to generate vertically resolved estimates of phytoplankton photosynthesis. Persistent vertical patterns of photosynthesis are identified across trophic and mixing gradients using an extensive set of measurements in Lake Erie, and subsequently compared to similar opportunistic measurements in Lake Superior and Georgian Bay. This is the first study to explicitly examine vertical patterns of photosynthesis in any freshwater lake using a spectrally-resolved high-resolution bio-optical approach.

Estimates of areal phytoplankton production (ΣPP) in freshwater bodies including the Laurentian Great Lakes have generally followed a consistent methodology and scaling approach that necessarily simplifies the vertical distribution of photosynthesis (for a review see Table 3.1). At the core of this approach, often a single discrete or integrated water sample is drawn from the epilimnion and incubated i*n vitro* to determine light-dependent changes in photosynthesis that are subsequently modeled with a photosynthetic-irradiance (PE) curve (Section 1.3, Figure 4.1A). This PE curve is then scaled to an *in situ* irradiance field defined by the exponential depth-dependent decrease in irradiance mathematically defined by the vertical attenuation of k_{PAR} (Figure 4.1B). When a single PE curve is scaled to the water column this approach implicitly assumes that 1) phytoplankton biomass and 2) light-dependent changes in photosynthetic efficiency are static through depth. The resultant vertical distribution of

photosynthesis stemming from the first two assumptions is therefore defined by the shape of the PE curve transposed to the *in situ* light environment.

A second approach to measure ΣPP, that forgoes *in vitro* incubations and its attendant assumptions of *in situ* scaling, involves suspending bottles at fixed depths throughout the water column and monitoring changes in oxygen evolution or carbon assimilation after a specified period of time (4-24 hours, Table 3.1). Though resultant vertical distributions of photosynthesis from i*n situ* incubations have challenged aforementioned scaling assumptions (Moll and Stoermer 1982), such measurements are largely impractical (Fee 1978), and constraining phytoplankton at fixed depths may augment photoinhibition in near surface samples that would otherwise be mixing (Oliver et al. 2003; Hiriart-Baer and Smith 2004).

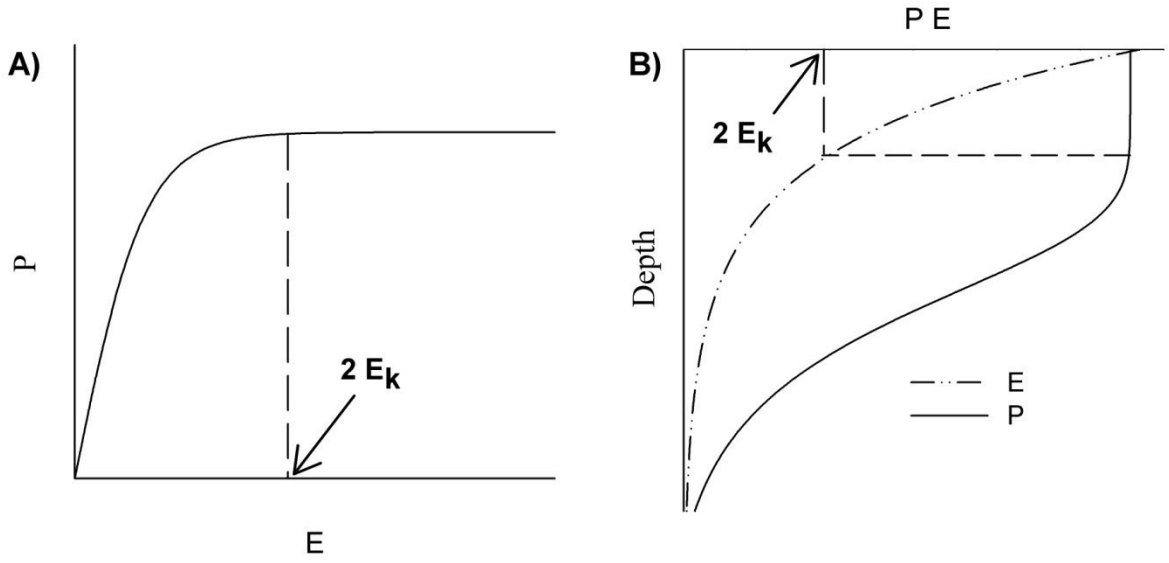

Figure 4.1: A) PE curve derived *in vitro* and fitted to B) *in situ* irradiance (E) to yield the depth dependent distribution of photosynthesis (P).

This chapter investigates how persistent vertical patterns of *in situ* photosynthesis deviate from nominally scaled *in vitro* measurements and identifies when the latter assumptions yield erroneous estimates of ΣPP. Two lines of evidence suggest that, when *in vitro* measurements are

drawn from the epilimnion only, ΣPP may be subsequently underestimated in the Laurentian Great Lakes. First, during periods of stratification, sub-epilimnetic deep chlorophyll maxima (DCM) have been widely reported in Lakes Superior (Auer and Bub 2004), Michigan (Fahnenstiel and Scavia 1987), Huron (Fahnenstiel et al. 1989), Ontario (Munawar et al. 1974) and Erie (Barbiero and Tuchman 2001). Despite this widely reported phenomena, there are some in the freshwater scientific community who argue that the light available to DCMs is sufficiently small such that any phytoplankton production originating from this layer is dwarfed by epilimnetic production (personal observation). A second line of evidence is that in the few comparable instances where epilimnetic and sub-epilimnetic photosynthetic rates have been measured, sub-epilimnetic populations often have higher biomass-specific photosynthetic rates relative to epilimnetic populations (Smith et al. 2005). These two factors are now examined in greater detail below.

Section 4.1.1: The Vertical Distribution of Phytoplankton Biomass.

The vertical distribution of phytoplankton biomass has been frequently studied through microscopic cell enumeration, beam attenuation, and chl *a* biomass (extracted or fluorescence). This distribution is in part governed by the strength, periodicity and vertical extent of physical mixing and its interplay with the intrinsic buoyancy (either positive or negative) of non-motile phytoplankton (Reynolds 2006). Thermal stratification in lakes and oceans constrains passive mixing of non-motile phytoplankton and nutrients into discrete layers and, in non-eutrophic aquatic ecosystems, often leads to disparate vertical gradients in light and nutrients (Wetzel 2001). The vertical distribution of phytoplankton can be further altered by depth-dependent loss processes including herbivorous grazing (Lampert and Taylor 1985), but generally biomass maxima are thought to coincide with the depth(s) where the supply of resources (light and

nutrients) are optimally balanced (Christensen et al. 1995). In oligotrophic and mesotrophic aquatic ecosystems, the most conspicuous vertical pattern during periods of stratification is the presence a DCM. DCMs have been observed in small and large lakes (Fee 1976; Moll and Stoermer 1982; Abbott et al. 1984) and in the oceans (Cullen 1982; Takahashi et al. 1989).

Moll and Stoermer (1982) extended the phytoplankton succession paradigm of a temperate dimictic lake to include general observations of DCMs. Recreated in Figure 4.1, Panel A shows the seasonal distribution of epilimnetic phytoplankton biomass and Panel B shows the summer vertical distribution of chlorophyll in three lakes that span a trophic gradient. In Moll and Stoermer's model, deep chlorophyll maxima (DCMs) form shortly after the onset of seasonal stratification in oligotrophic and mesotrophic lakes. Following the traditional succession model, a spring epilimnetic bloom of negatively buoyant diatoms forms in many lakes when nutrients are sufficient and the water column well mixed. At the onset of thermal stratification the vertical extent of surface mixing is reduced and subsequent sedimentation of the dominant diatoms depletes epilimnetic nutrient concentrations. At this time a DCM forms consisting primarily of sedimenting epilimnetic diatoms, where relatively higher nutrient concentrations may alleviate nutrient deficiency and lessen sinking rates (Titman and Kilham 1976). Moll and Stoermer (1982) observe that the DCM persists throughout stratification and distinct metalimnetic phytoplankton communities may often dominate until thermal stratification breaks down when deep mixing entrains phytoplankton throughout the water column. DCMs are rarely observed in eutrophic lakes where persistent high levels of epilimnetic nutrients maintain a large standing crop of surface phytoplankton that effectively shades out any deeper populations.

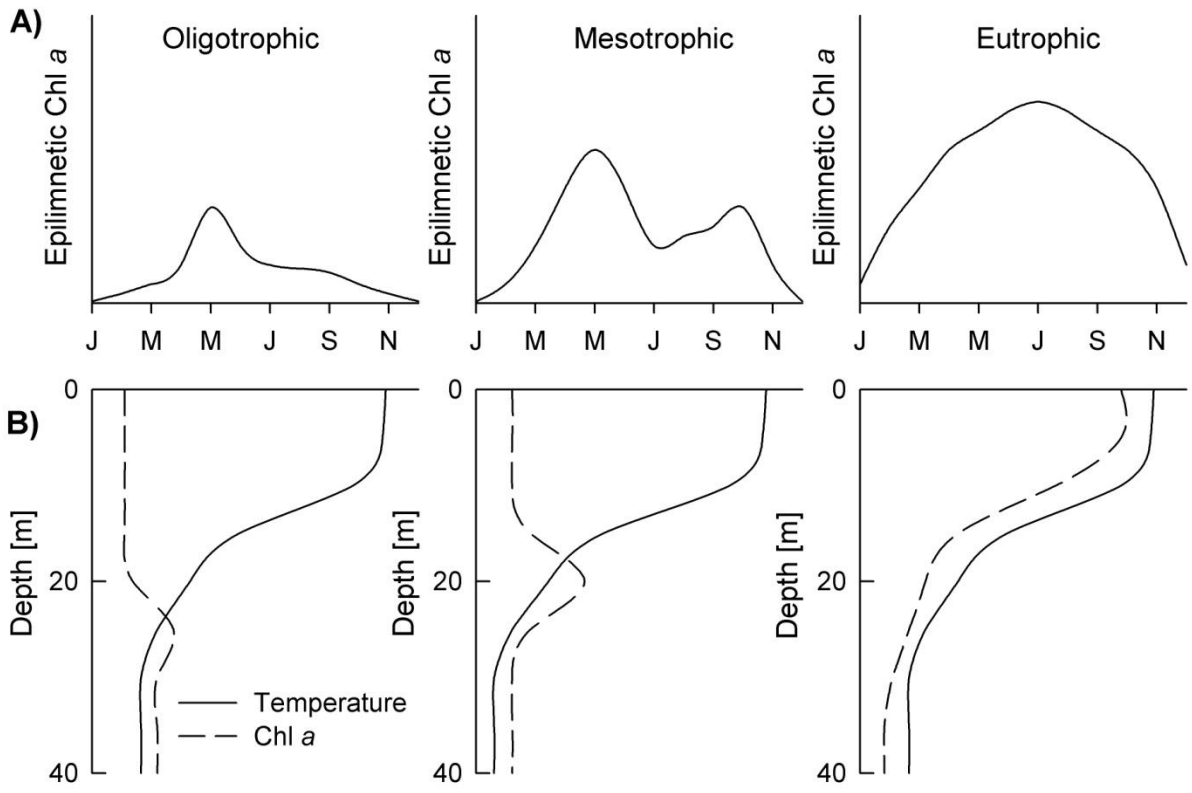

Figure 4.2: A) Idealized annual distribution of epilimnetic chlorophyll a (chl *a*) in an oligotrophic, mesotrophic and eutrophic lake. B) The corresponding vertical distribution of temperature and chl *a* during the summer for each type of lake. Modified from Moll and Stoermer (1982).

Section 4.1.2: The vertical distribution of phytoplankton photosynthetic efficiency

Three processes that can augment light-limited oxygenic photosynthesis are considered here: Increases in cellular pigment concentrations in response to changes in spectral quantity (photoadaptation), changes in pigment composition in response to changes in spectral composition (chromatic adaptation), and increases in the quantum efficiency of oxygenic photosynthesis.

Photoadaptation – As irradiance decreases, the chlorophyll content of phytoplankton cells can increase five to ten-fold (Falkowski 1980). This strategy increases the overall light-

harvesting capacity of phytoplankton though the effect is non-linear and yields diminishing returns: The accumulation of successive pigments progressively causes self-shading of thylakoid membranes, a process referred to as the 'package effect' (Falkowksi and Raven 2007). Indeed observation of DCMs may be solely due to cellular increases in chlorophyll concentration independent of any vertical phytoplankton biomass gradients (Cullen 1982). Using particulate carbon (C) as a proxy for phytoplankton biomass, Barbiero and Tuchman (2001) have shown that significantly higher chl *a* concentrations in Lake Huron's DCM did not correspond with any vertical gradients in particulate carbon. The same study showed that chl *a*:C ratios of DCMs in the Laurentian Great Lakes were on average twice a s high as epilimnetic values, thus accounting for much of the presence of DCMs. If elevated chl *a*:C ratios are a persistent feature in the Laurentian Great Lakes, then reported elevated sub-epilimnetic light-limited chl *a* normalized photosynthetic rates (α^*) are in fact more remarkable: Given α^* and chl a:C values ~1.5 and 2 fold higher in the DCM (Smith et al. 2005; Barbiero and Tuchman 2001), then light limited photosynthesis per unit carbon is 3-fold higher in the DCM.

Chromatic adaptation. The spectral quality of light as a selective force shaping phytoplankton communities is receiving increasing attention (Stomp et al. 2004). In high-light environments, chromatic adaptation may be manifested in the production of accessory pigments that dissipate excess excitation energy as heat to minimize photoinhibition (Demmig-Adams and Adams 1992), whereas in low-light environments such as DCMs the production of accessory pigments serve to maximize light harvesting by matching spectral absorption with an increasingly constricted light field. In freshwater lakes, spectrally resolved measurements of photosynthesis are exceedingly rare (Markager and Vincent 2001), so little is known of its quantitative importance. This chapter focuses solely on the relationship between the spectral

quality of irradiance as related to the spectral shape of a_{PSII} and its direct quantitative influence on photosynthetic rates through space and time. In the Laurentian Great Lakes, the seasonal evolution of distinct metalimnetic communities indirectly suggest that chromatic adaptation may be important in these environments (Moll and Stoermer 1982). In Lake Erie's central basin, phycoerythrin-rich cyanobacteria were consistently detected in the summer from 2002 to 2005 with higher abundances in the metalimnion and hypolimnion relative to the epilimnion (Wilhelm et al. 2006). Diurnal changes in dissolved oxygen concentrations at the depths of peak abundance demonstrate that not only are these cyanobacteria photosynthetically active, but may even delay hypolimnetic deoxygenation in the central basin.

Quantum efficiency of photosynthesis. Chapter 2 discusses how alternative electron sinks reduce the apparent quantum efficiency of photosynthesis in high light environments and ultimately impede the ability of the bio-optical model used here to effectively model light-saturated photosynthesis. Instead, the model estimates the quantum efficiency of photosynthesis in the absence of photo-physiological reductions to estimate light-limited rates of photosynthesis that in turn are used to estimate light-saturated photosynthetic rates using the parameter E_K. This distinction is repeated here as the bulk of studies examining vertical patterns of the quantum efficiency of photosynthesis focus on light-mediated reductions through the water column. Moore et al. (2005) present three night time FRRF profiles taken in the North Atlantic during a spring bloom. 2 of the 3 profiles presented have a distinct metalimnetic peak in F_V/F_M that in one profile corresponds with a DCM, however both F_V/F_M peaks are only ~15% higher than the epilimnetic minima. Given the overall high values of F_Q'/F_M' presented in Chapter 2 that are consistent with the concept of balanced growth (Suggett et al. 2009), it seems unlikely that vertical gradients in the quantum efficiency of photosynthesis are significant drivers of vertical

patterns of photosynthesis.

Section 4.2: Materials and Methods

Study Site and Summary. Four spatial surveys were conducted in Lake Erie in 2005 (May 2-5th, June 7-11th, July 18-21st, September 6-9th). Stations west of 80°W were sampled only in the June and September cruises. Raw data for this chapter is given in Appendix A and Appendix B lists the locations of all sampled stations. Spatial analysis in this chapter is performed by categorizing data into one of four basins shown in Figure 4.3. Consistent with other spatial studies (eg Smith et al. 2005), the central basin is subdivided into a central-west and central-east basin (the latter herein simply referred to as the central basin). The delineation between central-west and central basin is based on the mean summer circulation pattern in Lake Erie where the two regions are separated by opposite flowing gyres. Vertical patterns of photosynthesis are supplemented by less intensive surveys in Georgian Bay (Colpoy's Bay), and Lake Superior.

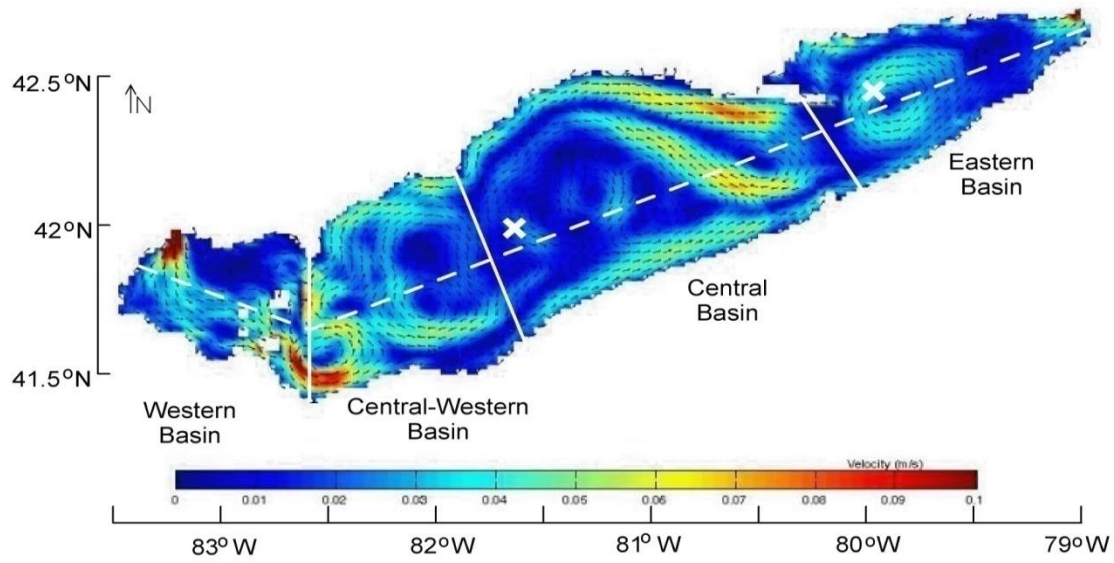

Figure 4.3: Mean summer circulation in Lake Erie (Leon et al. 2005) used in conjunction with bathymetry (Figure 2.2) to delineate basins (solid white lines). White X's correspond to locations of two thermistor strings (Figure 3.3) and dashed white line corresponds to location of longitudinal curtain used throughout this chapter.

Physical methods – CTD profiles (Seabird 911, Bellevue, Washington) at each station measured water temperature through depth with a vertical resolution of ~ 0.10 m. Delineation of metalimnetic and hypolimnetic depths was based on a numerical analysis of two thermistor strings located in the central (16 depths of measurement ranging from 1.0 to 23.5 m) and east basin (14 depths of measurement ranging from 1.0 to 52.5 m) of Lake Erie (Figure 4.2). Temperature data from thermistor strings and CTD profiles were binned into 0.5 m intervals and converted to density following Zeebe and Wolf-Gladrow (2001). The seasonal thermocline was defined as the depth(s) where the density gradient between 0.5 m bins exceeded 0.2 $kg.m^{-3}$. Metalimnetic and hypolimnetic depths were then delineated as the respective upper and lower bounds of the seasonal thermocline as shown in Figure 4.4. At some stations, particularly the shallow west basin of Lake Erie, density gradients were often diffuse through depth and despite >5°C temperature changes through the water column density gradients between 0.5 m bins did not exceed 0.2 $kg.m^{-3}$. When the above procedure did not yield thermal strata, a second recursive model was used: Using the density at 2.5 m as a reference (to minimize any diurnal heating effect), if the density beneath 2.5 m exceeded 0.2 $kg.m^{-3}$ this depth was taken as the metalimnion. Figure 4.4 documents the cumulative heat capacity (Q) of the water column at the two thermistor stations relative to day 125 (where Q is set to 0). Following Eqn 4.1, Q is calculated as the product of the water column mass (m = density and volume of water), the specific heat capacity of water (c, 4186 J kg^{-1} K^{-1}) and the change in water column (ΔT) temperature measured at daily intervals.

Optical methods - PAR measurements through depth were performed with scaler quantum sensors (LI-COR, Omaha, Nebraska) attached to either the CTD or bio-optical

instrumentation. The vertical attenuation of PAR (k_{PAR}) was calculated using the logarithmic slope of PAR through depth. Where multiple thermal strata were present, then strata specific k_{PAR} values were calculated. k_{PAR} was linearly related to measurements of beam attenuation at 650 nm (Wetlabs, Philomath, Oregon; $r^2 = 0.89$, $n = 59$, $p < 0.01$), and this relationship was used to estimate k_{PAR} from beam attenuation in the absence of reliable measurements (e.g. nocturnal profiles).

Water chemistry – Water for nutrient and chl *a* analysis was collected at discrete depths using a 1-m long Niskin samplers. Triplicate measurements of chl *a* were performed by passing 200 ml of water through 47 mm Whatman GF/F filters and immediately frozen. In the lab, filters were immersed in 20 ml of 90% acetone and passively extracted at 4°C for 24 hours. Extracts were quantified fluorometrically before and after acidification on a 10-AU fluorometer (Turner Design, Sunnyvale, California) calibrated with pure chl *a* standard (Sigma) to determine concentrations of chl a *a*nd pheophytin *a* respectively (Holm-Hansen et al. 1965). Nutrient data was collected under the international field year of Lake Erie (IFYLE) project. Briefly, for total phosphorus (TP), 50 ml of lakewater was measured into acid cleaned 150mm Pyrex test tubes. Soluble reactive phosphorus (SRP), ammonium (NH_4) and silica (SiO_2) were first passed through 0.2 μm nylon syringe units and 10 ml were dispensed into 14 ml Falcon tubes. SRP and NH_4 were frozen until analysis, and TP and SiO_2 were refrigerated until analysis. All nutrient analyses were conducted using standard automated colorimetric procedures on a Technicon AutoAnalyzer II following the details of Davis and Simmons (1979). Briefly, TP, SRP and SiO_2 were all measured using the molybdate ascorbic acid method following persulphate digestion while NH_4 was analyzed using the phenol method.

Photosynthetic rates: Methodology – Following section 2.3.4, the parameterization of the

light-limited photosynthetic rate (α) in Eqn 4.1 is the product of PSII photochemical efficiency in actinic irradiance normalized to its empirical maximum ($F_Q'/F_M' \bullet (0.65)^{-1}$), PSII absorption ($a_{PSII}$) as described above and a constant 43.2 representing unit conversion. As described in Section 2.2, a data filter was applied to F_Q'/F_M' to minimize photo-physiological reductions of Fq'/F_M' above 50 $\mu mol.m^{-2}.s^{-1}$. In this chapter a_{PSII} is derived solely from *in situ* spectral fluorometric measurements scaled to photosynthetic pigment absorption spectra (a_{PS}) as described in Section 2.3.3. Fluorometrically derived values of a_{PSII} are chosen here as they provide highly resolved vertical measurements. The maximum photosynthetic rate (P_M) shown in Eqn 4.2 is calculated as the product of α and E_K. Eqn 4.3 shows the derivation of photosynthetic rates (P) following the formula of Jassby and Platt (1976), substituting Eqn 4.2 into Eqn 4.3 recasts Jassby and Platt (1976) as a function of α and E_K only (Eqn 4.4) that is used throughout this chapter to calculate P. In Eqn 4.4, $E_{[Z,\lambda]}$ is calculated using Eqn 4.5 where E_0 is set to the mean PAR measured from the central basin meteorological buoy averaged over a 10 day window centered around each of the four cruises (E_K = 415, 449, 440 and 374 $\mu mol.m^{-2}.s^{-1}$ in May, June, July and September respectively). Also, based on the limited variability of E_K within a given cruise (Section 2.3.5), E_K was held constant in Eqn 4.4 where E_K = 75, 125, 125 or 100 $\mu mol.m^{-2}.s^{-1}$ for May, June, July and September respectively.

[Eqn 4.1] $\alpha_{[Z,\lambda]} = F_Q'/F_M'_{[Z]} \bullet (0.65)^{-1} \bullet a_{PSII\,[Z,\lambda]} \bullet 43.2$

[Eqn 4.2] $P_M = \alpha_{[Z,\lambda]} \bullet E_K$

[Eqn 4.3] $P_{[Z,\lambda]} = P_M \bullet \tanh [E_{Z[Z,\lambda]} \bullet \alpha_{[Z,\lambda]} \bullet (P_M)^{-1}]$

[Eqn 4.4] $P_{[Z,\lambda]} = \alpha_{[Z,\lambda]} \bullet E_K \tanh [E_{[Z,\lambda]} \bullet (E_K)^{-1}]$

[Eqn 4.5] $E_{[Z,\lambda]} = E_{0[\lambda]} \bullet \exp[-k_{PAR[\lambda]} \bullet z]$

Photosynthetic rates: Scaling – Three scaling methods are used to extrapolate P (Eqn 4.4) through the water column that deviate in two important ways. First, two different methods are used to populate Eqn 4.1 with bio-optical measurements. One scaling method uses vertically resolved (Z for depth) measurements of F_Q'/F_M' and a_{PSII} binned into 0.25 m intervals so measurements are denoted with $P_{[Z]}$, while a second scaling method assumes that an integrated sample (INT) of the epilimnion has been incubated *in vitro* such that F_Q'/F_M' and a_{PSII} in Eqn 4.1 are set to their respective epilimnetic averages so measurements are denoted with $P_{[INT]}$. The second deviation is is whether or not P has been spectrally resolved to the *in situ* environment. For spectrally resolved measurements (λ), spectral correction factors (SCF) that scale a_{PSII} measurements to the *in situ* light spectra are derived using Eqn 4.6 where $F_{Z[\lambda]}$ is the wavelength-specific spectral fluorescence (450, 525, 570, 590, 610 nm) and $E_{Z[\lambda]}$ is the *in situ* irradiance at the corresponding wavelength at depth z. For non-spectrally resolved measurements, photosynthetic rates are multiplied by Eqn 4.7 that scales the a_{PSII} to an *in vitro* high pressure sodium vapour lamp whose spectrum is shown in Figure 3.3 (SCF_{SV}). As described in Section 2.2, both SCF and SCF_{SV} are multiplied by 1.07 to account for the mean bias in deriving the SCF using only 5 wavelengths. The three scaling methods are summarized in Eqns 4.8 – 4.10.

[Eqn 4.6] $SCF = \Sigma[F_{Z[\lambda]} \bullet E_{Z[\lambda]}] \bullet \Sigma[E_{Z[\lambda]}]^{-1} \bullet [\Sigma[F_{Z[\lambda]}] \bullet 5^{-1}]^{-1} \bullet 1.07$

[Eqn 4.7] $SCF_{SV} = \Sigma[F_{Z[\lambda]} \bullet E_{SV[\lambda]}] \bullet \Sigma[E_{SV[\lambda]}]^{-1} \bullet (\Sigma[F_{Z[\lambda]} \bullet E_{Z[\lambda]}] \bullet \Sigma[E_{Z[\lambda]}]^{-1})^{-1} \bullet 1.07$

[Eqn 4.8] $P_{[Z,\lambda]} = [F_Q'/F_M'_{[Z]} \bullet (0.65)^{-1} \bullet a_{PSII\,[Z,\lambda]} \bullet SCF \bullet 43.2] \bullet E_K \tanh [E_{[Z,\lambda]} \bullet (E_K)^{-1}]$

[Eqn 4.9] $P_{[INT,\lambda]} = [F_Q'/F_M'_{[INT]} \bullet (0.65)^{-1} \bullet a_{PSII\,[INT,\lambda]} \bullet SCF \bullet 43.2] \bullet E_K \tanh [E_{[Z,\lambda]} \bullet (E_K)^{-1}]$

[Eqn 4.10] $P_{[INT,SV]} = [F_Q'/F_M'_{[INT]} \bullet (0.65)^{-1} \bullet a_{PSII\,[INT,\lambda]} \bullet SCF_{SV} \bullet 43.2] \bullet E_K \tanh [E_{[Z,\lambda]} \bullet (E_K)^{-1}]$

Statistical and numerical methods – All statistics and numerical methods were performed using the package 'stats' in R (www.r-project.org) with the exception of Kruskal-Wallis tests were derived from first principles following Zar (1996). Spatio-temporal analysis for Lake Erie data (k_{PAR}, chl *a*, nutrients, a_{PSII}, SCF, ΣPP) was performed by first separating data into cruises, and then averaged by basin (Figure 4.3) and thermal strata where present. When data for a given cruise and basin is divided by strata, mean water column values are estimated by weighting strata-specific values calculated as the percentage of volume the strata occupies within the given basin. For example, in June the epilimnion, metalimnion and hypolimnion represent 28.3%, 22.2% and 49.5% of total volume in the central-west basin so strata-specific measurements are multiplied by these numbers to determine the basin mean. Mean lakewide concentrations are also presented and calculated based on the areal extent of a basin in Eqn 4.7. With the exception of nutrient and chl *a* data culled from the IFYLE project, the east basin was not sampled in May and July. To satisfy Eqn 4.7 in these instances, east basin values were estimated as the product of central basin values and the mean gradient between central and east basins recorded in the June and September cruises. Statistically significant differences in spatial (across basins) and vertical (through strata) gradients of the various data were assessed using the Kruskal-Wallis test, as the majority of the data was not normally distributed.

[Eqn 4.7] Lakewide value = W • 0.135 + CW • 0.249 + C • 0.422 + E • 0.195

Section 4.3: Results

Section 4.3.1: Physical Properties

Lake Erie - Figure 4.4 documents the cumulative heat capacity, thermal structure and seasonal evolution of thermal stratification in Lake Erie's central and east basin. Meteorological and temperature measurements through depth commence at day of the year (day) 125 when the water columns at both stations are isothermal and cold (~4°C). From day 125, the central basin steadily gains heat until it reaches its seasonal temperature maxima by day 200. Progressive warming in the central basin induces a shallow (~5 m) and weak metalimnion ($\Delta\rho_{MAX}$ <0.2 kg.m^{-2}) by day 150, and within 25 days the metalimnion strengthens and descends to 11 – 15 m where it remains for most the stratified season. Between days 150 and 240 epilimnetic and metalimnetic temperatures statistically co-vary (ancova, $p < 0.05$), and the metalimnion is on average 6°C cooler. On day 240 the metalimnion quickly deepens and the subsequent hypolimnetic constriction coincides with the onset of widespread hypolimnetic hypoxia in the central basin (Rao et al. 2008). By day 270 stratification breaks down in the central basin and the progressive cooling and sinking of surface waters maintains isothermy until the end of measurements at day 300.

Similar spatiotemporal patterns occur in the east basin with a few noted deviations: Between days 150 and 270 metalimnetic depths are approximately 1.5 m shallower in the east basin, perhaps because the mean wind speed over this period was 2.08 fold higher at the central basin station. Also, thermal stratification does not breakdown in the east basin at day 270, instead the metalimnion plunges to progressively deeper depths with distinct strata still present when the instrumentation was removed on day 300.

Long-term temperature and meteorological records were not available in the shallower

west basin, though extensive CTD profiling during each cruise provide some inferences. Between days 120-125, the west basin was isothermal and warm (~8-10°C) relative to the other basins. 20 of 25 profiles satisfied the criteria of a metalimnion used here during subsequent cruises centred around days 160 and 200, while only 6 of 16 profiles satisfied this criteria on a cruise centered around day 250. Regardless of the cruise, west basin metalimnetic depths were generally around 5 m.

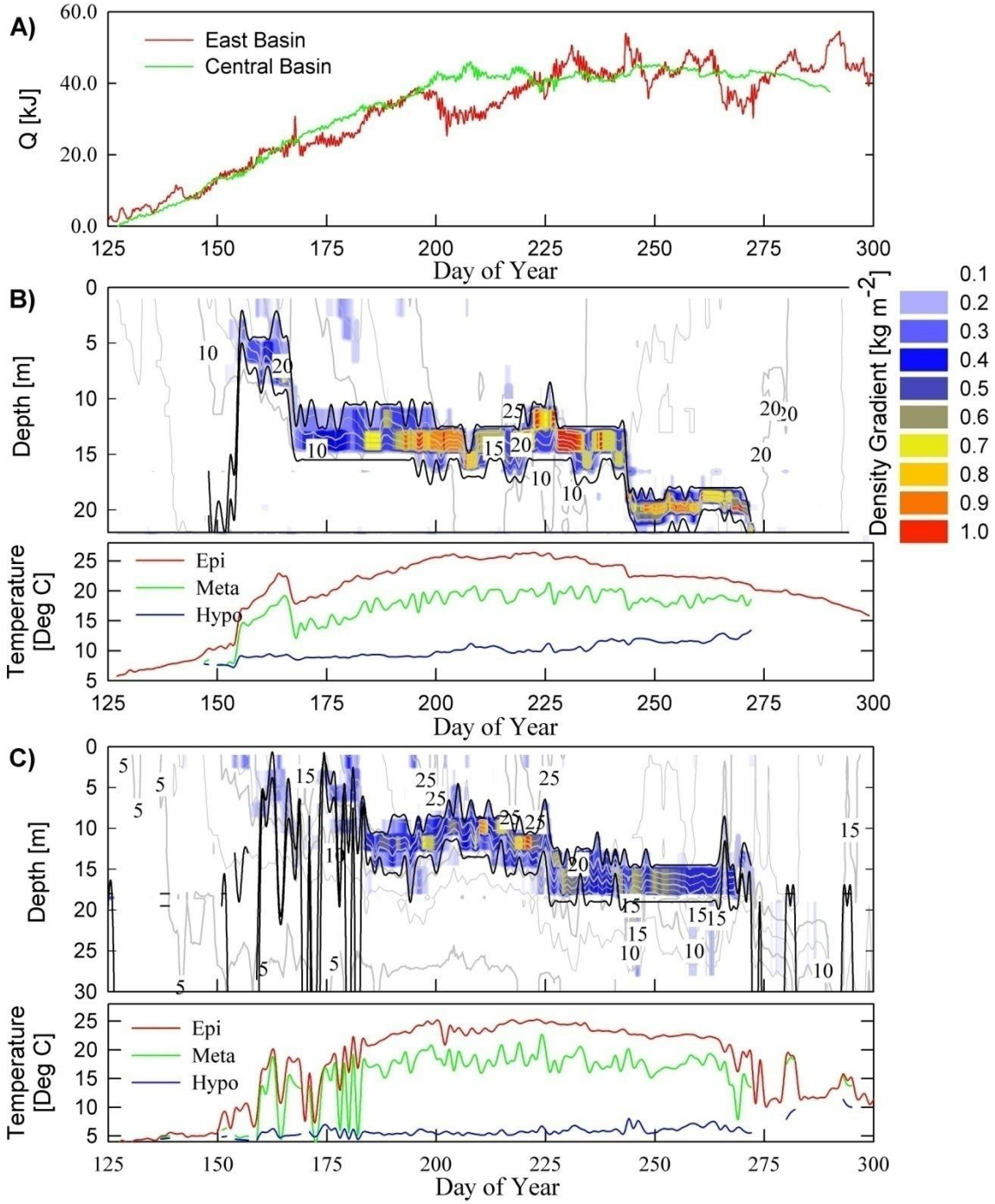

Figure 4.4: A) Cumulative changes in heat capacity (Q) in the central and east basin's of Lake Erie. B) Density gradient through depth in the central basin, solid lines demarcate the top and bottom of the metalimnion. The corresponding mean epilimnetic, metalimnetic and hypolimnetic water temperatures are given below. C) As described in B) but for the East basin.

Section 4.3.2: Optical Properties

Table 4.1 and Figure 4.5 summarize k_{PAR} for each basin and strata investigated in this study: At all times k_{PAR} was statistically highest (Kruskal-Wallis test, $p < 0.10$) in the west basin and generally declined across an eastward longitudinal gradient. Temporally, lakewide spatially weighted epilimnetic k_{PAR} values were lowest in June, similar in May and September and highest in July. Figure 4.5 shows the vertical distribution of optical depths (ζ) relative to lake morphometry and strata across the longitudinal gradient shown in Figure 4.3. The combination of a shallow seasonal thermocline and relatively transparent waters in June provided a well lit metalimnion with ζ values well above the often cited compensation depth of 1% surface irradiance ($\zeta = 4.6$; Fee 1980). Metalimnetic ζ exceeded 4.6 in most central and central-west basins stations in July, but by September the combination of higher epilimnetic k_{PAR} values and the downward displacement of the seasonal thermocline reduced metalimnetic ζ below 4.6.

Stated in Chapter 2, k_{PAR} co-varies with chl *a* though the relationship is not strong ($k_{PAR} = 0.18 \bullet \text{chl } a^{0.78}$; $r^2 = 0.51$, $n = 88$, $p < 0.05$) and is greater than the derived value for oceanic 'Case 1' waters (Morel 1988). The relationship between k_{PAR} and chl *a* varied temporally, as the slope of linear regressions between these two parameters within individual cruises were not statistically similar (ancova, $p<0.01$). Chl *a* per unit k_{PAR} increased over the sampling season and was significantly higher in September relative to all other cruises (Kruskal-Wallis test, $p <0.05$), also chl *a* per unit k_{PAR} in July was significantly higher than in May.

The optical properties of Lake Erie varied vertically during periods of stratification. In June, k_{PAR} increased with depth in the central-west basin, was vertically static in the central basin, while in the east basin epilimnetic and metalimnetic k_{PAR} measurements were significantly

higher than hypolimnetic measurements (Kruskal-Wallis test, $p < 0.10$). In July, k_{PAR} measurements the hypolimnion in the central and central west basin were significantly higher than epilimnetic measurements (Kruskal-Wallis test, $p < 0.10$). In September, epilimnetic k_{PAR} were statistically higher than metalimnetic values in the central-west and central basins (Kruskal-Wallis test, $p < 0.10$), and also decreased through depth in the east basin though this gradient was not statistically significant.

Table 4.1: Spatial and temporal patterns of k_{PAR} [m^{-1}] in Lake Erie. Mean values are presented with standard deviation and sample size for each basin and strata across four cruises. W, CW, C and E refer to the west, central-west, central and east basin respectively. Epi, M and H refer to the epilimnion, metalimnion and hypolimnion respectively. For values in Epi, superscripts refer to basin(s) with statistically significant smaller values (Kruskal-Wallis test, $p < 0.10$). For values in the M and H, superscripts refer to statistically significant intra-basin differences (Kruskal-Wallis test, $p < 0.10$). Italicized numbers are the spatially weighted mean values for basins and the lake.

Month		**Basin**			
Days	**Strata**	**W**	**CW**	**C**	**E**
May	Epi	0.70 (0.16,13) ^{CW,C}	0.42 (0.17,6)	0.39 (0.14,10)	
120-124	*Mean*	*Lake: 0.41*			
June	Epi	0.54 (0.31,16) ^{All}	0.26 (0.05,8)	0.25 (0.04,21)	0.22 (0.03,8) ^{H}
158-163	M		0.25 (0.04,8)	0.24 (0.04,21)	0.21 (0.04,8) ^{H}
	H		0.32 (0.07,8)	0.25 (0.06,21)	0.15 (0.05,8)
	Mean	*Lake: 0.28*	*0.29*	*0.25*	*0.17*
	Epi	0.90 (0.60, 7) ^{C}	0.39 (0.12,4)	0.35 (0.22,7)	
July	M		0.36 (0.02,3)	0.31 (0.16,6)	
200-203	H		0.56 (0.01,2) ^{Epi}	0.63 (0.51,5) $^{Epi, M}$	
	Mean	*Lake: 0.50*	*0.41*	*0.31*	
	Epi	0.78 (0.35,16) ^{All}	0.42 (0.12,8) ^{E,M}	0.35 (0.06,22) ^{M}	0.29 (0.04,8)
	M		0.23 (0.03,7)	0.25 (0.07,20)	0.26 (0.09,7)
	H		0.28 (0.04,7)	0.26 (0.11,20)	0.23 (0.10,7)
	Mean	*Lake: 0.40*	*0.41*	*0.34*	*0.27*

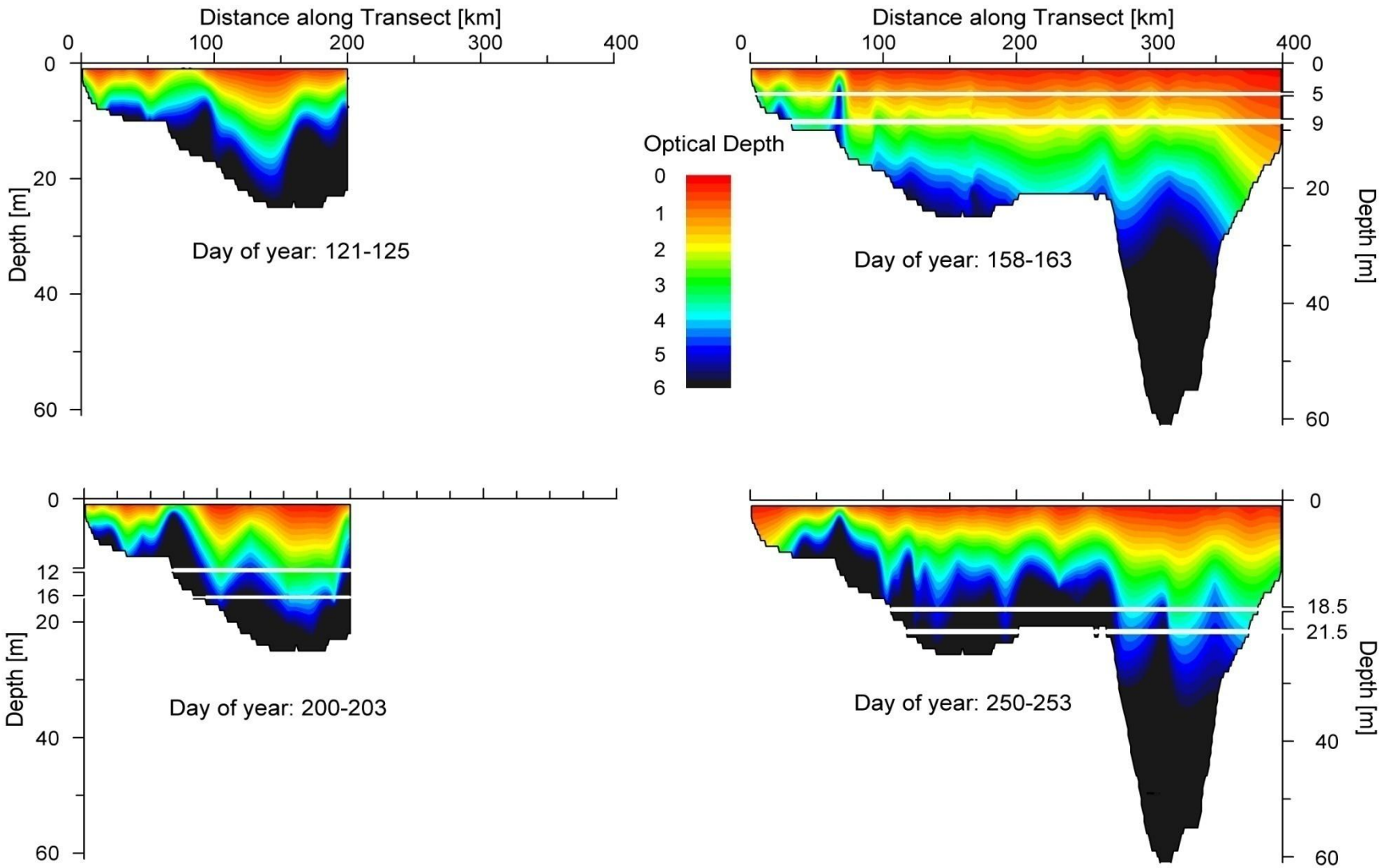

Figure 4.5: Longitudinal curtains (Figure 4.3) of optical depths during 4 surveys. Solid white lines represent the upper and lower limits of the mean metalimnetic and hypolimnetic depths for each cruise.

Section 4.3.3: Nutrients

Figures 4.6 to 4.9 and Tables 4.3 to 4.7 document spatial and temporal patterns of total phosphorus (TP), soluble reactive phosphorus (SRP), ammonium (NH_4) and silica (SiO_2) in Lake Erie. Nearshore (z_{MAX} < 10 m, n =37) stations are omitted from this analysis as the most nutrient measurements made under the IFYLE program are from the offshore (z_{MAX} > 10 m, n = 495). TP, SRP and NH_4 were all higher in the nearshore, though only the nearshore-offshore TP gradient was statistically significant (student t-test, $p < 0.05$). At each offshore station, one epilimnetic sample and a minimum of one sub-epilimnetic sample were taken, allowing for a descriptive examination of the vertical pattern of nutrients through space and time.

Temporal and Basin Patterns – Lakewide mean averages of TP and SRP exhibit a bi-modal seasonal pattern with high values in May that quickly decline in June and gradually increase to their observed maxima in September, consistent with previous studies (Guildford et al. 2005). Conversely, lakewide mean averages of NH_4 and SiO_2 are lowest in May and steadily increase through the season. The west basin of Lake Erie receives ~60% of the annual TP point source loading (Dolan and McGunagle 2005) so disparate spatial patterns of nutrient loadings yield longitudinal gradients in ambient concentrations. With the exception of NH_4 and SiO_2 in September, basin averaged nutrient concentrations were highest in the west basin throughout and most differences were statistically significant (Kruskal-Wallis test, $p < 0.10$). Across basins TP and SRP generally declined towards the east basin, this pattern was reflected in all strata. Relative to all other measured nutrients, NH_4 had the highest intra-basin variability and least statistically significant differences between basins. In May and June the highest mean NH_4 concentrations occurred in the west and east basin respectively, in July NH_4 in the west basin was statistically higher than all other basins (Kruskal-Wallis test, $p < 0.10$), and in September

NH_4 was highest in the central-west basin.

Vertical Patterns - Figures 4.6 to 4.9 and Tables 4.2 to 4.5 documents that statistically elevated sub-epilimnetic nutrient concentrations occurred at the onset of stratification in June, persisted through July, and were nutrient-specific in September. Statistically significant elevated sub-epilimnetic concentrations were most prevalent in the central-west and central basins. Vertical gradients were generally diminished in the relatively nutrient poor east basin, though this basin had the least intensive sampling. In June hypolimnetic TP, NH_4, and $Si0_2$ concentrations were significantly higher than epilimnetic concentrations in the central-west and central basins (Kruskal-Wallis test, $p < 0.10$). The metalimnion was also more nutrient enriched, but the differences between strata were not statistically significant. SRP concentrations in June were also elevated in the hypolimnion, but the differences were not statistically significant. By July hypolimnetic and metalimnetic TP and SiO_2 were significantly higher the metalimnion in the central-west and central basins (Kruskal-Wallis test, $p < 0.10$). Relative to the epilimnion in July, SRP was significantly larger in the central-west metalimnion and central basin hypolimnion, and NH_4 was significantly larger in the central basin metalimnion and hypolimnion as well as the east basin hypolimnion (Kruskal-Wallis test, $p < 0.10$). In September, the only statistically significant vertical gradients were elevated NH_4 and SiO_2 concentrations in the metalimnion and hypolimnions of the central basin (Kruskal-Wallis test, $p < 0.10$).

Table 4.2: Spatial and temporal patterns of TP [μg L^{-1}] in Lake Erie. Labels and superscripts are described in Table 4.1.

Month		**Basin**			
Days	**Strata**	**W**	**CW**	**C**	**E**
May	Epi	35.1 (35.9,39) ^{C,E}	10.8 (4.5,18) ^{C,E}	8.6 (10.2,45)	5.6 (0.8,11)
130-135	*Mean*	*Lake: 11.5*			
June	Epi	19.0 (13.3,28) ^{All}	8.3 (2.0,13)	6.6 (1.9,18)	6.6 (1.4, 3)
158-163	M		10.4 (3.3,11)	7.1 (1.7,15)	4.9 (0.7, 5)
	H		10.5 (1.6,16) ^{Epi}	8.2 (2.1,30) ^{Epi}	6.1 (1.7, 7)
	Mean	*Lake: 9.5*	*9.8*	*7.6*	*6.0*
July	Epi	26.0 (15.4 28) ^{All}	7.0 (2.2,19)	5.7 (1.3,27)	4.7 (0.6, 4)
197-200	M		10.7 (2.4,10) ^{Epi}	7.8 (1.7,13) ^{Epi}	5.5 (0.0, 1)
	H		11.0 (1.8, 9) ^{Epi}	7.8 (2.7,21) ^{Epi}	5.7 (2.1, 6)
	Mean	*Lake: 9.4*	*10.4*	*6.6*	*5.8*
September	Epi	29.9 (20.0, 23) ^{All}	11.0 (1.6,22) ^{C,E}	8.5 (1.2,28)	7.9 (0.9, 6)
250-253	M		11.3 (1.1,6)	9.1 (1.7,15)	7.6 (0.6, 3)
	H		10.2 (0.8,2)	8.0 (2.0,10)	6.4 (0.3, 2)
	Mean	*Lake: 11.8*	*11.0*	*8.5*	*7.3*

Table 4.3: Spatial and temporal patterns of SRP [μg L^{-1}] in Lake Erie. Labels and superscripts are described in Table 4.1.

Month		**Basin**			
Days	**Strata**	**W**	**CW**	**C**	**E**
May	Epi	1.63 (4.24,38) ^{C,E}	0.38 (0.17,18)	0.38 (0.46,41)	0.22 (0.04,11)
130-135	*Mean*	*Lake: 0.52*			
June	Epi	0.98 (1.35,30) ^{CW,C}	0.29 (0.18,10)	0.26 (0.14,17)	0.60 (0.28, 2)
158-163	M		0.23 (0.09, 9)	0.27 (0.15,14)	0.33 (0.11, 3)
	H		0.33 (0.15,13)	0.38 (0.29,29)	0.44 (0.18, 7)
	Mean	*Lake: 0.43*	*0.29*	*0.33*	*0.46*
July	Epi	1.07 (1.14,32) ^{All}	0.14 (0.06,13)	0.05 (0.06,25)	0.03 (0.05, 4)
197-200	M		0.22 (0.08,10) ^{Epi}	0.09 (0.12,12)	
	H		0.20 (0.09, 9)	0.13 (0.15,21) ^{Epi}	0.08 (0.08, 6)
	Mean	*Lake: 0.23*	*0.16*	*0.07*	*0.05*
September	Epi	1.93(1.92,17) ^{C,E}	0.51 (0.17,27) ^{C,E}	0.35 (0.13,31)	0.25 (0.08, 7)
250-253	M		0.37 (0.12, 6)	0.34 (0.12,15)	0.20 (0.10, 3)
	H		0.80 (0.00, 2) ^{M}	0.35 (0.11, 9)	0.40 (0.14, 2)
	Mean	*Lake: 0.59*	*0.51*	*0.35*	*0.30*

Table 4.4: Spatial and temporal patterns of NH_4 [$\mu g\ L^{-1}$] in Lake Erie. Labels and superscripts are described in Table 4.1.

Month		**Basin**			
Days	**Strata**	**W**	**CW**	**C**	**E**
May	Epi	23.9 (37.7,38)	9.2 (3.2, 18)	8.0 (3.8, 45)	9.5 (3.8,11)
130-135	*Mean*	*Lake: 10.5*			
June	Epi	17.9 (21.0,30)	5.9 (2.0, 10)	6.5 (2.7, 17)	20.3 (21.8,2)
158-163	M		8.3 (7.8, 9)	7.6 (4.1, 14)	17.2 (10.3,3)
	H		18.7 (10.2,13) Epi,M	20.0 (13.5,29) Epi,M	18.0 (10.8,7)
	Mean	*Lake: 15.1*	*12.8*	*14.1*	*15.1*
July	Epi	33.4 (32.7,32) All	14.1 (10.6,13)	10.7 (9.3, 25)	6.9 (0.9, 4)
197-200	M		25.6 (15.6,10)	24.2 (19.3,12) Epi	11.4 (0.0, 1)
	H		25.0 (14.3, 9)	23.8 (13.1,21) Epi	30.8 (15.6,6) Epi
	Mean	*Lake: 19.3*	*17.8*	*16.0*	*18.5*
September	Epi	11.3 (10.1,23)	25.2 (19.6,22)	22.8 (27.3,28)	12.4 (14.5,6)
250-253	M		33.6 (20.8, 6)	45.0 (23.1,15) Epi	21.1 (11.1,3)
	H		27.6 (31.0, 2)	58.9 (51.2, 9) Epi	4.5 (2.3, 2)
	Mean	*Lake: 20.9*	*25.7*	*26.4*	*10.3*

Table 4.5: Spatial and temporal patterns of SiO_2 [$mg\ L^{-1}$] in Lake Erie. Labels and superscripts are described in Table 4.1.

Month		**Basin**			
Days	**Strata**	**W**	**CW**	**C**	**E**
May	Epi	1.32 (0.44,39) All	0.38 (0.22,18)	0.39 (0.40,45)	0.38 (0.14,11)
130-135	*Mean*	*Lake: 0.51*			
June	Epi	1.00 (0.44,30) CW,C	0.25 (0.12,10)	0.27 (0.16,17)	0.38 (0.08,2)
158-163	M		0.24 (0.14, 9)	0.28 (0.17,14)	0.52 (0.16,3)
	H		0.74 (0.42,13) Epi,M	0.63 (0.34,29) Epi,M	0.53 (0.14,7)
	Mean	*Lake: 0.55*	*0.49*	*0.47*	*0.50*
July	Epi	1.74 (0.79,32) All	0.67 (0.77,13)	0.30 (0.20,25)	0.24 (0.02,4)
197-200	M		1.46 (0.59,10) Epi	0.69 (0.28,12) Epi	0.25 (0.00,1)
	H		1.31 (0.24, 9) Epi	0.92 (0.40,21) Epi	0.59 (0.26,6) Epi
	Mean	*Lake: 0.75*	*0.91*	*0.51*	*0.40*
September	Epi	1.11 (0.41,23) E	2.38 (1.57,22) E,C	1.08 (1.26,27)	0.33 (0.33,6)
250-253	M		3.66 (0.70, 6)	2.91 (1.16,15) Epi	0.99 (0.25,3)
	H		3.48 (1.05, 2)	2.63 (1.35, 9) Epi	1.12 (0.13,2)
	Mean	*Lake: 1.44*	*2.48*	*1.30*	*0.65*

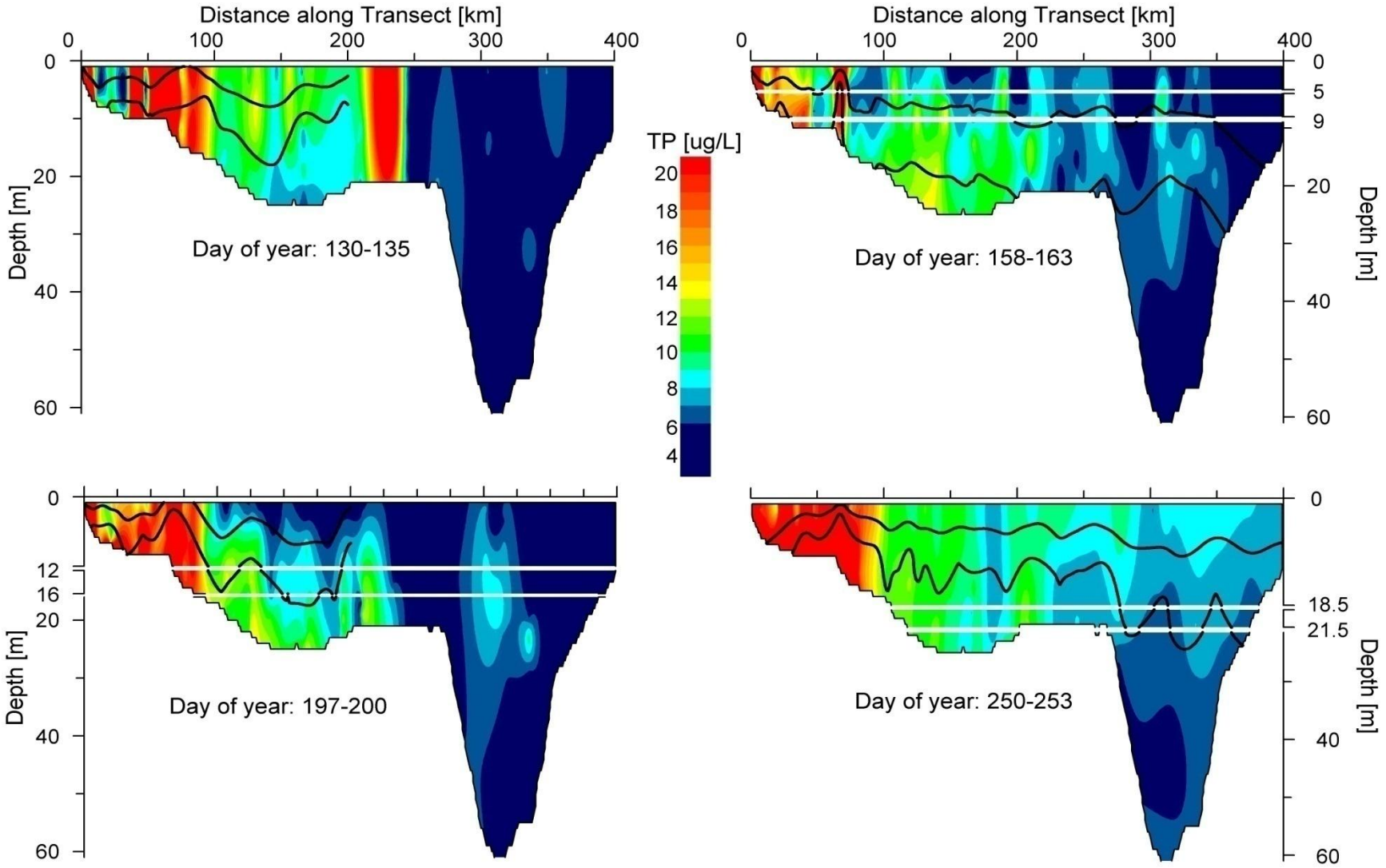

Figure 4.6**:** Longitudinal curtains (Figure 4.3) of total phosphorus (TP) during 4 surveys. Solid white lines represent the upper and lower limits of the mean metalimnetic and hypolimnetic depths for each cruise, solid black lines represent optical depths of 2 and 4.6.

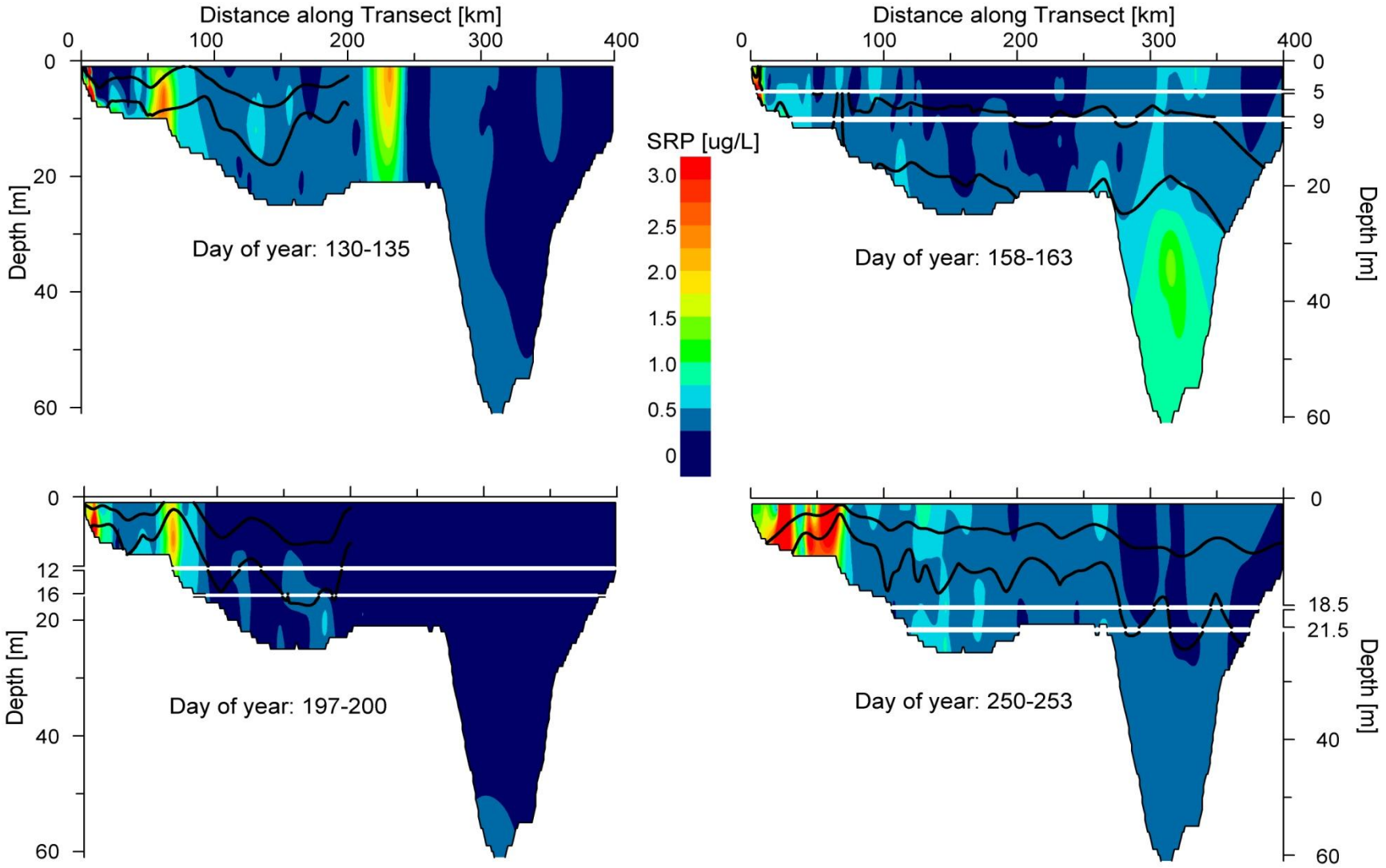

Figure 4.7: Longitudinal curtains (Figure 4.3) of soluble reactive phosphorus (SRP) during 4 surveys. Solid white lines represent the upper and lower limits of the mean metalimnetic and hypolimnetic depths for each cruise, solid black lines represent optical depths of 2 and 4.6.

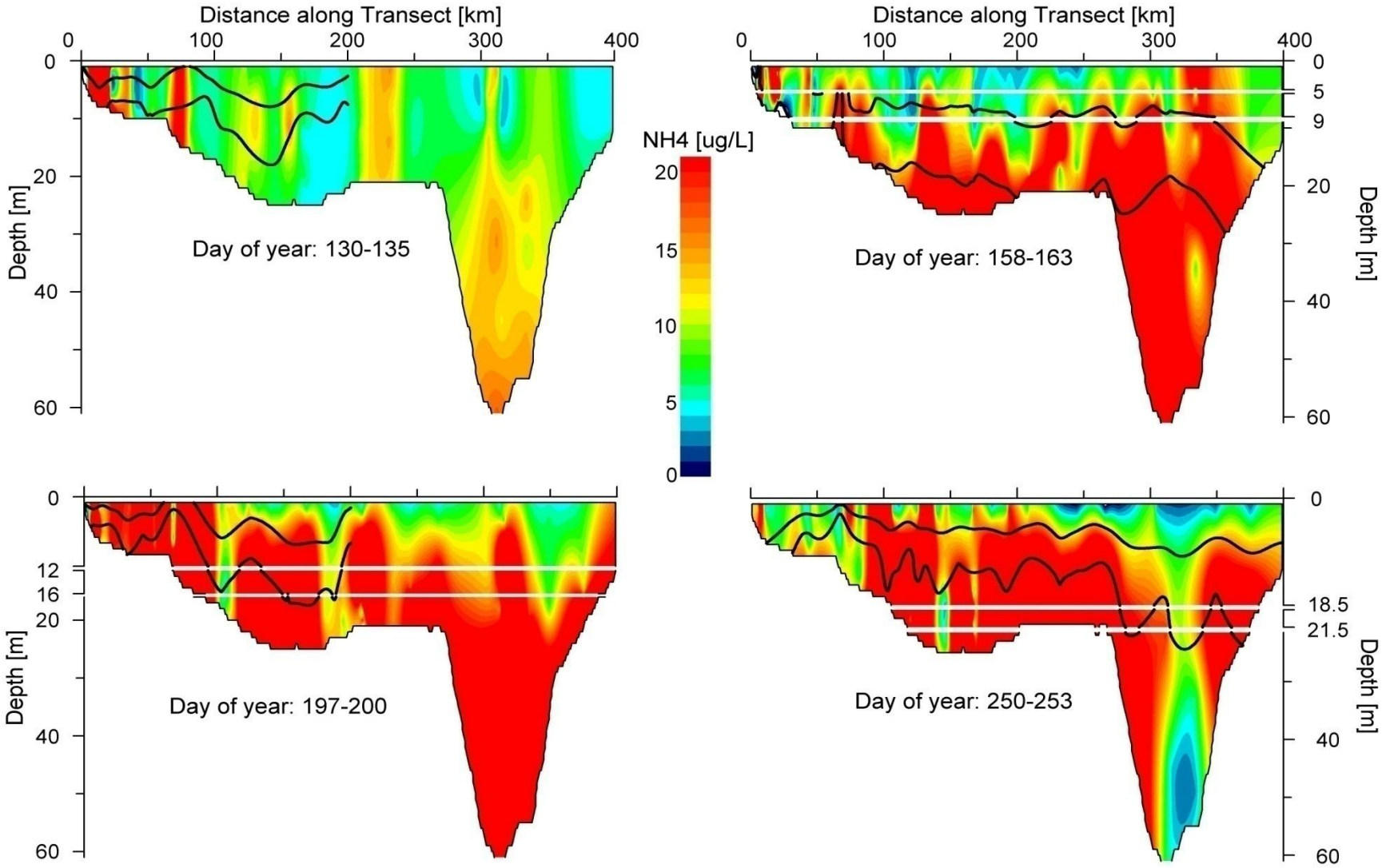

Figure 4.8**:** Longitudinal curtains (Figure 4.3) of ammonium (NH_4) during 4 surveys. Solid white lines represent the upper and lower limits of the mean metalimnetic and hypolimnetic depths for each cruise, solid black lines represent optical depths of 2 and 4.6.

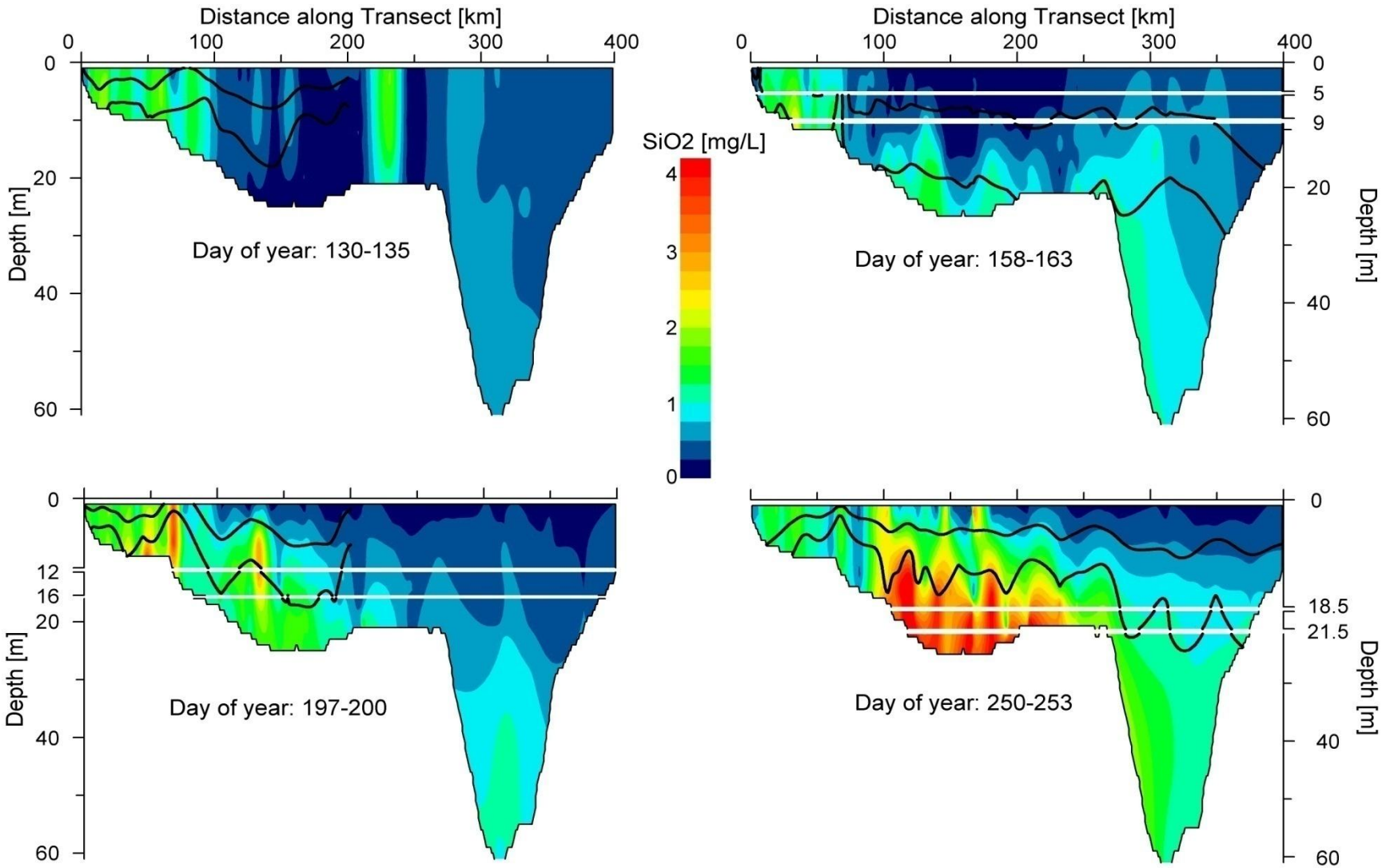

Figure 4.9: Longitudinal curtains (Figure 4.3) of silicon dioxide (SiO_2) during 4 surveys. Solid white lines represent the upper and lower limits of the mean metalimnetic and hypolimnetic depths for each cruise, solid black lines represent optical depths of 2 and 4.6.

Section 4.3.4: Vertical Patterns of chl *a*, a_{PSII} and SCFs

Chl a - Table 4.7 summarizes spatial and temporal patterns of extracted chl *a*. Lakewide mean averages of chl *a* progressively increased through the season, and by September were 1.9 fold higher than in May. In May, chl *a* increased along an eastward gradient though mean differences between basins were not statistically significant (Kruskal-Wallis test, $p < 0.10$); this is the opposite spatial pattern than measured nutrients at this time. During all other surveys the west basin had statistically higher concentrations than all other basins and generally decreased along an eastward gradient (Kruskal-Wallis test, $p < 0.10$). In June, metalimnetic and hypolimnetic concentrations in the central-west and central basins were statistically higher than epilimnetic concentrations (Kruskal-Wallis test, $p < 0.10$). A similar pattern emerged in July, though the vertically gradients were not as strong and not statistically significant. In September the opposite pattern emerged as the highest concentrations were found in the epilimnion of the central-west, central and east basin.

Table 4.6: Spatial and temporal patterns of chl *a* [mg m^{-3}] in Lake Erie. Labels and superscripts are described in Table 4.1.

Month		**Basin**			
Days	**Strata**	**W**	**CW**	**C**	**E**
May	Epi	2.43 (1.07,13)	2.55 (1.05,13)	3.09 (1.76,13)	
120-124	*Mean*	*Lake: 2.64*			
June	Epi	3.84 (2.73,42) ^{All}	1.52 (0.58,19)	1.19 (0.59,20)	1.52 (1.20, 17)
158-163	M		2.92 (0.98,16) ^{Epi}	2.35 (1.47,10) ^{Epi}	1.92 (1.56, 16)
	H		4.77 (2.07,14) ^{Epi}	3.89 (1.95,18) ^{Epi}	2.78 (3.18, 19)
	Mean	*Lake: 3.07*	*3.44*	*2.89*	*2.43*
July	Epi	10.85 (9.33,7) ^{CW,C}	2.53 (1.34,7)	1.98 (0.53,4)	
200-203	M		2.45 (0.90,5)	2.45 (0.0,1)	
	H		3.16 (0.71,4)	3.76 (0.0,1)	
	Mean	*Lake: 3.82*	*2.62*	*3.14*	
September	Epi	10.20 (4.24,29) ^{All}	5.82 (2.44,17) ^{E,M,H}	4.44 (1.36,17) ^{E,M,H}	2.70 (0.40,15) ^{M,H}
250-253	M		2.79 (1.10,11)	2.55 (1.21,18)	1.29 (0.57, 8)
	H		2.43 (0.23,10)	2.54 (0.98,18)	1.10 (0.82, 4)
	Mean	*Lake: 4.97*	*5.56*	*4.28*	*2.07*

a_{PSII} - Figure 4.10 and Table 4.8 summarizes spatial and temporal patterns of a_{PSII}. Spatial patterns of a_{PSII} were broadly similar to those of chl *a*. In May, a_{PSII} increased along an eastward gradient while during all other surveys the west basin had the statistically highest concentrations and a_{PSII} generally decreased along an eastward gradient. Unlike chl *a* however, lakewide mean averages of a_{PSII} peaked in July, were high in September and lowest in June.

Figure 4.10A shows basin specific vertical gradients of a_{PSII} during May when the water column was isothermal. At this time, a_{PSII} was vertically homogenous through depth in the west basin, but increased through depth by an average of 12% and 20% per optical depth in the central-west and central basins respectively. During the June cruise that corresponded with the onset of a shallow metalimnion, a_{PSII} dramatically increased with depth in all basins and hypolimnetic values were significantly larger than epilimnetic values in the central-west and central basins (Kruskal-Wallis test, $p < 0.10$). The mean physical depth of the a_{PSII} peak at this time was shallowest in the west basin and deepest in the east basin, however binning the data into optical depths (ζ) revealed that this peak occurred at $\zeta \sim 4$ in each basin, or 2% of surface irradiance. During the July cruise that corresponded to a deeper and vertically stable metalimnion, a_{PSII} was homogenous through depth in the west basin, though due to a battery failure in the instrumentation only two stations were sampled. In the central-west basin a_{PSII} was vertically homogenous through the first 3.5 optical depths, but quickly increased and metalimnetic and hypolimnetic values were significantly larger than epilimnetic values (Kruskal-Wallis test, $p < 0.10$). In the central basin a_{PSII} was highest at the bottom of the seasonal thermocline but there were no statistically significant differences between mean a_{PSII} values. During the September cruise that corresponded to a deeper metalimnion and seasonal hypoxia in

the central and central west basins, the vertical structure of a_{PSII} increased moderately through depth in the west basin (12% increase per optical depth) but in all other basins the highest values were in the epilimnion. At this time the seasonal thermocline was displaced below the first 6 optical depths at most stations in the central-west and central basin and was also relatively deep ($\zeta \sim 5$) in the east basin.

At stations where stratification was present, epilimnetic measurements of a_{PSII} normalized to chl *a* (a^*_{PSII}) were on average 6% higher than sub-epilimnetic values, though the differences were not statistically significant (t-test, $p = 0.33$). No significant temporal differences in mean a^*_{PSII} values emerged (Kruskal-Wallis test), though values in May and July were similar and approximately 17% higher than measurements in June and September.

To estimate the degree to which vertical gradients of a_{PSII} were a product of increased phytoplankton biomass or photoadaptation (increased pigment content per unit biomass), a_{PSII} was normalized to vertical measurements of the beam attenuation coefficient (a proxy for phytoplankton biomass; Behrenfeld and Boss 2003) in June and September when these measurements were available. In June, beam attenuation measurements were lowest in the epilimnion and highest in the hypolimnion in each basin (data not shown), though unlike a_{PSII} the only statistically significant gradient occurred in the central-west basin (Kruskal-Wallis, $p < 0.05$). Relative to epilimnetic measurements in June, the beam attenuation was 24%, 15% and 8% higher in the hypolimnion of the central-west, central and east basin respectively. Comparing beam attenuation vertical gradients to those of a_{PSII} in June, it is apparent that increases in the latter can primarily be attributed to increased pigment packaging per unit biomass. For example in the central-west and central basin, a_{PSII} per unit beam attenuation were respectively 2.56 and 3.25-fold higher in the hypolimnion than the epilimnion. In September,

there were no statistically significant differences between mean beam attenuation coefficients in the central-west, central and east basin (Kruskal-Wallis, $p>0.10$).

SCF - Figure 4.10 and Table 4.9 summarizes spatial and temporal patterns of SCF where values in the light-saturated region ($E_0 > 2 \bullet E_K$) have been omitted. SCF values are critical when estimating PP as they linearly scale a_{PSII} and light limited photosynthesis (Eqn 4.4). In a relative sense, SCF values below 1 indicate phytoplankton communities that are poorly adapted to their light environment and values above 1 are indicative of phytoplankton communities well adapted to their light environment (Markager and Vincent 2001).

Figure 4.11 provides an illustrative example of temporal patterns in spectral shapes of E_Z and a_{PSII} and their influence on SCFs. Data from this figure corresponds to measurements taken at an optical depth of 5 from two stations (954 on days 123 and 200, ER37 on days 160 and 251) separated by a distance of 14.5 km in the central basin of Lake Erie. k_{PAR} values at these two stations were 0.52, 0.21, 0.28 and 0.32 on days 123, 160, 200 and 251 respectively. Following Chapter 3, the wavelength of mean spectral irradiance is highest (543 nm) on day 123 when k_{PAR} = 0.52 m^{-1} and lowest (521 nm) on day 160 when k_{PAR} = 0.21 m^{-1} as indicated in Figure 4.11 with color coded arrows. When normalized to $F_{[450\ nm]}$, the evolution of the spectral shapes of a_{PSII} demonstrates that as the stratified season progressed, a_{PSII} became increasingly composed of accessory pigments (absorption between 525 – 610 nm) thereby increasing the wavelength of mean spectral absorption over time. In May, the wavelengths of mean spectral irradiance and absorption are separated by 29 nm and the resultant SCF (0.78) is indicative of a phytoplankton community poorly adapted to the light environment. During all other cruises the wavelengths of mean spectral irradiance and absorption are separated by less than 6 nm and the resultant SCFs (1.13 – 1.15) are indicative of phytoplankton communities well adapted to their light

environment.

Summarized in Table 4.9, SCF values are at their seasonal minima in May, especially in the west basin where the lowest recorded values were found. By June, SCF values increased in all basins with similarly high values found in July. Mean lakewide SCF values decreased in September. Spatially, the highest values in May were in the central-west basin while during all other cruises the highest values were found in the central basin. SCF values were lowest in the west basin throughout, though the dominance of phycocyanin-rich cyanobacteria in June and July (Rattan 2009) increased SCFs relative to other surveys. Vertically, in May SCFs decreased through depth in all basins. In June, SCF values also decreased with depth in the west basin, were slightly higher in the metalimnion than all other strata in the central-west and central basins and were highest in the hypolimnion of the east basin. In July, SCF values were homogenous through depth in the west basin, and increased dramatically in the hypolimnion of the central-west basin where values were significantly higher than the epilimnion. A similar vertical pattern occurred at this time in the central basin though no significant differences were found. In September vertical variations were less pronounced, though metalimnetic and hypolimnetic values in the central-west and central basins were slightly higher than epilimnetic values.

Table 4.7: Spatial and temporal patterns of a_{PSII} [$m^{-1} \bullet 10^{-2}$] in Lake Erie. Labels and superscripts are described in Table 4.1.

Month		**Basin**			
Days	**Strata**	**W**	**CW**	**C**	**E**
May	Epi	1.62 (0.63,12)	2.05 (0.90,9)	2.23 (0.96,7)	
120-124	*Mean*	*Lake: 1.96*			
June	Epi	3.53 (5.60,8)^{All}	0.76 (0.42,6)	0.53 (0.33,4)	0.68 (0.23, 5)
158-163	M		1.19 (0.75,6)	0.78 (0.49,4)	0.94 (0.68, 5)
	H		2.51 (1.13,5)^{Epi}	2.01 (1.19,4)^{Epi}	1.09 (0.97, 5)
	Mean	*Lake:1.68*	*1.72*	*1.38*	*0.99*
July	Epi	21.9 (27.4,2)^{C}	1.46 (0.42,7)	1.63 (0.43,4)	
200-203	M		2.46 (1.01,6)^{Epi}	1.82 (0.07,3)	
	H		2.95 (1.70,5)^{Epi}	2.12 (0.72,2)	
	Mean	*Lake: 4.51*	*1.88*	*1.96*	
September	Epi	6.0 (4.9,7)^{E}	4.40 (1.46,4)^{E}	3.07 (0.66,5)^{Epi}	2.00 (0.26, 5)
250-253	M		1.67 (0.00,1)	1.68 (0.39,3)	1.63 (0.44, 3)
	H			1.21 (0.81,2)	1.58 (0.60, 2)
	Mean	*Lake: 3.45*	*4.18*	*2.95*	*1.83*

Table 4.8: Spatial and temporal patterns of SCF in Lake Erie. Labels and superscripts are described in Table 4.1.

Month		**Basin**			
Days	**Strata**	**W**	**CW**	**C**	**E**
May	Epi	0.89 (0.04,12)	1.00 (0.05,9)^{W}	0.93 (0.08,7)	
120-124	*Mean*	*Lake: 0.93*			
June	Epi	1.03 (0.08,8)	1.11 (0.02,6)	1.20 (0.13,4)^{W}	1.09 (0.04, 5)
158-163	M		1.13 (0.05,6)	1.25 (0.20,4)	1.08 (0.04, 5)
	H		1.10 (0.06,5)	1.17 (1.06,4)	1.16 (0.09, 5)
	Mean	*Lake:1.14*	*1.11*	*1.19*	*1.13*
July	Epi	1.04 (0.13,2)	1.06 (0.05,7)	1.06 (0.07,4)	
200-203	M		1.20 (0.13,6)	1.04 (0.15,3)	
	H		1.35 (0.16,5)^{Epi}	1.21 (0.08,2)	
	Mean	*Lake: 1.12*	*1.13*	*1.15*	
September	Epi	0.93 (0.06,7)^{E}	0.97 (0.09,4)	1.09 (0.63,5)^{W}	1.05 (0.03, 5)
250-253	M		1.08 (0.00,1)	1.13 (0.14,3)	1.03 (0.12, 3)
	H			1.17 (0.07,2)	0.96 (0.07, 2)
	Mean	*Lake: 1.03*	*0.98*	*1.10*	*1.02*

Table 4.9: Spatial and temporal patterns of SCF_{SV} in Lake Erie. Labels and superscripts are described in Table 4.1.

Month		**Basin**			
Days	**Strata**	**W**	**CW**	**C**	**E**
May	Epi	0.71 (0.06,12)^{CW}	0.62 (0.05,9)	0.67 (0.08,7)	
120-124					
June	Epi	0.77 (0.29,8)^{CW,C,E}	0.52 (0.07,6)	0.51 (0.18,4) ^{W}	0.47 (0.06, 5)
158-163	M		0.52 (0.10,6)	0.52 (0.07,4)	0.46 (0.14, 5)
	H		0.53 (0.05,6)	0.54 (0.04,4)	0.53 (0.13, 5)
July	Epi	1.05 (0.43,2)	0.76 (0.28,7)	0.67 (0.06,4)	
200-203	M		0.65 (0.07,6)	0.68 (0.13,3)	
	H		0.58 (0.03,5) ^{Epi}	0.60 (0.04,2)	
September	Epi	0.92 (0.26,7)	0.84 (0.05,4)	0.79 (0.08,5)	0.84 (0.10, 5)
250-253	M		0.67 (0.00,1)	0.79 (0.10,3)	0.87 (0.10, 3)
	H			0.72 (0.08,2)	0.74 (0.00, 1)

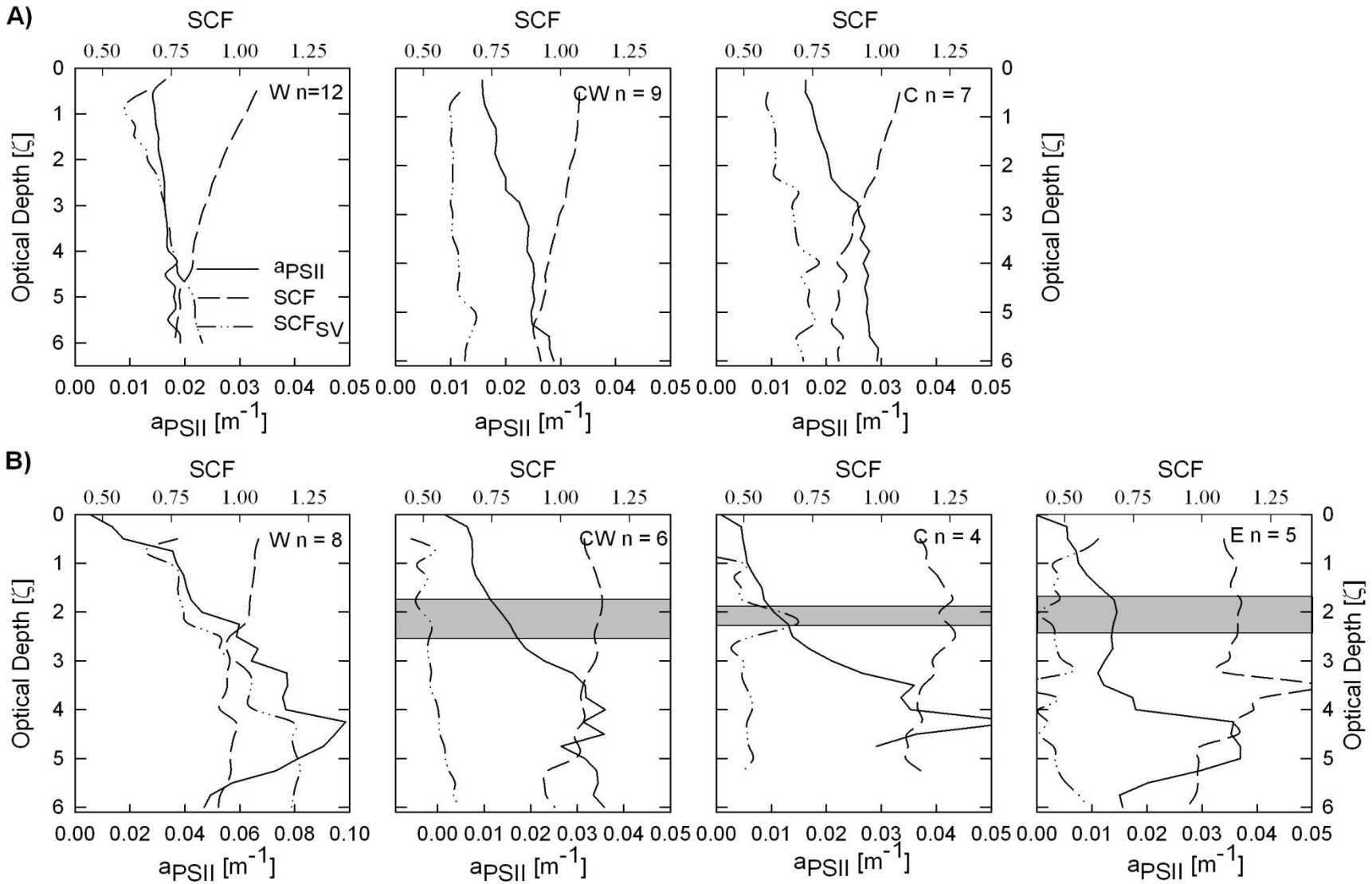

Figure 4.10: Mean vertical distribution of a_{PSII} and SCF in A) May (Day 120-124) and B) June (Day 158-163) for each basin. Grey shadow is the approximate optical depth of the seasonal thermocline.

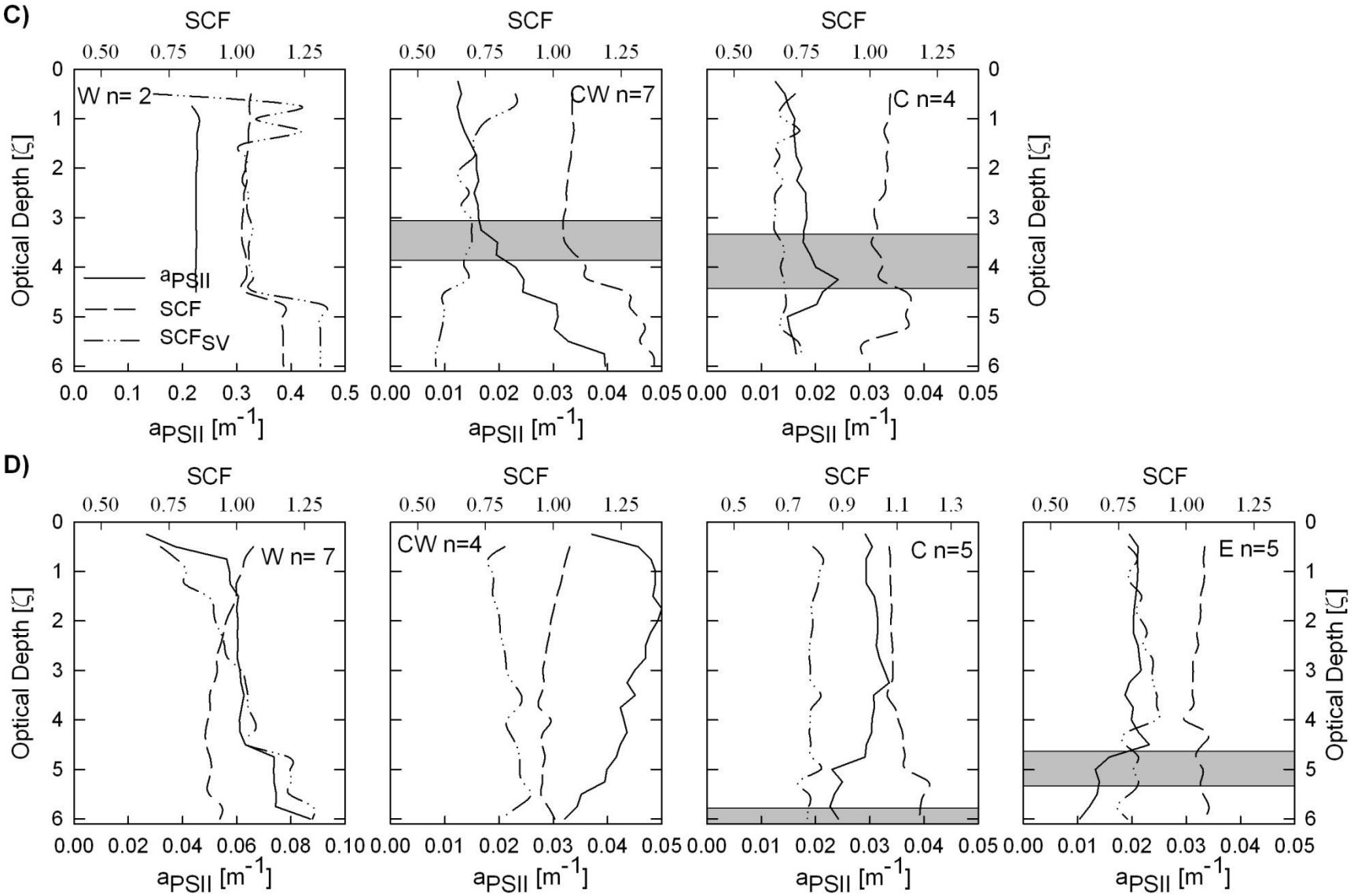

Figure 4.10 continued: Mean vertical distribution of a_{PSII} and SCF in C) July (Day 200-203) and D) September (Day 250-253) for each basin. Grey shadow is the approximate optical depth of the seasonal thermocline.

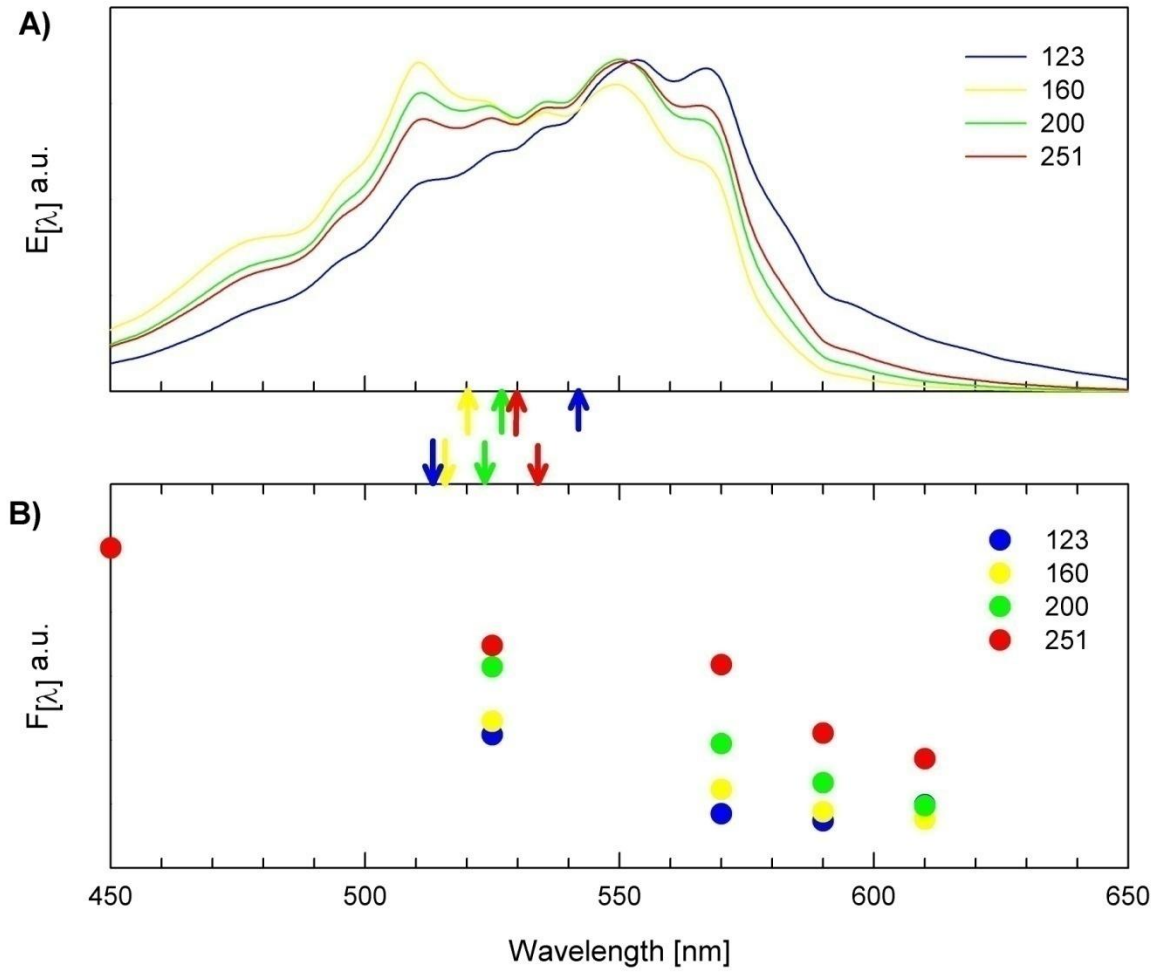

Figure 4.11: Temporal variation in A) the relative spectral distribution of PAR [arbitrary units] at optical depth = 5 and B) corresponding spectral fluorescence normalized to $F_{[450\ nm]}$. The day of year for each spectra are shown in the legend, arrows correspond to the wavelength of mean spectral irradiance or fluorescence.

Section 4.3.5: The Vertical Distribution of f_{PSII}

Table 4.11 summarizes the spatial and temporal patterns of Fq'/F_M' in Lake Erie. As in Chapter 2, a data filter was applied to these measurements to minimize photo-physiological suppression of Fq'/F_M' (see Section 2.2: Materials and Methods). Following this data filter, values were normalized to 0.65, the empirical upper limit of Fq'/F_M', binned by optical depth and separated into thermal strata where thermal stratification was present. As for a_{PSII}, data presented in Table 4.11 is limited to the first six optical bins only. As summarized in Chapter 2, in the absence of photo-physiological suppression, Fq'/F_M' values were in general numerically high and empirically constrained and thus may represent either nutrient sufficient phytoplankton or nutrient deficient phytoplankton under balanced growth (Suggett et al. 2008). The bulk of Fq'/F_M' data presented in Chapter 2 is of epilimnetic origin, and as shown in Table 4.8 similarly high values were present in both the metalimnion and hypolimnion. High Fq'/F_M' measurements corrected for background fluorescence beneath the epilimnion are of particular importance, as they demonstrate that phytoplankton communities at these depths are photosynthetically functional and not simply a conglomerate of dead cells that have sedimented out of the epilimnion. Within cruises, the high and constrained Fq'/F_M' values precluded any statistically significant patterns to emerge (Kruskal-Wallis test, $p < 0.10$), though spatial patterns did broadly reflect similar spatial patterns of phosphorus deficiency (Rattan 2009). Temporally, lakewide Fq'/F_M' values were lowest in May and markedly consistent across all other cruises.

Table 4.10: Spatial and temporal patterns of $F_q'/F_M' 0.65^{-1}$ in Lake Erie. Labels and superscripts are described in Table 4.1.

Month		**Basin**			
Days	**Strata**	**W**	**CW**	**C**	**E**
May	Epi	0.53 (0.25,12)	0.53 (0.10,6)	0.57 (0.18,10)	
120-124	*Mean*	*Lake:0.56*			
June	Epi	0.73 (0.16,9)	0.61 (0.14,4)	0.79 (0.08,6)	0.72 (0.07, 5)
158-163	M		0.65 (0.11,4)	0.78 (0.06,6)	0.75 (0.10, 5)
	H		0.69 (0.11,4)	0.73 (0.05,5)	0.77 (0.07, 5)
	Mean	*Lake:0.73*	*0.66*	*0.76*	*0.76*
July	Epi	0.45 (0.12,2)	0.76 (0.13,4)	0.65 (0.22,7)	
200-203	M		0.70 (0.05,3)	0.79 (0.08,6)	
	H		0.67 (0.02,2)	0.78 (0.08,5)	
	Mean	*Lake:0.72*	*0.73*	*0.75*	
September	Epi	0.83 (0.07,7)	0.72 (0.07,3)	0.70 (0.80,6)	0.77 (0.05, 5)
250-253	M			0.69 (0.04,4)	0.71 (0.18, 3)
	H			0.61 (0.00,1)	0.77 (0.06, 2)
	Mean	*Lake:0.73*	*0.72*	*0.70*	*0.77*

Section 4.3.6: The Vertical Distribution of Photosynthesis

Figure 4.13 and Tables 4.12 and 4.13 summarize vertical patterns of spectrally resolved phytoplankton photosynthetic rates (P) and daily areal phytoplankton production (ΣPP) derived through three scaling methods, $P_{[Z,\lambda]}$, $P_{[INT,\lambda]}$ and $P_{[INT,SV]}$ outlined in Section 4.2. Spatial and temporal patterns of ΣPP varied according to scaling method and underscore the importance of accurate characterization of the vertical distribution of PP.

Shown in Figure 4.12A, in May vertically resolved estimates of P varied between methods and yielded non-statistically significant differences in ΣPP (Table 4.13). The integrated sample methodologies, $P_{[INT,\lambda]}$ and $P_{[INT,SV]}$ actually overestimated *in situ* $\Sigma PP_{[Z,\lambda]}$ at this time. In May a_{PSII} increased with depth through the epilimnion in all basins (Figure 4.10), so vertically integrated samples that homogenize a_{PSII} over the water column overestimate a_{PSII} and photosynthesis at the surface. The largest disparities between methods occurred in June. In the shallow west basin, $\Sigma PP_{[Z,\lambda]}$ overestimated $P_{[INT,\lambda]}$ and $P_{[INT,SV]}$ by 7% and 25% respectively. In all other basins in June, $\Sigma PP_{[Z,\lambda]}$ was significantly higher than the other two scaling methods (Kruskal-Wallis test, $p < 0.10$). Integrated epilimnetic samples failed to capture the significantly higher measurements of a_{PSII} in the metalimnion and hypolimnion (Table 4.8) where 49-64% of $\Sigma PP_{[Z,\lambda]}$ occurred (Table 4.13). Despite the vertical gradients in a_{PSII}, the highest *in situ* photosynthetic rates ($P_{[Z,\lambda]}$) occurred in the epilimnion and no deep photosynthetic maxima were apparent. In July in the west basin all scaling methods were within 7% of each other, though the small sample size precludes any definitive pattern to emerge. In the central-west and central basins $\Sigma PP_{[Z,\lambda]}$ exceeded both $P_{[INT,\lambda]}$ and $P_{[INT,SV]}$, though the differences were not statistically significant. *In situ* photosynthetic rates were higher in the metalimnion and hypolimnion relative to the two scaling techniques, owing to moderately higher values of a_{PSII} and SCFs relative to

epilimnetic samples. In September $\Sigma PP_{[Z,\lambda]}$ and $\Sigma PP_{[INT,\lambda]}$ were similar across all stations and routinely overestimated $\Sigma PP_{[INT,SV]}$ though no statistically significant differences in ΣPP estimates between methodologies emerged.

Shown in Figure 4.12, temporal patterns of lakewide (spatially weighted) ΣPP generally mirrored those of chl *a* as ΣPP increased over the period of investigation. However where $P_{[INT,\lambda]}$ and $P_{[INT,SV]}$ document a gradual increase over time, both methods underestimate $\Sigma PP_{[Z,\lambda]}$ at the onset of stratification as actual *in situ* rates of phytoplankton production more than doubled between the May and June surveys and were within 5% of spatially weighted $\Sigma PP_{[Z,\lambda]}$ measurements in July.

Table 4.11: Spatial and temporal patterns of strata specific *in situ* ΣPP [g O_2 m^{-2} day^{-1}] in Lake Erie. Labels and superscripts are described in Table 4.1.

Month		**Basin**			
Days	**Strata**	**W**	**CW**	**C**	**E**
May	Epi	0.47 (0.32,11)	1.50 (1.07,9)	0.82 (0.40,7)	
120-124					
June	Epi	2.44 (1.67,7)	0.76 (0.55,5)	0.76 (0.43,4)	0.97 (0.49, 5)
158-163	M		0.35 (0.23,5)	0.37 (0.37,4)	0.23 (0.21, 5)
	H		0.94 (0.43,5)	0.97 (0.97,4)	0.68 (0.91, 5)
July	Epi	2.11 (0.76,2)	2.18 (0.95,7)	1.78 (1.18,4)	
200-203	M		0.19 (0.09,7)	0.21 (0.17,4)	
	H		0.12 (0.04,6)	0.09 (0.09,3)	
September	Epi	3.39 (1.16,4)	3.39 (2.29,2)	3.46 (0.93,4)	2.71 (0.40,4)
250-253	M		0.00 (0.00,2)	0.01 (0.00,4)	0.02 (0.01, 3)
	H		0.00 (0.00,2)	0.00 (0.00,4)	0.00 (0.01, 2)

Table 4.12: Spatial and temporal patterns of ΣPP [g O_2 m^{-2} day^{-1}] in Lake Erie derived from three different scaling methods. Labels are described in Table 4.1, subscripts correspond to scaling models that produced significantly lower estimates of PP.

Month		**Basin**			
Days	**Method**	**W**	**CW**	**C**	**E**
May	1. $\Sigma PP_{[Z,\lambda]}$	0.47 (0.32,11)	1.50 (1.07,9)	0.82 (0.40,7)	
120-124	2. $\Sigma PP_{[Int,\lambda]}$	0.65 (0.40,11)	1.94 (1.10,9)	1.41 (0.45,7) [1]	
	3. $\Sigma PP_{[Int,SV]}$	0.43 (0.25,11)	1.14 (0.66,9)	0.94 (0.34,7)	
June	1. $\Sigma PP_{[Z,\lambda]}$	2.44 (1.67,7)	2.04 (1.09,5) [2, 3]	2.10 (1.23,4) [2,3]	1.87 (1.16,5) [2, 3]
158-163	2. $\Sigma PP_{[Int,\lambda]}$	2.28 (1.62,7)	1.27 (0.71,5)	1.32 (0.78,4)	1.52 (0.56,5) [3]
	3. $\Sigma PP_{[Int,SV]}$	1.96 (2.25,7)	0.67 (0.40,5)	0.66 (0.47,4)	0.69 (0.37,5)
July	1. $\Sigma PP_{[Z,\lambda]}$	2.11 (0.76,2)	2.47 (0.93,7)	2.07 (1.32,4)	
200-203	2. $\Sigma PP_{[Int,\lambda]}$	2.22 (0.73,2)	2.44 (0.89,7)	2.16 (1.24,4)	
	3. $\Sigma P_{[Int,SV]}$	2.06 (0.12,2)	1.66 (0.58,7)	1.40 (0.80,4)	
September	1. $\Sigma PP_{[Z,\lambda]}$	3.39 (1.16,4)	3.40 (2.29,2)	3.47 (0.93,4)	2.73 (0.40,4)
250-253	2. $\Sigma PP_{[Int,\lambda]}$	3.45 (1.28,4)	3.54 (2.26,2)	3.61 (0.91,4)	2.79 (0.37,4)
	3. $\Sigma PP_{[Int,SV]}$	3.02 (1.77,4)	2.64 (1.56,4)	2.70 (0.70,4)	2.15 (0.33,4)

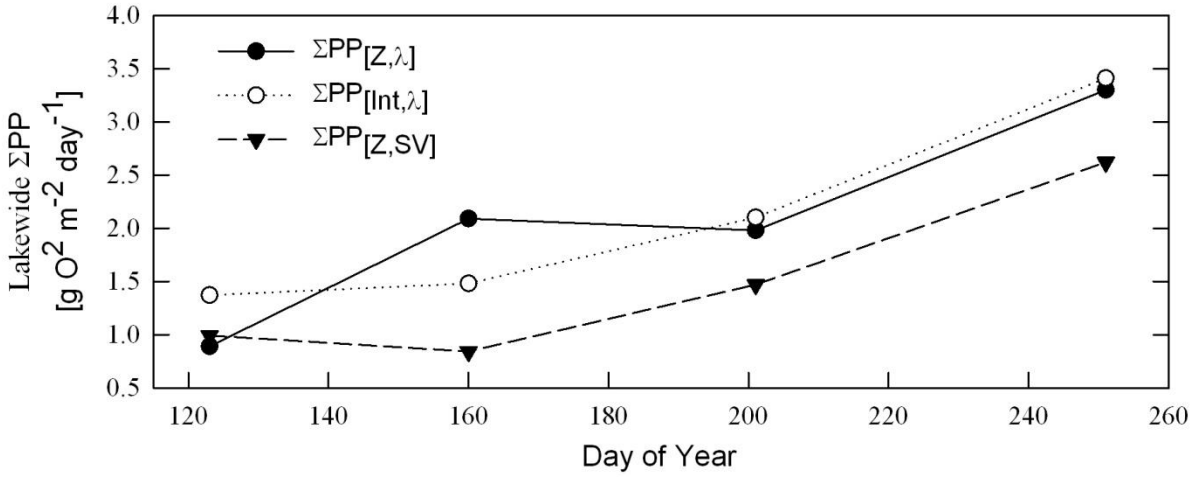

Figure 4.12: Temporal patterns of spatially weighted ΣPP derived from three scaling methods.

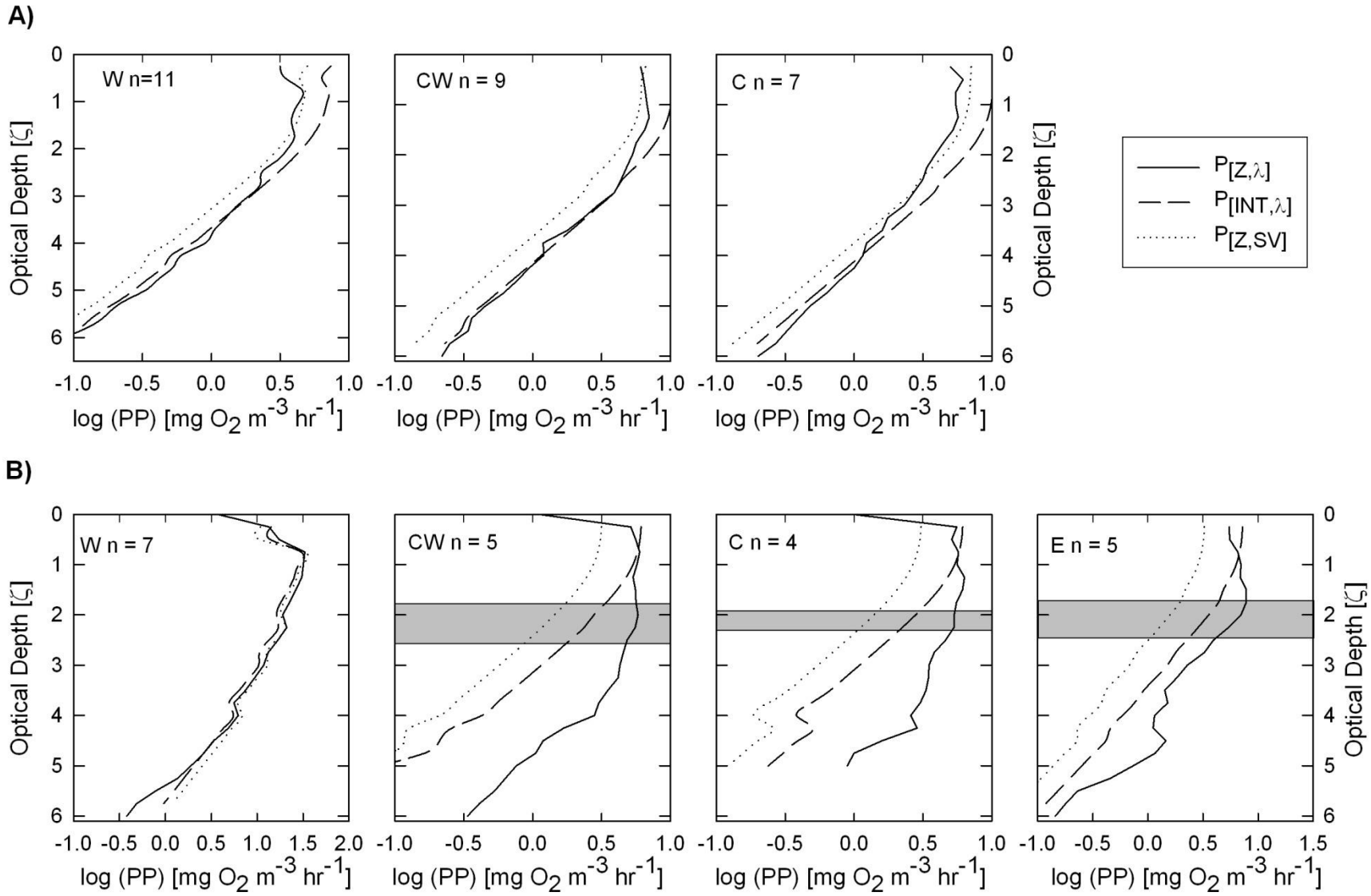

Figure 4.13: Mean vertical distribution of PP derived from three scaling methods in A) May (Day 120-124) and B) June (Day 158-163) for each basin. Grey shadow is the approximate optical depth of the seasonal thermocline.

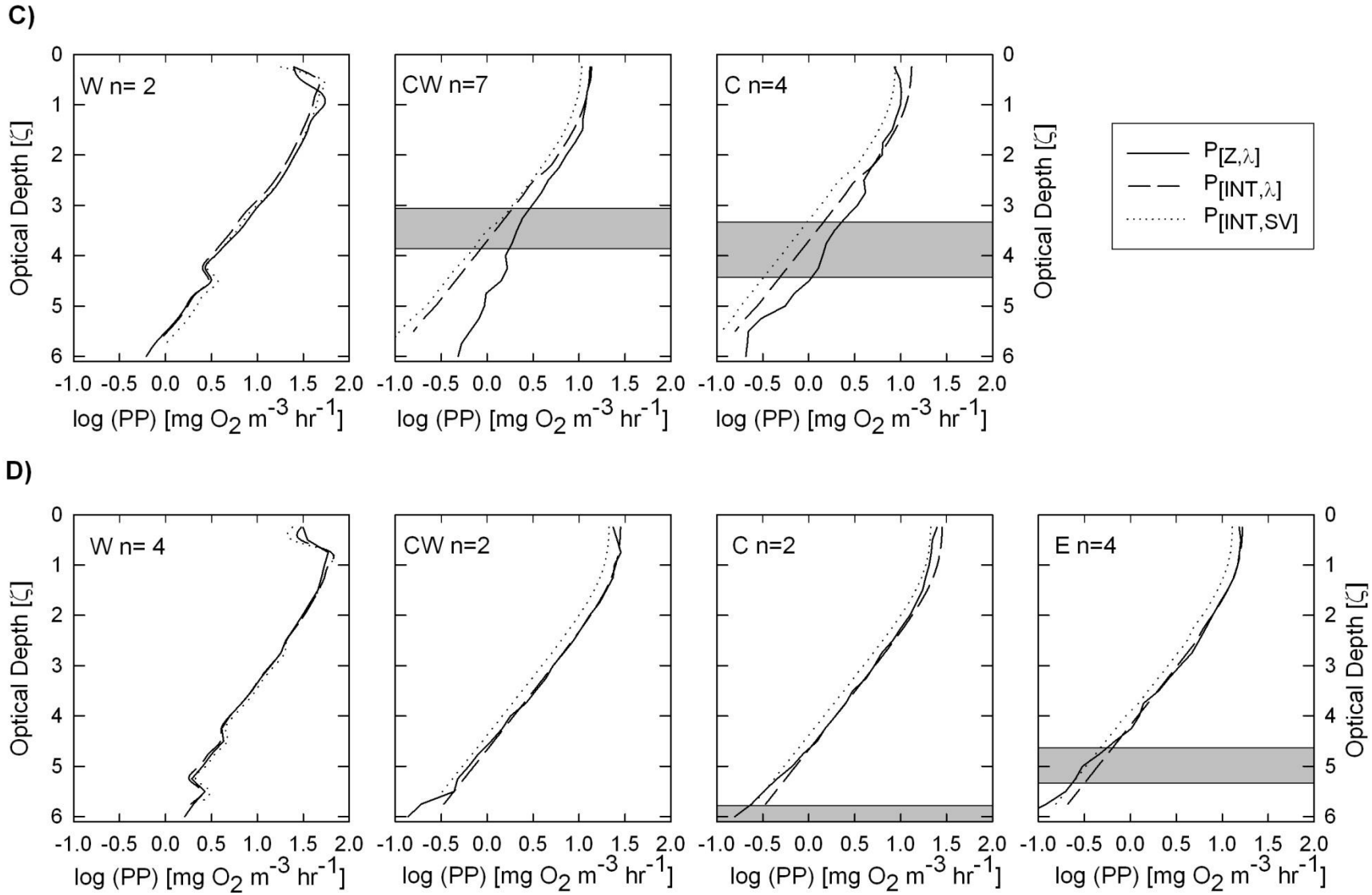

Figure 4.13 continued: Mean vertical distribution of PP derived from three scaling methods in C) July (Day 200-203) and D) September (Day 250-253) for each basin. Grey shadow is the approximate optical depth of the seasonal thermocline.

Section 4.3.7: Vertical Distribution of Photosynthesis in Georgian Bay and Lake Superior.

Figure 4.14 and 4.15 document opportunistic bio-optical profiles in Georgian Bay and Lake Superior respectively. Georgian Bay was first sampled in mid-July (day 199) following a major wind event that likely caused the observed monotonic density gradient through depth that, by the definition used here had an epilimnetic depth of 10 m. Subsequent sampling in mid-August (day 228) coincided with a deeper (29 m) epilimnion and decreased water clarity (k_{PAR} = 0.143 m^{-1}) relative to mid-July (k_{PAR} = 0.115 m^{-1}). Lake Superior was sampled in late July (day 212) when the seasonal thermocline commenced at 10 m depth and the water column was optically clear (k_{PAR} = 0.116 m^{-1}). Bio-optical profiling at both sites showed that a_{PSII} peaked around the third optical depth and phytoplankton had relatively high values of F_Q'/F_M' through depth. SCFs increased at all sites through depth, and the highest values observed in this study (SCF > 1.5) occurred within the Georgian Bay seasonal thermocline. Unlike Lake Erie stations, *in situ* phytoplankton production maxima occurred at or just above the first optical depth in Lake Superior and Georgian Bay, and consequently traditional scaling techniques ($P_{[INT,\lambda]}$ and $P_{[INT,SV]}$) severely underestimated *in situ* photosynthesis ($\Sigma PP_{[Z,\lambda]}$) at depth.

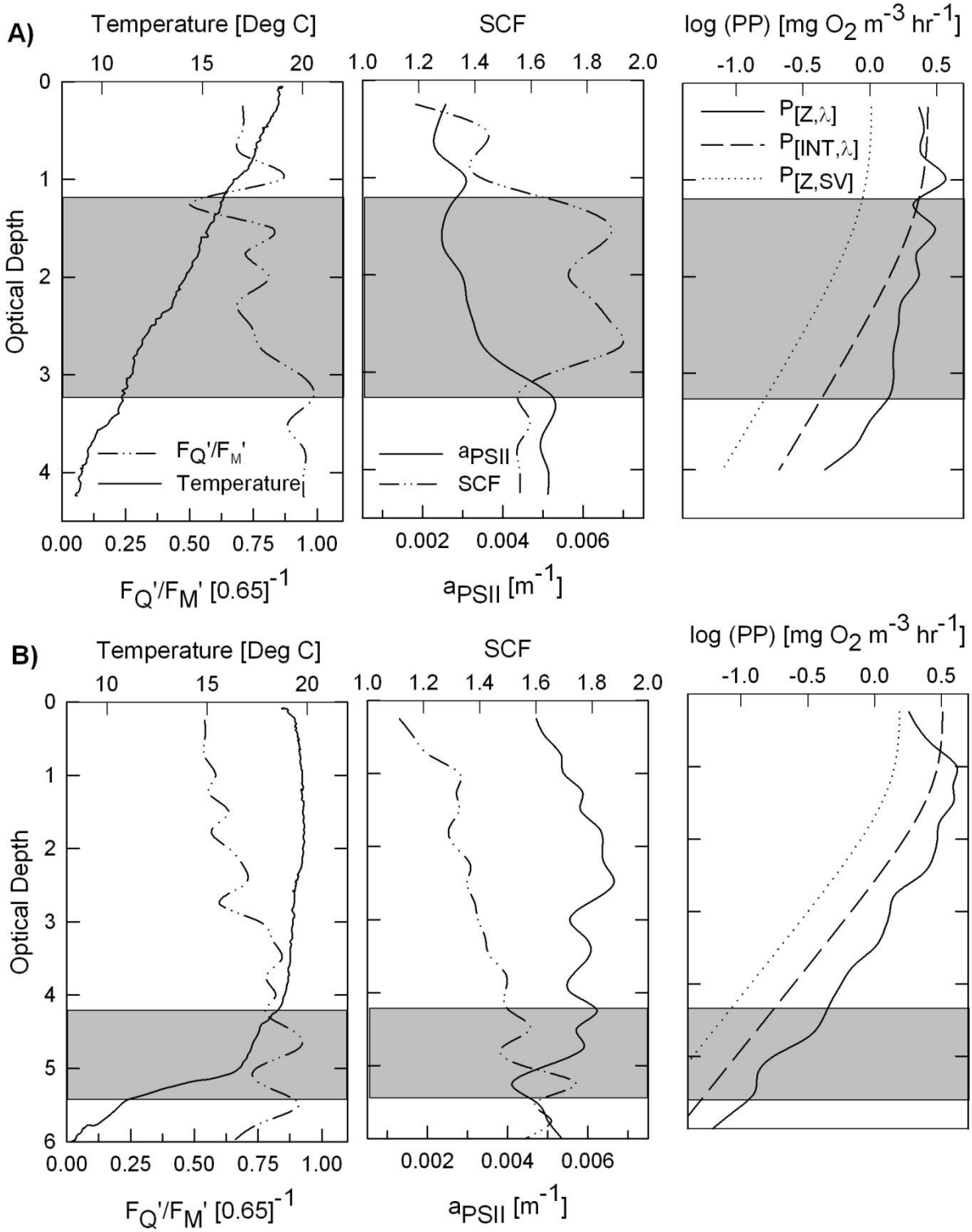

Figure 4.14: Vertical patterns of temperature, F_Q'/F_M', SCF, a_{PSII} and PP derived from three scaling methods in Georgian Bay on day of the year A) 199 and B) 228. Grey shadow is the approximate optical depth of the seasonal thermocline.

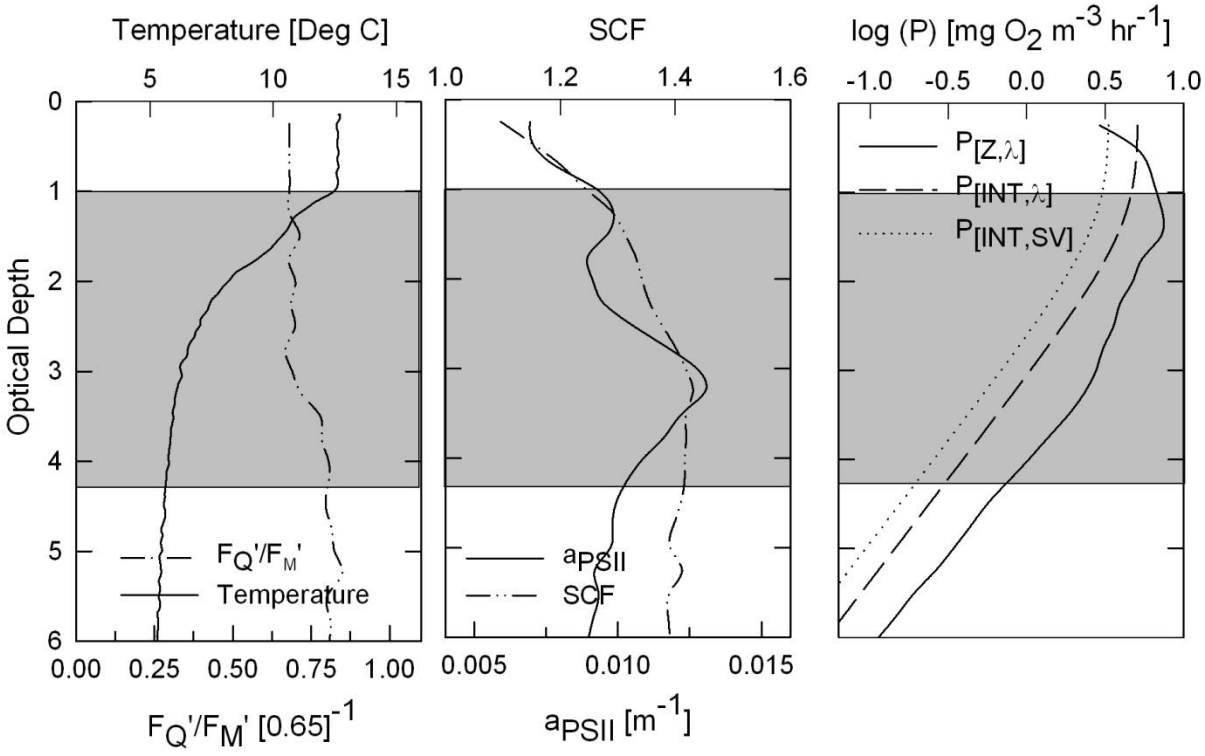

Figure 4.15: Vertical patterns of temperature, F_Q'/F_M', SCF, a_{PSII} and PP derived from three scaling methods in Lake Superior. Grey shadow is the approximate optical depth of the seasonal thermocline.

Figure 4.16 summarizes the vertical patterns of photosynthesis derived in this study through different scaling techniques. Figure 4.16A documents the relative contribution of *in situ* sub-epilimnetic areal phytoplankton production to total areal phytoplankton production for all stratified stations as a function of the ratio of epilimnetic to euphotic depth (z_{epi}:z_{eu}). A hyperbolic tangent curve predicts that as z_{epi}:z_{eu} decreases, an increasing percentage of areal phytoplankton production occurs beneath the epilimnion (r^2 =0.87, n=36, $p < 0.01$). This relationship described in Figure 4.16A is not simply a function of increased light availability beneath the seasonal epilimnion, as it also takes into account increases in a_{PSII} and SCF through depth: Shown in Figure 4.16B and C, the ratio of $\Sigma PP_{[INT,\lambda]}$ and $\Sigma PP_{[INT,SV]}$ to $\Sigma PP_{[Z,\lambda]}$ as a

function of the ratio of epilimnetic to euphotic depth (z_{epi}:z_{eu}). Figure 4.16B and 4.16C both clearly shows that as z_{epi}:z_{eu} decreases $\Sigma PP_{[INT,\lambda]}$ and $\Sigma PP_{[INT,SV]}$ increasingly underestimate *in situ* photosynthesis as the probability of sub-epilimnetic phytoplankton communities better acclimated to low-light environment increases.

.

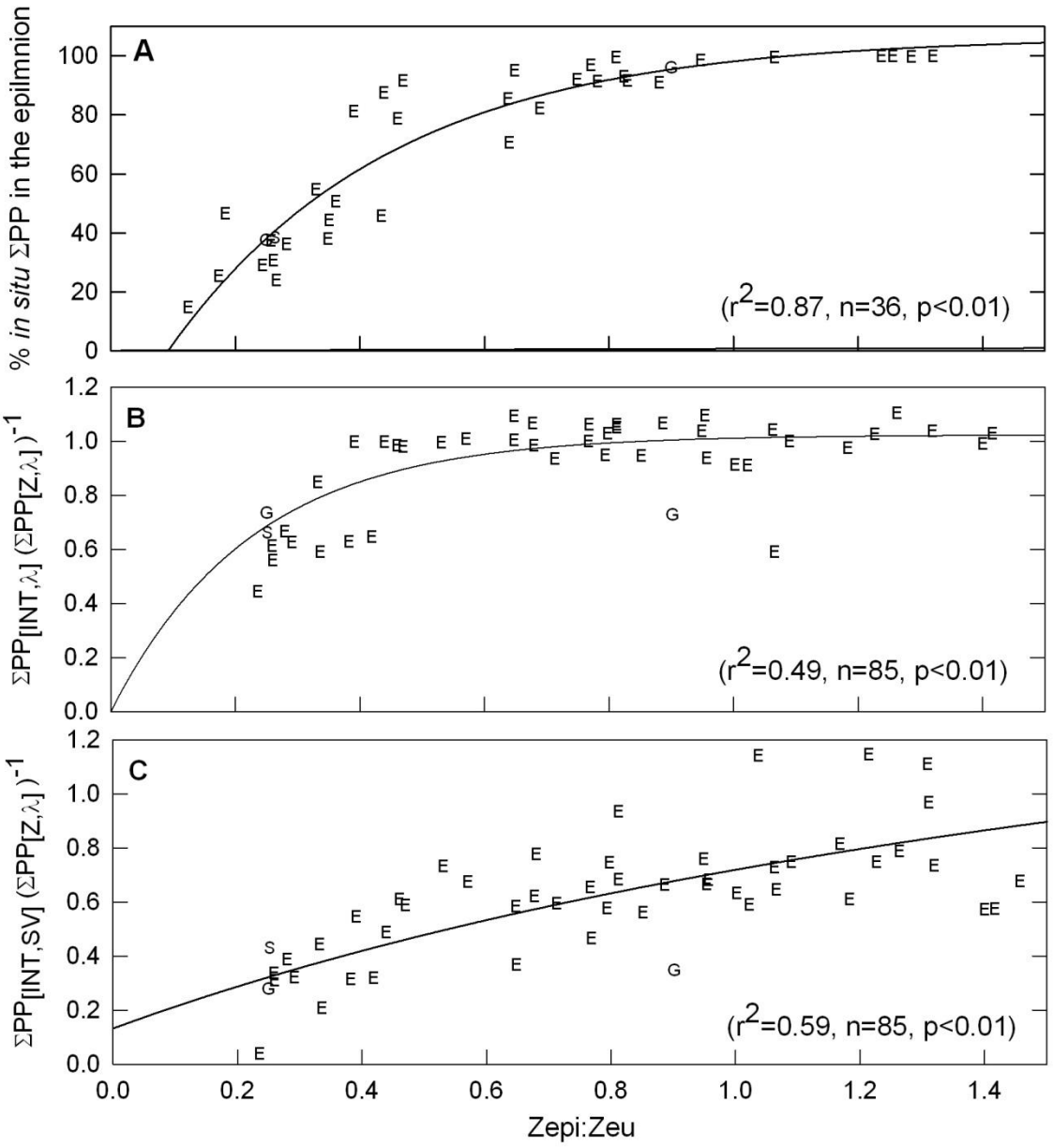

Figure 4.16: A) % of *in situ* ΣPP in the epilimnion and B) ratio of areal phytoplankton production derived from epilimnetic integrated sample to *in situ* ΣPP as a function of epilimnetic depth (Z_{Epi}) to euphotic depth (Z_{EU}).

Section 4.4: Discussion

This chapter is the first to explicitly employ bio-optical techniques to analyze vertical patterns of photosynthesis and its constituents in freshwater lakes. This discussion begins reviewing ecosystem implications of the vertical distribution of photosynthesis. Vertical and seasonal distributions of the bio-optical model constituents a_{PSII}, SCF and F_Q'/F_M' are then interpreted, followed by a discussion on persistent vertical patterns of photosynthesis. Finally, methodological sources of error are presented.

Section 4.4.1: Ecological implications of the vertical distribution of phytoplankton photosynthesis and biomass

The vertical distribution of phytoplankton biomass and photosynthesis can affect the community ecology of zooplankton and animal-mediated nutrient cycling in aquatic environments. The vertical distribution of zooplankton is dictated by water temperature, food and predation risk, so many species seek refuge in the dark hypolimnion during the day and undergo nocturnal vertical migration to feed (Lampert et al. 2003). The presence of a DCM truncates the vertical migration for many zooplankton species (Harris 1988) and in the Laurentian Great Lakes often coincides with distinct zooplankton communities that graze exclusively in either the epilimnion or around the DCM (Watson and Carpenter 1974). Grazing within the DCM increases as the temperature gradient between the epilimnion and metalimnion converge (Lampert et al. 2003), and metalimnetic food sources can offer greater nutritional quality than epilimnetic food sources (Williamson et al. 1996). Nutrient translocation refers to animal mediated processes that transform (particulate to dissolved) and transport nutrients across physical barriers (Vanni 2002). Nutrient translocation by zooplankton and their consumers across the thermal gradients that physically impede nutrient diffusion can be a substantial source

of 'new' (sensu Vanni 2002) nutrients within the eplimnetic strata. The presence of a DCM with active zooplankton grazing, excretion and predation by secondary consumers therefore can dampen the vertical extent of nutrient translocation.

The vertical distribution of phytoplankton can also directly influence the physio-chemical properties of their environment (Reynolds 2004). Non-uniformity of the vertical distribution of phytoplankton creates micro-regions of comparatively high heat absorption that are then subject to buoyancy driven mixing and may ultimately augment the depth of vertical mixing (Lewis et al. 1983). This mechanism would transport DCM cells from the metalimnion, and indeed Fee (1976) noted that fall phytoplankton succession leading to an epilimnetic bloom consisted almost entirely of metalimnetic species. Finally, and of direct relevance to the management of Lake Erie, if the presence of measurable photosynthesis in the central basin hypolimnion (Wilhelm et al. 2006, this study) exceeds respiration, hypolimnetic deoxygenation may be initially impeded though the eventual mineralization of this 'new' biomass may ultimately fuel deoxygenation.

Section 4.4.2: The vertical and seasonal distribution of a_{PSII}, SCFs and f_{PSII}

a_{PSII} - A study implicitly examining DCM in all five Laurentian Great Lakes generally showed the size of the DCM peak increased with increased epilimnetic water clarity (Barbiero and Tuchman 2001). Though the highest a_{PSII} peaks in this study coincided with the most optically clear epilimnions, there was no significant relationship between either the percent increase in a_{PSII} through depth or the magnitude of the a_{PSII} peak with optical clarity (k_{PAR}, $p>0.10$). Barbiero and Tuchman (2001) also noted the physical depth of the DCM increased with decreasing k_{PAR}, transforming their data into optical depths demonstrates that >50% of reported DCMs in their survey occurred within the fourth optical depth, consistent with the most

frequently observed DCM optical depths in this study (Figure 4.10).

The vertical structure of a_{PSII} through time and space broadly matched similar patterns in nutrients; statistically significant vertical gradients of a_{PSII} coincided with statistical gradients in TP, SRP and SiO_2. Of all nutrients measured TP was the best predictor of a_{PSII} as phosphorus is the most growth limiting nutrient in Lake Erie where it is significantly correlated with chl *a* and ΣPP (Guildford et al. 2005; Smith et al. 2005). When all data binned by cruise and strata was pooled the correlation between TP and a_{PSII} was weak (r^2=0.28, n=29, $p < 0.05$) but improved when data was segregated by cruise (r^2 ranged from 0.70 in September to 0.95 in July). Low epilimnetic TP concentrations in June and July coincided with significantly enriched measurements of a_{PSII} in the metalimnion and hypolimnion. In September epilimnetic nutrient enrichment increased a_{PSII} in this strata, and in conjunction with a downward displacement of the seasonal thermocline severely diminished the light available to sub-epilimnetic phytoplankton populations to the extent that a_{PSII} was minimal at depth. It is interesting to note that the return of isothermal conditions in the fall is often invoked as the mechanism responsible for epilimnetic nutrient and algal enrichment at this time (Wetzel 2001). Nutrient, chl *a*, and a_{PSII} data shown here demonstrates that this enrichment begins when the water column is still stratified. Whether the cause of this enrichment is physical entrainment of both nutrients and phytoplankton into the epilimnion or animal mediated nutrient translocation that ultimately fuels new phytoplankton biomass remains unclear.

In Lake Erie, sub-epilimnetic increases in a_{PSII} are predominantly a function of increased pigment content and not algal biomass, indicating that photoadaptation is the likely mechanism responsible for observed DCMs. Primary consumers do not subsist on chlorophyll alone as organic carbon is a better proxy for the caloric content of phytoplankton (Cullen 1982), thus the

DCMs in Lake Erie are not significantly enriched food sources for zooplankton and microheterotrophs relative to epilimnetic phytoplankton.

Spectral Correction Factors (SCF) – SCFs are a function of the spectral overlap of radiant energy and a_{PSII}. Chapter 3 discussed that spectral niches are created along an optical gradient for phytoplankton pigment groups. This gradient is largely consistent with reported DCM community compositions across optical gradients in the Laurentian Great Lakes (Barbiero and Tuchman 2001; Wilhelm et al. 2006) and can be empirically verified with SCFs. In the optically clearer waters of Georgian Bay, Lake Superior and Lake Erie at the onset of stratification the underwater spectra is blue-shifted. Blue-shifted phytoplankton pigment groups (with accessory chlorophylls and photosynthetic carotenoids; Figure 1.1) dominate the DCM in these environments (Barbiero and Tuchman 2001) and SCFs reported here for these environments are comparatively high. As k_{PAR} increases the underwater spectra becomes red-shifted, creating a niche for phycoerythrin-containing phytoplankton groups (Stomp et al. 2007). This spectral transition occurs through the stratified season in Lake Erie as shown in Figure 4.11, and high metalimnetic and hypolimnetic SCF values at this time are consistent with the phycoerythrin-rich prokaryotes that dominate DCM populations in Lake Erie's central basin in the late summer (Wilhelm et al. 2006). During the May survey diatoms dominated the community composition (Rattan 2009) though high k_{PAR} values at this time favor a more red-shifted phytoplankton group, consequently SCFs in May are comparatively reduced.

F_Q'/F_M' - F_Q'/F_M' measurements were markedly consistent across basins and through depth when Lake Erie was stratified, and the most notable spatial or temporal pattern was the reduced F_Q'/F_M' values measured in all basins during May. An accompanying examination of spatio-temporal patterns of F_Q'/F_M' and its drivers has been performed elsewhere (Rattan 2009),

though in that study background fluorescence and instrument noise were not corrected for so reported values here are comparatively less variable and on average higher (sensu Figure 2.6). Regardless, non-fluorometric indices of nutrient deficiency were most prevalent in May (Rattan 2009), consistent with other studies in Lake Erie (Guildford et al. 2005). Though under balanced growth nutrient limited phytoplankton can maintain high values of F_Q'/F_M' (Parkhill et al. 2001; Suggett et al. 2008), colder water temperatures in May likely decrease phytoplankton growth rates that may impede acclimation to balanced growth conditions (Geider et al. 1998), consistent with low SCFs at this time. Overall, spatial-temporal variability of F_Q'/F_M' is dwarfed by similar patterns in a_{PSII} and therefore have a relatively muted effect on the vertical distributions photosynthesis presented here.

Section 4.4.3: The vertical distribution of photosynthesis

This chapter unequivocally demonstrates that a substantive fraction of areal phytoplankton production can occur beneath the epilimnion. Figure 4.16A demonstrates that as the ratio of epilimnetic to euphotic depth (z_{Epi}:z_{EU}) decreases, the percent contribution of sub-epilimnetic ΣPP increases. This finding is consistent with Fee (1980) whose intensive *in situ* studies showed that sub-epilimnetic phytoplankton production is quantitatively unimportant in eutrophic lakes but can account for up to 50% of annual phytoplankton production in oligotrophic lakes. Moreover, routine assumptions that scale epilimnetic measurements of photosynthesis through the water column increasingly underestimate ΣPP along a decreasing z_{Epi}:z_{EU} gradient (Figure 4.16B). Taken together, Figure 4.16 shows that increasing sub-epilimetic production is not simply an artefact of increased light availability when z_{Epi}:z_{EU} is less than 1, as it has clearly been demonstrated that sub-epilimnetic phytoplankton in these ecosystems are chromatically well adapted to sub-saturating light environments. This finding

calls into question the accuracy of previously published ΣPP estimates in oligotrophic environments based on *in vitro* incubations, and may in part explain the reported imbalance in Lake Superior's carbon balance (Urban et al. 2005) and increasing net heterotrophy along a decreasing trophic gradient (Del Giorgio and Peters 1994).

In situ bio-optical estimates of photosynthesis in freshwater lakes are currently constrained to large lakes (Pemberton et al. 2007; this study). Relative to the Laurentian Great Lakes, smaller lakes generally have lower z_{Epi}:z_{EU} ratios where diminished fetch lengths reduce wind speed and consequently the depth of the seasonal thermocline (Mazumbder and Taylor 1994; Fee et al. 1996). If the findings of Figure 4.16 are applicable across a gradient of lake sizes, then the quantitative contribution of sub-epilimnetic production will be even larger in smaller lakes along similar optical gradients as the Laurentian Great Lakes.

Section 4.4.4: Assumptions and sources of error.

Chapter 2 presents sources of error related to the methodological derivation of photosynthetic rates from bio-optical models. What follows is a brief discussion of two sources of error related to applying the bio-optical model *in situ* to determine the vertical distribution of photosynthesis and attendant estimations of ΣPP. Specifically these sources of error are photoinhibition and variability in the light-saturation constant E_K.

This bio-optical model excludes photo-physiologically reduced values of F_Q'/F_M' and so resultant vertical distributions of photosynthesis do not account for photoinhibitory losses. Basin specific measurements done over the course of the stratified season in Lake Erie have shown photoinhibition reduces daily ΣPP by 4-14% (Hiriart-Baer and Smith 2005), and the percent reduction is highest in west basin and decreases with increasing optical clarity. This spatial

pattern may seem counterintuitive but per unit euphotic depth UVA radiation, the predominant driver of photoinhibition in Lake Erie (Hiriart-Baer and Smith 2004), increases as overall euphotic depths decrease. Regardless of spatio-temporal patterns, photoinhibition is constrained to the epilimnion so estimates of the importance of sub-epilimnetic phytoplankton production are likely underestimates. The inability of the bio-optical model used here to account for photoinhibitory losses is not unique, photosynthetic rates derived from traditional *in-vitro* methods also routinely fail to account for photoinhibition. In fact bio-optical instrumentation can be an effective tool for measuring *in situ* photoinhibition (Marwood et al. 2000; Oliver et al. 2003), but for simplicity has been omitted from this thesis.

A simple sensitivity analysis was performed to estimate the influence of E_K on spatial and temporal patterns on ΣPP in Lake Erie. Briefly, ΣPP was recalculated for all bio-optical profiles by holding vertically resolved measurements of a_{PSII}, SCF, F_Q'/F_M', and k_{PAR} constant while varying E_K ± 25% and ± 50%. On average across all Erie measurements, varying E_K by ± 25% and ± 50% changed ΣPP by ±11% and ±19% respectively. Analyzing data at only the stations where thermal stratification occurred within the first 6 optical depths showed that as the fraction of total areal production in the epilimnion decreased, the percent change of ΣPP also decreased (r^2 = 0.33 to 0.36, n = 44, $p<0.01$ for all four sensitivity analyses). This simple exercise empirically demonstrates what is otherwise intuitive; light-limited phytoplankton production dominates in regions with substantive sub-epilimnetic populations and so areal phytoplankton production in these regions is relatively insensitive to errors or fluctuations in E_K.

Section 4.5: Conclusions and Recommendations

Chapter 2 demonstrates the validity of bio-optical methodology in estimating discrete measurements of oxygenic photosynthetic rates; this chapter demonstrates the utility of *in situ* bio-optical measurements through space and time. Consistent with previous studies in the Laurentian Great Lakes, when sufficient light penetrates through the epilimnion phytoplankton pigment biomass is maximal at or below the seasonal thermocline. Active fluorescence measurements clearly show that these phytoplankton communities are photosynthetically functional and not simply dead cells sedimenting out of the epilimnion. This chapter further demonstrates that spectral composition of PAR varies predictably at depth along an optical (k_{PAR}) gradient in the Laurentian Great Lakes. The spectral composition of PAR creates niches for phytoplankton pigment groups (Stomp et al. 2007) that is largely consistent with reported metalimnetic phytoplankton communities (Barbiero and Tuchman 2001; Wilhelm et al. 2006). Consequently metalimnetic and hypolimnetic phytoplankton communities are chromatically adapted to their light limited environment, as shown here with high reported SCFs at depth. Taken together, photoadaptation and chromatic adaptation augment light-limited photosynthetic rates beneath the epilimnion, to the extent that sub-epilimnetic production may dominate (>50%) total areal production (ΣPP), especially in oligotrophic environments when euphotic depths extend beyond the seasonal thermocline. Scaling techniques that extrapolate epilimnetic measurements of phytoplankton and photosynthesis through the water column can therefore significantly underestimate (>2-fold) ΣPP.

Chapter 5: General Conclusions and Recommendations

Phytoplankton production is amongst the most fundamental process in aquatic ecosystems, yet measurements of phytoplankton production in Laurentian Great Lakes are rare and often performed using different methodologies and scaling assumptions. This thesis has devolped and validated a bio-optical methodology that provides reliable measurements of *in situ* photosynthesis. Bio-optical models are largely a function of two parameters, the absorption spectrum of photosystem II (a_{PSII}) and the photochemical efficiency of PSII (f_{PSII}). In Lake Erie f_{PSII} is relatively constrained suggesting that even nutrient limited phytoplankton achieve balanced growth by adjusting the supply of energy through changes in light harvesting (a_{PSII}) to match the demand for photosynthetic energy. This thesis has demonstrated that the success of bio-optical models depends largely on the formulation of a_{PSII}. Alternative methods to derive a_{PSII}, largely ignored in published bio-optical models, were reviewed, formulated, and when incorporated into a bio-optical model and compared to synchronous *in vitro* production measurements, the bio-optical model outperforms all other comparative studies performed across a taxonomic gradient.

Having established a method that provides reliable *in situ* estimates of phytoplankton production, this thesis has quantified the magnitude of error associated with common assumptions that are inherent to *in vitro* estimates of phytoplankton production. Photosynthetic rates vary with the spectral quality of irradiance and euphotic zone spectra are highly variable through time and space, especially over depth, and are often poorly reproduced by i*n vitro* light sources. Spectral correction factors (SCFs) can be derived to estimate the disparity of phytoplankton production estimates that arise through differences between *in situ* and *in vitro* light environments. Through the development of an empirical model, this thesis has

demonstrated that the magnitude of SCFs vary predictably across optical and chl *a* gradients. Moreover the model shows that for commonly employed *in vitro* light sources, phytoplankton production is routinely underestimated by traditional *in vitro* methods, especially in oligotrophic waters. When applied to historic phytoplankton production estimates in Lake Erie, the model predicts that the reported lakewide decreases of phytoplankton production following nutrient loading abatement has been overestimated by a factor of 2. This thesis also investigated how persistent vertical patterns of *in situ* photosynthesis deviate from nominally scaled *in vitro* measurements across mixing, trophic and taxonomic gradients in Lake Erie and opportunistic measurements in Lake Superior and Georgian Bay. The presence of deep chlorophyll maxima (DCM) in these lakes significantly enhances *in situ* production relative to nominal *in vitro* scaling assumptions. Not only is DCM production enhanced through elevated biomass relative to the epilimnion, but DCM phytoplankton communities appear to be spectrally adapted to these low light environments.

Taken together, the common assumptions employed in traditional *in vitro* phytoplankton production measurements may underestimate *in situ* photosynthesis by a factor of 2. The disparities between *in vitro* and *in situ* estimates are greatest in oligotrophic waters where DCMs are likely to occur when the water column is stratified and where *in situ* spectral irradiance can deviate significantly from *in vitro* light sources. These disparities are large relative to the accuracy of bio-optical estimates of phytoplankton production shown here. Thus the bio-optical model developed here often yields better estimates of phytoplankton photosynthesis than the commonly used traditional approach.

The various methods and equipment required to parameterize the bio-optical model have been rigorously investigated and validated in marine environments and now in freshwater

environments. These methodologies are straight forward and require only an *in situ* active fluorometer, a spectral-radiometer and a spectral fluorometer, a small investment for the various governmental agencies tasked with monitoring the Laurentian Great Lakes. These instruments can all be operated auotonomously, so it is possible to deploy all relevant bio-optical instrumentation alongside existing meteorological buoys and thermistor strings to provide temporally resolved estimates of ΣPP. Such an undertaking would provide a tool that, year after year, provides a means to better characterize dynamic changes in the phytoplankton community and better assess changes in ΣPP and its ecological drivers in the years to come.

Bibliography

Auer, M.T. and L.A. Bub. 2004. Selected features of the distribution of chlorophyll along the southern shore of Lake Superior. J. Great Lakes Res. 30: 269-284.

Babin, M, A. Morel, H. Claustre, A. Bricaud, Z. Kolber and P.G. Falkowski. 1996. Nitrogen- and irradiance-dependent variations of the maximum quantum yield of carbon fixation in eutrophic, mesotrophic and oligotrophic marine systems. Deep-Sea Research. 43(8): 1241-1272.

Barbiero, R.P., and M.L. Tuchman. 2001. Results from the U.S. EPA's biological open water surveillance program of the Laurentian Great Lakes: II. Deep Chlorophyll Maxima. *J. Great Lakes Res.* 27: 155-166.

Barlow, R.G., J. Aiken, P.M. Holligan, D.G. Cummings, S. Maritorena and S. Hooker. 2002. Phytoplankton pigment and absorption characteristics along meridional transects in the Atlantic Ocean. Deep-Sea Research I. 47:637-660.

Behrenfeld, M.J. and P.G. Falkowski. 1997. A consumer's guide to primary productivity models. Limnol. Oceanogr. 42: 1479-1491.

Behrenfeld, M.J. and E. Boss. 2003. The beam attenuation to chlorophyll ratio: an optical index of phytoplankton physiology in the surface ocean? Deep-Sea Research I: 50: 1537-1549.

Behrenfeld, M.J., O. Prasil, M. Babin and F. Bruyant. 2004. In search of a physiological basis for covariations in light-limited and light-saturated photosynthesis. J. Phycol. 40: 4-25.

Behrenfeld, M.J., K. Worthington, R.M. Sherrell, F.P. Chavez, P. Strutton, M. McPhaden and D.M. Shea. 2006. Controls on tropical Pacific Ocean productivity revealed through nutrient stress diagnostics. Nature. 443: 1025-1028.

Berges, J.A., D. O. Charlebois, D.C. Mauzerall and P.G. Falkowski. 1996. Differential effects of nitrogen limitation on photosynthetic efficiency of photosystems I and II in microalgae. Plant. Physiol. 110: 689-696.

Bidigare, R.R. and M.E. Ondrusek. 1990. *In vivo* absorption properties of algal pigments. SPIE Ocean Optics X. 1302:290-302.

Binding, C.E., J.H. Jerome, R.P. Bukata and W.G. Booty. 2008. Spectral absorption properties of dissolved and particulate matter in Lake Erie. Remote Sensing of Environment. 112: 1702-1711.

Blanco, P.E., P. Cermeno, M. Espineira and E. Fernandez. 2007. Phytoplankton photosynthetic efficiency and primary production rates estimated from fast repetition rate fluorometry at

coastal embayments affected by upwelling (Rias Baixas, NW of Spain). J. Plank. Res. 28(12): 1153-1165.

Boyd, P.W., J. Aiken and Z. Kolber.. 1997. Comparison of radiocarbon and fluorescence based (pump and probe) measurements of phytoplankton photosynthetic characteristics in the Northeast Atlantic Ocean. Mar. Ecol. Prog. Ser. 149:215-226.

Bricaud, A., M. Babin, A. Morel and H. Claustre. 1995. Variability in the chlorophyll-specific absorption coefficients of natural phytoplankton: Analysis and parameterization. J. Geophy. Res. 100: 13321-13332.

Bricaud, A., H. Claustre, J. Ras nad K. Oubelkheir. 2004. Natural variability of phytoplanktonic absorption in oceanic waters: Influence of the size structure of algal populations. J. Geophys. Res. 109. C11010.

Christensen, D.L., S.R. Carpenter and K.L. Cottingham. 1995. Predicting chlorophyll vertical distribution in response to epilimnetic nutrient enrichment in small stratified lakes. J. Plank. Res. 17(7): 1461-1477.

Corno, G., R.M. Letelier, M.R. Abbott and D.M. Karl. 2005. Assessing primary production variability in the north Pacific tropical gyre: A comparison of fast repetition rate fluorometry and 14C measurements. J. Phycol. 42:51-60.

Culver, M. E. and M.J. Perry. 1999. The response of photosynthetic absorption coefficients to irradiance in culture and in tidally mixed estuarine waters. Limnol. Oceanogr. 44(1):24-36.

Davis, C.O. and M.S. Simmons. 1979. Water chemistry and phytoplankton field and laboratory procedures. Special Rep. No. 70. Great Lakes Research Division. Univ. Michigan. Ann Arbor, USA.

Demmig-Adams, B., and W.W. Adams III. 1992. Photoprotection and other responses of plants to high light stress. Annual Review of Plant Physiology and Plant Molecular Biology. 43: 599-626.

Del Giorgio, P.A. and R.H. Peters. 1994. Patterns in planktonic P:R ratios in lakes: Influence of lake trophy and dissolved organic carbon. Limnol. Oceanogr. 39(4): 772-787.

Depew, D., R.E.H. Smith and S. Guildford. 2006. Production and respiration in Lake Erie Plankton Communities. J. Great Lakes Res. 32: 817-831.

Depew, D.C., S.J. Guildford and R.E.H. Smith. 2006. Nearshore-offshore comparison of chlorophyll a and phytoplankton production in the dreissenid-colonized eastern basin of Lake Erie. Can. J. Fish. Aquat. Sci. 63: 1115-1129.

Dolan, D.M. and K.P. McGunagle. 2005. Lake Erie total phosphorus: Loading analysis and

update: 1996-2002. J. Great Lakes Res. 31(Suppl. 2):11-22.

Downing, J.A., C. Plante and S. Lalonde. 1990. Fish production correlated with primary productivity, not the morpheodaphic index. Can. J. Fish. Aqaut. Sci. 47: 1929-1936.

Dubinsky, Z., P.G. Falkowksi and K. Wyman. 1986. Light harvesting and utilisation by phytoplankton. Plant Cell Phhysiol. 27: 1335-1349.

Eijckelhoff, C. and J.P. Dekker 1997. A routine method to determine the chlorophyll *a*, pheophytin *a* and β-carotene contents of isolated Photosystem II reaction center complexes. Photosyn. Res. 52: 69-73.

Eisner, L.B., M.S. Twardowski, T.J. Cowles and M.J. Perry. 2003. Resolving phytoplankton photoprotective:photosynthetic carotenoid ratios on fine scales using in situ absorption measurements. Limnol. Oceanogr. 48(2): 632-646.

Emerson, R. and W. Arnold 1932. The photochemical reaction in photosynthesis. The Journal of General Physiology. 16: 191-205.

Eppley, R.W. 1980. Estimating phytoplankton growth rates in the central oligotrophic oceans. *In* Primary productivity in the sea.

Fahnenstiel, G.L. and D. Scavia. 1987. Dynamics of Lake Michigan phytoplankton: The deep chlorophyll layer. J. Great Lakes Res. 13: 285-295.

Fahnenstiel, G.L., J.F. Chandler, H.J. Carrick and D. Scavia. 1989. Photosynthetic characteristics of phytoplankton communities in Lakes Huron and Michigan: P-I parameters and end-products. J. Great Lakes Res. 15: 394-407.

Falkowksi, P.G., T.G. Owens, A.C. Ley and D.C. Mauzerall. 1981. Effects of growth irradiance levels on the ratio of reaction centres in two species of marine phytoplankton. Plant Physiol. 68: 969-973.

Falkowksi, P.G., M.E. Katz, A.H. Knoll, A. Quigg, J.A. Raven, O. Schofield and F.J.R. Taylor. 2004. The evolution of modern eukaryotic phytoplankton. Science. 305: 354-360.

Falkowski, P.G. and J.A. Raven. 2007. Aquatic photosynthesis. Blackwell Science U.K.

Fee, E.J. 1976. The vertical and seasonal distribution of chlorophyll in lakes of the Experimental Lakes Area, northwestern Ontario: Implications for primary production estimates. Limnol. Oceanogr. 21: 767-783.

Fee, E.J. 1978. A procedure for improving estimates of *in situ* primary production at low irradiances with an incubator technique. Int. Ver. Theor. Angew. Limnol. Verh. 20: 59-67.

Fee, E.J. 1978. Studies of hypolimnion chlorophyll peaks in the Experimental Lakes Area,

north-western Ontario. Can. Fish. Mar. Serv. Tech. Rep. 752. 21p,

Fee, E.J. 1980. Important factors for estimating phytoplankton production in the Experimental Lakes Area. Can. J. Fish Aquat. Sci. 37: 513-522.

Fee, E.J., J.A. Shearer, E.R. DeBruyn and E.U. Schindler. 1992. Effects of lake size on phytoplankton photosynthesis. Can. J. Fish. Aquat. Sci. 49: 2445-2459.

Fee, E.J., R.E. Hecky, S.E.M. Kasian and D.R. Cruikshank. 1996. Effects of lake size, water clarity and climatic variability on mixing depths in Canadian Shield lakes. *Limnol. Oceanogr.* 41(5): 912-920.

Figueiras, F.G., B. Arbones and M. Estrada. 1999. Implications of bio-optical modelling of phytoplankton photosynthesis in Antarctic waters: Further evidence of no light limitation in the Bransfield Strait. Limnol. Oceanogr. 44(7):1599-1608.

Flameling, I.A. and J. Kromkamp. 1998. Light dependence of quantum yiels of PSII charge separation and oxygen evolution in eukaryotic algae. Limnol. Oceanogr. 43(2): 284-297.

Fuchs, E., R.C. Zimmerman and J.S. Jaffe. 2002. The effect of elevated levels of phaeophytin in natural water on variable fluorescence measured from phytoplankton. J. Plank. Res. 24:1221-1229.

Gaarder, T. and H.H. Gran. 1927. Investigations of the production of plankton in the Olso Fjord. Rapp. Cons. Explor. Mer. 42: 1-48.

Genty, B., J.-M. Braintais and N.R. Baker. 1989. The relationship between the quantum yield of photosynthetic electron transport and quenching of chlorophyll fluorescence. Biochimica et Biophysica Acta. 990: 87-92.

Geider, R.J., H.L. MacIntyre and T.M. Kana. 1997. Dynamic model of phytoplankton growth and acclimation: responses of the balanced growth rate and the chlorophyll *a*:carbon ratio to light, nutrient-limitation and temperature. Mar. Ecol. Prog. Ser. 148: 187-200.

Glooshenko,W.A., J.E. Moore, and R.A. Vollenweider. 1973. Chlorophll a distribution in Lake Huron and its relationship to primary productivity. Proc. 16th Conf. Great Lakes Res. 40-49.

Glooshenko, W.A., J.E. Moore, M. Munawar, and R.A. Vollenweider. 1974. Primary production in Lakes Ontario and Erie: A comparative study. J. Fish. Res. Bd. Can. 31: 253-265.

Greene, R.M., Z.S. Kolber, D.G. Swift, N.W. Tindale and P.G. Falkowski. 1994. Physiological limitation of phytoplankton photosynthesis in the eastern equatorial Pacific determined from variability in the quantum yield of fluoresecence. Limnol. Oceanogr. 39(5): 1061-1074.

Guildford, S.J., R.E. Hecky, R.E.H. Smith, W.D. Taylor, M.N. Charlton, L. Barlow-Busch and

R.L. North. 2005. Phytoplankton nutrient status in Lake Erie in 1997. J. Great Lakes Res. 31(Suppl. 2):72-88.

Harris, R.P. 1988. Interactions between diel vertical migratory behavior of marine zooplankton and the subsurface chlorophyll maximum. Bulletin of Marine Science: 43(3): 663-674.

Hiriart-Baer, V.P. and R.E.H. Smith. 2004. Models for ultraviolet radiation-dependent photoinhibition of Lake Erie phytoplankton. Limnol. Oceanogr. 49(1): 202-214.

Hiriart-Baer, V.P. and R.E.H. Smith. 2005. The effect of ultraviolet radiation on freshwater planktonic primary production: The role of recovery and mixing processes. Limnol. Oceanogr. 50(5): 1352-1361.

Holm-Hansen, O., C.J. Lorenzn, R.W. Holmes and J.D.H. Strickland. 1965. Fluorometric determination of chlorophyll. J. Cons. Perm. Int. Explor. Mer. 30: 3-15.

IPCC 2007: Climate Change 2007: The physical science basis. Contribution of working group I to the fourth assessment report of the intergovernmental panel on climate change. [Solomon, S., D. Qin, M. Manning, Z. Chen, M. Marquis, K.B. Averyt, M. Tignor and H.L. Millers (eds.)]. Cambridge University Press, Cambridge, United Kingdom. 996 pp.

Jassby, A.D., and T. Platt. 1976. Mathematical formulation of the relationship between photosynthesis and light for phytoplankton. . Limnol. Oceanogr. 21: 540-547.

Jerlov, N.G. 1976. Marine Optics. Elsevier. Amsterdam, The Netherlands.

Johnsen, G., B. B. Prezelin and R.V.M. Jovine. 1997. Fluorescence excitation spectra and light utilization in two red tide dinoflagellates. Limnol. Oceanogr. 42: 1166-1177.

Johnsen, G. and E. Sakshaug. 2007. Biooptical characteristics of PSII and PSI in 33 species (13 pigment groups) of marine phytoplankton, and the relevance for pulse amplitude-modulated and fast-repetition-rate fluorometry. J. Phycol. 48: 1236-1251.

Kaiblinger, C. and M.T. Dokulil. 2006. Application of fast repetition rate fluorometry to phytoplankton photosynthetic parameters in freshwaters. Photosyn. Res. 88:19-30.

Kasting, J.F. 1993. Earth's early atmosphere. Science. 259: 920-926.

Kirk, J.T.O. 1994. Light and photosynthesis in aquatic ecosystems. Cambridge University Press.

Knap, A., A. Michaels, A. Close, H. Ducklow and A. Dickson. 1996. Protocols for the Joint Global Ocean Flux Study (JGOFS) core measurements. JGOFS Report No. 19. Reprint of the IOC Manuals and Guides No. 29, 1994. UNESCO.

Kolber, Z. and P.G. Falkowski. 1993. Use of active fluorescence to estimate phytoplankton photosynthesis in situ. Limnol. Oceanogr. 38: 1646-1665.

Kolber, Z.S., O. Prášil and P.G. Falkowski. 1998. Measurements of variable chlorophyll fluorescence using fast repetition rate techniques: defining methodology and experimental protocols. Biochim. Biophys. Acta 1367: 88-106.

Krause, G.H. and E. Weis. 1991. Chlorophyll fluorescence and photosynthesis: The basics. Annu. Rev. Plant Physiol. Plant Mol. Biol. 42: 313-349.

Kromkamp, J. and R.M. Forster. 2003. The use of variable fluorescence measurements in aquatic ecosystems: Differences between multiple and single turnover measuring protocols and suggested terminology. Eur. J. Phycol. 38: 103-112.

Kromkamp, J., N.A. Dijkam, J. Peene, S.G.H. Simis and H.J. Gons. 2008. Estimating phytoplankton primary production in Lake IJsselmeer (The Netherlands) using variable florescence (PAM-FRRF) and C-uptake techniques. Eur. J. Phycol. 43: 327-344.

Lampert, W. and B.E. Taylor. 1985. Zooplankton grazing in a eutrophic lake: Implications of diel vertical migration. Ecology: 66(1):68-82.

Lampert, W., E. McCauley and B.F.J. Manley. 2003. Trade-offs in the vertical distribution of zooplankton: ideal free distribution with costs? Proc. Biol Sci. 270(1516) 765-773.

Laney, S.R. 2003. Assessing the error in photosynthetic properties determined by fast rate repetition fluorometry. Limnol. Oceanogr. 48: 2234-2242.

Laney, S.R. and R.M. Letelier. 2008. Artifacts in measurements of chlorophyll fluorescence transients, with specific application to fast repetition rate fluorometry. Limnol. Oceanogr. Methods. 6: 40-50.

Laws, E.A, G.R. Ditullio, K.L. Carder, P.R. Betzer and S. Hawes. 1990. Primary production in the deep blue sea. Deep-Sea research. 37(5): 715.730.

Lewis, M.R. and Smith, J.C. 1983. A small-volume, short-incubation time method for the measurement of photosynthesis as a function of incident irradiance. Mar. Ecol. Prog. Ser. 13: 99-102.

Lewis, M.R., J.J. Cullen and T. Platt. 1983. Phytoplankton and thermal structure in the upper ocean: Consequences of nonuniformity in chlorophyll profile. J. Geophy. Res. 88 (C4): 2565-2570.

Lewis, M.R., R.E. Warnock and T. Platt. 1985. Absorption and photosynthetic action spectra for natural phytoplankton populations: Implications for production in the open ocean. Limnol. Oceanogr. 30(4): 794-806.

Ley, A.C. and D. Mauzerall. 1982. Absolute absorption cross sections for photosystem II and the minimum quantum requirement for photosynthesis in Chlorella vulgaris. Biochim. Biophys. Acta 680: 95-106.

Lippemeier, S., D.M.F. Frampton, S.I. Blackburn, S.C. Geier and A.P. Negri. 2003. Influence of phosphorus limitation on toxicity and photosynthesis of *Alexandrium minutum* (Dinophyceae) monitored by in-line detection of variable chlorophyll fluorescence. J. Phycol. 38: 320-331.

Lindley, S.T., R.R. Bidigare and R.T. Barber. 1995. Phytoplankton photosynthesis parameters along 140 W in the equatorial Pacific. Deep-Sea Research II. 42: 441-463.

MacIntyre, S. 1993. Vertical mixing in a shallow, eutrophic lake: Possible consequences for the light climate of phytoplankton. Limnol. Oceanogr. 38(4): 798-817,

Makarewicz, J.C., P. Bertran and T.W. Lewis. 2000. Chemistry of the offshore surface waters of Lake Erie: Pre and post-Driessena introduction. J. Great Lakes Res. 26(1):82-93.

Markager, S. And W.F. Vincent. 2001. Light absorption by phytoplankton: development of a matching parameter for algal photosynthesis under different spectral regimes. J. Plankton Res. 23(12):1373-1384.

Marra, J., C.C. Trees, R.R. Bidigare and R.T. Barber. 2000. Pigment absorption and quantum yields in the Arabian Sea. Deep-Sea Research II. 47:1279-1299.

Marra, J., C.C. Trees and J.E. O'Reilly. 2007. Phytoplankton pigment absorption: A strong predictor of primary productivity in the surface ocean. Deep-Sea Research I. 54: 155-163.

Marra, J. 2009. Net and gross productivity: weighing in with ^{14}C. Aquat. Microb. Ecol. 56: 123-131.

Marwood, C.A., R.E.H. Smith, J.A. Furgal, M.N. Charlton, K.R. Solomon and G.M. Greenburg. 2000. Photoinhibition of natural phytoplankton assemblages in Lake Erie exposed to solar ultraviolet radiation. Canadian Journal of Fisheries and Aquatic Sciences. 57: 371-379.

Mazumbder, A. and W.D. Taylor. 1994. Thermal structure of lakes varying in size and water clarity. *Limnol. Oceanogr.* 39(4): 968-976.

Melrose, D.C., C.A. Oviatt, J.E. O'Reilly and M.S. Berman. 2006. Comparisons of fast repetition rate fluorescence estimated primary production and 14C uptake by phytoplankton. Mar. Ecol. Prog. Ser. 311: 37-46.

Millard, E.S., D.D. Myles, O.E. Johansson and K.M. Ralph. 1996. Phytoplankton photosynthesis at two indix stations in Lake Ontario 1987-1992. Assessment of the long-term response to phosphorus control. Can. J. Fish. Aquat. Sci. 53: 1092-1111.

Millard, E.S., E.J. Fee, D.D. Myles and J.A. Dahl. 1999. Comparison of phytoplankton photosynthesis methodology in Lake Erie, Ontario, the Bay of Quinte and the Northwest Ontario Lake size series. In State of Lake Erie ± SOLE) – Past, Present and Future. Munawar, M., T. Edsall and I.F. Munawar [eds]. Backhuys Publishers, Leiden, Netherlands. Pp. 441-468.

Moll, R.A. and E.F. Stoermer. 1982. A hypothesis relating trophic status and subsurface chlorophyll maxima of lakes. Archives fur hydrobiologie. 94: 425-440.

Moore, C.M., D. Suggett, P.M. Holligan, J. Sharples, E.R. Abraham, M.I. Lucas, T.P. Rippeth, N.R. Fisher, J.H. Simpson and D.J. Hydes. 2003. Physical controls on phytoplankton physiology and production at a shelf sea front: A fast repetition-rate fluorometer based study. Mar. Ecol. Prog. Ser. 259: 29-45.

Moore, C.M., M.I. Lucas, R. Sanders and R. Davidson. 2005. Basin-scale variability of phytoplankton bio-optical characteristics in relation to bloom state and community structure in the Northeast Altantic. Deep-Sea Research: 52: 401-419.

Moore, C.M., D.J. Suggett, A.E. Hickman, Y.-N. Kim, A.F. Tweddle, J. Sharples, R.J. Geider and P.M. Holligan. 2006. Phytoplankton photoacclimation and photoadaptation an response to environmental gradients in a sea shelf. Limnol. Oceanogr. 51(2): 939-949.

Morel, A. 1988. Optical Modeling of the upper ocean in relation to its biogenous matter content (Case 1 Waters). J. Geophy. Res. 93: 10749-10768.

Munawar, M., P. Stadelman and I.F. Munawar. 1974. Phytoplankton biomass, species composition and primary production at a nearshoreand a midlake station of Lake Ontario during IFYGL. In *Proc. 17th Conf. Great Lakes Res.*, pp. 629-652. Internat. Assoc. Great Lakes Res.

Oliver, R.L., J. Whittington, Z. Lorenz and I.T. Webster. 2003. The influence of vertical mixing on the photoinhibition of variable chlorophyll *a* fluorescence and its inclusion in a model of phytoplankton photosynthesis. Journal of Plankton Research. 25 (9): 1107-1129.

Oxborough, K. and N.R. Baker. 1997. Resolving chlorophyll a fluorescence images of photosynthetic efficiency into photochemical and non-photochemical components – calculations of qp and Fv'/Fm' without measuring Fo'. Photosynth. Rs. 54: 135-142.

Parkhill, J.P., G. Maillet and J.J. Cullen. 2001. Fluorescence-based maximal quantum yield for PSII as a diagnostic of nutrient stress. J. Phycol. 37: 517-529.

Pauly, D., V. Christensen and C. Walters. 2000. Ecopath, Ecosim and Ecospace as tools for evaluating ecosystem impact of fisheres. ICES Journal of Marine Sciences. 57: 697-706.

Pemberton, K.L. R.E.H. Smith, G.M. Silsbe, T. Howell and S.B. Watson. 2007. Controls on phytoplankton physiology in Lake Ontario during the late summer: Evidence from new fluorescence methods. Can. J. Fish. Aquat. Sci. 64: 58-73.

Peterson, B.J. 1980. Aquatic primary productivity and the ^{14}C-CO_2 method: A history of the productivity problem. Ann. Rev. Ecol. Syst. 11: 359-385.

Pope, R.M. and E.S. Fry. 1997. Absorption spectrum (380-700 nm) of pure water. Integrating cavity measurements. Applied Optics. 36(33): 8710-8723.

Prasil, O., D.J. Suggett, J.J. Cullen, M. Babin and Govindjee. 2008. Aquaflo 2007: chlorophyll fluorescence in aquatic sciences, an international conference held in Nove Hrady. Photosynth. Res. 95: 111-115.

Raateoja, M.P. and J. Seppala. 2001. Light utilization and photosynthetic efficiency of *Nannochloris* sp. (Chlorophyceaa) approached by spectral absorption characteristics and fast repetition rate fluorometry. Boreal Environment Research. 6: 205-220.

Raateoja, M., J. Seppala and H. Kuosa. 2004a. Bio-optical modelling of primary production in the SW Finnish coastal zone, Baltic Sea: Fast repetition rate fluorometry in Case 2 waters. Mar. Ecol. Prog. Ser. 267: 9-26.

Raateoja, M., J. Seppala and P. Ylostalo. 2004b. Fast repetition rate fluorometry is not applicable to studies of filamentous cyanobacteria from the Baltic Sea. Limnol. Oceanogr. 49(4) 1006-1012.

Rao, Y.R., N. Hawley, M.N. Charlton and W.M. Schertzer. 2008. Physical processes and hypoxia in the central basin of Lake Erie. Limnol. Oceanogr. 53(5): 2007-2020.

Rattan, K.J. 2009. Traditional and new fluorometric methods to determine phytoplankton nutrient status in freshwater lakes. Ph.D. Thesis. University of Waterloo. Waterloo, ON, Canada.

Reynolds, C.S. 2006. Ecology of Phytoplankton. Cambridge University Press. New York, USA.

Roesler, C.S. 1998. Theoretical and experimental approaches to improve the accuracy of particulate absorption coefficients derived from the quantitative filter technique. Limnol. Oceanogr. 43(7): 1649-1660.

Ross, O.N., C.M. Moore, D.J. Suggett, H.M. MacIntyre and R.J. Geider. 2008. A model of photosynthesis and photo-protection based on reaction center damage and repair. Limnol. Oceaongr. 53(5):1835-1852.

Sakshaug, E., G. Johnsen, K. Andersen and M. Vernet. 1991. Modeling of light-dependent algal photosynthesis and growth: Experiments with the Barents Sea diatoms *Thalassiosira nordenkioeldii* and *Chaetoceros furcellatus*. Deep-Sea Res. 38:415-430.

Schelske, C.L. and J.R. Roth. 1973. Limnological survey of lakes Michigan, Superior, Huron and Erie. Univ. Mich., Great Lakes Res. Div. Publ. 17: 108p.

Silsbe, G.M., Hecky, R. E., Guildford, S. J. and Mugidde, R. 2006. Variability of chlorophyll a and photosynthetic parameters in a nutrient-saturated tropical great lake. Limnol. Oceanogr. 51(5): 2052–2063.

Smith, R.C. and K.S. Baker. 1978. Optical classification of natural waters. Limnol. Oceanogr. 23(2): 260-267.

Smith, R.E.H., V.P. Hiriart-Baer, S.N. Higgins, S.J. Guildford and M.N. Charlton. 2005. Planktonic primary production in the offshore waters of dreissenid-infested Lake Erie in 1997. J. Great Lakes Res. 31 Suppl. 2: 50-62.

Smyth, T.J., K.L. Pemberton, J. Aiken and R.J. Geider. 2004. A methodology to determine primary production and phytoplankton photosynthetic parameters from fast repetition rate fluorometry. J. Plank. Res. 26(11): 1337-1350.

Stadelmann, P.J., E. Moore and E. Pickett. 1974. Primary production in relation to temperature structure, biomass concentration, and light conditions at an inshore and offshore station in Lake Ontario. J. Fish. Res. Bd. Can. 31: 1215-1232.

Steeman-Nielsen, E. 1952. The use of radioactive carbon (C4) for measuring organic production in the sea. J. Cons. Int. Exlp. Mer. 18: 117-140.

Stomp, M., J. Huisman, F. De Jongh, A.J. Veraart, D. Gerla, M. Rihkeboer, B.W. Ibelings, U.I.A. Wollenzien and L.J. Stal. 2004. Adaptive divergence in pigment composition promotes phytoplankton biodiversity. Nature: 432: 104-108.

Stomp, M., J. Huisman, L.J. Stal and H.C.P. Matthijs. 2007. Colorful niches of phototrophic microogarnisms shaped by vibrations of water molecules. ISME Journal. 1:271-282.

Stomp, M., J. Huisman, L. Voros, F.R. Pick, M. Laamanen, T. Haverkamp and L.J. Stal. 2007B. Colourful coexistence of red and green picocyanobacteria in lakes and seas. *Ecology Letters*. 10 (4): 290-298.

Strutton, P.G., J.G. Mitchell, J.S. Parslow and R.M. Greene. 1997. Phytoplankton patchiness: Quantifying the biological contribution using fast repetition rate fluorometry. J. Plank. Res. 19(9): 1265-1274.

Subramaniam, A., E.J. Carpenter, D. Karentz, and P.G. Falkowski. Bio-optical properties of the marine diazotrophic cyanobacteria *Trichodesmium* spp. Absorption and photosynthetic action spectra. Limnol. Oceanogr. 44(3): 608-617.

Suggett, D., G. Kraay, P. Holligan, M. Davey, J. Aiken and R. Geider. 2001. Assessment of photosynthesis in a spring cyanobacterial bloom by use of a fast repetition rate fluorometer. Limnol. Oceanogr. 46(4): 802-810.

Suggett, D., H.L. MacIntyre and R.J. Geider. 2004. Evaluation of biophysical and optical determinations of light absorption by photosystem II in phytoplankton. Limnol. Oceanogr: Methods. 2: 316-332.

Suggett, D.J., S.C. Maberly and R.J. Geider. 2006. Gross photosynthesis and lake community metabolism during the spring phytoplankton bloom. Limnol. Oceanogr. 51(5):2064-2076.

Suggett, D.J., C.M. Moore, A.E. Hickman and R.J. Geider. 2009. Interpretation of fast repetition rate (FRR) fluorescence: Signatures of phytoplankton community versus physiological state. Mar. Ecol. Prog. Ser. 376:1-19.

Sukenic, A., K.D. Wyman, J. Bennett and P.G. Falkowski. 1987. A novel mechanism for regulating the excitation of photosystem II in a green alga. Nature: 327:704-707.

Takahashi, M., S. Ichimura, M. Kishino and N. Okami. 1989. Shade and chromatic adaptation of phytoplankton photosynthesis in a thermally stratified sea. Mar. Biol. 100: 401-409.

Talling, J.F. 1957. The phytoplankton population as a compound photosynthetic system. New. Phytol. 56: 133-149.

Tassan. S. and G.M. Ferrari. 1995. An alternative approach to absorption measurements of aquatic particles retained on filters. Limnol. Oceanogr. 40(8): 1358-1368.

Titman, D. and P. Kilham. 1976. Sinking in freshwater phytoplankton: Some ecological implications of cell nutrient status and physical mixing processes. Limnol. Oceanogr. 21(3): 409-417.

Urban, N.R., M.T. Auer, S.A. Green, X. Lu, S. Apul, K.D. Powell and L. Bub. 2005. Carbon cycling in Lake Superior. J. Geophys. Res. 110: C06S90: doi: 10.1029 / 2003JC002230.

UNESCO working group 15. 1965. Report of the first meeting of the joint group of experts on photosynthetic radiant energy. UNESCO Tech. Pap. Mar. Sci. 2: 11 pp.

Vadeboncoeur, Y., E. Jeppesen, M.J. Vander Zanden, H.-H. Schierup, K. Christoffersen., D.M. Lodge. 2003. From Greenland to green lakes: Cultural eutrophication and the loss of benthic pathways in lakes. Limnol. Oceanogr. 48(4): 1408-1418.

Vanni, M.J. 2002. Nutrient cycling by animals in freshwater ecosystems. Annu. Rev. Ecol. Syst. 33: 341-370.

Voros, L., C. Calliere, K.V. Balogy and R. Bertoni. 1998. Freshwater picocyanobacteria along a trophic gradient and light quality range. Hydrobiologia. 369: 117-125.

Waston, N.H.F. and G.F. Carpenter. 1974. Seasonal abundance of crustacean zooplankton and net plankton biomass of Lakes Huron, Erie and Ontario. J. Fish. Res. Board. Can. 31: 309-317.

Watson, N.H.F., H.F. Nicholson and L.R. Culp. 1975. Chlorophyll a and primary production in Lake Superior, May to November, 1973. Fisheries and Marine Service. Technical Report 525. Environment Canada.

Wetzel, R.G. 2001. Limnology: Lake and river ecosystems. Academic Press.

Wetzel, R.G. and G.E. Likens. 1991. Limnological Analyses. 2nd edition. Springer-Verlag, New York. 39 pp.

Wilhelm, S.W., G.S. Bullerjahn, M.L. Eldridge, J.M. Rinta-Kanto, L. Poorvin and R.A. Bourbonniere. 2006. Seasonal hypoxia and the genetic diversity of prokaryote populations in the central basin hypolimnion of Lake Erie: Evidence for abundant cyanobacteria and photosynthesis. J. Great Lakes Res. 32: 657-671.

Williamson, C.E., R.W. Sanders, R.E. Moeller and P.L. Stutzman. 1996. Utilization of subsurface food resources for zooplankton reproduction: Implications for diel vertical migration theory. *Limnol. Oceanogr.* 41: 224-253.

Xiong, J. and C.E. Bauer. 2002. Complex evolution of photosynthesis. Annu. Rev. Plant Biol. 53: 503-521.

Zar, J.H. 1996. Biostatistical analysis. Prentice Hall. Upper Saddle River, New Jersey.

Zeebe, R.E. and D. Wolf-Gladrow. 2001. CO2 in seawater: equilibrium, kinetics and isotopes. Elsevier. New York, USA.

Appendix A

Limnological Data

Table 6.1: Summary of ^{14}C, chl *a* and k_{PAR} data. α has units [mg C m^{-3} hr^{-1} ($\mu mol.m^{-2}.s^{-1})^{-1}$] and P_M has units [mg C m^{-3} h^{-1}]. n.m. is not measured.

				14C PE Parameters		
Day of Year	Time	Depth [m]	Station	α	P_M	Chl *a* [mg m^{-3}]
123	17	2	84	0.038	3.76	2.35
123	625	2	956	0.054	6.73	1.03
123	1018	2	955	n.m.	n.m.	6.68
123	1213	2	84	n.m.	n.m.	2.49
123	1421	2	954	0.319	28.89	4.31
123	1741	2	952	0.119	6.08	2.05
123	1855	2	951	0.128	8.21	3.54
123	1855	9	951	0.087	4.88	1.96
123	2011	2	950	0.120	8.08	2.37
124	45	2	84	0.104	5.98	2.46
124	45	9	84	0.089	5.05	1.07
124	745	2	964	0.036	4.49	0.73
124	927	2	963	0.058	3.13	3.01
124	1053	2	962	0.069	4.14	4.49
124	1239	2	961	0.065	4.49	3.33
124	1239	9	961	0.095	6.53	2.33
124	1420	2	960	0.087	8.71	3.60
124	1420	9	960	0.088	6.61	2.79
124	1420	15	960	0.112	5.78	3.21
124	1526	2	959	0.039	4.70	1.30
124	1921	2	966	n.m.	n.m.	3.42
124	2154	2	357	0.140	5.77	3.23
125	733	2	971	0.119	10.91	1.10
125	849	2	972	0.013	1.91	0.78
125	1011	2	973	0.082	5.50	1.62
125	1052	2	882	0.075	8.68	2.90
125	1211	2	974	0.147	8.04	2.70
125	1211	6	974	0.101	11.89	1.97
125	1335	2	357	0.056	5.96	3.04
125	1517	2	969	0.044	2.98	1.38
125	1654	2	968	0.031	2.06	1.69
125	1817	2	967	n.m.	n.m.	3.66
125	2016	2	357	0.062	2.77	4.11

Table 6.1: Continued.

Day of Year	Time	Depth [m]	Station	14C PE Parameters		Chl *a* [mg m^{-3}]
				α	P_M	
159	201	3.5	ER92	0.043	4.50	1.75
159	412	4.5	968	0.068	5.67	1.49
159	620	3	ER58	0.045	5.31	1.37
159	620	8.5	ER58	0.102	6.40	1.94
159	726	3	969	0.053	9.30	1.68
159	1013	2.5	1163	1.613	155.24	11.06
159	1445	3.6	1005	0.024	4.26	1.34
159	1903	4	412	0.013	1.61	0.99
159	1903	15.4	412	0.106	3.69	4.36
160	5	4.5	962	n.m.	n.m.	1.45
160	645	5	ER73	0.018	2.36	0.93
160	645	14.5	ER73	n.m.	n.m.	1.80
160	1328	0.6	ER37	0.030	4.19	1.98
160	1328	16.5	ER37	0.135	4.78	6.02
160	2322	3.6	950	0.018	1.46	1.03
161	320	5	ER31	0.028	2.10	0.81
161	320	18.5	ER31	0.143	2.90	4.67
161	902	4.5	1003	0.009	0.72	0.34
161	1516	5	ER15	0.039	4.46	1.93
161	1516	9.5	ER15	0.144	5.07	4.09
161	1516	41	ER15	0.017	1.36	0.52
161	2027	2.5	449	0.017	2.36	0.87
162	406	3	931	0.012	1.55	0.52
162	802	5.5	936	0.039	4.66	1.19
162	802	18	936	0.046	2.60	0.96
162	1345	6.5	942	0.048	6.08	1.33
163	425	2	958	0.032	3.57	1.67
163	425	10	958	0.187	5.91	3.02
200	7	2	84	0.047	3.46	1.41
200	7	17	84	0.093	8.50	3.44
200	743	2	956	0.094	8.72	2.60
200	1136	2	84	0.032	3.30	1.36
200	1136	14	84	0.102	2.90	1.82
200	1136	23	84	0.143	7.09	2.58
200	1307	2	954	0.035	3.28	1.36
200	1633	2	952	0.046	6.26	1.78
200	1633	14	952	0.063	5.85	2.45
200	1633	17	952	0.233	10.76	3.76
200	1853	2	950	0.049	5.19	2.19
201	11	2	84	0.022	2.70	1.34
201	11	14	84	0.195	4.35	2.45

Table 6.1: Continued.

				14C PE Parameters		
Day of Year	Time	Depth [m]	Station	α	P_M	Chl *a* [mg m^{-3}]
201	11	23	84	0.186	7.67	3.03
201	745	2	964	0.093	13.11	4.91
201	1035	2	962	0.060	9.33	3.59
201	1035	15	962	0.113	11.46	3.99
201	1231	2	961	0.072	10.28	2.49
201	1231	13	961	0.121	11.28	3.21
201	1231	17	961	n.m.	n.m.	4.18
201	1534	2	959	0.099	14.86	2.60
201	1534	6	959	0.040	2.92	1.33
201	2245	2	357	0.062	7.81	3.84
202	759	2	1163	5.834	644.96	30.02
202	1008	2	969	0.504	78.34	11.47
202	1220	2	968	0.282	31.97	5.45
202	1541	2	357	0.147	26.17	4.81
202	1828	2	882	0.681	86.44	14.60
202	2106	2	971	0.265	12.27	5.74
250	1445	2	496	0.700	67.61	n.m.
250	1447	2	1163	1.833	181.29	24.27
250	1737	2	969	0.163	25.69	6.44
250	2027	2	835	0.326	42.82	8.09
250	2106	2	973	0.461	30.52	6.10
250	2353	2	881	0.229	26.21	9.28
251	132	2	580	0.191	17.20	8.86
251	506	2	968	0.203	24.95	7.93
251	739	2	1005	0.282	40.50	10.24
251	1319	2	412	0.147	12.08	5.28
251	2110	2	ER73	0.253	13.85	6.61
251	2110	23.5	ER73	0.061	3.55	2.38
251	2305	2	ER37	0.170	9.02	5.34
252	322	2	950	0.149	7.31	3.47
252	702	2	ER31	0.123	9.15	7.18
252	702	21	ER31	0.121	6.82	4.58
252	1251	2	1003	0.159	13.63	5.62
252	1251	17.9	1003	n.m.	n.m.	n.m.
252	1742	2	ER15	0.135	9.23	2.97
252	1742	21.7	ER15	0.021	1.42	0.61
252	2103	2	449	0.093	6.35	2.63
253	221	2	931	0.055	4.45	2.06
253	740	2	942	0.114	7.90	3.49
253	844	2	936	0.109	8.92	2.35
253	844	16	936	0.132	9.33	1.52

Table 6.2: Summary of bio-optical measurements. σ_{PSII} has units Angstrom^2 quanta^{-1}, a_{PS} and a_{PSII} have units m^{-1}. All other parameters are dimensionless. SCF_{APS} and SCF_F normalize the *in vitro* tungsten-halogen light spectrum to a flat (constant) spectrum using the spectrum from a_{PS} and the fluoroprobe respectively.

Day of		Depth		FRRF Parameters				Bio-optical Parameters					
Year	Time	[m]	Station	F_M	F_V/F_M	F_q/F_M	σ_{PSII}	a_{PS}	a_{PSII}	P_{NO}	$P_{0.5}$	SCF_{APS}	SCF_F
123	17	2	84	7.45	0.67	0.65	345	0.047	0.025	0.97	0.54	0.76	0.71
123	625	2	956	2.22	0.74	0.72	286	n.m.	0.009	n.m.	n.m.	n.m.	0.72
123	1018	2	955	7.83	0.77	0.63	246	0.038	0.032	1.38	0.84	0.88	0.71
123	1213	2	84	5.89	0.72	0.63	347	0.035	0.009	0.60	0.26	0.76	0.75
123	1421	2	954	12.61	0.79	0.77	331	0.052	0.038	1.13	0.73	0.82	0.68
123	1741	2	952	6.10	0.71	0.63	331	0.037	0.014	0.65	0.37	0.79	0.77
123	1855	2	951	5.95	0.72	0.66	323	0.038	0.022	0.80	0.57	0.77	0.69
123	1855	9	951	5.86	0.71	0.67	309	n.m.	0.022	n.m.	n.m.	n.m.	0.69
123	2011	2	950	8.35	0.96	0.94	287	0.046	0.020	0.57	0.43	0.66	0.67
124	45	2	84	5.29	0.61	0.63	351	0.030	0.022	0.92	0.74	0.76	0.72
124	45	9	84	5.89	0.67	0.63	317	n.m.	0.022	n.m.	n.m.	n.m.	0.72
124	745	2	964	1.19	0.37	0.67	400	n.m.	0.007	n.m.	n.m.	n.m.	0.79
124	927	2	963	5.66	0.71	0.54	318	0.055	0.020	0.70	0.37	0.76	0.71
124	1053	2	962	9.91	0.76	0.68	320	0.073	0.031	0.86	0.43	0.76	0.70
124	1239	2	961	13.17	0.81	0.69	225	0.017	0.017	0.75	0.97	0.88	0.74
124	1239	9	961	6.92	0.66	0.40	223	n.m.	0.036	n.m.	n.m.	n.m.	0.73
124	1420	2	960	6.83	0.80	0.66	335	0.063	0.014	0.58	0.21	0.72	0.74
124	1420	9	960	6.83	0.80	0.66	335	n.m.	0.025	n.m.	n.m.	n.m.	0.68
124	1420	15	960	6.19	0.80	0.68	338	n.m.	0.026	n.m.	n.m.	n.m.	0.66
124	1526	2	959	0.57	0.38	0.38	133	0.035	0.021	0.32	0.61	0.66	0.93
124	1921	2	966	5.60	0.57	0.52	403	0.039	0.021	0.84	0.53	0.77	0.64
124	2154	2	357	4.44	0.85	0.84	337	0.028	0.018	0.80	0.65	0.78	0.72
125	733	2	971	2.58	0.63	0.63	322	0.015	0.007	1.21	0.48	0.90	0.78
125	849	2	972	1.39	0.72	0.47	552	0.019	n.m.	n.m.	n.m.	0.76	n.m.
125	1011	2	973	3.97	0.75	0.75	347	0.031	0.013	0.80	0.41	0.81	0.68
125	1052	2	882	4.72	0.92	0.78	318	0.038	0.016	0.93	0.42	0.79	0.70
125	1211	2	974	3.45	0.75	0.75	331	0.035	0.033	0.71	0.95	0.80	0.83

Table 6.2: Continued.

Day of Year	Time	Depth [m]	Station	FRRF Parameters				Bio-optical Parameters					
				F_M	F_V/F_M	F_q/F_M	σ_{PSII}	a_{PS}	a_{PSII}	P_{NO}	$P_{0.5}$	SCF_{APS}	SCF_F
125	1211	6	974	3.45	0.75	0.75	331	n.m.	0.039	n.m.	n.m.	n.m.	0.81
125	1335	2	357	5.33	0.81	0.81	406	0.037	0.012	0.70	0.33	0.77	0.73
125	1517	2	969	1.98	0.81	0.60	263	0.022	0.009	0.91	0.42	0.84	0.72
125	1654	2	968	2.65	0.66	0.50	311	0.042	0.015	0.69	0.35	0.74	0.72
125	1817	2	967	n.m.	n.m.	n.m.	n.m.	0.049	0.022	0.96	0.44	0.78	0.70
125	2016	2	357	7.61	0.90	0.88	330	0.039	0.025	1.03	0.65	0.79	0.69
158	1119	2	881	n.m.	n.m.	n.m.	n.m.	0.048	0.025	1.06	0.51	0.82	0.70
158	1530	1.8	973	3.20	0.51	0.51	377	0.084	0.018	0.79	0.21	0.80	0.72
158	1634	1.9	835	2.47	0.81	0.79	327	n.m.	0.037	n.m.	n.m.	n.m.	0.89
159	201	3.5	ER92	3.73	0.83	0.88	561	0.029	0.012	0.65	0.43	0.74	0.72
159	412	4.5	968	3.08	0.80	0.85	590	0.028	0.012	0.99	0.44	0.76	0.68
159	620	3	ER58	2.00	0.77	0.77	512	0.026	0.009	0.94	0.36	0.78	0.72
159	620	8.5	ER58	3.05	0.80	0.80	462	0.031	0.015	1.11	0.48	0.83	0.75
159	726	3	969	1.70	0.87	0.80	393	0.025	0.010	0.91	0.39	0.80	0.76
159	1013	2.5	1163	7.25	0.62	0.60	315	0.144	0.198	0.62	1.37	0.83	1.13
159	1445	3.6	1005	1.77	0.62	0.62	682	0.025	0.006	0.46	0.24	0.72	0.72
159	1903	4	412	1.11	0.73	0.68	547	0.020	0.005	0.66	0.26	0.74	0.67
159	1903	15.4	412	8.23	0.75	0.77	445	0.058	0.028	1.14	0.48	0.79	0.69
160	5	4.5	962	2.32	0.80	0.78	523	0.022	0.009	0.78	0.42	0.77	0.71
160	645	5	ER73	1.50	0.73	0.74	513	0.016	0.005	0.59	0.33	0.75	0.68
160	645	14.5	ER73	n.m.	n.m.	n.m.	n.m.	0.016	0.018	2.30	1.09	1.14	0.70
160	1328	0.6	ER37	0.46	0.74	0.74	163	0.032	0.007	0.40	0.23	0.71	0.74
160	1328	16.5	ER37	11.23	0.85	0.63	547	0.062	0.052	1.38	0.84	0.81	0.67
160	2322	3.6	950	1.46	0.73	0.77	484	0.018	0.005	0.57	0.26	0.77	0.71
161	320	5	ER31	1.31	0.75	0.71	454	0.015	0.006	0.65	0.36	0.79	0.73
161	320	18.5	ER31	6.77	0.71	0.76	368	0.065	0.033	1.06	0.51	0.84	0.73
161	902	4.5	1003	0.22	0.90	0.90	140	0.008	0.002	0.21	0.21	0.77	0.82
161	1516	5	ER15	3.49	0.72	0.62	584	0.043	0.014	0.77	0.33	0.67	0.63
161	1516	9.5	ER15	6.92	0.71	0.66	373	0.080	0.030	0.82	0.37	0.69	0.65
161	1516	41	ER15	0.75	0.69	0.71	409	0.009	0.002	0.46	0.26	0.73	0.82
161	2027	2.5	449	1.74	0.81	0.71	561	0.022	0.006	0.44	0.28	0.66	0.57

Table 6.2: Continued.

Day of Year	Time	Depth [m]	Station	FRRF Parameters F_M	F_V/F_M	F_q/F_M	σ_{PSII}	Bio-optical Parameters a_{PS}	a_{PSII}	P_{NO}	$P_{0.5}$	SCF_{APS}	SCF_F
162	406	3	931	1.24	0.71	0.75	517	0.012	0.004	0.79	0.33	0.73	0.66
162	802	5.5	936	2.33	0.96	0.73	516	0.018	0.008	0.59	0.45	0.71	0.64
162	802	18	936	1.64	0.84	0.71	481	0.020	0.006	0.52	0.31	0.75	0.66
162	1345	6.5	942	2.69	0.90	0.74	548	0.018	0.008	0.53	0.45	0.75	0.67
163	425	2	958	n.m.	n.m.	n.m.	n.m.	0.030	0.013	0.93	0.43	0.71	0.64
163	425	10	958	n.m.	n.m.	n.m.	n.m.	0.037	0.031	1.09	0.83	0.78	0.66
200	7	2	84	2.41	0.78	0.77	541	n.m.	0.013	n.m.	n.m.	n.m.	0.75
200	7	17	84	3.48	0.80	0.86	359	n.m.	0.026	n.m.	n.m.	n.m.	0.87
200	743	2	956	3.04	0.92	0.75	395	n.m.	0.016	n.m.	n.m.	n.m.	0.82
200	1136	2	84	1.43	0.85	0.61	361	n.m.	0.008	n.m.	n.m.	n.m.	0.83
200	1136	14	84	2.56	0.84	0.65	379	n.m.	0.016	n.m.	n.m.	n.m.	0.81
200	1136	23	84	2.65	0.81	0.78	378	n.m.	0.019	n.m.	n.m.	n.m.	0.83
200	1307	2	954	2.36	0.84	0.70	367	n.m.	0.007	n.m.	n.m.	n.m.	0.88
200	1633	2	952	2.86	0.68	0.61	395	n.m.	0.014	n.m.	n.m.	n.m.	0.75
200	1633	14	952	3.39	0.83	0.75	395	n.m.	0.021	n.m.	n.m.	n.m.	0.77
200	1633	17	952	3.16	0.73	0.69	315	n.m.	0.031	n.m.	n.m.	n.m.	0.89
200	1853	2	950	2.95	0.77	0.60	281	n.m.	0.021	n.m.	n.m.	n.m.	0.75
201	11	2	84	1.81	0.77	0.74	507	n.m.	0.009	n.m.	n.m.	n.m.	0.78
201	11	14	84	3.49	0.85	0.85	418	n.m.	0.021	n.m.	n.m.	n.m.	0.83
201	11	23	84	2.93	0.78	0.92	396	n.m.	0.019	n.m.	n.m.	n.m.	0.82
201	745	2	964	3.40	0.89	0.84	343	n.m.	0.020	n.m.	n.m.	n.m.	0.79
201	1035	2	962	3.06	0.88	0.85	336	n.m.	0.013	n.m.	n.m.	n.m.	0.79
201	1035	15	962	2.25	0.74	0.68	221	n.m.	0.030	n.m.	n.m.	n.m.	0.94
201	1231	2	961	3.76	0.84	0.77	384	n.m.	0.012	n.m.	n.m.	n.m.	0.76
201	1231	13	961	3.74	0.82	0.81	343	n.m.	0.027	n.m.	n.m.	n.m.	0.88
201	1231	17	961	3.03	0.70	0.70	209	n.m.	0.058	n.m.	n.m.	n.m.	0.98
201	1534	2	959	2.34	0.65	0.59	252	n.m.	0.018	n.m.	n.m.	n.m.	0.76
201	1534	6	959	2.67	0.73	0.72	238	n.m.	0.014	n.m.	n.m.	n.m.	0.76
201	2245	2	357	4.64	0.80	0.78	411	n.m.	0.026	n.m.	n.m.	n.m.	0.77
202	759	2	1163	3.00	0.58	0.58	147	n.m.	0.416	n.m.	n.m.	n.m.	1.14
202	1008	2	969	11.00	0.86	0.78	294	n.m.	n.m.	n.m.	n.m.	n.m.	n.m.

Table 6.2: Continued.

Day of Year	Time	Depth [m]	Station	FRRF Parameters				Bio-optical Parameters					
				F_M	F_V/F_M	F_q/F_M	σ_{PSII}	a_{PS}	a_{PSII}	P_{NO}	$P_{0.5}$	SCF_{APS}	SCF_F
202	1220	2	968	11.59	0.96	0.87	438	n.m.	n.m.	n.m.	n.m.	n.m.	n.m.
202	1541	2	357	7.68	0.86	0.77	343	n.m.	n.m.	n.m.	n.m.	n.m.	n.m.
202	1828	2	882	14.51	0.89	0.83	307	n.m.	n.m.	n.m.	n.m.	n.m.	n.m.
202	2106	2	971	5.75	0.91	0.86	424	n.m.	n.m.	n.m.	n.m.	n.m.	n.m.
250	1445	2	496	n.m.	n.m.	n.m.	n.m.	n.m.	n.m.	n.m.	n.m.	n.m.	n.m.
250	1447	2	1163	13.99	0.75	0.80	335	0.270	0.182	0.60	0.67	0.80	1.07
250	1737	2	969	5.83	0.67	0.75	393	0.088	0.036	1.11	0.41	0.78	0.75
250	2027	2	835	n.m.	n.m.	n.m.	n.m.	0.112	0.030	1.12	0.27	0.88	0.85
250	2106	2	973	n.m.	n.m.	n.m.	n.m.	0.071	0.040	1.14	0.56	0.86	1.01
250	2353	2	881	13.73	0.90	0.89	412	0.089	0.056	1.07	0.62	0.82	0.69
251	132	2	580	10.52	0.85	0.80	366	0.093	0.046	0.99	0.49	0.78	0.70
251	506	2	968	n.m.	n.m.	n.m.	n.m.	n.m.	0.040	n.m.	n.m.	n.m.	0.72
251	739	2	1005	n.m.	n.m.	n.m.	n.m.	0.065	0.058	1.02	0.89	0.84	0.75
251	1319	2	412	3.42	0.76	0.71	359	0.063	0.027	0.72	0.43	0.79	0.80
251	2110	2	ER73	5.69	0.74	0.74	427	0.101	0.041	0.49	0.41	0.73	0.84
251	2110	23.5	ER73	1.69	0.67	0.88	248	0.008	0.009	-0.14	1.17	0.66	0.82
251	2305	2	ER37	4.56	0.79	0.78	455	0.073	0.031	0.57	0.43	0.75	0.82
252	322	2	950	n.m.	n.m.	n.m.	n.m.	n.m.	0.026	n.m.	n.m.	n.m.	0.75
252	702	2	ER31	3.30	0.67	0.64	390	0.121	0.042	0.30	0.34	0.66	0.97
252	702	21	ER31	3.28	0.66	0.69	438	0.040	0.032	0.38	0.81	0.72	0.95
252	1251	2	1003	2.57	0.69	0.62	389	n.m.	0.025	n.m.	n.m.	n.m.	0.87
252	1251	17.9	1003	n.m.	n.m.	n.m.	n.m.	n.m.	0.006	n.m.	n.m.	n.m.	0.87
252	1742	2	ER15	2.86	0.80	0.79	425	0.050	0.021	0.57	0.43	0.72	0.82
252	1742	21.7	ER15	1.39	0.73	0.83	374	0.011	0.008	0.64	0.71	0.84	0.91
252	2103	2	449	2.82	0.74	0.77	464	0.049	0.019	0.71	0.39	0.75	0.81
253	221	2	931	2.71	0.72	0.76	487	0.032	0.017	0.71	0.53	0.79	0.80
253	740	2	942	n.m.	n.m.	n.m.	n.m.	0.046	0.025	0.60	0.54	0.81	0.92
253	844	2	936	2.66	0.71	0.63	403	0.043	0.020	0.74	0.47	0.78	0.81
253	844	16	936	1.82	0.73	0.76	381	0.018	0.012	0.76	0.67	0.85	0.82
253	1247	2	402	3.02	0.76	0.72	366	0.072	0.018	0.38	0.24	0.69	0.87
253	1247	18	402	0.99	0.68	0.68	350	0.027	0.008	0.51	0.31	0.73	0.89

Appendix B

Geographic Data

Table 6.3: Station locations and distances along longitudinal curtain shown in Figure 4.3.

Station	Longitude (Degrees)	Latitude (Degrees)	Easting (m)	Northing (m)	Basin	Distance (km)
973	-83.333	41.791	306179	4629257	West	5
835	-83.348	41.751	304769	4624833	West	6
881	-83.208	41.969	317074	4648711	West	7
882	-83.322	41.764	307012	4626229	West	7
ER60	-83.197	41.891	317736	4640045	West	11
972	-83.199	41.866	317530	4637248	West	12
580	-83.106	41.849	325156	4635119	West	20
971	-83.050	41.950	330087	4646257	West	20
ER61	-83.045	41.946	330478	4645859	West	20
974	-83.150	41.725	321196	4621477	West	22
ER59	-83.150	41.727	321150	4621664	West	22
357	-82.970	41.826	336426	4632376	West	31
ER91	-82.917	41.841	340826	4633881	West	35
ER58	-82.934	41.685	339067	4616610	West	40
969	-82.925	41.608	339626	4608080	West	44
ER92	-82.688	41.950	360093	4645621	West	47
966	-82.625	41.983	365384	4649203	West	50
967	-82.667	41.892	361712	4639122	West	51
968	-82.733	41.742	355868	4622545	West	53
496	-82.723	41.569	356359	4603413	West	62
1163	-82.703	41.475	357819	4592869	West	67
311	-82.500	41.666	375111	4613836	West	74
965	-82.501	41.501	374723	4595482	West	82
1005	-82.394	41.835	384281	4632432	Central-West	92
964	-82.182	41.518	401360	4596974	Central-West	94
963	-82.181	41.575	401511	4603296	Central-West	96
962	-82.185	41.716	401453	4618923	Central-West	103
M8	-82.200	41.833	400359	4631967	Central-West	107
961	-82.183	41.908	401858	4640275	Central-West	112
1191	-82.200	41.932	400526	4642922	Central-West	112
412	-82.190	42.099	401627	4661490	Central-West	120
960	-82.184	42.102	402132	4661742	Central-West	121
ER43	-81.945	41.789	421465	4626781	Central-West	124
959	-82.183	42.195	402344	4672135	Central-West	125
ER42	-82.042	41.965	413685	4646452	Central-West	125

Table 6.3: Continued.

Station	Longitude (Degrees)	Latitude (Degrees)	Easting (m)	Northing (m)	Basin	Distance (km)
958	-81.703	41.549	441357	4599980	Central-West	131
1192	-81.697	41.733	442035	4620386	Central-West	140
ER73	-81.756	41.978	437327	4647610	Central-West	147
1190	-81.816	42.140	432542	4665662	Central-West	150
84	-81.643	41.927	446682	4641835	Central-West	153
956	-81.469	41.707	460981	4617371	Central-East	156
955	-81.442	41.799	463284	4627604	Central-East	163
ER36	-81.479	41.935	460303	4642634	Central-East	166
ER37	-81.575	42.110	452462	4662131	Central-East	167
ER38	-81.672	42.282	444606	4681269	Central-East	167
954	-81.442	42.025	463436	4652615	Central-East	173
953	-81.441	42.208	463587	4672940	Central-East	181
M10	-81.251	41.883	479216	4636854	Central-East	181
952	-81.441	42.359	463674	4689688	Central-East	188
ER78	-81.250	42.117	479333	4662742	Central-East	192
951	-81.441	42.475	463787	4702611	Central-East	194
1061	-81.365	42.361	469957	4689868	Central-East	194
950	-81.443	42.556	463619	4711570	Central-East	197
ER32	-81.012	42.082	499022	4658844	Central-East	208
ER30	-81.205	42.430	483137	4697560	Central-East	209
ER31	-81.107	42.254	491174	4677928	Central-East	209
947	-80.642	41.990	529681	4648765	Central-East	232
M13	-80.799	42.251	516554	4677609	Central-East	232
402	-80.559	42.145	536467	4665933	Central-East	245
1003	-80.641	42.284	529599	4681372	Central-East	245
489	-80.300	42.167	557834	4668500	Central-East	266
1047	-80.274	42.361	559826	4690096	Central-East	276
1108	-80.139	42.719	570498	4729989	East	302
942	-79.830	42.260	596487	4679344	East	305
ER15	-79.894	42.516	590839	4707662	East	312
449	-79.987	42.761	582860	4734791	East	315
ER63	-79.800	42.417	598744	4696738	East	315
ER09	-79.616	42.538	613650	4710441	East	334
ER10	-79.692	42.680	607192	4726129	East	334
936	-79.393	42.510	632008	4707636	East	349
932	-79.211	42.792	646326	4739233	East	375
931	-78.942	42.849	668183	4746138	East	398